UNIVERSITÀ
DEGLI STUDI
DI PADOVA

Sede Amministrativa: Università degli Studi di Padova

Dipartimento di Ingegneria Industriale

SCUOLA DI DOTTORATO DI RICERCA IN INGEGNERIA INDUSTRIALE
INDIRIZZO: INGEGNERIA CHIMICA, DEI MATERIALI E DELLA PRODUZIONE
CICLO: XXVI

STUDY OF NON CATALYTIC GAS-SOLID REACTIONS: DEVELOPMENT OF A SINGLE PARTICLE MODEL

Direttore della Scuola : Ch.mo Prof. Paolo Colombo
Coordinatore d'indirizzo: Ch.mo Prof. Enrico Savio
Supervisore :Ch.mo Prof. Paolo Canu

Dottorando : Tommaso Melchiori

Abstract

This thesis investigates single particle models to describe non catalytic gas-solid reactions. A comparative study was made between the traditional shrinking core model and more detailed continuous models, involving the solution of microscopic balances for the solid and gas phases inside a single porous particle. Such a study proved that in some cases the use of the shrinking core model can lead to severe errors in the prediction of conversion, and that kinetic parameters in SCM are affected by the particle size. Different diffusion models were tested for the continuous model, and the inaccuracy of the Fick law compared to multicomponent Stefan-Maxwell was evaluated, depending on the concentration of the reaction gas in the mixture. The thesis also proved that natural convection inside the particle can be neglected by changing the balance from mass to molar basis or vice versa, depending on the type of reaction considered. An equation for the local particle porosity was also included, to account for the local changes of gas diffusivity as effect of the reaction. The effect of the pore size distribution was studied, by writing the particle model as a population balance, including different diffusive resistances for different pore sizes, for the cases when Knudsen or solid state diffusion can be important. Sintering phenomena were included, by extending the grain model with an empiric equation. Simulations with simultaneous gas solid reactions were performed, also considering non uniform initial distributions of the solid phases inside the particle: sensitivity studies proved that the position of the solid reagents in the particle may have a great influence on the model results, even when intra particle diffusion is fast compared to the chemical reactions. Gas-solid models were also used to simulate real processes. In particular, thanks to collaboration with an industrial research project, a kinetic study with a CFD model was developed, applying a shrinking core model to simulate real reactors for the direct reduction of iron ores with syn gas at high temperature and pressure. Finally, thanks to the collaboration with the Technical University of Eindhoven, a continuous model was used to simulate reactions of reduction of iron-titanium oxides in chemical looping combustion processes, comparing the results with experimental data.

Riassunto

Questa tesi investiga modelli di singola particella per descrivere reazioni gas-solido non catalitiche. E' stato fatto uno studio comparativo fra il tradizionale shrinking core model e modelli continui più dettagliati che comprendono la risoluzione dei bilanci microscopici per le fasi gas e solida dentro una singola particella porosa. Tale studio ha provato che in alcuni casi lo shrinking core model può condurre ad errori importanti nella predizione della conversione, e che i parametri cinetici nel SCM dipendono dalla dimensione della particella. Sono stati testati diversi modelli di diffusione all'interno del modello continuo, e la non accuratezza della legge di Fick rispetto alla Stefan-Maxwell multicomponente è stata valutata, a seconda della concentrazione del gas reagente nella miscela. La tesi prova anche che la convezione naturale all'interno della particella può essere trascurata cambiando i bilanci da massivi a molari o vice versa, a seconda del tipo di reazione considerata. Un'equazione che descrive la porosità locale della particella è stata inclusa al modello, per tener conto dei cambiamenti della diffusività effettiva del gas per effetto della reazione. L'effetto della distribuzione della dimensione dei pori è stato investigato, riscrivendo il modello di particella come bilancio di popolazione, includendo diverse resistenze diffusive per diverse dimensioni dei pori, per i casi in cui La diffusione di Knudsen o la diffusione in stato solido possono essere importanti. Fenomeni di sinterizzazione sono stati inclusi, estendendo il tradizionale grain model con un'equazione empirica. Sono state fatte simulazioni di reazioni gas solido con più reazioni, considerando anche distribuzioni disomogenee delle fasi solide all'interno della particella: studi di sensitività hanno dimostrato che la posizione dei reagenti solidi nella particella possono avere un effetto importante sui risultati del modello, anche nel caso in cui la diffusione all'interno della particella è veloce rispetto alle reazioni chimiche. Modelli di reazione gas-solido sono stati usati anche per simulare processi reali. In particolare, grazie alla collaborazione con un progetto di ricerca industriale, uno studio cinetico con modelli CFD è stato sviluppato, applicando lo shrinking core model per simulare reattori reali per la riduzione diretta di ossidi di ferro con gas di sintesi ad alte temperature e pressioni. Infine, grazie alla collaborazione con l'Università Tecnica di Eindhoven, un modello continuo è stato usato per simulare reazioni di riduzione di ossidi di ferro-titanio in processi di chemical looping combustion, confrontando i risultati con i dati sperimentali.

Contents

Chapter 1. Introduction

The occurrence of reacting porous solids in many industrial applications is impressive. They span well beyond the traditional chemical and metallurgical areas, to the energy production (coal, biomass), agrochemicals, food and pharmaceuticals, aerospace propulsion and others. Processes involving reactions with gases are more common than liquids; in this thesis, the study was focused on gas-solids applications. The reaction systems concerned are of considerable industrial importance and are readily found in chemical and metallurgical industries. Examples are the reduction of iron oxide or the oxidation of iron by steam, the roasting and smelting of ores, the combustion of solid fuels and solid propellant, the gasification of coal, the regeneration of catalysts, just to mention a few.

These systems involving heterogeneous reactions can occur in various types of reactors. In general, they are usually extremely complex, and the experimental campaigns carried out to estimate the intrinsic kinetics can easily fail to reveal the true mechanism because of the great number of variables involved. The successful determination of such variables, and the consequent design of a reactor depend greatly on the knowledge of reliable rate data. The rates of heterogeneous reactions often depend on the conditions under which the experiment is performed. Physical effects such as diffusion and heat transfer can result in an erroneous rate expression if they are not properly accounted for. The order of reaction, the activation energy, and the selectivity determined may be so misleading that, if used in scale-up, the result may lead to severe errors. It is therefore important to make a careful study of the interaction and to account for both physical effects and purely chemical processes in a correct way. Even for an isothermal reaction system, the overall reaction rates are influenced by the rate of chemical reactions occurring in or at the surface of a solid, by the mass transfer rates of fluids through the solid as well as across the fluid-film surrounding the solid. Besides, other factors can play a role, which are more strictly related to the properties of the porous matrix, such local pore size and surface characteristics, but also solid reactivity of crystallite orientation, crystallite size, etc. The description is further complicated by the fact that all of these characteristics can change in time. This change can be caused by external stresses, by high temperature sintering, or, more simply, by the chemical reaction itself. The transformation of the solid phase into a new one, with different molar volume, modifies the morphology of the solid on the scale of the pores, and sometimes the whole pellet.

For these reasons, a rigorous treatment seems very difficult to obtain, even for the solid of the simplest geometry. Besides, a great number of difficult problems exist in practical systems, such as the changing size and shape of the solid during the reaction and formation of a product around the solid reactant. Finally, the complex velocity profile of the surrounding fluid makes the problems of mass and energy transfers to the solid reactant more difficult to analyze.

The porous solid particles treated industrially are generally porous pellets. For a general reaction, involving both a solid and a gas phase in both reagents and products, the physical steps concerning the gas in the process are the following:

(i) Transfer within the external gas to the surface of the pellet.
(ii) Diffusion through the intergranular pores.

(iii) Adsorption into the solid reacting phase.
(iv) Reaction at the gas/solid interface.
(v) Desorption of the produced gas.
(vi) Diffusion of the product gas to the external particle surface.
(vii) Transfer of the produced gas from the particle surface to the bulk gas.

Each of these steps has its own kinetics and can limit, also in part, the overall rate of conversion. The process can be successfully described either as a chemical regime, when a surface process controls the overall kinetics, or as a diffusional regime when the rate is determined by diffusion, or as a mixed regime.

If the reaction is exo- or endothermic, or if the external temperature varies, the associated heat evolution or consumption phenomena, and heat transfer both within the pellet and with the exterior can have an influence on all of the mentioned steps.

In the literature, these issues have partly been discussed, and in many cases, some simplifications are assumed, in order to formulate models that are applicable to the description of full scale reactors, as much as possible. A very comprehensive, classical treatment of the subject is the seminal book of Szekely[1]. In spite of the impact, the quantitative treatment of reactive solids remains predominantly based on oversimplification of the actual physics, that can be extremely complicated by the already mentioned issues.

Looking at the different models that have been developed to describe non catalytic gas-solid reactions, two main approaches can be identified. The most rigorous one requires solving the microscopic conservation equations for the gas and the solid species within the single particle. According to this, the porous phase is treated as pseudo-homogeneous continuous phase, with a local porosity, and a local concentration of accessible surface per unit volume [2]. Important examples of these kind of continuous models are the volumetric model[3], the grain model[1], the sintering model[4] and the random pore model[5, 6]. The main difference between these is the dependency of the expression of the reaction rate on the solid reactant concentration, as Gomez-Barea and Ollero tried to classify[7]. Different degree of detail can also derive from the choice of the terms to include into the microscopic balances. Patisson et al.[8] pointed out the importance to include the gas convection generated by non equimolar reactions. Valipour et al.[9] remarked the difference that can arise while assuming pseudo steady state for the gas species with respect to the solid phase, particularly when simulating particles in non isothermal conditions. Different diffusion models can be considered, from the more rigorous Stefan Maxwell model[8], to a binary Fick[10], with diffusivity possibly dependent on the gas composition[9]. Most of the authors agree that Knudsen diffusion must also be taken into account together with molecular diffusion, with an effective coefficient depending on the porosity of the particle.

A more simplified approach assumes non-porous particles[11], or non-porous shrinking core model (SCM)[12]. The latter is widely used. According to it, the reaction is supposed to take place only on a surface separating the unreacted core by the product layer in the particle, and moving to the center as the reaction goes on. This physical description is not always correct, and in general it is not predictable whether or not a gas-solid reaction occurs by forming a core-shell structure, because that depends on the reaction conditions (structure and size of the particle, temperature, pressure, composition of the fed gas, etc). Even with this limitation, the SCM is still widely used [13-18], as it provides a simple analytical solution for most

cases, and it can still account for the presence of mass transfer resistances inside and outside the reacting solid, even if in a simplified way.

Figure 1.1 shows the comparison of the qualitative description of a single spherical reacting particle, according to the two approaches (Continuous model and Shrinking Core model).

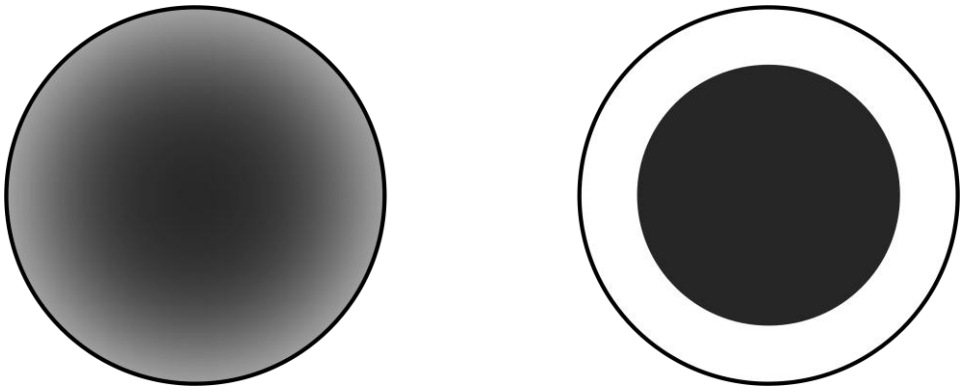

Figure 1.1: Representation of a single reacting particle with two model approaches: Continuous model (left), and shrinking core model (right)

In this thesis, these two types of models have been studied in detail, and finally applied to existing processes. The predictivity of both SCM and CM has been evaluated, and possible modifications are proposed, based on experimental evidences. Different theoretical studies have also been made, in order to evaluate, with a low number of parameters, the importance of the different kinetic and mass transfer phenomena into the global process. This can be useful to assess the impact of different kind of simplifications to the accuracy of the model.

In chapter §2, different versions and formulations of the Shrinking Core Model are presented, together with the assumptions leading to its mathematical expression. In chapter §3, an industrial application of SCM to full scale reactor models is presented: this was carried out thanks to the coupling with CFD codes. The results of a kinetic investigation on the process of direct reduction of iron ores are presented.

In chapter §4, a general form of the continuous model is discussed. Also, a review is made on the main approaches used to describe the form of the reaction rates, depending on the mechanisms of interaction of the solid and gas phase that can be considered.

The importance of the description of mass transfer mechanisms is treated in detail: in chapter §5, different expressions of diffusion models are presented, together with their adaptation to the description of diffusion inside a continuous porous matrix, having locally different characteristics. Then, in chapter §6 the different behavior of rigorous and simplified multicomponent diffusion models is evaluated, with respect to the global quantification of the particle conversions. The errors of simplified models are quantified, depending on the characteristics of the gas mixture and the controlling regime. The effect of natural convection was also considered, depending on the possible mechanisms that can generate a global gas flux (production/consumption of moles, temperature changes, porosity evolution).

In chapter §7, a continuous model approach is used to try to explain the experimental data of reduction of solids in chemical looping combustion processes. Different interpretations are formulated, based on the available evidences, and related to the detailed description of the solid matrix. In particular, they involve the inclusion of sintering, non uniform pore size distribution, gas diffusion in dense solid, effect of solid phase segregation, gas adsorption mechanisms.

In chapter §8, a comparative study between the Shrinking Core Model and the Continuous Model is shown. A mathematical function was found to relate the parameters used in the two approaches, so that the simplified SCM can better match the results of the continuous model. Also, the errors made with the SCM are evaluated, as a function of the process conditions.

Finally, in chapter §9, a numerical technique is elaborated to couple the mathematical description of the single particle to reactor models, based on polynomial collocation methods. Also, a simple PDE coupling is shown for the case of a one dimensional moving bed reactor.

Chapter 2. The shrinking core model

Let's consider a solid particle where a single gas-solid reaction occurs, in the form:

a A(s) + b B(g) → c C(s) + d D(g)

One simple way of describing the reaction of a solid particle with a gas is by using the shrinking core model [12, 19, 20]. The main assumption of this model is that the reaction develops topochemically, only on a single surface which separates two zones within the solid. An unreacted core, made of pure solid reagent, which has not been reached by the reacting gas yet, and a reacted outer layer, made of pure solid product, which is porous, and where the gas diffuses but doesn't react, because the solid matrix is completely inert. The core shell interface moves inward, as long as the core is consumed, and the shell becomes thicker. This concept can be applied to different particle geometries. For spherical pellets, the core shell interface is a spherical surface concentric to the external one.

One advantage of assuming a core-shell type reaction is that the global conversion of the single particle is simply related to the position of the core-shell interface. The conversion is in fact defined as:

$$X(t) = \frac{n(0) - n(t)}{n(0)} \qquad 2.1$$

Where n is the number of moles of the reagent solid into the particle. If the reagent is present only in the core, then the amount of reagent in the particle is linearly related to the volume of the core, via the reagent density:

$$n(t) = \frac{\rho_c}{MW_c} V_c(t) \qquad 2.2$$

So, combining equations 2.1 and 2.2 the particle conversion is:

$$X(t) = 1 - \frac{V_c(t)}{V_c(0)} \qquad 2.3$$

As a function of the pellet radius:

$$X(t) = 1 - \frac{r_i(t)^3}{r_0^3} \qquad 2.4$$

The inverse function of equation 2.4 that gives the interface position as a function of the global conversion:

$$r_i(t) = r_0\big(1 - X(t)\big)^{1/3} \qquad 2.5$$

If the layer is completely occupied by the solid product, the reagent gas only diffuses through it, without reacting. So the microscopic balance for the gas species B and D will be:

$$\frac{\partial \varepsilon c_B}{\partial t} = -\frac{1}{r^2}\frac{\partial}{\partial r}\left(r^2(x_B N + J_B^*)\right) \quad 2.6$$

$$\frac{\partial \varepsilon c_D}{\partial t} = -\frac{1}{r^2}\frac{\partial}{\partial r}\left(r^2(x_D N + J_D^*)\right) \quad 2.7$$

In this model, the reaction appears in the boundary conditions, which are:

$$r = r_i \qquad x_B N + J_B^* = -b \cdot R\left(c_B(r_i), c_D(r_i)\right) \quad 2.8$$

$$r = r_i \qquad x_D N + J_D^* = d \cdot R\left(c_B(r_i), c_D(r_i)\right) \quad 2.9$$

$$r = r_0 \qquad x_B N + J_B^* = h_B \cdot c_t \cdot \left(x_B(r_0) - x_{B,bulk}\right) \quad 2.10$$

$$r = r_0 \qquad x_D N + J_D^* = h_D \cdot c_t \cdot \left(x_D(r_0) - x_{D,bulk}\right) \quad 2.11$$

Where R is the superficial reaction rate occurring at the interface r_i. At the core shell interface, the molar flux of the single species is equal to the its superficial production rate (equations 2.8 – 2.9). At the particle surface, the molar fluxes of the gas species are equal to those calculated considering the external mass transfer resistance (equations 2.10 – 2.11). This is done by considering the mass transfer coefficients for each component.

The total molar flux N is given by the total concentration balance, which is the sum of equations 2.6 and 2.7 if the gas mixture is made only by species B and D.

$$\frac{\partial \varepsilon c_t}{\partial t} = -\frac{1}{r^2}\frac{\partial}{\partial r}(r^2 N) \quad 2.12$$

The boundary conditions for this equation are also found by summing equations 2.8-2.9 and 2.10-2.11, respectively:

$$r = r_i \qquad N = (d - b) \cdot R\left(c_B(r_i), c_D(r_i)\right) \quad 2.13$$

$$r = r_0 \qquad N = h_B \cdot c_t \cdot \left(x_B(r_0) - x_{B,bulk}\right) + h_D \cdot c_t \cdot \left(x_D(r_0) - x_{D,bulk}\right) \quad 2.14$$

The total concentration of the solid species can be obtained by adding the global solid material balances to the system of equations 2.6-2.7. The equations for species A and C are:

$$\frac{\partial C_A}{\partial t} = -a \cdot \frac{3\, r_i^2}{r_0^3} \cdot R\left(c_B(r_i), c_D(r_i)\right) \quad 2.15$$

$$\frac{\partial C_C}{\partial t} = c \cdot \frac{3\, r_i^2}{r_0^3} \cdot R\left(c_B(r_i), c_D(r_i)\right) \quad 2.16$$

It's important to note that in this notation C_A and C_C are the concentration of A and C considering the whole particle volume, whereas c_B and c_D are the local concentration of gas B and D, and are variable with r. The local concentration profiles of the solid ($c_A(r)$ and $c_C(r)$) are already solved once the interface position r_i is known. In fact they will be:

$$c_A = c_A^0 \cdot \big(1 - H(r > r_i)\big) \quad 2.17$$

$$c_A = c_A^0 \cdot \frac{c}{a}\big(H(r > r_i)\big) \quad 2.18$$

Where c_A^0 is the initial concentration of A (assuming that the particle composition is initially uniform), and $H(r > r_i)$ is the Heaviside function, which is equal to one if $r > r_i$ and is equal to zero otherwise. In other words, the solutions for the solids are step functions. Equation 2.12 can also be written in terms of particle conversion X, as follows:

$$\frac{\partial X}{\partial t} = \frac{a}{c_A^0} \cdot \frac{3\, r_i^2}{r_0^3} \cdot R\big(c_B(r_i), c_D(r_i)\big) \quad 2.19$$

So, equation 2.19 can be solved to calculate the interface position r_i at the current time, by also using equation 2.5. This is necessary because r_i is involved in the boundary conditions for the gas equations (2.8, 2.9, 2.13).

The system of equations for the gas and solid can be easily solved, by considering a number of possible simplifications. First of all, the total concentration balance 2.12 can be neglected, in the following conditions: if the layer solid structure is uniform, then the layer porosity is radially homogeneous; if the temperature and pressure of the gas inside the particle are also constant, then the total gas concentration is constant; so the time derivative into equation 2.8 is then equal to zero, which means that the total molar flux N is:

$$N(r) = \frac{r_i^2\,(d-b) \cdot\, R\big(c_B(r_i), c_D(r_i)\big)}{r^2} \quad 2.20$$

In particular, if d = b (gas equimolar reaction), the total molar flux is constantly zero. The diffusive fluxes of the gases can be expressed by the Fick's law, if the mixture is binary. If the total gas concentration is also constant (uniform temperature and pressure), then the fluxes are:

$$J_B^* = -D_{BD}\frac{\partial c_B}{\partial r} \quad 2.21$$

$$J_D^* = -D_{BD}\frac{\partial c_D}{\partial r} \quad 2.22$$

The diffusivity D_{BD} is an effective coefficient, that depends on the local porosity and tortuosity of the medium. If the solid structure of the layer is uniform, and gas pressure and temperature are also constant with the radial coordinate, D_{BD} is constant, and can be calculated as:

$$D_{BD} = \mathfrak{D}_{BD}\frac{\varepsilon}{\tau} \quad 2.23$$

Where $\mathfrak{D}_{BD}$ is the molecular binary diffusion coefficient of species B in D (that of the gas mixture out of the solid matrix). A final hypothesis can be made in order to further simplify the material balances in equations 2.6-2.7. The time variation of the gas concentration profiles is usually very fast if compared to the time variation of the interface position (and consequently of the solid conversion). In this situation, the time derivatives in equations 2.6-2.7 are not very important, and the gas balances can be solved in steady state at a given core-shell interface position, r_i. This doesn't mean that the gas concentration profiles are not time-dependent, because their balances are still coupled with the solid equations, where the time derivatives are still present.

The system of equations can be solved, once the expression of the kinetic rate is defined. For a single, irreversible, first order reaction, it is:

$$R\big(c_B(r_i), c_D(r_i)\big) = k' \cdot c_B(r_i) \quad 2.24$$

Where k' is the superficial kinetic constant. With all the mentioned assumptions, the system of equations for the gas and solid reagents to solve is:

$$D_{BD}\frac{1}{r^2}\frac{\partial}{\partial r}\left(r^2\frac{\partial c_B}{\partial r}\right) = 0 \quad 2.25$$

$$\frac{\partial X}{\partial t} = \frac{a}{c_A^0}\cdot\frac{3\,r_i^2}{r_0^3}\cdot k' c_B(r_i) \quad 2.26$$

With the boundary and initial conditions:

$$r = r_i \qquad D_{BD}\frac{\partial c_B}{\partial r} = b\cdot k' c_B(r_i) \quad 2.27$$

$$r = r_0 \qquad D_{BD}\frac{\partial c_B}{\partial r} = h_B\cdot\left(c_{B,bulk} - c_B(r_0)\right) \quad 2.28$$

$$t = 0 \qquad X = 0 \quad 2.29$$

Equation 2.25 can be easily integrated, giving:

$$c_B(r) = -\frac{A}{r} + B \quad 2.30$$

In this equation, A and B are integration constants, that can be calculated by imposing the boundary conditions 2.27-2.28. Applying equation 2.30 to equations 2.27-2.28 we obtain:

$$D_{BD}\frac{A}{r_i^2} = b\cdot k'\left(-\frac{A}{r_i} + B\right) \quad 2.31$$

$$D_{BD}\frac{A}{r_0^2} = h_B\cdot c_{B,bulk} - h_B\left(-\frac{A}{r_0} + B\right) \quad 2.32$$

A linear system in A and B is obtained:

$$\begin{pmatrix} \left(\frac{D_{BD}}{r_i^2}+\frac{bk'}{r_i}\right) & (-bk') \\ \left(\frac{D_{BD}}{r_0^2}-\frac{h_B}{r_0}\right) & (h_B) \end{pmatrix} \cdot \begin{pmatrix} A \\ B \end{pmatrix} = \begin{pmatrix} 0 \\ h_B \cdot c_{B,bulk} \end{pmatrix} \quad 2.33$$

Whose solution is:

$$A = \frac{bk' r_i^2 r_0^2 h_B}{h_B r_0^2 D_{BD} + h_B r_0^2 bk' r_i + bk' r_i^2 D_{BD} - bk' r_i^2 h_B r_0} c_{B,bulk} \quad 2.34$$

$$B = \frac{(D_{BD} + bk' r_i) r_0^2 h_B}{h_B r_0^2 D_{BD} + h_B r_0^2 bk' r_i + bk' r_i^2 D_{BD} - bk' r_i^2 h_B r_0} c_{B,bulk} \quad 2.35$$

So, the complete solution can be found by using equations 2.34-2.35 into equation 2.30. The result is the following:

$$c_B(r) = \frac{c_{B,bulk}}{1 + \frac{bk' r_i}{D_{BD}}\left(1-\frac{r_i}{r_0}\right) + \frac{bk' r_i^2}{h_B r_0^2}} \left(1 + \frac{bk' r_i}{D_{BD}}\left(1-\frac{r_i}{r}\right)\right) \quad 2.36$$

The explicit solution for the gas concentration profile can be found only for a first order kinetic expression. Thanks to equation 2.36, the concentration of the gas reagent at the interface position can be calculated analytically, as a function to the gas bulk concentration outside the particle. For $r = r_i$, we obtain:

$$c_B(r_i) = \frac{c_{B,bulk}}{1 + \frac{bk' r_i}{D_{BD}}\left(1-\frac{r_i}{r_0}\right) + \frac{bk' r_i^2}{h_B r_0^2}} \quad 2.37$$

This concentration can be applied to equation 2.26 to calculate the evolution of the global particle conversion in time. The resulting differential equation in time becomes:

$$\frac{\partial X}{\partial t} = \frac{a}{c_A^0} \cdot \frac{3}{r_0^3} \cdot \frac{c_{B,bulk}}{\frac{1}{r_i^2 k'} + \frac{b}{r_i D_{BD}}\left(1-\frac{r_i}{r_0}\right) + \frac{b}{h_B r_0^2}} \quad 2.38$$

Finally, using equation 2.5 into equation 2.38 the variable r_i can be replaced by its function of the conversion X, so we get to an equation with only one dependent variable:

$$\frac{\partial X}{\partial t} = \frac{3\,a}{c_A^0} \cdot \frac{c_{B,bulk}}{\frac{r_0}{k'}\left(1-X(t)\right)^{-2/3} + \frac{b\,r_0^2}{D_{BD}}\left(\left(1-X(t)\right)^{-1/3}-1\right) + \frac{b\,r_0}{h_B}} \quad 2.39$$

Equation 2.39 is the shrinking core model equation for a spherical particle, considering a single irreversible reaction. It is a very useful model, because it can give the change of the particle conversion as a function of the bulk gas reactant concentration alone. So, no information about the inner gas concentration profiles is necessary to solve it. This is quite important because it can be easily applied to simulate systems where a high number of reacting particles is involved. The shrinking core model can be coupled with a gas concentration balance solved in the inter particle channels, that can provide the value of $c_{B,bulk}$ as a function of time. If $c_{B,bulk}$ is constant (this is the case when a high gas flowrate is fed around the particle at a constant composition), equation 2.39 has an analytical solution, which is:

$$t = \tau_K \cdot \left[1 - (1 - X)^{1/3}\right] + \tau_D \cdot 3\left[1 - (1 - X)^{2/3} - \frac{2}{3}\,X\right] + \tau_M \cdot X \qquad 2.40$$

The parameters τ_K, τ_D, τ_M are the characteristic times related to the kinetic, diffusive and external mass transfer resistances, respectively, which are defined by equations 2.41-2.43.

$$\tau_K = \frac{r_0\, c_A^0}{a\, k' c_{B,bulk}} \qquad 2.41$$

$$\tau_D = \frac{b\, r_0^2\, c_A^0}{6a\, D_{BD} c_{B,bulk}} \qquad 2.42$$

$$\tau_M = \frac{b\, r_0\, c_A^0}{3a\, h_B\, c_{B,bulk}} \qquad 2.43$$

The values of the characteristic times are related to the importance of their respective resistances in the process. For instance a high value of τ_D means that diffusion is not negligible, and in fact it can be related to a low value of the diffusion coefficient. To understand which is the controlling regime it is useful to calculate the ratios between the characteristic times. In particular two non dimensional numbers can be defined: Damkohler, which is the ratio between the diffusive and kinetic times, and Biot, which is the ratio between the diffusive and mass transfer characteristic times:

$$Da = \frac{\tau_D}{\tau_K} = \frac{b\, k'\, r_0}{6\, D_{BD}} \qquad 2.44$$

$$Bi = \frac{\tau_D}{\tau_M} = \frac{h_B\, r_0}{2\, D_{BD}} \qquad 2.45$$

Figure 2.1 shows the results of the shrinking core model obtained by equation 2.40 for three different controlling regimes.

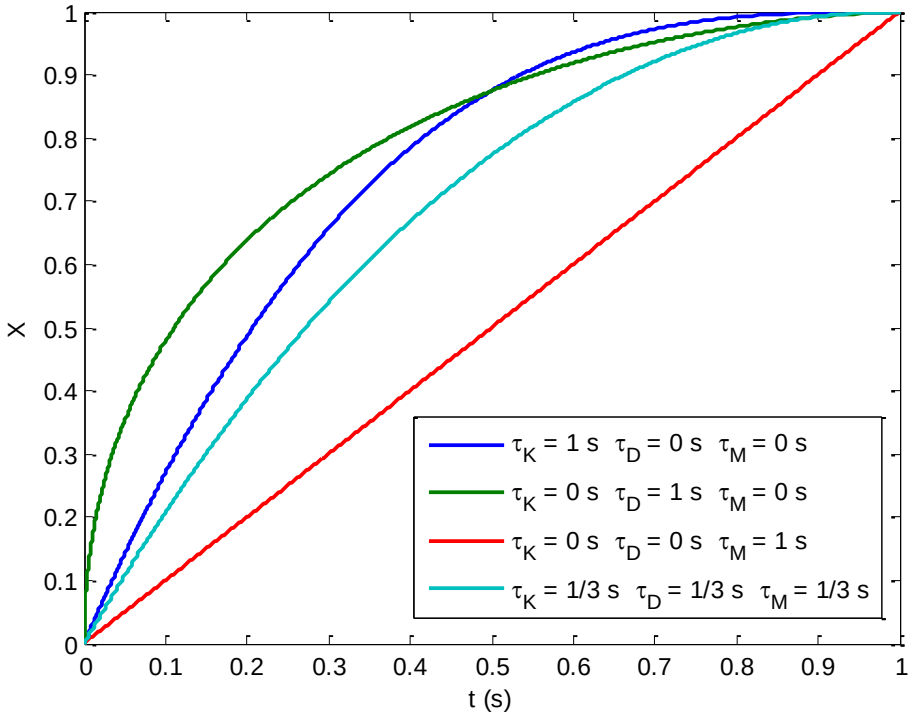

Figure 2.1: Solution of Shrinking core model for different controlling regimes

2.1 Shrinking Core Model for cylindrical particles

An analogous version of the mentioned model can be found for cylindrical pellets. For a cylinder, it is assumed that the gas diffuses radially from the side, whereas the effect of diffusion in the axial direction, starting from the bases, is neglected. This means that the model is more accurate if the radius of the particle is much smaller than its height. This assumption allows considering a one dimensional problem, again. The system of equations to solve, in analogy with 2.25-2.29, is:

$$D_{BD}\frac{1}{r}\frac{\partial}{\partial r}\left(r\frac{\partial c_B}{\partial r}\right)=0 \tag{2.46}$$

$$\frac{\partial X}{\partial t}=\frac{a}{c_A^0}\cdot\frac{2\,r_i}{r_0^2}\cdot k' c_B(r_i) \tag{2.47}$$

With the boundary and initial conditions:

$$r=r_i \qquad D_{BD}\frac{\partial c_B}{\partial r}=\ b\cdot\ k' c_B(r_i) \tag{2.48}$$

$$r=r_0 \qquad D_{BD}\frac{\partial c_B}{\partial r}=h_B\cdot\left(c_{B,bulk}-c_B(r_0)\right) \tag{2.49}$$

$$t=0 \qquad X=0 \tag{2.50}$$

The general solution of equation 2.46 is:

$$c_B(r) = A \cdot ln(r) + B \qquad 2.51$$

Using the boundary conditions, A and B are found by solving the system:

$$\begin{pmatrix} \left(\frac{D_{BD}}{r_i} - bk' \ln(r_i)\right) & (-bk') \\ \left(\frac{D_{BD}}{r_0} + h_B \ln(r_0)\right) & (h_B) \end{pmatrix} \cdot \begin{pmatrix} A \\ B \end{pmatrix} = \begin{pmatrix} 0 \\ h_B \cdot c_{B,bulk} \end{pmatrix} \qquad 2.52$$

Whose solution is:

$$A = \frac{bk' r_i r_0 h_B}{h_B r_0 D_{BD} - h_B r_0 bk' r_i \ln(r_i) + bk' r_i D_{BD} + bk' r_i h_B r_0 \ln(r_0)} c_{B,bulk} \qquad 2.53$$

$$B = \frac{(D_{BD} - bk' r_i \ln(r_i)) r_0 h_B}{h_B r_0 D_{BD} - h_B r_0 bk' r_i \ln(r_i) + bk' r_i D_{BD} + bk' r_i h_B r_0 \ln(r_0)} c_{B,bulk} \qquad 2.54$$

The gas reagent concentration profile inside the solid product layer, at a given core-shell position interface, results as follows:

$$c_B(r) = \frac{c_{B,bulk}}{1 + \frac{bk' r_i}{D_{BD}} \ln\left(\frac{r_0}{r_i}\right) + \frac{bk' r_i}{h_B r_0}} \left(1 + \frac{bk' r_i}{D_{BD}} \ln\left(\frac{r}{r_i}\right)\right) \qquad 2.55$$

If r = r_i, we obtain the analytical expression of the gas concentration at the reaction interface, as a function of the bulk concentration, decreased for effect of the three resistances:

$$c_B(r_i) = \frac{c_{B,bulk}}{1 + \frac{bk' r_i}{D_{BD}} \ln\left(\frac{r_0}{r_i}\right) + \frac{bk' r_i}{h_B r_0}} \qquad 2.56$$

So the differential equation to solve to get the global particle conversion is:

$$\frac{\partial X}{\partial t} = \frac{a}{c_A^0} \cdot \frac{2}{r_0^2} \cdot \frac{c_{B,bulk}}{\frac{1}{k' r_i} + \frac{b}{D_{BD}} \ln\left(\frac{r_0}{r_i}\right) + \frac{b}{h_B r_0}} \qquad 2.57$$

Or, as a function of the conversion alone:

$$\frac{\partial X}{\partial t} = \frac{2\,a}{c_A^0} \cdot \frac{c_{B,bulk}}{\frac{r_0}{k'}\left(1 - X(t)\right)^{-1/3} - \frac{b r_0^2}{3\,D_{BD}} \ln\left(1 - X(t)\right) + \frac{b\,r_0}{h_B}} \qquad 2.58$$

Again, equation 2.58 can be easily integrated if $c_{B,bulk}$ is constant in time: the solution of the shrinking core model for a cylindrical geometry, for one single irreversible reaction is:

$$t = \tau_K \cdot \left[1 - (1 - X)^{2/3}\right] + \tau_D \cdot [(1 - X)\ln(1 - X) + X] + \tau_M \cdot X \quad 2.59$$

Where the characteristic times are:

$$\tau_K = \frac{3\, r_0\, c_A^0}{4\, a\, k' c_{B,bulk}} \quad 2.60$$

$$\tau_D = \frac{b\, r_0^2\, c_A^0}{6a\, D_{BD} c_{B,bulk}} \quad 2.61$$

$$\tau_M = \frac{b\, r_0\, c_A^0}{2a\, h_B\, c_{B,bulk}} \quad 2.62$$

2.2 Shrinking Core Model for time changing particle size

The analysis made so far assumed that the particle radius, r_0, remains constant as long as the reaction proceeds. This is not always true. The loss or gain of mass of the solid during the reaction, the layer porosity and the restructuring of the product to a crystal structure with different density can lead to a change of the particle size. The total volume of the particle can be calculated at any time by considering a total mass balance. The volume of the core, V_A, can be obtained as a function of the conversion by using equation 2.5:

$$V_A(t) = \frac{4}{3}\pi \left(r_0(0)\right)^3 \left(1 - X(t)\right) \quad 2.63$$

Where $r_0(0)$ is the particle radius at t = 0. Consequently, the number of moles of the solid reactant A in the particle is:

$$n_A(t) = \frac{\rho_A}{MW_A}\frac{4}{3}\pi \left(r_0(0)\right)^3 \left(1 - X(t)\right) \quad 2.64$$

According to stoichiometry, the number of moles of the product C must be the number of reacted moles of A, scaled by the ratio between the coefficients c and a. SO it will be:

$$n_C(t) = \frac{c}{a}\frac{\rho_A}{MW_A}\frac{4}{3}\pi \left(r_0(0)\right)^3 X(t) \quad 2.65$$

So the volume occupied by the product C, which is equal to the volume of the layer according to the shrinking core model, can be calculated as follows:

$$V_C(t) = \frac{c}{a}\frac{\rho_A}{\rho_C}\frac{MW_C}{MW_A}\frac{4}{3}\pi\left(r_0(0)\right)^3 X(t) \qquad 2.66$$

The total particle volume can be calculated by the sum of equations 2.63 and 2.66:

$$V_{tot}(t) = \frac{4}{3}\pi\left(r_0(0)\right)^3\left[\left(1 - X(t)\right) + \frac{c}{a}\frac{\rho_A}{\rho_C}\frac{MW_C}{MW_A}X(t)\right] \qquad 2.67$$

So the particle radius, as a function of the conversion is:

$$r_0(t) = r_0(0)\cdot[1 + \psi\, X(t)]^{1/3} \qquad 2.68$$

Where:

$$\psi = \frac{c}{a}\frac{\rho_A}{\rho_C}\frac{MW_C}{MW_A} - 1 \qquad 2.69$$

Depending on the value of ψ, three situations are possible:

- If ψ > 0: the particle increases in volume with conversion.
- If ψ = 0: the particle size remains unchanged.
- If ψ < 0: the particle volume decreases with conversion.

It's important to point out that ρ_C is the apparent density of the product phase, so it takes into account the porosity of the layer: this means that ρ_C will be, in general, lower than the intrinsic density of the product C. The evolution of the particle porosity can be independent from the intrinsic properties of the solid phases involved in the reaction, and this means that the quantification of ψ can be non trivial.

The particle shrinking and swelling can have an influence on the process, because the diffusion resistance is related to the thickness of the layer. For a spherical particle, equation 2.39 is still valid, but r_0 is not a constant in the integration, but a function of the conversion, as stated by equation 2.68. So the model becomes:

$$\frac{\partial X}{\partial t} = \frac{3}{c_A^0}\frac{a}{\cdot}\frac{c_{B,bulk}}{\frac{r_0(0)}{k'}(1+\psi\,X)^{1/3}(1-X)^{-2/3} + \frac{b\left(r_0(0)\right)^2}{D_{BD}}(1+\psi\,X)^{2/3}((1-X)^{-1/3}-1) + \frac{b\,r_0}{h_B}(1+\psi\,X)^{1/3}} \qquad 2.70$$

Analogously, for a cylindrical pellet, the particle radius will be:

$$r_0(t) = r_0(0)\cdot[1 + \psi\, X(t)]^{1/2} \qquad 2.71$$

So the shrinking core model becomes:

$$\frac{\partial X}{\partial t} = \frac{2\,a}{c_A^0} \cdot \frac{c_{B,bulk}}{\frac{r_0(0)}{k'}(1+\psi\,X)^{1/2}(1-X)^{-1/3} - \frac{b\left(r_0(0)\right)^2}{3\,D_{BD}}(1+\psi\,X)\ln(1-X) + \frac{b\,r_0(0)}{h_B}(1+\psi\,X)^{1/2}} \quad 2.72$$

2.3 Shrinking Core Model for a reversible reaction

The models previously presented consider that the reaction at the core shell interface is irreversible, so it only depends on the concentration of the gas reagent. Now let's consider the case where the equilibrium reaction is involved:

a A(s) + b B(g) ↔ c C(s) + d D(g)

If equilibrium is involved, the concentration balance for the product gas D must be coupled with the system of equations. For a spherical particle it is:

$$D_{BD}\frac{1}{r^2}\frac{\partial}{\partial r}\left(r^2\frac{\partial c_B}{\partial r}\right) = 0 \quad 2.73$$

$$D_{BD}\frac{1}{r^2}\frac{\partial}{\partial r}\left(r^2\frac{\partial c_D}{\partial r}\right) = 0 \quad 2.74$$

$$\frac{\partial X}{\partial t} = \frac{a}{c_A^0}\cdot\frac{3\,r_i^2}{r_0^3}\cdot k'\left(c_B(r_i) - \frac{1}{K}c_D(r_i)\right) \quad 2.75$$

With the boundary and initial conditions:

$$r = r_i \qquad D_{BD}\frac{\partial c_B}{\partial r} = bk'\left(c_B(r_i) - \frac{1}{K}c_D(r_i)\right) \qquad D_{BD}\frac{\partial c_D}{\partial r} = -dk'\left(c_B(r_i) - \frac{1}{K}c_D(r_i)\right) \quad 2.76$$

$$r = r_0 \qquad D_{BD}\frac{\partial c_B}{\partial r} = h_B\cdot\left(c_{B,bulk} - c_B(r_0)\right) \qquad D_{BD}\frac{\partial c_B}{\partial r} = h_D\cdot\left(c_{D,bulk} - c_D(r_0)\right) \quad 2.77$$

$$t = 0 \qquad X = 0 \quad 2.78$$

Like the solution for the irreversible reaction case, the gas reagent and product concentration profiles are in the form:

$$c_B(r) = -\frac{A_1}{r} + B_1 \quad 2.79$$

$$c_D(r) = -\frac{A_2}{r} + B_2 \quad 2.80$$

Four integration parameters need to be found by applying the four boundary conditions in 2.76-2.77:

$$D_{BD}\frac{A_1}{r_i^2} = bk'\left(-\frac{A_1}{r_i} + B_1 - \frac{1}{K}\left(-\frac{A_2}{r_i} + B_2\right)\right) \quad 2.81$$

$$D_{BD}\frac{A_2}{r_i^2} = -dk'\left(-\frac{A_1}{r_i} + B_1 - \frac{1}{K}\left(-\frac{A_2}{r_i} + B_2\right)\right) \quad 2.82$$

$$D_{BD}\frac{A_1}{r_0^2} = h_B \cdot c_{B,bulk} - h_B\left(-\frac{A_1}{r_0} + B_1\right) \quad 2.83$$

$$D_{BD}\frac{A_2}{r_0^2} = h_D \cdot c_{D,bulk} - h_D\left(-\frac{A_2}{r_0} + B_2\right) \quad 2.84$$

A linear system in A_1, A_2, B_1 and B_2 is obtained:

$$\begin{pmatrix} \left(\frac{D_{BD}}{r_i^2} + \frac{bk'}{r_i}\right) & \left(-\frac{bk'}{K\,r_i}\right) & (-bk') & \left(\frac{bk'}{K}\right) \\ \left(-\frac{dk'}{r_i}\right) & \left(\frac{D_{BD}}{r_i^2} + \frac{dk'}{K\,r_i}\right) & (dk') & \left(-\frac{dk'}{K}\right) \\ \left(\frac{D_{BD}}{r_0^2} - \frac{h_B}{r_0}\right) & 0 & (h_B) & 0 \\ 0 & \left(\frac{D_{BD}}{r_0^2} - \frac{h_D}{r_0}\right) & 0 & (h_D) \end{pmatrix} \cdot \begin{pmatrix} A_1 \\ A_2 \\ B_1 \\ B_2 \end{pmatrix} = \begin{pmatrix} 0 \\ 0 \\ h_B\,c_{B,bulk} \\ h_D\,c_{D,bulk} \end{pmatrix} \quad 2.85$$

Solving the system, the concentrations of B and D at the reaction interface can be found. Equation 2.75 becomes:

$$\frac{\partial X}{\partial t} = \frac{a}{c_A^0} \cdot \frac{3\,r_i^2}{r_0^3} \cdot \frac{\left(c_{B,bulk} - \frac{c_{D,bulk}}{K}\right)}{\frac{1}{k'} + \frac{r_i}{D_{BD}}\left(\frac{d}{K} + b\right)\left(1 - \frac{r_i}{r_0}\right) + \frac{r_i^2}{r_0^2}\left(\frac{d}{K\,h_D} + \frac{b}{h_B}\right)} \quad 2.86$$

And, expressing the interface position in terms of conversion:

$$\frac{\partial X}{\partial t} = \frac{3\,a}{c_A^0} \cdot \frac{\left(c_{B,bulk} - \frac{c_{D,bulk}}{K}\right)}{\frac{r_0}{k'}(1-X)^{-2/3} + \frac{r_0^2}{D_{BD}}\left(\frac{d}{K} + b\right)\left((1-X)^{-1/3} - 1\right) + r_0\left(\frac{d}{K\,h_D} + \frac{b}{h_B}\right)} \quad 2.87$$

Comparing this expression with the model for irreversible reaction, two more resistances appear in equation 2.87: they are related to the diffusion of the product gas in the layer and the mass transfer of the product from the particle surface to the bulk. It is trivial to prove that if K tends to infinite (the equilibrium is completely shifted to the products) equation 2.87 becomes identical to equation 2.39. Equation 2.87 can be further generalized, in the case that the gas B and D are not in a binary mixture, but are diluted in an inert species, I. The Fick law is still applicable on the problem, if the fractions of B and D are small if

compared to the fraction of inert. In this case, the diffusion coefficient D_{BI} and D_{DI} of the reagent and product into the inert gas can be sometimes very different from each other. An equation for the global particle conversion can still be found, analogously to what already reported. The final solution is:

$$\frac{\partial X}{\partial t} = \frac{3\,a}{c_A^0} \cdot \frac{\left(c_{B,bulk} - \frac{c_{D,bulk}}{K}\right)}{\frac{r_0}{k'}(1-X)^{-2/3} + r_0^2\left(\frac{d}{K\,D_{DI}} + \frac{b}{D_{BI}}\right)((1-X)^{-1/3} - 1) + r_0\left(\frac{d}{K\,h_D} + \frac{b}{h_B}\right)} \qquad 2.88$$

This model can also be extended to describe particles with changing size, by expressing r_0 through equation 2.68.

2.4 Multiple interfaces Shrinking Core

The shrinking core model can be extended to consider for multiple reactions [21] [19], in the case that the solid product of the first reaction can further react with the same gas. The model predicts the formations of multiple layers, surrounding a core made of the first solid reagent. In this section it is reported the case for two reactions, assuming that the same gas reagent and product are involved in both reactions:

a $A(s) + b_1\,B(g) \leftrightarrow c_1\,C(s) + d_1\,D(g)$

$c_2\,C(s) + b_2\,B(g) \leftrightarrow e\,E(s) + d_2\,D(g)$

It is still assumed that both reactions are localized in two surfaces, dividing three different areas of the particle, the solid species will be distributed as shown in figure 2.2:

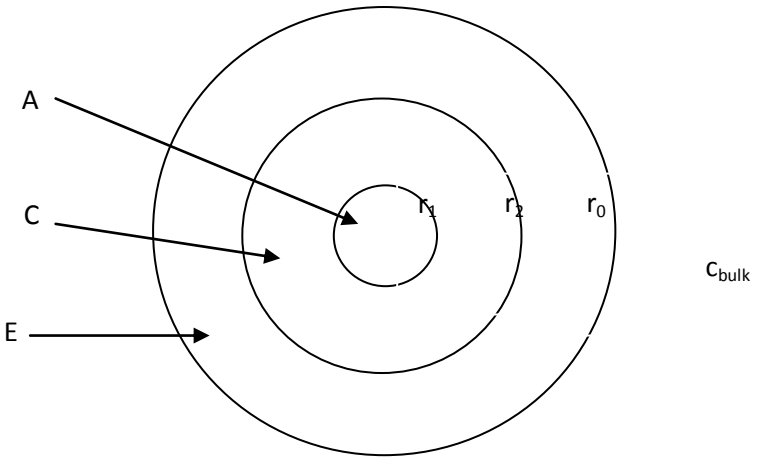

Figure 2.2 Representation of the pellet simulated according to a two interfaces shrinking core model. The two reactions take place at r_1 and r_2

The first reaction, consuming A and producing C, occurs at the interface r_1, while the second reaction, consuming C and producing E, occurs at the interface r_2. The two reaction rates, referred to the whole

particle volume, can be expressed through equations 2.89 -2.90. Once again they consider first order dependence on the gas concentrations:

$$R_1 = 3\,\frac{r_1^2}{r_0^3}\,k'_1\left(c_B(r_1) - \frac{c_D(r_1)}{K_1}\right) \qquad 2.89$$

$$R_2 = 3\,\frac{r_2^2}{r_0^3}\,k'_2\left(c_B(r_2) - \frac{c_D(r_2)}{K_2}\right) \qquad 2.90$$

The goal is once again to express the concentrations of B and D at the two interfaces as a function of the bulk concentrations outside the particle. Again, the material balances for the gas species B and D only consider diffusion through the solid matrices, but it's possible that the effective diffusivities of the gases in the layers with species C and species E are different from each other. This is true, for instance, if the layers have different porosities. In this case the model for the gas is:

$$r_1 < r < r_2 \qquad \frac{1}{r^2}\frac{d}{dr}\left(r^2 D_B^C\,\frac{dc_B}{dr}\right) = 0 \qquad \frac{1}{r^2}\frac{d}{dr}\left(r^2 D_D^C\,\frac{dc_D}{dr}\right) = 0 \qquad 2.91$$

$$r_2 < r < r_0 \qquad \frac{1}{r^2}\frac{d}{dr}\left(r^2 D_B^E\,\frac{dc_B}{dr}\right) = 0 \qquad \frac{1}{r^2}\frac{d}{dr}\left(r^2 D_D^E\,\frac{dc_D}{dr}\right) = 0 \qquad 2.92$$

In this case, D_B^C and D_B^E are the effective diffusivities of B inside the layer occupied by the solid C and E, respectively. An analogous pair of coefficients, D_D^C and D_D^E are defined for the gas product D. For the solid species, the total concentrations of A and C in the particle can be expressed through the following equations:

$$\frac{dC_A}{dt} = -a\,R_1 \qquad 2.93$$

$$\frac{dC_C}{dt} = c_1\,R_1 - \,c_2\,R_2 \qquad 2.94$$

The boundary and initial conditions for the problem are:

$$r = r_1 \qquad D_B^C\frac{\partial c_B}{\partial r} = \;+b_1 k_1'\left(c_B(r_1) - \frac{1}{K_1}c_D(r_1)\right) \qquad 2.95$$

$$D_D^C\frac{\partial c_D}{\partial r} = \;-d_1 k_1{}'\left(c_B(r_1) - \frac{1}{K_1}c_D(r_1)\right)$$

$$r = r_2 \qquad D_B^E\left(\frac{\partial c_B}{\partial r}\right)^+ = \;D_B^C\left(\frac{\partial c_B}{\partial r}\right)^- + b_2 k_2'\left(c_B(r_2) - \frac{1}{K_2}c_D(r_2)\right) \qquad 2.96$$

$$D_D^E\left(\frac{\partial c_D}{\partial r}\right)^+ = \;D_D^C\left(\frac{\partial c_D}{\partial r}\right)^- - d_2 k_2{}'\left(c_B(r_2) - \frac{1}{K_2}c_D(r_2)\right)$$

$$r = r_0 \qquad D_B^E \frac{\partial c_B}{\partial r} = h_B \cdot \left(c_{B,bulk} - c_B(r_0)\right) \qquad 2.97$$

$$D_D^E \frac{\partial c_B}{\partial r} = h_D \cdot \left(c_{D,bulk} - c_D(r_0)\right)$$

$$t = 0 \qquad c_A = c_A^0 \qquad c_C = 0 \qquad 2.98$$

The boundary conditions are defined by writing the mass balances at the three surfaces: the difference between the inlet and outlet molar fluxes of each species must be equal to the fluxes produced by the chemical reactions. Note that the boundary conditions at r = r_2 (equations 2.96), as well as the different values of the diffusivities in the two layers, introduce a discontinuity in the derivative of the solutions of equations 2.91 and 2.92. The concentration profiles of the gases result as piecewise functions:

$$c_B(r) = \begin{cases} -\frac{A_{11}}{r} + B_{11} & for\ r_1 \le r \le r_2 \\ -\frac{A_{12}}{r} + B_{12} & for\ r_2 \le r \le r_0 \end{cases} \qquad 2.99$$

$$c_D(r) = \begin{cases} -\frac{A_{21}}{r} + B_{21} & for\ r_1 \le r \le r_2 \\ -\frac{A_{22}}{r} + B_{22} & for\ r_2 \le r \le r_0 \end{cases} \qquad 2.100$$

Eight integration constants must be determined. Six of the eight equations needed to determine them are found by using equations 2.99-2.100 into the boundary conditions:

$$D_B^C \frac{A_{11}}{r_1^2} = b_1 k_1' \left(-\frac{A_{11}}{r_1} + B_{11} - \frac{1}{K_1}\left(-\frac{A_{21}}{r_1} + B_{21}\right)\right) \qquad 2.101$$

$$D_D^C \frac{A_{21}}{r_1^2} = -d_1 k_1' \left(-\frac{A_{11}}{r_1} + B_{11} - \frac{1}{K_1}\left(-\frac{A_{21}}{r_1} + B_{21}\right)\right) \qquad 2.102$$

$$D_B^E \frac{A_{12}}{r_2^2} = D_B^C \frac{A_{11}}{r_2^2} + b_2 k_2' \left(-\frac{A_{11}}{r_2} + B_{11} - \frac{1}{K_2}\left(-\frac{A_{21}}{r_2} + B_{21}\right)\right) \qquad 2.103$$

$$D_D^E \frac{A_{22}}{r_2^2} = D_D^C \frac{A_{21}}{r_2^2} - d_2 k_2' \left(-\frac{A_{11}}{r_2} + B_{11} - \frac{1}{K_2}\left(-\frac{A_{21}}{r_2} + B_{21}\right)\right) \qquad 2.104$$

$$D_B^E \frac{A_{12}}{r_0^2} = h_B \cdot c_{B,bulk} - h_B \left(-\frac{A_{12}}{r_0} + B_{12}\right) \qquad 2.105$$

$$D_D^E \frac{A_{22}}{r_0^2} = h_D \cdot c_{D,bulk} - h_D \left(-\frac{A_{22}}{r_0} + B_{22}\right) \qquad 2.106$$

Two more equations are found by imposing the continuity of the solutions at r = r_2.

$$-\frac{A_{11}}{r_2}+B_{11}=-\frac{A_{12}}{r_2}+B_{12} \quad 2.107$$

$$-\frac{A_{21}}{r_2}+B_{21}=-\frac{A_{22}}{r_2}+B_{22} \quad 2.108$$

Solving this linear system, it is possible to calculate the concentrations of B and D at r_1 and r_2, and then explicitly obtain the reaction rates R_1 and R_2 as a function of the gas bulk concentrations. The system can then be solved, once the interface positions, r_1 and r_2 are expressed as a function of the solid concentrations:

$$r_1(t)=r_0\cdot\left(\frac{C_A(t)}{C_A(0)}\right)^{1/3} \quad 2.109$$

$$r_2(t)=r_0\cdot\left(\frac{C_A(t)+\frac{c_1}{a}\cdot C_C(t)}{C_A(0)}\right)^{1/3} \quad 2.110$$

We report the solution of the problem for the simplified case where $D_B^C = D_D^C = D_B^E = D_D^E = D^*$, $h_B = h_D = h^*$ and $b_1 = b_2 = d_1 = d_2 = 1$. The expression for the reaction rates become:

$$R_1=\frac{3}{r_0}\frac{1}{W}\left[(AA_2+BB_2+FF)\left(c_{B,bulk}+c_{B,eq1}\right)-(BB_2+FF)\left(c_{B,bulk}+c_{B,eq2}\right)\right] \quad 2.111$$

$$R_2=\frac{3}{r_0}\frac{1}{W}\left[(AA_1+BB_1+BB_2+FF)\left(c_{B,bulk}+c_{B,eq2}\right)-(BB_2+FF)\left(c_{B,bulk}+c_{B,eq1}\right)\right] \quad 2.112$$

Where the parameters are expressed as follows:

$$AA_1=\frac{r_0^2}{r_1^2 k'_1\left(1+\frac{1}{K_1}\right)} \qquad AA_2=\frac{r_0^2}{r_2^2 k'_2\left(1+\frac{1}{K_2}\right)} \quad 2.113$$

$$BB_1=\frac{r_2-r_1}{r_1 r_2}\cdot\frac{r_0^2}{D^*} \qquad BB_2=\frac{r_0-r_2}{r_2}\cdot\frac{r_0}{D^*} \quad 2.114$$

$$FF=\frac{1}{h^*} \quad 2.115$$

$$W=[(AA_1+BB_1)(AA_2+BB_2+FF)+AA_2(BB_2+FF)] \quad 2.116$$

$$c_{B,eq1}=\frac{c_{B,bulk}+c_{D,bulk}}{1+K_1} \qquad c_{B,eq2}=\frac{c_{B,bulk}+c_{D,bulk}}{1+K_2} \quad 2.117$$

Figure 2.3 shows an example of the results of the model for the solid species for a given set of parameters and operating conditions (r_0 = 1 mm, D*= 1e-5 m2/s, h* = 1 m/s, k_1' = 1 m/s, k_2' = 0.1 m/s, K_1 = 2, K_2 = 1, cA0 = 1e4 mol/m^3, $c_{B,bulk}$ = 9 mol/m^3, $c_{D,bulk}$ = 1 mol/m^3). The results for the gas radial profiles are shown in figure 2.4 for a reaction time of 30 s.

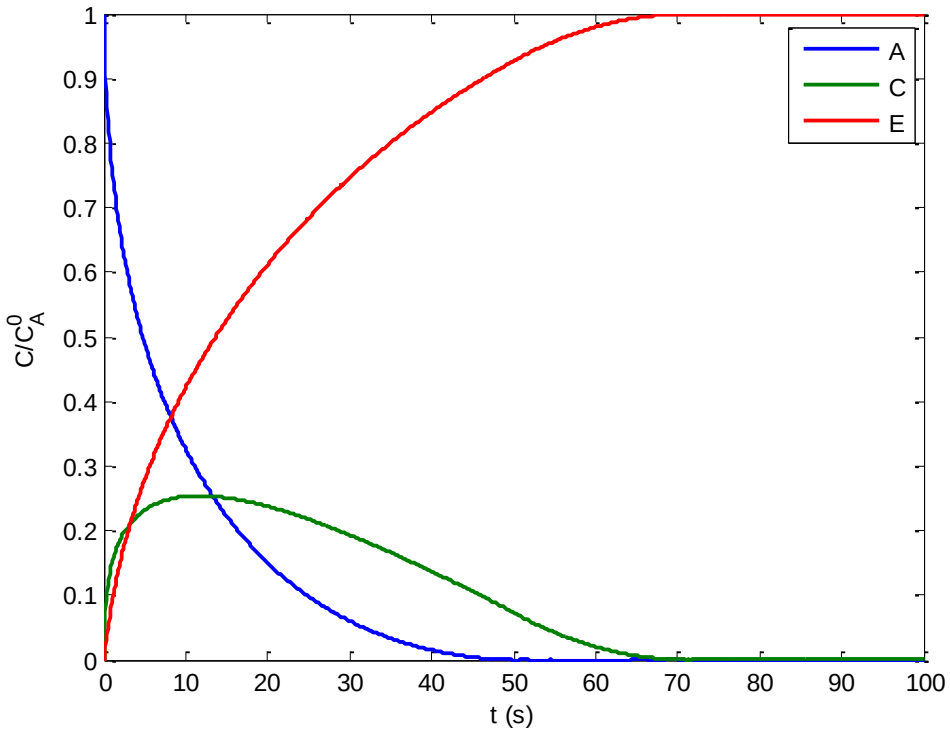

Figure 2.3: Time concentration profiles of the solid A, C and E in the whole particle according to the 2 interfaces SCM simulated with r_0 = 1 mm, D*= 1e-5 m2/s, h* = 1 m/s, k_1' = 1 m/s, k_2' = 0.1 m/s, K_1 = 2, K_2 = 1, cA0 = 1e4 mol/m^3, $c_{B,bulk}$ = 9 mol/m^3, $c_{D,bulk}$ = 1 mol/m^3

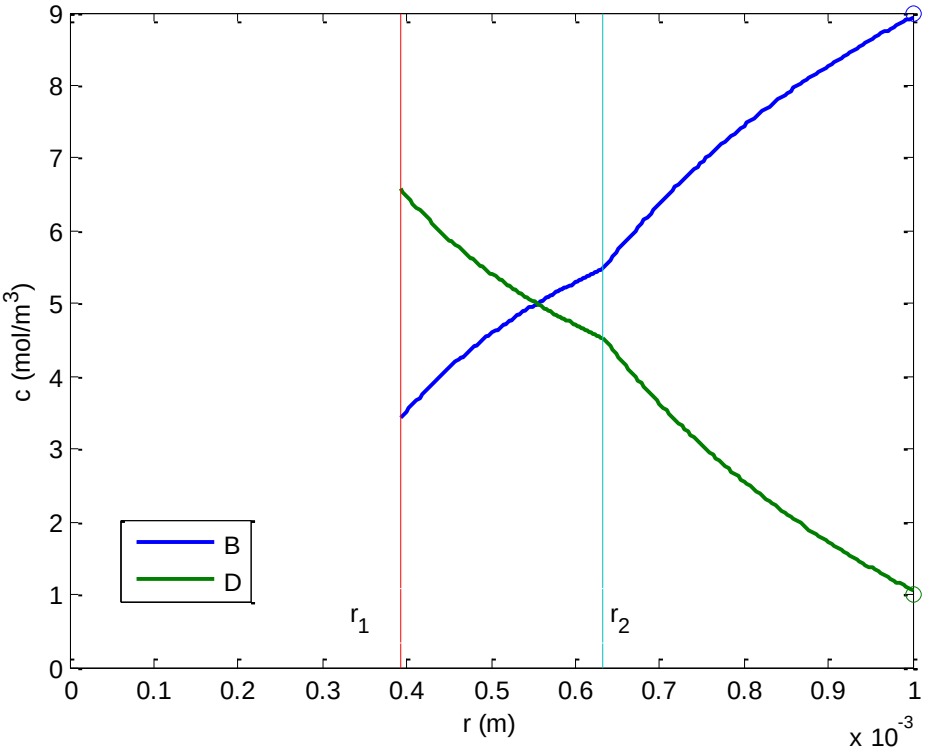

Figure 2.4: Radial concentration profiles for gas species B and D for a reaction time of 30 s, simulated with a two interfaces shrinking core model, with (r_0 = 1 mm, D*= 1e-5 m2/s, h* = 1 m/s, k_1' = 1 m/s, k_2' = 0.1 m/s, K_1 = 2, K_2 = 1, cA0 = 1e4 mol/m^3, $c_{B,bulk}$ = 9 mol/m^3, $c_{D,bulk}$ = 1 mol/m^3)

The solution becomes even more complex if the diffusion coefficients and mass transfer coefficient are different for the reagent and product. An analogous study can be developed for a system of three or more consecutive reactions.

2.5 Limitations of the Shrinking Core Model

In the previous sections, different versions of the shrinking core model were shown, together with all the details about the derivations of the equations. A number of assumptions were made to get to the final results. In summary:

- The gas-solid reaction is confined to a single interface (more interfaces in the case of multiple reactions), separating the solid reagent and product.
- The particle porosity is uniform in each layer.
- Temperature and pressure are constant inside the particle.
- Natural molar convection of the gas inside the particle, associated to a global generation or consumption of gas moles in the pellet, is negligible if compared to the diffusive fluxes.
- The gas mixture is binary (regent-product), or the components are very diluted in an inert gas.
- The dynamic of the change of the gas concentration profile is very fast if compared to the change of the reaction interface position.
- Kinetics is first order dependent on the concentration of the gas reagent (and product, if the reaction is reversible).

These assumptions can lead to some limitations of applicability of the model, which must be carefully considered before using it. In particular, the following issues must be pointed out:

a) The reaction located on a surface is the most important assumption of the model. This is not always physically correct. In particular, if the particle is initially porous, it doesn't behave like a shrinking core, unless the controlling regime is diffusion: in such a case, in fact, the gas reactant concentration drops to zero near the core shell interface, so the gas cannot diffuse (and react) into the core because it is instantly consumed before reaching it. If the reaction is very fast if compared to diffusion, the gas diffuses in region where the solid reagent has already been consumed. On the contrary, if kinetic is controlling over intra particle diffusion, a porous particle will react homogeneously, because the gas composition is always radially uniform. So the shrinking core model is applicable in the case of kinetic regime only if the particle is initially not porous.
b) The absence of natural convection is verified only if there is not a net production or consumption of moles do to the reaction, which is true only if the reaction is equimolar with respect to the gas species.
c) First order kinetics can be correct, but sometimes adsorption phenomena can be important: these usually reduce the apparent kinetic order.
d) Thermal homogeneity of the particle must be evaluated. This is usually a correct assumption for small particles, but this is also related to the value of heat of reaction.
e) Reversible gas solid reactions are quite common. The idea of a reversible reaction occurring at the core shell interface is that, depending on the relative amount of gas reagent and product present at

that interface, the interface can shift towards the particle centre or towards the external surface if the reaction rate is globally positive or negative, respectively. This is not what happens, though. In fact, the model always considers that the gas only diffuses through the solid product layer, without reacting. If this is certainly true for the gas reagent, this cannot be true for the solid product, if the reaction is reversible. In fact the solid product is a reagent for the gas product, so it must necessarily react also in the layer. The core shell behavior could still be approximated for diffusive regimes, because in these cases the gas product concentration is always maximum near the center of the particle, where it is produced by the forward reaction that occurs because the solid reagent concentration is higher. The core-shell assumption is however generally wrong for reversible reactions.

f) For the same reason, multiple interfaces shrinking core are not physically possible. Again, in all the layers between the core and the external shell, the gas is supposed to diffuse without reacting. But the intermediate layers are actually made of solid phases that are not inert to the gas that is moving through them. The model could be still correct for the case of very fast reactions (diffusive regime). What happens in this case is that all the interfaces converge to a single radial coordinate, and this also means that all the reaction steps take place simultaneously in a single point. In summary, the particle behaves like a one interface shrinking core, where the only considered reaction is the sum of all the reaction steps.

Despite these limitations, the shrinking core model is still widely used also for the more critical cases considered, and several works with reversible and multi step reactions can be found in the literature. It is still possible to make use of it, because of its simplicity and easy applicability to complex reactor problems.

Notation

a, b, c, d	Reaction stoichiometric coefficients
Bi	Biot number
c_i, c_t	Local molar local concentration of i, total (mol/cm^3)
C_i	Total concentration of i inside the particle (mol/cm^3)
D_{ij}	Effective diffusion coefficient of i in j (cm^2/s)
D_i^k	Effective diffusion coefficient of i in the solid phase k (cm^2/s)
$\mathfrak{D}_{ij}$	Binary diffusion coefficient of i in j (cm^2/s)
Da	Damkohler number
h_i	Mass transfer coefficient of i (cm/s)
J_i^*	Molar diffusive flux of i (mol/cm^2/s)
k'	Superficial kinetic constant (cm/s)
K	Equilibrium constant
MW_c, MW_i	Molecular weight of the core, of the i-th species (g/mol)
n	Number of moles of reacting solid into the particle
n_i	Number of moles of the i-th species into the particle
N	Total molar gas flux (mol/cm^2/s)
r	Radial coordinate (cm)
r_0	Particle radius (cm)

r_i	Radius of the core-shell interface (cm)
R	Reaction rate (mol/cm^3/s)
t	Time (s)
V_c, V_i	Volume of the core, of the i-th species (cm^3)
x_i , $x_{i,bulk}$	Molar fraction of I, inside the particle, in the gas bulk phase
X	Particle conversion

Greek letters

ε	Porosity
ψ	Size change factor
ρ_c, ρ_i	Density of the core, of the i-th species (g/cm^3)
τ	Tortuosity
τ_K, τ_D, τ_M	Characteristic times of kinetic, diffusive, and external mass transfer resistances

Chapter 3. Application of SCM: Simulation of full scale reactors for Direct Reduction of Iron

In chapter §2, the different formulations of the shrinking core model have been presented. Despite its possible limitations, already discussed, the SCM is a simple approach to the description of gas solid reactions, that can be successfully applied to describe full scale reactors. In particular, the SCM can be used when a system of solid particles and gas is represented by a fully Eulerian approach: this implies that the single particles are not tracked, but the gas-solid system is seen as a medium, and in any point of the reactor the characteristics of the two phases (velocity field, composition and temperature) are quantified. This is possible because the shrinking core model expresses the reaction rate of the whole particle as a function of the global particle conversion and gas composition outside the particle, so no information is needed about the local composition of the solid phases and diffusing gas inside the pellet itself. This also means that the form of the reaction rates does not depend on the history of the reaction of the single particle, but just on the current value of its degree of conversion, that automatically defines the distribution of the solid phases into the particle.

In this chapter, an application of the SCM is presented. A 2D axial symmetric model of a DRP (direct reduction plant) shaft furnace that includes momentum, species and enthalpy balances for the solid and the gas phases was solved. The process consists in the reduction of iron ore pellets with H_2 and CO mixtures at high temperature. The process gas can contain natural gas, which is catalytically converted on metallic iron by steam reforming and cracking reactions into syngas and carbon. This work was made thanks to the collaboration to an industrial research project between the University of Padova and Centro Ricerche Danieli. The industrial partner provided the data from real plants and dedicated pilot plants to fully characterize the necessary kinetic parameters. The model was developed by means of a commercial CFD code (Comsol Multiphisics [22]), that was occasionally coupled with an optimization routine in Matlab [23], in order to fit the parameters of the SCM. The details of this work are reported in the next section [24].

3.1 Model overview

As a first step, a mathematical model was used to simulate the flow field of a granular material inside a silo. The 2D axial-symmetric model was validated through a small scale (1:15) experimental reactor and it is able to reproduce the flow and pressure fields of the solid [25]. This study assessed that, if the fluidization index is well below unity, the influence of the gas flow field into the solid velocity is negligible and the calculation of the solid flow field can be performed only once and then kept constant in the solution of the other variables (gas flow field and temperature and composition profiles of both gas and solid), unless solid flow rate is changed. Moreover, the solids velocity profile in the cylindrical zone is quite uniform, except in the narrow shearing layer close to the wall.

In this work the model of the continuous shaft reactor was developed with the introduction of the chemical reactions between the gas and the solid and the addition of the energy balances for both phases. This allowed the prediction of composition and temperature distribution, both for the solid and the gas. Similar works, in 1D or 3D, which describe other direct reduction processes, are included in references [18, 26, 27]. None of those models describes the local velocity of the dense granular bed, always assuming plug flow, with no attrition on the reactor walls, disregarding geometric singularities such as flow feeders and reactor shape variations. Regarding the gas phase, when methane is among the reactants in the feed gas, these models do not account for the methane chemistry, i.e. cracking and reforming, which instead is proven to have great influence on the reduction kinetics [28]. The present study is originated by a tangible need to gain more insight in the industrial process and to understand the effect of any action taken by the control unit of the plant.

3.2 Mathematical model used in CFD

The granular material is treated as a non-Newtonian continuum fluid. In this method the viscosity of the pseudo fluid is a function of a scalar called granular temperature, which is influenced by the flow profiles and the interparticle contacts. At the wall a "slip length" is implemented, which allows reproducing correctly the interactions between the shearing solid bed and the wall (e.g. boundary layer behavior).

The gas flow field is described by the Brinkman equation, a momentum balance suitable to represent a gas flowing through a porous bed, and by a continuity equation that accounts for the mass generation/consumption in the single phase due to the multiphase reaction between solids and gas.

The reduction reactions involve a solid species and a gas species. The iron ore, whose iron oxide is primarily hematite, Fe_2O_3, is reduced progressively to magnetite (Fe_3O_4), wüstite (FeO) and iron (Fe) in three steps. The ore contains some gangue, as well, which is assumed to be an inert in the reduction process. Since the reaction from hematite to magnetite is very fast if compared to the other steps, only two steps, i.e. the reduction from hematite to wüstite and from wüstite to iron, are considered, both with hydrogen and carbon monoxide. Reactions from wüstite to iron are considered reversible and linked to the thermodynamic equilibrium FeO/Fe.

$R_{1,H2}$: $Fe_2O_3 + H_2 \rightarrow 2FeO + H_2O$ $\Delta H_{R,298} = 46.6$ kJ/mol (3.1)

$R_{1,CO}$: $Fe_2O_3 + CO \rightarrow 2FeO + CO_2$ $\Delta H_{R,298} = 5.49$ kJ/mol (3.2)

$R_{2,H2}$: $FeO + H_2 \leftrightarrows Fe + H_2O$ $\Delta H_{R,298} = 25.5$ kJ/mol (3.3)

$R_{2,CO}$: $FeO + CO \leftrightarrows Fe + CO_2$ $\Delta H_{R,298} = -15.7$ kJ/mol (3.4)

The species production/consumption rates are based on the shrinking core model, in the form of the two interfaces formulation reported in chapter §2. The parameters of the model were taken both from literature [29, 30] and from internal data coming from the ENERGIRON plants (developed by Tenova and Danieli). Furthermore, an experimental campaign was held in Danieli R&D, where a semi-batch reactor with

a capacity of 2 kg of iron ore and fed with the same process gas as in the industrial plant, working up to 12 bar gauge and 1100°C, was installed. Gas diffusivities in solids increase from hematite to wüstite and from wüstite to sponge iron, with internal porosity varying from a 20% of hematite to 60-70% of sponge iron [31]. As reported in literature [28], the carbon deposited on the pellet puts another barrier to diffusion and slows down the reactions, both the catalytic and the reduction ones. Therefore, the reaction rates are multiplied by a reducing factor accounting for the local amount of carbon.

Reducing gas (RG), rich in H_2, CO and CH_4, coming in contact with metallic iron, participates to the catalytic reactions:

Steam Reforming, R_{SR}:	$CH_4 + H_2O \leftrightarrows CO + 3H_2$	$\Delta H_{R,298}$ = 206.9 kJ/mol	3.5
Water Gas Shift, R_W:	$CO + H_2O \leftrightarrows CO_2 + H_2$	$\Delta H_{R,298}$ = −41.16 kJ/mol	3.6
Methane Cracking, R_C:	$CH_4 \rightarrow C_S + 2H_2$	$\Delta H_{R,298}$ = 75.5 kJ/mol	3.7
Coke Gasification, R_G:	$C_S + H_2O \rightarrow CO + H_2$	$\Delta H_{R,298}$ = 131.4 kJ/mol	3.8

In addition to the species conservation equation, for both solid and gas phases, the energy balances are solved including conductive heat losses from the reactor walls.

3.3 Model results

The main advantage of this model is the coupling between the flow field of solid and gas and the kinetic and thermal equations. There are several gas streams entering the reactor in different positions without mixing and influencing the internal macro-structure, i.e. the mapping of the different zones wetted by a particular gas.

In Table 3.1 an example of the process conditions that could be applied in the DRP reactor, with a productivity of 200 t/h, is reported. This set point is not to obtain some optimal product properties but it was chosen with the purpose to show more clearly the behavior of the model.

Table 3.1: Gas streams, defined through flow rate, pressure, temperature and volumetric percentages.

	Flow	**P**	**T**	**H_2**	**CO**	**H_2O**	**CO_2**	**CH_4**	**N_2**
	[Nm^3/h]	**[bar g]**	**[°C]**	**[%]**	**[%]**	**[%]**	**[%]**	**[%]**	**[%]**
Reducing	345000	6.8	950	66	16	3	5	8	2
NG	7000	6.3	30	0	0	0	0	97	3
Top	367000	5.8	420	41	13	29	8	7	2

The gas and solid flow patterns in the reactor are shown in Figure 3.1. For the gas there are two inlets:

1) Halfway through the shaft reactor the reducing gas enters the reactor and flows upwards through the cylindrical (upper) zone.

2) At the bottom there is a natural gas (NG) injection.

Reducing gas has an inflow velocity directed downwards with a 30-45° with respect to the symmetry axis, flowing through the streamlines shown in panels a) and b).

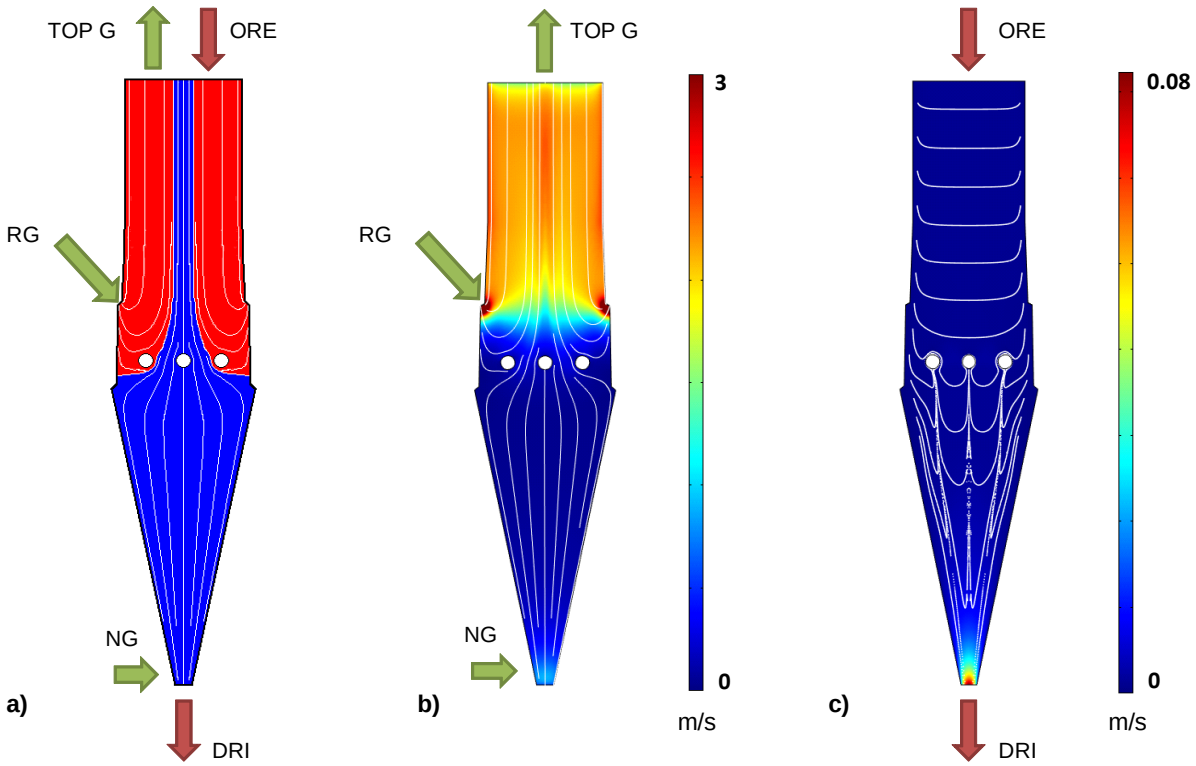

Figure 3.1: Scheme of the gas streams entering/exiting the reactor. Different zones wetted by the reducing gas (red) and the NG (blue) (a). Gas velocity pattern, as magnitude and streamlines (b). Solid velocity magnitude, with flow profiles (c).

As evident in Figure 3.1, the gas residence time is not uniform; paths are longer if they run tangentially the lower wall, thus flowing deeper inside the reactor, while those entering closer to the upper wall flow through a shorter path towards the top outlet and the gas has a lower residence time in the reactor. Natural Gas flows upwards through the cone and it focuses at the center of the cylindrical zone confined by the reducing gas that enters from the periphery. These two streams have a minimal mixing by diffusion at their interface, but they mainly go across the reactor in a segregated way, occupying a cross section proportional to their flowrate (approx. 1/50), until both of them leave the reactor at the top. In panel a) the reducing zone (red) and the natural gas zone (blue) are highlighted. The solid enters the reactor at the top, countercurrents the gas, and is discharged at the bottom with a fixed flow rate, set by the volumetric discharge valve. The calculated solid velocity profile is shown in Figure 3.1, panel c). Consistently with

previous experiments [25], in the cylindrical zone a plug flow prevails in most of the cross section (Figure 3.1 c). However, flow modifications determined by the flow feeders are correctly predicted.

Gas species composition is shown in Figure 3.2. H_2 enters the reactor mainly with the reducing gas, but it is also produced by the reforming and cracking reactions right after the reducing gas entrance and by the sole cracking reaction in the zone below the reducing gas, where the hot solid meets the natural gas (see also Figure 3.4). H_2 gets consumed flowing upwards due to the reduction reactions. CO only occupies the reducing gas zone and its composition slightly increases right after the reducing gas entrance due to steam reforming and reverse water gas shift and then diminishes flowing towards the top. CH_4 is included in the reducing gas but at this particular composition, coming from a reformed gas, because of the relatively high amount of oxidants (or low methane content) CH_4 participates partly to cracking but mostly to further reforming. In fact, with the ratio $(CO_2+H_2O)/CH_4=1$ in a high H_2 atmosphere, the thermodynamics [32] predicts that graphite is stable only after some cooling down of the gas has occurred, up to around 800°C.

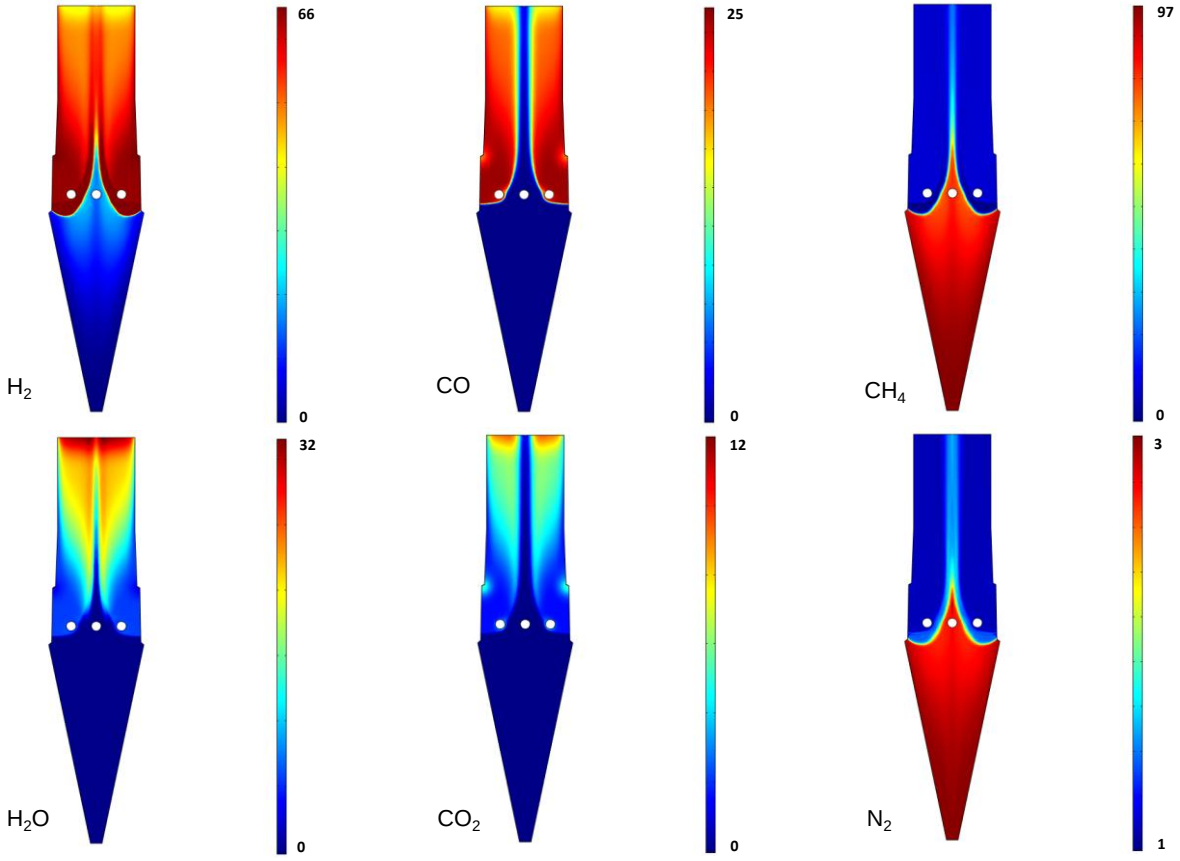

Figure 3.2: Gas composition maps [% vol]. H_2, CO, CH_4, H_2O, CO_2 and N_2.

On the contrary, the CH_4 in the natural gas does not have steam available for the reforming reaction and reacts uniquely in the cracking reaction, depositing solid carbon on the pellets and releasing H_2. As a consequence, carbon deposition occurs slightly in the reducing zone and mostly in the natural gas zone. H_2O at the reducing gas inlet is consumed by the steam reforming and produced by the reverse water gas

shift. Further on, steam is produced more abundantly by the reduction reactions in the cylindrical zone and in very little extent in the conical zone. CO_2 is consumed by the reverse water gas shift reaction (the model does not account for dry reforming) and then produced, but only in the zone occupied by the reducing gas, complementarily to CO.

Solids composition is shown in Figure 3.3. Pellets enter the reactor with a composition of around 2% humidity, 3% gangue and 95% hematite. Humidity is promptly evaporated and exits the reactor with the top gas and gangue is modeled as an inert that affects only the heat balances. The reduction from hematite to wüstite is fairly quick and gets to completion within the first 2 meters, which corresponds to approximately half an hour residence time, even though the gas is losing reducing species and temperature. The second set of reduction reactions, from wüstite to iron, requires higher temperature (higher activation energies) and lower concentration of oxidant species. Indeed, it occurs closer to the reducing gas inlet, where both temperature and concentration of H_2 and CO are actually higher. A high concentration of metallic Fe can be found in the annular region below reducing gas injection. Only the center line of the reactor presents conditions of temperature and concentration not ideal for the second reaction and the reduction goes not as far as in the annular region. Nonetheless, this is a very small fraction of solid and the mean wüstite residue in the product is lower than 5%wt.

In Figure 3.4 the main features of the product are shown: temperature, metallization and total carbon (Fe_3C plus C), in weight percent. The temperature is similar for gas and solid, except at the boundaries where they still have to thermally equilibrate. The heat supplied for the reactions enters the reactor with the gas as sensible heat. Temperature decreases moving away from the process gas inlet in every direction: upwards, downwards and inwards.

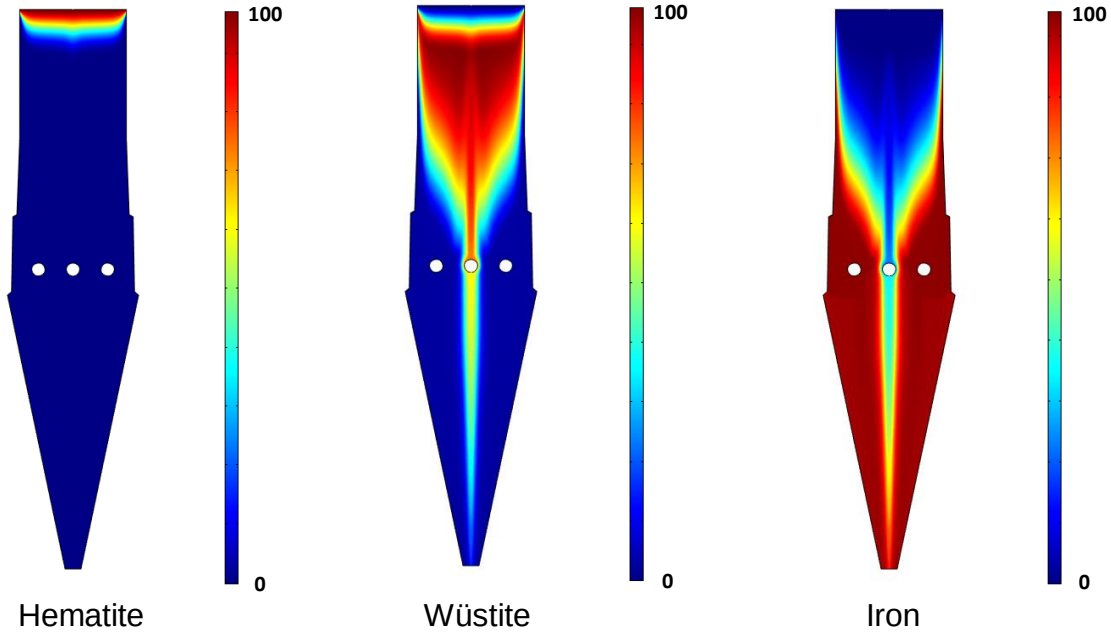

Figure 3.3: Composition of iron/iron-oxides [% wt]. Hematite, wüstite and iron.

Right after the gas inlet, there is a first temperature decrease due to the reforming reaction and to the reverse water gas shift reaction, which occur mainly in the high temperature zone where the hot gas is in contact with the metallic iron. In the present case, reforming has not a very high impact on composition because of the low steam content in the reducing gas while the reverse water gas shift has visible effects on CO/CO_2 compositions near the gas inlet.

Further on, the water gas shift reaction and the reduction reactions occur in the upper zone, the first releasing heat mildly and the second absorbing it more effectively. In this zone, the heat losses are very low thanks to the insulation applied to the wall. The flow feeders, which help the motion of the solid in the reactor and reduce the stresses on the reactor walls, are internally cooled, as well as the walls in lower part of the reactor, surrounded by water jackets. The total amount of heat loss, lower than 10 MW, is quite low in relation to the whole heat flux exchanged in the reactor (about 400 MW). The cracking and gasification reactions are both significantly endothermic; they occur in the zone below the reducing gas zone (more or less below the flow feeders) and bring the solid below the temperature (650-700°C) at which the reduction reactions, particularly from wüstite to iron, get too slow to occur quantitatively, as well as the pyrolytic carbon deposition. After undergoing some carburization, the solid passes through the cone without any other reaction occurring on it.

Metallization profiles inside the reactor have both axial and radial gradients. From the solid species compositions shown in Figure 3.3 a progression was evident in the axial direction from hematite to wüstite to iron. There are also some radial gradients, because the gas flows from the external to the internal of the reactor and downwards, so that the gas flowing inwards, to the center of the reactor, goes through longer path lines and spends more time in contact with the solid than the gas that flows upwards in the annular zone near the reactor wall, thus it is cooler and lacks reducing gas. Therefore, the pellet that flows in the reactor centerline reaches a lower metallization than the one that flows in the periphery, but this fraction is small, in terms of cross section occupied and thus in terms of flow, and the mean metallization of the charge still keeps sufficiently high, assessing to a 95.5%. In fact, the annular zone reaches almost full conversion above the reducing gas inlet, i.e. after about 3h residence time with a productivity of 200 t/h and the gas streams shown in Table 3.1.

Carbon deposition in the typical conditions of the ENERGIRON process is due to methane cracking, which is partly inhibited by H_2O and CO_2 that are contained in the process gas and that are also produced by the reduction reactions. Therefore, carbon deposits mainly in the lower part of the reactor, where the concentration of H_2O and CO_2 is still low. Cracking kinetics is the sum of a catalytic contribution and a pyrolytic one, the first one requiring the availability of Fe and the second one the permanence in a high temperature zone. Carbon deposited on the pellet can dissolve in the austenitic matrix, above 723°C, up to about 2% depending on T, while its solubility into the ferritic iron is very low. Carbon dissolved is assumed transparent to reactant diffusion, while the amount exceeding the solubility value is assumed to be deposited as Fe_3C and free carbon and forms a dense barrier through which reactants diffuse slower and slower. Fe_3C and free carbon are formed in a zone where the reduction is almost complete and, in the case of Fe_3C it is desirable thanks to its capability of passivation of the product, to prevent re-oxidation in air. They inhibit the reduction reactions, the gas phase reactions and the catalytic cracking itself. Carbon deposition is thus self-regulating, up to a limit which is extended with respect to that of graphite, to account for the higher carbon content linked to the formation of iron carbide (up to $6.67\%_{wt}$).

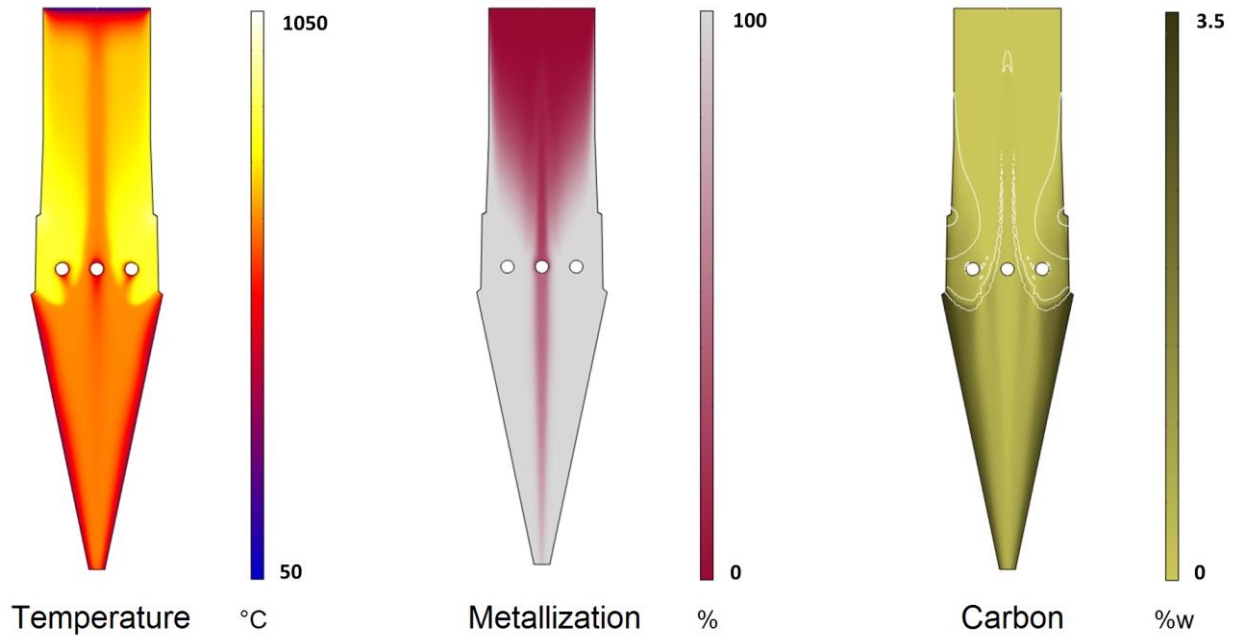

Figure 3.4: Maps of solid carbon, metallization and temperature. The carbon map contains the contour (in white) of the region where carbon is deposited.

Results thus indicate several interactions between the local status (velocity, composition and temperature) and the reactions:

1) Carbon that forms in the lower part of the reactor is a further diffusion resistance for the reactants.

2) Nonetheless, oxidant species (H_2O and CO_2) intervene in the thermodynamic equilibrium of graphite/Fe_3C, preventing or decelerating the cracking of methane.

3) Metallic iron is a requisite to have catalytic activity in the reforming and catalytic cracking reactions.

4) High temperature is required to have pyrolytic cracking, gasification, steam reforming and, to a lesser extent, reduction of wüstite.

5) Cracking and mainly steam reforming are highly endothermic and strongly affect the temperature map inside the reactor.

6) Carbon dissolved in the iron matrix (thus not blocking the diffusion of reactants) depends on temperature.

3.4 Conclusions

A 2D axial symmetric model of the DRP shaft reactor has been developed to study the internal behavior of the reactor. Reduction and gas phase reactions were included in the model, as well as the complex

interactions between the species (gas and solid) distribution and the kinetics. Simulations put in evidence the following main features:

- The flow field inside the reactor is calculated, both for solid and for gas, and the relative contact time is evaluated, evidencing different zones of wetting which can more or less favor the reduction reactions.

- The map of temperature is determined by and in turns determines the kinetics of the reactions occurring in the shaft reactor, where the only heat is supplied by the process gas. Consistent modeling of the local heat fluxes is crucial.

- Gas and solid compositions together with the kinetics of reduction and cracking where localized and characterized, in a complex net of interconnections that enhance or restrain the reduction and carburization of the product. In particular, it was understood that the chemistry of methane is the uppermost factor influencing the performances of the shaft reactor: temperature, metallization and especially carbon deposition.

The simulation model allows gaining a fundamental understanding of the major phenomena that intervene in determining the measured temperature, metallization and carburization of the DRI. The model will be used as a tool for choosing the optimum operation set points in terms of metallization, carbon content and energy consumption of the process.

Chapter 4. Continuous Models

In the previous sections, details about shrinking core models and their possible applicability have been discussed. SCM can in some cases be successfully used to describe non catalytic gas solid reaction processes, when its limitations are taken into account. For a more accurate description of a gas solid reacting system, a continuous model must be used.

4.1 Material balances

In SCM the reaction is assumed to take place only on a surface, fully characterized by a coordinate within the pellet. On the contrary, continuous models assume that the gas solid reaction can take place in any point of the particle, together with gas transport phenomena. The gas concentration transport inside the particle is ruled by the chemical species conservation equation:

$$\frac{\partial \varepsilon c_i^g}{\partial t} = -\nabla \cdot \left(\boldsymbol{N}_i^g\right) + s_i^g \qquad i = 1,2,NG \tag{4.1}$$

In this formulation, c_i^g is the molar concentration of gas species i, ε is the local particle porosity, N_i^g is the molar flux of i, and s_i is the source term, associated with the reaction. The local porosity is defined as the ratio between the volume occupied by the gas and the total volume (gas + solid). It can vary both in space and time for effect of the reaction and physical phenomena related to the change of the solid structure (for instance sintering, particle shrinking or swelling). The porosity term is present in the time derivative because in equation 4.1, c_i^g is defined as the number of moles of i per unit of volume of gas, whereas the global equation is expressed in terms of variation of number of moles per unit of total volume. The molar flux of i can be expressed as the sum of a convective and a diffusive part:

$$\boldsymbol{N}_i^g = x_i^g \cdot \boldsymbol{N}^g + \boldsymbol{J}_i^* \tag{4.2}$$

Where x_i^g is the molar fraction of i, N^g is the total molar gas flux, and J_i^* is the molar diffusive flux of i. The advantage of using this formulation is that J_i^* can be expressed as a function of the gradient of concentration of the gas species, thanks to Fick's law or multicomponent diffusion models. This part will be discussed in detail in section 5. The total molar flux can be instead calculated by the total concentration balance:

$$\frac{\partial \varepsilon c^g}{\partial t} = -\nabla \cdot (\boldsymbol{N}^g) + \sum_j^{NG} s_j^g \tag{4.3}$$

In this formulation, c is the total gas concentration. Since it is expressed per unit of volume of gas, it can be directly calculated through an equation of state, for instance the ideal gas law:

$$c^g = \frac{P}{R_g T} \tag{4.4}$$

Equation 4.3 derives from the sum of all equations 4.1 expressed for every gas species. The total gas flux is in fact equal to the sum of the convective fluxes of all species, whereas the sum of all diffusive fluxes is always zero by definition. Equation 4.3 describes the total conservation of mass in gas phase in terms of number of moles. Since the total gas concentration is already expressed by equation 4.4, equation 4.3 can be solved in the divergence of $\boldsymbol{N}^g$. For the solid phase, the concentration balance for the i-th species can be expressed by:

$$\frac{\partial c_i^s}{\partial t} = -\nabla \cdot (x_i^s \cdot \boldsymbol{N}^s) + s_i^s \qquad i = 1,2,NS \tag{4.5}$$

In this equation, porosity is not present in the time derivative, because c_i is expressed as the concentration of the solid i per unit of total volume (otherwise a factor 1-ε should be included). The total molar flux of solid N^s can be associated to a local shrinking or swelling of the solid.

A total concentration balance can also be expressed for the solid phase, by summing all of the balances for the solid species:

$$\frac{\partial c^s}{\partial t} = -\nabla \cdot (\boldsymbol{N}^s) + \sum_j^{NS} s_j^s \tag{4.6}$$

Where c^s is the local concentration of solid phase. Differently from what previously stated for equation 4.3, no equation of state can be used to determine c^s, so equation 4.6 cannot be solved in terms of N^s unless another equation is found to express c^s or its variation in time. It's not trivial to understand the physical meaning of the left hand side of equation 4.6, but it can be actually related to the variation of the local porosity in time. Using the definition of local porosity we obtain:

$$\varepsilon = 1 - \frac{V^s}{V} \tag{4.7}$$

Where V^s is the volume occupied by the solid phase, and V is the total volume. By multiplying the ratio in equation 4.7 by the total number of moles of solid, nm^s, we get:

$$\varepsilon = 1 - \frac{V^s}{V} \cdot \frac{nm^s}{nm^s} = 1 - \frac{V^s}{nm^s} \cdot c^s \tag{4.8}$$

Where we recognized that the ratio between the total number of solid moles and the total volume is equal to c^s, by definition. The total volume of solid can be expressed as the sum of the volumes occupied by the single solid species, considering the dense materials:

$$V^s = \sum_{j=1}^{NS} V_j = \sum_{j=1}^{NS} nm_j^s \cdot \frac{MW_j}{\rho_j} \quad 4.9$$

Where MW_j and ρ_j are the molecular weight and the intrinsic density of the j-th solid species, respectively. The intrinsic density is a constant property of the dense material, and only depends on the type of atoms forming the chemical species, and its crystal structure. By using equation 4.9 into 4.8, the equation of porosity becomes:

$$\varepsilon = 1 - c^s \sum_{j=1}^{NS} x_j^s \cdot \frac{MW_j}{\rho_j} \quad 4.10$$

This equation relates the porosity to the total solid concentration. Taking the derivative of equation 4.10 in time, we obtain:

$$\frac{\partial \varepsilon}{\partial t} = \frac{\partial}{\partial t}\left(1 - \sum_{j=1}^{NS} c^s x_j^s \cdot \frac{MW_j}{\rho_j}\right) = -\sum_{j=1}^{NS} \frac{\partial c_j^s}{\partial t} \cdot \frac{MW_j}{\rho_j} \quad 4.11$$

Finally, using the equation for the single solid species 4.5 into 4.11, we obtain the equation of conservation of total mass for the solid phase, written in terms of porosity:

$$\frac{\partial \varepsilon}{\partial t} = \sum_{j=1}^{NS} \frac{MW_j}{\rho_j}\left(\nabla \cdot \left(x_j^s \boldsymbol{N}^s\right) - s_j^s\right) \quad 4.12$$

This equation states that the variations of porosity in time may be due either to a local effect of shrinking or swelling of the particle (terms associated to the divergence of $x_j N^s$), or to the change of composition caused by chemical reaction, involving species with different intrinsic densities (terms associated with the source factors s_j).

The source terms for both the gas and solid balances are a function of the reaction rates:

$$for\ i = 1,2 \ldots NG \qquad s_i^g = \sum_{j=1}^{NR} \nu_{ij}^g R_j \quad 4.13$$

$$for\ i = 1,2 \ldots NS \qquad s_i^s = \sum_{j=1}^{NR} \nu_{ij}^s R_j \quad 4.14$$

Where $\nu_{ij}^g$and ν_{ij}^s are the stoichiometric coefficients of the i-th gas species and i-th solid species in the reaction j, respectively.

4.2 Energy balance

A heat production or consumption is generally associated with the chemical reactions within the particle. An energy balance must be included in the model in order to characterize the temperature in any point of the particle. This can be estimated, considering a single pseudo phase made of both solid and gas, by starting from the equation of transport of total enthalpy in the system:

$$\frac{\partial c^t H^t}{\partial t} = -\nabla \cdot (\boldsymbol{N}^t H^t + \boldsymbol{q}^t) \quad 4.15$$

In this equation, $c^t H^t$ is the total enthalpy of the system per unit of total volume, $\mathrm{N^t H^t}$ is the total flux of enthalpy associated with convection, and $\mathrm{q^t}$ is the total flux associated with thermal conduction. These quantities can be expressed as a function of the properties of the two phases, solid and gas, composing the medium. In particular:

$$c^t H^t = \varepsilon c^g H^g + c^s H^s \quad 4.16$$

Where H^g is the enthalpy of gas per unit of mole of gas mixture and H^s is the enthalpy of solid per unit of mole of solid mixture. A porosity factor is present in the gas part, because the total gas concentration is defined with respect to the volume of gas whereas the total solid concentration as a function of the total volume. The total convective flux of enthalpy is:

$$\boldsymbol{N}^t H^t = \boldsymbol{N}^g H^g + \boldsymbol{N}^s H^s \quad 4.17$$

The conductive flux can be expressed through the Fourier law, considering a pseudo conductivity of the medium, weighted on the relative amount of occupied volume:

$$\boldsymbol{q}^t = -(\varepsilon k^g + (1-\varepsilon) k^s) \nabla T \quad 4.18$$

Where $\mathrm{k^g}$ and $\mathrm{k^s}$ are the conductivities of the gas and solid phases, respectively. They can be calculated using a rule of mixtures, as the one reported:

$$k^g = \sum_{j=1}^{NG} x_j^g k_j^g \quad 4.19$$

$$k^s = \sum_{j=1}^{NS} x_j^s k_j^s \quad 4.20$$

Equation 4.15 becomes, making use of 4.16-4.18:

$$\frac{\partial \varepsilon c^g H^g}{\partial t} + \frac{\partial c^s H^s}{\partial t} = -\nabla \cdot (\boldsymbol{N}^g H^g) - \nabla \cdot (\boldsymbol{N}^s H^s) + \nabla \cdot \left((\varepsilon k^g + (1-\varepsilon) k^s) \nabla T\right) \quad 4.21$$

The total enthalpies of gas and solid phase can be expressed through a simple rule of mixture, neglecting the enthalpies of mixing. So, for instance, for the gas:

$$H^g = \sum_{j=1}^{NG} x_j^g H_j^g \qquad 4.22$$

The derivatives in the differential equation 4.21 can be decomposed as a function of the phases compositions and temperature, making use of the definition of heat capacity:

$$Cp_j^g = \frac{\partial H_j^g}{\partial T} \qquad 4.23$$

Consistently with the units used so far, this heat capacity is defined on a molar base (J/mol/K or its multiples).

The accumulation term relative to the gas phase can be decomposed as follows:

$$\frac{\partial \varepsilon c^g H^g}{\partial t} = \sum_{j=1}^{NG} H_j^g \frac{\partial \varepsilon c_j^g}{\partial t} + \varepsilon c^g \sum_{j=1}^{NG} x_j^g \frac{\partial H_j{}^g}{\partial t} = \sum_{j=1}^{NG} H_j^g \frac{\partial \varepsilon c_j^g}{\partial t} + \varepsilon c^g \sum_{j=1}^{NG} x_j^g Cp_j^g \frac{\partial T}{\partial t} \qquad 4.24$$

The same rule of mixtures of the enthalpy can be applied to the heat capacity of the gas, phase:

$$Cp^g = \sum_{j=1}^{NG} x_j^g Cp_j^g \qquad 4.25$$

So equation 4.24 becomes:

$$\frac{\partial \varepsilon c^g H^g}{\partial t} = \sum_{j=1}^{NG} H_j^g \frac{\partial \varepsilon c_j^g}{\partial t} + \varepsilon c^g Cp^g \frac{\partial T}{\partial t} \qquad 4.26$$

The same mathematical procedure can be applied to the convective part, obtaining:

$$\nabla \cdot (\boldsymbol{N}^g H^g) = \sum_{j=1}^{NG} H_j^g \nabla \cdot \left(x_j^g \boldsymbol{N}^g\right) + Cp^g \boldsymbol{N}^g \cdot \nabla T \qquad 4.27$$

By summing equations 4.26 and 4.27, we obtain:

$$\frac{\partial \varepsilon c^g H^g}{\partial t} + \nabla \cdot (\boldsymbol{N}^g H^g) = \varepsilon c^g Cp^g \frac{\partial T}{\partial t} + Cp^g \boldsymbol{N}^g \cdot \nabla T + \sum_{j=1}^{NG} H_j^g \left(\frac{\partial \varepsilon c_j^g}{\partial t} + \nabla \cdot \left(x_j^g \boldsymbol{N}^g\right) \right) \qquad 4.28$$

It can be immediately recognized that the factors in the sum in equation 4.28 can be expressed by making use of the equation of conservation of the single gas species (4.1 and 4.3), so that:

$$\frac{\partial \varepsilon c^g H^g}{\partial t} + \nabla \cdot (\boldsymbol{N}^g H^g) = \varepsilon c^g Cp^g \frac{\partial T}{\partial t} + Cp^g \boldsymbol{N}^g \cdot \nabla T + \sum_{j=1}^{NG} H_j^g s_j^g - \sum_{j=1}^{NG} H_j^g \nabla \cdot (\boldsymbol{J}_j^*) \quad 4.29$$

For the solid phase we can get to a similar result:

$$\frac{\partial c^s H^s}{\partial t} + \nabla \cdot (\boldsymbol{N}^s H^s) = c^s Cp^s \frac{\partial T}{\partial t} + Cp^s \boldsymbol{N}^s \cdot \nabla T + \sum_{j=1}^{NS} H_j^s s_j^s \quad 4.30$$

Equations 4.29 and 4.30 can be used in equation 4.21, obtaining equation 4.31:

$$(\varepsilon c^g Cp^g + c^s Cp^s) \frac{\partial T}{\partial t} = -(Cp^g \boldsymbol{N}^g + Cp^s \boldsymbol{N}^s) \cdot \nabla T - \sum_{j=1}^{NG} H_j^g \nabla \cdot (\boldsymbol{J}_j^*) + \nabla \cdot \left((\varepsilon k^g + (1-\varepsilon) k^s) \nabla T\right) - \sum_{j=1}^{Nt} H_j s_j \quad 4.31$$

In equation 4.31, the two sums of the source terms have been collected in a single sum, related to all the species (solid + gas). That term source term can be further developed, by using equations 4.13-4.14, and recalling the definition of heat of reaction:

$$\Delta H_j^R = \sum_{i=1}^{Nt} \nu_{ij} H_i \quad 4.32$$

The final result for the energy balance is:

$$(\varepsilon c^g Cp^g + c^s Cp^s) \frac{\partial T}{\partial t} = -(Cp^g \boldsymbol{N}^g + Cp^s \boldsymbol{N}^s) \cdot \nabla T - \sum_{j=1}^{NG} H_j^g \nabla \cdot (\boldsymbol{J}_j^*) + \nabla \cdot \left((\varepsilon k^g + (1-\varepsilon) k^s) \nabla T\right) - \sum_{j=1}^{NR} \Delta H_j^R R_j \quad 4.33$$

This final form shows in a better way the relationship between the temperature changes inside the gas-solid medium and the different mechanisms of transport of mass and energy. In particular, temperature changes may be due to:

- Transport of energy associated with the convective flux of gas $\boldsymbol{N}^g$.
- Transport of energy associated with the convective flux of solid $\boldsymbol{N}^s$.
- Transport of energy associated with the diffusive fluxes of gas species $\boldsymbol{J}_j^*$.
- Transport of energy by conduction in both solid and gas phases.
- Heat production generated by the chemical reactions R_j.

In common practice, when describing the energy transport in porous solids, the first and third contributions are neglected. A simplified version of equation 4.33 is used instead, which is:

$$(cCp) \frac{\partial T}{\partial t} = -\nabla \cdot (Cp^g \boldsymbol{N}^g - \mathrm{k_t} \nabla \mathrm{T}) - \sum_{j=1}^{NR} \Delta H_j^R R_j \quad 4.34$$

Where the global heat capacity and conductivity are:

$$cCp = \varepsilon\, c^g Cp^g + c^s Cp^s \qquad 4.35$$

$$\mathrm{k_t} = \varepsilon k^g + (1-\varepsilon)k^s \qquad 4.36$$

In general, a number of parameter are temperature dependent in the energy balance (c^g, Cp^g, Cp^s, k^g, k^s, H_j^g, ΔH_j^R).

4.3 Model for spherical particles

According to the continuous model described so far, the evolution of the gas-solid medium can be described through the system of equations 4.1, 4.3, 4.5, 4.6, 4.10 and 4.33 (possibly replaced by 4.34). The variables to solve are c_i^g, c_i^s, $\boldsymbol{N}^g$, $\boldsymbol{N}^s$, ε, P, T. Considering that the total fluxes have generally three components for a 3D system, the number of equations is not sufficient to determine the solution. For the gas phase, a momentum balance could be added. In this sense, the Darcy equation is usually a good choice: this relates the gas pressure gradient with the gas velocity field, through the viscosity and permeability parameters. Once the velocity field is calculated, the molar flux can be found by scaling it by the total gas concentration.

Usually, the continuous model dimensionality can be simplified, thanks to the symmetric behavior of the described geometry. For the case of solid spherical particles, if the boundary and initial conditions applied to the system are homogeneous along the angular coordinates, the presented model can be reduced to a mono dimensional one, where only the radial components of the gradients and divergences are taken into account. The equations of conservation of the gas and solid species, and the energy balance become, according to this simplifications:

$$\frac{\partial \varepsilon c_i^g}{\partial t} = -\frac{1}{r^2}\frac{\partial}{\partial r}\left(r^2\left(x_i^g N^g + J_i^*\right)\right) + s_i^g \qquad i = 1, 2 \ldots NG \qquad 4.37$$

$$\frac{\partial \varepsilon c^g}{\partial t} = -\frac{1}{r^2}\frac{\partial}{\partial r}(r^2 N^g) + \sum_{j=1}^{NG} s_j^g \qquad 4.38$$

$$\frac{\partial c_i^s}{\partial t} = -\frac{1}{r^2}\frac{\partial}{\partial r}\left(r^2(x_i^s N^s)\right) + s_i^s \qquad i = 1, 2 \ldots NS \qquad 4.39$$

$$\frac{\partial c^s}{\partial t} = -\frac{1}{r^2}\frac{\partial}{\partial r}(r^2 N^s) + \sum_{j=1}^{NS} s_j^s \qquad 4.40$$

$$(cCp)\frac{\partial T}{\partial t} = -\frac{1}{r^2}\frac{\partial}{\partial r}\left(r^2\left(Cp^g N^g - k_t\frac{\partial T}{\partial r}\right)\right) - \sum_{j=1}^{NR}\Delta H_j^R R_j \qquad 4.41$$

In this formulation, N^g and N^s are the radial components of the total molar fluxes of gas and solid, respectively, while J_i^* is the radial component of the diffusive flux of the i-th gas species. These five equations must be added to the equation of porosity (4.10), the gas equation of state (4.4), and the equations for the production rates (4.13-4.14). Besides, a diffusion model is needed to express J_i^* and a kinetic model is needed to express R_j. These will be discussed further on. Usually the value of the gas pressure P can be assumed to be radially constant. If this is true, no momentum equation is needed, and the total molar flux of gas can be calculated from the total concentration equation (4.8). In fact, this becomes:

$$\frac{1}{r^2}\frac{\partial}{\partial r}(r^2 N^g) = -c^g \frac{\partial \varepsilon}{\partial t} + \varepsilon \frac{c^g}{T}\frac{\partial T}{\partial t} + \sum_{j=1}^{NG} s_j^g \qquad 4.42$$

Where the time derivative of porosity can be expressed through equation 4.11 and the time derivative of temperature through equation 4.41.

The system still needs a closure to determine the solid flux N^s. Nevertheless, in most application the effect of change in size of the particle can be neglected. If this is true, N^s can be assumed to be zero. The equation of conservation of the solid species and total solid concentration become:

$$\frac{\partial c_i^s}{\partial t} = s_i^s \qquad i = 1, 2 \dots NS \qquad 4.43$$

$$\frac{\partial c^s}{\partial t} = \sum_{j=1}^{NS} s_j^s \qquad 4.44$$

In this formulation, no spatial derivatives are present in the equations for the solid. It's important to point out that this does not imply that c_i^s and c^s only change in time and are constant in r, because the terms s_i^s will necessarily depend on the concentration of the gas species, which are generally different in any radial coordinate because the spatial derivatives in equations 4.37-4.38 are still present. The equation that describes the evolution of the porosity, according to the constant volume assumption becomes:

$$\frac{\partial \varepsilon}{\partial t} = -\sum_{j=1}^{NS} \frac{MW_j}{\rho_j} s_j^s \qquad 4.45$$

Finally, the equation for the total gas flux becomes:

$$\frac{1}{r^2}\frac{\partial}{\partial r}(r^2 N^g) = c^g \sum_{j=1}^{NS} \frac{MW_j}{\rho_j} s_j^s + \frac{\varepsilon c^g}{(cCp)T}\left(\frac{1}{r^2}\frac{\partial}{\partial r}\left(r^2\left(-Cp^g N^g + k_t \frac{\partial T}{\partial r}\right)\right) - \sum_{j=1}^{NR} \Delta H_j^R R_j\right) + \sum_{j=1}^{NG} s_j^g \qquad 4.46$$

This equation states that a total molar gas flux can be generated by these following phenomena:

- Chemical reactions with solid reagents and products having different densities and molecular weights.

- Radial gradients of temperature.
- Chemical reactions with nonzero net heat production.
- Chemical reactions with a net production of number of gas moles.

The first three phenomena are present in almost every case, whereas in some situations the gas solid reactions are equimolar with respect to the gas species, in which case the last sum of the right hand side of equation 4.46 is zero. From a different point of view, the terms related to the first three phenomena are usually of little importance in equation 4.46: in fact, in many cases the radial gradients are small and the particle temperature can be considered as more or less uniform, and the first sum in the right hand side of equation 4.46 is small. On the contrary the net production of gas moles can be important for non equimolar reactions.

4.4 Boundary and initial conditions

The system of partial differential equations obtained by the previous analysis can be solved, once a proper set of boundary and initial conditions is provided. For equations 4.37and 4.41, two boundary conditions are needed, whereas for equations 4.38, 4.39 and 4.40 only one is necessary. At the centre of the particle (r = 0), symmetry conditions must be used: in particular, all fluxes must be zero, otherwise a net production of mass or energy is created. This is equal to assume that the radial derivatives of all the variables are equal to zero.

$$for\ r = 0 \qquad \begin{aligned} N_i^g &= 0 \\ N^g &= 0 \\ x_i^s N^s &= 0 \\ N^s &= 0 \\ \frac{\partial T}{\partial r} &= 0 \end{aligned} \qquad 4.47$$

If equation 4.43 and 4.44 are used to describe the solid phase, no boundary conditions are needed from a mathematical point of view. However, the solid concentration profiles will implicitly satisfy a condition of zero derivative at the centre of the particle, that derives from the source term which is function of the gas concentration profile where that boundary condition is applied. At the external particle surface, r = r_0, the gas composition and temperature may be known, if no external mass and energy resistances are present: in such a case, a Dirichlet boundary condition can be used:

$$for\ r = r_0 \qquad \begin{aligned} c_i^g &= c_{i,bulk} \\ T &= T_{bulk} \end{aligned} \qquad 4.48$$

Where $c_{i,bulk}$ and T_{bulk} are the concentration of the i-th gas species and temperature at the bulk, respectively. This condition is usually true if the gas velocity is high outside the particle, so that convection can overcome the concentration gradients near the particle surface that naturally arise because of reaction.

If these gradients are still important, c_i^g and T are generally different from the bulk values. In this situation, a condition on the fluxes is applied at the boundary, using the heat and mass transfer coefficient approach:

$$for\ r = r_0 \qquad \begin{aligned} N_i^g &= h_i \cdot \left(c_i^g - c_{i,bulk}\right) \\ -k_t \frac{\partial T}{\partial r} &= h_t \cdot (T - T_{bulk}) \end{aligned} \qquad 4.49$$

Equations 4.49 state that the mass and energy fluxes approaching the particle surface from the inside must be equal to the ones calculated approaching from the outside. In this formulation, h_i and h_t are the mass transfer coefficient of the i-th species and the heat transfer coefficient, respectively. This approach allows not to model the transport phenomena outside the particle in detail, which will necessarily imply a 2D or 3D approach, because the gas velocity field outside the particle is always too much complex to be described with a monodimensional approach.

The initial conditions for the system are reported in equation 4.50:

$$for\ \ t = 0 \qquad \begin{aligned} c_i^g &= c_i^{g\,0}(r) \\ c_i^s &= c_i^{s\,0}(r) \\ T &= T^0(r) \end{aligned} \qquad 4.50$$

Usually, uniform radial profiles are assumed at the beginning of reaction.

4.5 Reaction models

In the sets of equations presented so far, a kinetic model must be provided to characterize the values of the reaction rates R_j as a function of the local gas and solid reagents, and temperature. A set of reactions can be considered, in the following form:

$$a\ A(s) + \ b\ B(g) \rightarrow c\ C(s) + \ d\ D(g) \qquad 4.51$$

Possible variations can consider solid or gas product, in which case the mathematical approach is very similar to the one presented. The form of the reaction rate associated to the presented stoichiometry can be expressed by the following general expression:

$$R = k(T) \cdot g(c_B^g, c_D^g) \cdot f(X_A) \qquad 4.52$$

Where $k(T)$ is the kinetic constant associated to the reaction, c_B^g and c_D^g are the concentrations of the gas reagent and product, and X_A is the conversion of the solid reagent, which is a function of the local concentration if the solid reagent, as follows:

$$X_A = 1 - \frac{c_A^S}{c_A^{S\,0}} \tag{4.53}$$

The formulation in equation 4.51 separates the dependency on the three variables into the product of three functions. The kinetic constant only depends on temperature, through the Arrhenius law:

$$k = A \exp\left(-\frac{Ea}{R_g T}\right) \tag{4.54}$$

Where A and Ea are the pre exponential factor and activation energy, respectively, and are characteristic of the chemical reaction. The form of the functions f and g can be different, according to different models.

4.5.1 Effect of the gas concentration

The dependency on the gas concentration of the reaction rate is expressed through the function g. The simplest approach is assuming a power law on the concentration of the reagent, that is:

$$g\left(c_B^g, c_D^g\right) = \left(c_B^g\right)^\beta \tag{4.55}$$

Where β is a parameter, usually assumed equal to the stoichiometric coefficient b or equal to one. A more complex function can be found, if an adsorption mechanism is included in the kinetic scheme. As a matter of fact, all gas-solid reactions are superficial, and the gas species must reach the solid phase before reacting. The global reaction described by equation 4.51 can be decomposed for the gas part into a series of elementary steps, as follows:

$$B(g) + S \leftrightarrow B^*(s) \tag{4.56}$$

$$b\,B^*(s) \rightarrow d\,D^*(s) \tag{4.57}$$

$$D^*(s) \leftrightarrow D(g) + S \tag{4.58}$$

In such a formulation, S is the free solid site, B^* and D^* are the adsorbed species B and D. The adsorption and desorption reactions of both B and D are taken into account. Assuming first order reaction for all of the elementary steps, the reaction rates associated with them are as follows:

$$R_1 = k_1 c_B^g \theta_S - k_{-1}\theta_{B^*} \tag{4.59}$$

$$R_2 = k\,\theta_{B^*} \tag{4.60}$$

$$R_3 = k_3 \theta_{D^*} - k_{-3} c_D^g \theta_S \tag{4.61}$$

The quantities θ_{B^*} and θ_{D^*} are the fractions of solid surface occupied by the gas B and D, respectively, while θ_S is the fraction of empty surface. The Langmuir-Hinshelwood approach allows finding an analytical expression for R_2 as a function of the concentrations of free gas alone. First of all, the pseudo steady state approximation is applied to the production rates of θ_S, θ_{B^*} and θ_{D^*}, obtaining the equations:

$$s_{\theta_{B^*}} = k_1 c_B^g \theta_S - k_{-1}\theta_{B^*} - b\ k\ \theta_{B^*} = 0 \quad 4.62$$

$$s_{\theta_{D^*}} = d\ k\ \theta_{B^*} - k_3\theta_{D^*} + k_{-3} c_D^g \theta_S = 0 \quad 4.63$$

These two equations can be coupled with the equation of overall balance of the surface:

$$\theta_S + \theta_{B^*} + \theta_{D^*} = 1 \quad 4.64$$

Equations 4.62-4.64 are a system of three equations that can be solved in the variables θ_S, θ_{B^*} and θ_{D^*}. A further simplification can be used: if it is assumed that the step of equation 4.60 is slow if compared to the other two, reactions 4.59 and 4.61 will be near equilibrium. This means that the reactions rates R_1 and R_3 are zero. The surface fractions occupied by B^* and D^* can then be calculated as a function of the fraction of free surface, as follows:

$$\theta_{B^*} = \frac{k_1}{k_{-1}} c_B^g \theta_S = K_A c_B^g \theta_S \quad 4.65$$

$$\theta_{D^*} = \frac{k_{-3}}{k_3} c_D^g \theta_S = K_D c_D^g \theta_S \quad 4.66$$

Now, using equation 4.64, θ_S is found:

$$\theta_S = \frac{1}{1 + K_A c_B^g + K_D c_D^g} \quad 4.67$$

Combining this with equations 4.65 and 4.60 we obtain:

$$R_2 = k \frac{K_A c_B^g}{1 + K_A c_B^g + K_D c_D^g} \quad 4.68$$

More simplifications can be introduced, depending on the equilibrium of adsorption and desorption. In particular, it is trivial to prove that if both adsorption and desorption equilibria are shifted to the products in reactions 4.56 and 4.58, then K_A approaches infinite and K_D approaches zero, which means that R2 becomes a first order expression in c_B.

It's important to point out that the Langmuir-Hinshelwood model was developed for catalysis problems, where the reaction generally does not have an effect on the solid composition and structure of the solid matrix. When the solid phase reacts, things are more complicated, because the reacting surface is changing itself. So equation 4.68 cannot fully replace equation 4.52. On the other hand, the phenomena related to the gas phase can still be described with the same approach. Equation 4.68 can then be used to express the function g:

$$g\left(c_B^g, c_D^g\right) = \frac{K_A c_B^g}{1 + K_A c_B^g + K_D c_D^g} \quad 4.69$$

The parameters K_A and K_D may be also dependent from temperature.

4.5.2 Effect of solid conversion

In gas-solid reaction problems, a factor depending on the solid composition must be included in the reaction rate formula. This is necessary because the reaction occurs only if the gas reagent adsorption takes place on the solid reagent. In this sense, in equation 4.52 the function f(X) describes the local abundance of solid A per unit volume of porous solids. Being the reaction heterogeneous in nature, the relevant measure of abundance is the amount of superficial reagent A per unit volume, which strongly depends on the local structure of the porous solids. This function can be expressed by making some assumptions on the evolution of the solid matrix due to the reaction. A classification of the available forms of f(X) was reported by Gomez-Barea and Ollero [7], and it is shown in table 4.1:

Table 4.1: Classification of gas-silid reaction models according to Gomez-Barea and Ollero

Name	f(X)	Parameters	Reference
Volumetric model	$(1-X)$	-	Adanez and De Diego (1993) Szekely et al. (1976) Adschiri et al. (1986)
Simplified grain model	$(1-X)^{2/3}$	-	Van den Aarsen (1985)
Random pore model	$(1-X)(1-\psi_0 \ln(1-X))^{1/2}$	ψ_0	Bhatia and Perlmutter (1980)
Struis	$(1+(p+1)\alpha t)(1-X)(1-\psi_0 \ln(1-X))^{1/2}$	p, α, ψ_0	Struis et al. (2002)
Simons model	$(1-X)(X+\alpha_0(1-X))^{1/2}$	α_0	Simons (1980)
Johnson model	$(1-X)^{2/3} e^{\alpha X^2}$	α	Johnson (1979)
Dutta model	$\left(1 \pm 100 X^{\gamma\beta} \exp(-\beta X)\right) \cdot (1-X)$	α, β	Dutta et al. (1977)
Gardner model	$(1-X)e^{\alpha X}$	α	Gardner et al. (1979)
Modified volumetric model	$a^{1/b} b (1-X)(-\ln(1-X))^{(b-1)/b}$	a, b	Kasaoka et al. (1985)
Traditional	$(1-X)^{\alpha}$	α	
Polynomial model	$\sum_{i=1}^{n} a_i X(1-X)^i$	a_i	Ollero et al. (2003) Gomez-Barea et al. (2005)

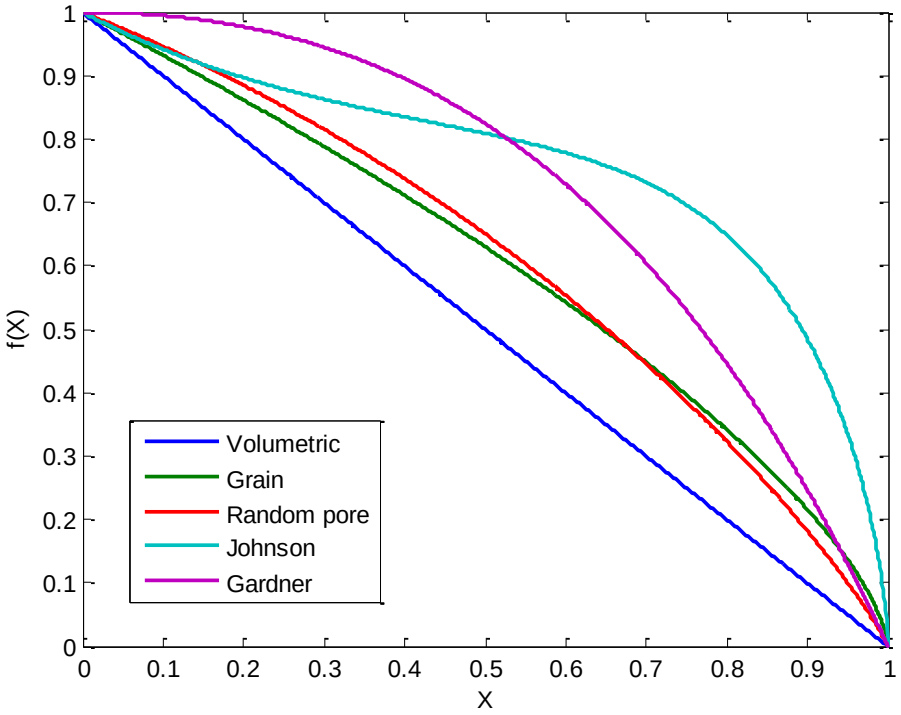

Figure 4.1: Shape of several superficial area models

Figure 4.1 shows the shape of f(X) according to some of these functions, considering unit values for the parameters. These functions are all equal to one at zero conversion, and equal to zero at complete conversion: from a physical point of view, this corresponds to the fact that the superficial area is maximum at the beginning of the reaction, and drops to zero at the end. The reaction rate will correctly be zero when there is no more solid reagent in the system.

4.5.2.1 The grain model

The simplest way of expressing f(X) is by considering the local geometry and the microscopic structure of the solid inside the particle. According to the grain model, proposed by Szekely [1] and still widely used, the solid reactant is described as made of micro spherical grains. The evolution of the structure of the micrograins is described through the shrinking core model, with a reaction interface moving from the grain surface to the center, as long as the reaction proceeds. The boundary condition for the gas at the grain surface is the local radial concentration of gas inside the particle. The micrograin structure can actually be observed in many porous ceramic materials (metal oxides). With such a scheme, the approach seen in chapter §2 is applied to the grain scale we have that:

$$f(X) = \left[(1-X)^{-\frac{2}{3}} + b\,\frac{k\,r_g}{a_0\,D_{B,g}}\left((1-X)^{-\frac{1}{3}} - 1\right)\right]^{-1} \qquad 4.70$$

In such expression, $D_{B,g}$ is the effective diffusivity of the gaseous reactant into the grain product layer, r_g is the grain radius and a_0 is the ratio between the initial surface of the solid reactant into the particle and the total volume of the particle itself. This ratio is still somehow related to the grain size (r_g), but also depends on more complex geometry parameters, related to their packing. Equation 4.70 represents the complete form of the grain model, where both kinetic and intra grain diffusion resistances are considered. A simplified form is commonly used, which only takes into account the kinetic component. Accordingly, equation 4.70 becomes:

$$f(X) = (1-X)^{2/3} \qquad 4.71$$

This function also approximates that there is no important diffusion resistance inside the micrograin (diffusion is only considered on the scale of the particle).

4.5.2.2 The traditional model

The simplified grain model in equation 4.71 above can be generalized as:

$$f(X) = (1-X)^{\alpha} \qquad 4.72$$

Where α can take into account different shapes of the micrograins. For instance, for cylindrical shape α = 1/2, for planar slabs α = 0. Note that α can also account for the reshaping phenomena occurring during the reaction, namely sintering of the solid due to high temperatures. If sintering occurs, α will become larger, because there will be a faster decrease of the superficial area at the beginning of the reaction.

It is important to point out that f(X) describes the ratio between the actual and initial surface of the solid reagent per unit of total volume. For the grain model it is the ratio between the spherical surface of the unreacted core of the micrograin and the total external surface of the grain. It will be shown further on that the shape of f(X) can have a major influence on the model results. This means that it is extremely important to correctly describe the evolution of the solid surface due both to chemical and physical phenomena. Figure 4.2 shows the effect of α on the function f(X):

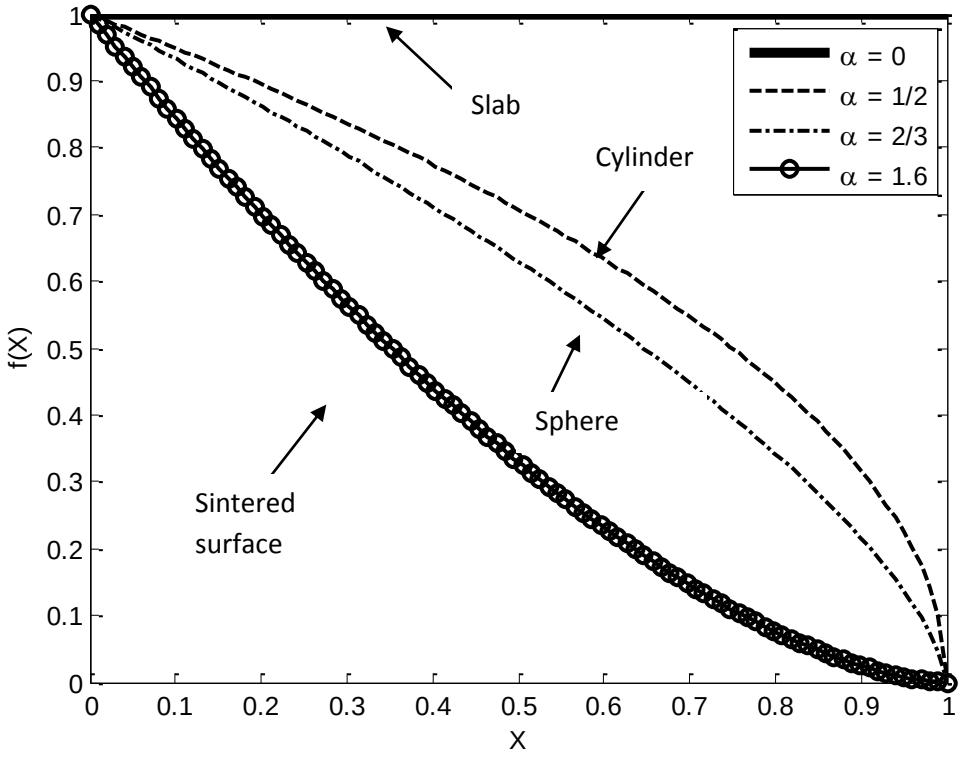

Figure 4.2: Change of the superficial area of solid reactant as a function of the conversion, for different values of α

If $\alpha > 0$, the available solid surface decreases more quickly with conversion, and so does the reaction rate. This can be the situation when sintering is important.

4.5.3 Effect of chemical equilibrium

In the previous cases, the gas-solid reaction was always assumed to be irreversible. If chemical equilibrium is important, the shape of the reaction rate function must be changed to take this into account. The reversible variation of reaction 4.51 is as follows:

$$a\,A(s) + b\,B(g) \rightleftarrows c\,C(s) + d\,D(g) \qquad 4.73$$

The form of the global reaction rate can be found by assuming that it is the sum of two reaction rates (the direct and inverse reaction). So, applying equation 4.52, we obtain:

$$R = \vec{k}(T) \cdot g_1\left(c_B^g, c_D^g\right) \cdot f(X_A) - \overleftarrow{k}(T) \cdot g_2\left(c_B^g, c_D^g\right) \cdot f(X_C) \qquad 4.74$$

Now it can be remembered that the ratio between $\vec{k}$ and $\overleftarrow{k}$ is equal to the equilibrium constant of the reaction, K, so expression 4.74 becomes:

$$R = \vec{k}(T) \cdot \left(g_1\left(c_B^g, c_D^g\right) \cdot f(X_A) - \frac{1}{K} \cdot g_2\left(c_B^g, c_D^g\right) \cdot f(X_C) \right) \qquad 4.75$$

This expression can be used, once K is calculated through thermodynamic relations.

4.6 Continuous model in terms of mass

In the previous sections, the continuous model for gas solid reactions in porous media has been described. The material balances for both gas and solid species were expressed in terms of number of moles. The energy balance was also developed by considering the specific enthalpies and heat capacity per unit of moles of single species or mixture. It is also possible to formulate the same model in terms of mass, mass fractions of the single components, mass densities, etc. The mathematical treatment of the equations is very similar to the molar case, so we only report the final set of equations. For a spherical particle, the model of equations 4.37-4.41 becomes:

$$\frac{\partial \varepsilon \rho_i^g}{\partial t} = -\frac{1}{r^2}\frac{\partial}{\partial r}\left(r^2\left(y_i^g n^g + j_i\right)\right) + s_i^g MW_i \qquad i = 1, 2 \dots NG \qquad 4.76$$

$$\frac{\partial \varepsilon \rho^g}{\partial t} = -\frac{1}{r^2}\frac{\partial}{\partial r}(r^2 n^g) + \sum_{j=1}^{NG} s_j^g MW_j \qquad 4.77$$

$$\frac{\partial \rho_i^s}{\partial t} = -\frac{1}{r^2}\frac{\partial}{\partial r}\left(r^2(y_i^s n^s)\right) + s_i^s MW_i \qquad i = 1, 2 \dots NS \qquad 4.78$$

$$\frac{\partial \rho^s}{\partial t} = -\frac{1}{r^2}\frac{\partial}{\partial r}(r^2 n^s) + \sum_{j=1}^{NS} s_j^s MW_j \qquad 4.79$$

$$\left(\rho \widehat{Cp}\right)\frac{\partial T}{\partial t} = -\frac{1}{r^2}\frac{\partial}{\partial r}\left(r^2\left(\widehat{Cp}^g n^g - k_t \frac{\partial T}{\partial r}\right)\right) - \sum_{j=1}^{NR} \Delta \hat{H}_j^R R_j \qquad 4.80$$

In this formulation, $\rho_i^g$and y_i^g are the mass concentration and mass fraction of the i-th gas species, respectively, ρ_i^s and y_i^s are the mass concentration and mass fraction of the i-th solid species, n^g and n^s

are the total mass fluxes of gas and solid, respectively, j_i is the mass diffusive flux of the i-th gas species, and MW_i is the molecular weight of i. The parameters inside the energy balance can be expressed as follows:

$$\rho\widehat{Cp} = \varepsilon\,\rho^g \sum_{j=1}^{NG} y_j^g \frac{{Cp_j}^g}{MW_j} + \sum_{j=1}^{NS} y_j^s \frac{{Cp_j}^s}{MW_j} \qquad 4.81$$

$$\Delta\widehat{H}_j^R = \sum_{i=1}^{Nt} \nu_{ij} \frac{H_i}{MW_i} \qquad 4.82$$

Also in this form the total flux of gas can be calculated through equation 4.77, obtaining:

$$\frac{1}{r^2}\frac{\partial}{\partial r}(r^2 n^g) = \rho^g \sum_{j=1}^{NS} \frac{MW_j}{\rho_j} s_j^s + \frac{\varepsilon\rho^g}{\rho\widehat{Cp}T}\left(-\frac{1}{r^2}\frac{\partial}{\partial r}\left(r^2\left(\widehat{Cp}^g n^g - k_t\frac{\partial T}{\partial r}\right)\right) - \sum_{j=1}^{NR}\Delta\widehat{H}_j^R R_j\right) + \varepsilon\rho^g \sum_{j=1}^{NG}\frac{\partial y_j}{\partial t}\frac{MW^g}{MW_j} + \sum_{j=1}^{NG} s_j^g\, MW_j \qquad 4.83$$

It is important to point out that this formulation of the continuous model has the same mathematical solution as the molar set equations (4.37-4.41). Yet, the results can be different if some contributions are neglected. This will be shown in more detail in section 6, with respect to the contribution of gas convection.

Notation

A	Pre exponential factor of Arrhenius law (mol,cm,s)
a_0	Initial specific surface of the solid matrix (1/cm)
c_i^g, c_i^s	Molar concentration, of the i-th gas species, of the i-th solid species (mol/cm^3)
$c_i^{g\,0}, c_i^{s\,0}$	Initial molar concentration, of the i-th gas species, of the i-th solid species (mol/cm^3)
$c_{i,bulk}$	Concentration of the i-th gas species outside the particle, in bulk phase (mol/cm^3)
c^g, c^s	Total concentration of gas phase, of solid phase (mol/cm^3)
c^t	Total concentration of combined phases (mol/cm^3)
cCp	Heat capacity of the medium (J/cm^3/K)
Cp_i^g, Cp_i^s	Heat capacity of the i-th gas species, of the i-th solid species (J/mol/K)
Cp^g, Cp^s	Heat capacity of the gas phase, of the solid phase (J/mol/K)
$\widehat{Cp}^g$	Massive heat capacity of the gas phase (J/g/K)
$D_{i,g}$	Effective diffusivity of i into the grain
Ea	Activation energy (J/mol)
h_i	Mass transfer coefficient of i (cm/s)
h_t	Heat transfer coefficient (W/cm^2/K)
H_i^g, H_i^s	Enthalpy of the i-th gas species, of the i-th solid species (J/mol)
H^g, H^s	Enthalpy of the gas phase, of the solid phase (J/mol)

H^t	Total enthalpy of combined phases (J/mol)
J_i^*	Molar diffusive flux of i (mol/cm^2/s)
k, k_i	Kinetic constant, of a general reaction, of the i-th reaction step (mol, cm, s)
$k_i{}^g, k_i{}^s$	Thermal conductivity of the i-th gas species, of the i-th solid species (W/cm/K)
k^g, k^s	Thermal conductivity of the gas phase, of the solid phase (W/cm/K)
k_t	Thermal conductivity of the medium (W/cm/K)
K, K_i	Equilibrium constant, of a generic reaction, of the i-th reaction step
MW_i	Molecular weight of the i-th species (g/mol)
nm_i^s, nm^s	Number of moles of the i-th solid species, total number of moles of solid
n^g, n^s	Total mass flux of the gas phase, of the solid phase (g/cm^2/s)
N_i^g, N_i^s	Molar flux, of the i-th gas species, of the i-th solid species (mol/cm^2/s)
N^g, N^s	Total molar flux of the gas phase, of the solid phase (mol/cm^2/s)
N^t	Total flux of combined phases (mol/cm^2/s)
NG	Number of gas species in the system
NR	Number of reactions
NS	Number of solid species in the system
Nt	Total number of species (gas + solid)
P	Pressure (Pa)
q^t	Conductive flux (W/cm^2)
r	Radial coordinate (cm)
r_0	Particle radius (cm)
r_g	Grain radius
R	Reaction rate (mol/cm^3/s)
R_g	Universal gas constant (J/mol/K)
s_i^g, s_i^s	Molar source term for the i-th gas species, for the i-th solid species (mol/cm^3/s)
t	Time (s)
T, T_{bulk}	Absolute temperature, local, outside the particle in bulk phase (K)
T^0	Initial local temperature (K)
x_i^g , x_i^s	Molar fraction of the i-th gas species, of the i-th solid species
V^s, V	Volume of solid phase, total volume (cm^3)
X_A	Conversion of the A solid phase
y_i^g, y_i^s	Mass fraction of the i-th gas species, of the i-th solid species

Greek letters

α	Sintering exponent
β	Gas partial reaction order
ΔH_j^R	Heat of the j-th reaction, molar based (J/mol)
$\Delta \widehat{H}_j^R$	Heat of the j-th reaction, mass based (J/g)
ε	Porosity
ν_{ij}	Stoichiometric coefficient of the i-th species in the j-th reaction
ν_{ij}^g	Stoichiometric coefficient of the i-th gas species in the j-th reaction
ν_{ij}^s	Stoichiometric coefficient of the i-th solid species in the j-th reaction
ρ_i	Intrinsic density of the i-th solid species (g/cm^3)
ρ_i^g, ρ_i^s	Mass density of the i-th gas species, of the i-th solid species (g/cm^3)
ρ^g, ρ^s	Mass density of the gas phase, of the solid phase (g/cm^3)
$\rho\widehat{Cp}$	Heat capacity of the medium (J/cm^3/K)
θ_i	Surface fraction occupied by the i-th gas phase

Chapter 5. Diffusion models

In the previous section, the possible forms of continuous models have been reported. In this part, the expression of the gas diffusion fluxes in the continuous model is explicated as a function of the gas concentration gradients, according to different degrees of detail [33, 34].

5.1 Gas diffusion and velocity

Let's define a physical spatial domain Ω, where there is a mixture of N chemical species. In each point of the domain a density ρ(x,y,z) and a total molar concentration c(x,y,z) can be defined. The relationship between the two will be:

$$\rho = c \cdot MW \tag{5.1}$$

Where MW is the molecular weight of the mixture, and in general will be different in any point. Let's consider a subdomain ∂V in which there are Nm_i molecules of the i-th species. Each molecule j of the species i will move with a velocity $\mathbf{v}_{ij}$. The average velocity of the species i in ∂V will be:

$$\boldsymbol{v}_i = \frac{\sum_{j=1}^{Nm_i} \mathbf{v}_{ij}}{Nm_i} \tag{5.2}$$

Each i species will move with a velocity $\boldsymbol{v}_i$(x,y,z). The coordinates of the center of mass of the system can be defined as follows:

$$\boldsymbol{R} = \frac{\sum_{j=1}^{Nm} m_j \cdot \boldsymbol{r}_j}{\sum_{j=1}^{Nm} m_j} \tag{5.3}$$

Where $\mathbf{r}_j$ is the position of the j-th molecule, and m_i is its mass. In the same way, a molar centre of mass can be defined, whose coordinates are:

$$\boldsymbol{R}' = \frac{\sum_{j=1}^{Nm} \boldsymbol{r}_j}{Nm} \tag{5.4}$$

The evolution of the system in the whole volume ∂V can be summarized by describing the evolution of its center of mass **R**, whose velocity will be:

$$\boldsymbol{v} = \frac{\sum_{j=1}^{Nm} m_j \cdot \boldsymbol{v}_j}{\sum_{j=1}^{Nm} m_j} = \frac{\sum_{i=1}^{N} Nm_i \cdot m_i \cdot \boldsymbol{v}_i}{\sum_{i=1}^{N} Nm_i \cdot m_i} \tag{5.5}$$

In the same way, the velocity of the molar center of mass can be defined as:

$$\boldsymbol{v}^* = \frac{\sum_{j=1}^{Nm} \boldsymbol{v}_j}{Nm} = \frac{\sum_{i=1}^{N} Nm_i \cdot \boldsymbol{v}_i}{Nm} \quad 5.6$$

Now we recognize that:

$$y_i = \frac{Nm_i \cdot m_i}{\sum_{i=1}^{N} Nm_i \cdot m_i} \quad 5.7$$

$$x_i = \frac{Nm_i}{Nm} \quad 5.8$$

Where y_i is mass fraction of i and x_i is the molar fraction of i. The equations become:

$$\boldsymbol{v} = \sum_{i=1}^{N} y_i \boldsymbol{v}_i \quad 5.9$$

$$\boldsymbol{v}^* = \sum_{i=1}^{N} x_i \boldsymbol{v}_i \quad 5.10$$

Considering the limit ∂V→0, the volume reduces to a point of Ω, with the same coordinates as **R** and **R'** whereas the definition of $\mathbf{v}_i$, **v** and **v*** is still valid, and can be extended at any point of Ω. The velocity fields $\mathbf{v}_i(x,y,z)$, **v**(x,y,z) and **v***(x,y,z) are thus defined.

In any point, the massive and molar total fluxes are defined as:

$$\boldsymbol{n} = \rho \boldsymbol{v} \quad 5.11$$

$$\boldsymbol{N} = c\boldsymbol{v}^* \quad 5.12$$

Massive and molar fluxes can be written for each species as well:

$$\boldsymbol{n_i} = \rho y_i \boldsymbol{v_i} \quad 5.13$$

$$\boldsymbol{N_i} = c x_i \boldsymbol{v_i} \quad 5.14$$

It's obvious to demonstrate, by equations 5.13, 5.14, 5.9 and 5.10 that:

$$\sum_{\boldsymbol{i=1}}^{\boldsymbol{N}} \boldsymbol{n_i} = \rho \cdot \sum_{i=1}^{N} y_i \cdot \boldsymbol{v_i} = \rho \cdot \boldsymbol{v} = \boldsymbol{n} \quad 5.15$$

$$\sum_{\boldsymbol{i=1}}^{\boldsymbol{N}} \boldsymbol{N_i} = c \cdot \sum_{i=1}^{N} x_i \cdot \boldsymbol{v_i} = c \cdot \boldsymbol{v}^* = \boldsymbol{N} \quad 5.16$$

In practice, it's rather useful to separate the flux of i into two components:

$$\boldsymbol{n_i} = \rho y_i \boldsymbol{v} + \boldsymbol{j}_i \quad 5.17$$

$$\boldsymbol{N_i} = cx_i\boldsymbol{v}^* + \boldsymbol{J_i^*} \quad 5.18$$

Where the first term of the right hand side is the convective mass flux of i, while $\mathbf{j}_i$ is the diffusive mass flux of i, which is:

$$\boldsymbol{j}_i = \rho y_i(\boldsymbol{v_i} - \boldsymbol{v}) \quad 5.19$$

In terms of molar quantities:

$$\boldsymbol{J}_i^* = cx_i(\boldsymbol{v_i} - \boldsymbol{v}^*) \quad 5.20$$

It is easy to demonstrate that:

$$\sum_{i=1}^{N}\boldsymbol{j}_i = \rho\sum_{i=1}^{N} y_i\boldsymbol{v_i} - \rho\boldsymbol{v}\sum_{i=1}^{N} y_i = \rho\boldsymbol{v} - \rho\boldsymbol{v} = 0 \quad 5.21$$

And analogously:

$$\sum_{i=1}^{N}\boldsymbol{J}_i^* = 0 \quad 5.22$$

5.2 Binary and multicomponent diffusion: Fick and Stefan-Maxwell

If the system is made of only two chemical species (let's say i and j), the massive and molar diffusive fluxes can be expressed by the first Fick's law:

$$\boldsymbol{j}_i = -\rho\mathfrak{D}_{ij}\nabla y_i \quad 5.23$$

$$\boldsymbol{J}_i^* = -c\mathfrak{D}_{ij}\nabla x_i \quad 5.24$$

Where $\mathscr{D}_{ij}$ is the Fick binary diffusion coefficient, and depends, more or less slightly, on x_i and x_j. Equation 5.20 can be manipulated as follows, starting from the definition of molar diffusive fluxes:

$$\boldsymbol{v}_i = \frac{\boldsymbol{J}_i^*}{cx_i} + \boldsymbol{v}^* \quad 5.25$$

$$\boldsymbol{v}_j = \frac{\boldsymbol{J}_j^*}{cx_j} + \boldsymbol{v}^* \quad 5.26$$

Subtracting eq. 5.26 from eq. 5.25:

$$(\boldsymbol{v}_i - \boldsymbol{v}_j) = \frac{1}{c}\left(\frac{\boldsymbol{J}_i^*}{x_i} - \frac{\boldsymbol{J}_j^*}{x_j}\right) = \frac{1}{x_ix_jc}(x_j\boldsymbol{J}_i^* - x_i\boldsymbol{J}_j^*) \quad 5.27$$

In a binary system, eq. 5.22 becomes:

$$\boldsymbol{J}_i^* = -\boldsymbol{J}_j^* \quad 5.28$$

Which, substituted in equation 5.27, gives:

$$(\boldsymbol{v}_i - \boldsymbol{v}_j) = \frac{1}{x_i x_j c}(x_j + x_i)\boldsymbol{J}_i^* = \frac{1}{x_i x_j c}\boldsymbol{J}_i^* \qquad 5.29$$

Now, using Fick's law:

$$(\boldsymbol{v}_i - \boldsymbol{v}_j) = -\frac{\mathfrak{D}_{ij}\nabla x_i}{x_i x_j} \qquad 5.30$$

Which gives the explicit form of Fick's law in terms of gradient:

$$\nabla x_i = -\frac{x_i x_j}{\mathfrak{D}_{ij}}(\boldsymbol{v}_i - \boldsymbol{v}_j) \qquad 5.31$$

Equation 5.31 is quite important, since it's been extended for describing diffusion in multicomponent systems where N>2. In such cases, the gradient of x_i is equal to:

$$\nabla x_i = -\sum_{j=1}^{N}\frac{x_i x_j}{\mathfrak{D}_{ij}}(\boldsymbol{v}_i - \boldsymbol{v}_j) \qquad 5.32$$

This equation is found to describe multicomponent diffusion with a good degree of approximation for mixtures of gases at low pressure. At these conditions, the binary Fick coefficient gets equal to the Stefan-Maxwell multicomponent diffusivities, $Đ_{ij}$, so that eq. 5.32 can be also written as:

$$\nabla x_i = -\sum_{j=1}^{N}\frac{x_i x_j}{Đ_{ij}}(\boldsymbol{v}_i - \boldsymbol{v}_j) \qquad 5.33$$

These are the so called Stefan-Maxwell equations for ideal mixtures of gases. Multicomponent diffusivities $Đ_{ij}$ identify a matrix [Đ], which is symmetric ($Đ_{ij} = Đ_{ji}$), as well as the matrix of Fick diffusivities [$\mathfrak{D}$]. The relationship between these two kinds of coefficient is given by:

$$\mathfrak{D}_{ij} = Đ_{ij}\left(1 + \frac{\partial ln\gamma_i}{\partial ln x_i}\right) \qquad 5.34$$

Where γ_i is the activity coefficient of i. In the case of ideal mixtures $\gamma_i = 1$, so that $\mathfrak{D}_{ij} = Đ_{ij}$.

Equation 5.33 is the implicit form of the Stefan-Maxwell equations. It is usually more useful to have an expression to calculate the flux of i as a function of the gradients of the molar fractions of the components. This can be obtained for a multicomponent system, by manipulating equation 5.33 as follows:

Using equations 5.25 and 5.26:

$$c\nabla x_i = -\sum_{j=1}^{N}\frac{x_i x_j}{Đ_{ij}}\left(\frac{\boldsymbol{J}_i^*}{x_i} - \frac{\boldsymbol{J}_j^*}{x_j}\right) = -\sum_{j=1}^{N}\frac{1}{Đ_{ij}}(x_j\boldsymbol{J}_i^* - x_i\boldsymbol{J}_j^*) = -\boldsymbol{J}_i^*\sum_{j=1}^{N}\frac{x_j}{Đ_{ij}} + x_i\sum_{j=1}^{N}\frac{\boldsymbol{J}_j^*}{Đ_{ij}} \qquad 5.35$$

Equation 5.35 says that the gradient of i depends on N molar fluxes, as many as the number of components of the system. Actually, it depends on N-1 fluxes, since the N-th flux can be obtained, according to equation 5.22, as:

$$\boldsymbol{J}_N^* = -\sum_{j=1}^{N-1} \boldsymbol{J}_j^* \tag{5.36}$$

In equation 5.35 we can thus extract the N-th member of the last sum, and use equation 5.36 to eliminate the N-th molar flux. We obtain:

$$c\nabla x_i = -\boldsymbol{J}_i^* \sum_{j=1}^{N} \frac{x_j}{Đ_{ij}} + x_i \sum_{j=1}^{N-1} \frac{\boldsymbol{J}_j^*}{Đ_{ij}} + \frac{x_i}{Đ_{iN}} \boldsymbol{J}_N^* = -\boldsymbol{J}_i^* \sum_{j=1}^{N} \frac{x_j}{Đ_{ij}} + x_i \sum_{j=1}^{N-1} \frac{\boldsymbol{J}_j^*}{Đ_{ij}} - \frac{x_i}{Đ_{iN}} \sum_{j=1}^{N-1} \boldsymbol{J}_j^* \tag{5.37}$$

$$c\nabla x_i = -\boldsymbol{J}_i^* \sum_{j=1}^{N} \frac{x_j}{Đ_{ij}} + x_i \sum_{j=1}^{N-1} \left(\frac{1}{Đ_{ij}} - \frac{1}{Đ_{iN}} \right) \boldsymbol{J}_j^* \tag{5.38}$$

We can now extract the i-th component from both sums of the right hand side of equation 5.38:

$$c\nabla x_i = -\boldsymbol{J}_i^* \frac{x_i}{Đ_{ii}} - \boldsymbol{J}_i^* \sum_{\substack{j=1 \\ j \neq i}}^{N} \frac{x_j}{Đ_{ij}} + x_i \left(\frac{1}{Đ_{ii}} - \frac{1}{Đ_{iN}} \right) \boldsymbol{J}_i^* + x_i \sum_{\substack{j=1 \\ j \neq i}}^{N-1} \left(\frac{1}{Đ_{ij}} - \frac{1}{Đ_{iN}} \right) \boldsymbol{J}_j^* \tag{5.39}$$

Simplifying the term with $Đ_{ii}$:

$$-c\nabla x_i = \left(\frac{x_i}{Đ_{iN}} + \sum_{\substack{j=1 \\ j \neq i}}^{N} \frac{x_j}{Đ_{ij}} \right) \boldsymbol{J}_i^* + \sum_{\substack{j=1 \\ j \neq i}}^{N-1} \left(\frac{x_i}{Đ_{iN}} - \frac{x_i}{Đ_{ij}} \right) \boldsymbol{J}_j^* \tag{5.40}$$

And, in a more compact way:

$$-c\nabla x_i = \sum_{j=1}^{N-1} \left(\frac{x_i}{Đ_{iN}} + \delta_{ij} \sum_{\substack{k=1 \\ k \neq i}}^{N} \frac{x_k}{Đ_{ik}} + (\delta_{ij} - 1) \frac{x_i}{Đ_{ij}} \right) \boldsymbol{J}_j^* \tag{5.41}$$

Where δ_{ij} is the delta of Kronecker, which is equal to 1 if i = j and is equal to zero otherwise.

We can define an (N-1xN-1) matrix [B], where the component B_{ij} is given by:

$$B_{ij} = \frac{x_i}{Đ_{iN}} + \delta_{ij} \sum_{\substack{k=1 \\ k \neq i}}^{N} \frac{x_k}{Đ_{ik}} + (\delta_{ij} - 1) \frac{x_i}{Đ_{ij}} \tag{5.42}$$

So that equation 5.41 becomes:

$$-\mathrm{c}\nabla x_i = \sum_{j=1}^{N-1} B_{ij} \cdot \boldsymbol{J}_j^* \quad 5.43$$

Or, in a matrix form:

$$-c[\nabla x] = [B][\boldsymbol{J}^*] \quad 5.44$$

Where $[\nabla x]$ is the (N-1x1) column vector of the gradients of the components, and $[J^*]$ is the (N-1x1) column vector of the molar fluxes. N-1 fluxes can be calculated by resolving the linear system expressed by eq. 5.44, so that:

$$[\boldsymbol{J}^*] = -c[B]^{-1}[\nabla x] \quad 5.45$$

We define [D] as the inverse matrix of B, thus obtaining:

$$[\boldsymbol{J}^*] = -c[D][\nabla x] \quad 5.46$$

Or, in a more explicit form:

$$\boldsymbol{J}_i^* = -c \sum_{j=1}^{N-1} D_{ij} \nabla x_j \quad 5.47$$

This is the so called generalized Fick's law, and is actually a manipulated version of the Stefan-Maxwell equations. Equation 5.46, together with equation 5.36, gives the total of N diffusive fluxes necessary to describe the system. Note that eq. 5.47 is not fully explicit, as it requires that the matrix B, depending on the compositions x_i, is inverted.

5.3 Other forms of the Stefan-Maxwell equations

There is a number of ways to express equation 5.33 rather than equation 5.47. In particular, it can be useful to calculate the mass fluxes instead of the molar ones. Here we consider two common expression of the generalized Fick's equation.

$$\boldsymbol{j}_i = -\rho y_i \sum_{j=1}^{N-1} D_{ij}^* \nabla x_i \quad 5.48$$

$$\boldsymbol{j}_i = -\rho \sum_{j=1}^{N-1} D_{ij}^0 \nabla y_i \quad 5.49$$

First of all, we can obtain the relationship between the mass and molar fluxes as follows. The difference between the velocity of the center of mass and the velocity of molar center of mass is:

$$(\boldsymbol{v} - \boldsymbol{v}^*) = \sum_{i=1}^{N} y_i \boldsymbol{v}_i - \boldsymbol{v}^* \quad 5.50$$

Where expression 5.9 is used to express v. We can multiply v* by the sum of y_i, which we know to be equal to one, so that:

$$(\boldsymbol{v}-\boldsymbol{v}^*)=\sum_{i=1}^{N} y_i\boldsymbol{v}_i-\sum_{i=1}^{N} y_i\boldsymbol{v}^*=\sum_{i=1}^{N} y_i(\boldsymbol{v}_i-\boldsymbol{v}^*) \qquad 5.51$$

Now we can use equation 5.51 into the definition of j_i, and we obtain:

$$\boldsymbol{j}_i=\rho y_i(\boldsymbol{v}_i-\boldsymbol{v})=\rho y_i\left[\boldsymbol{v}_i-\left(\boldsymbol{v}^*+\sum_{j=1}^{N} y_j\left(\boldsymbol{v}_j-\boldsymbol{v}^*\right)\right)\right]=\rho y_i\left[(\boldsymbol{v}_i-\boldsymbol{v}^*)-\sum_{j=1}^{N} y_j\left(\boldsymbol{v}_j-\boldsymbol{v}^*\right)\right] \qquad 5.52$$

And using the definition of J^*_i:

$$\boldsymbol{j}_i=\rho y_i\left[\frac{\boldsymbol{J}_i^*}{cx_i}-\sum_{j=1}^{N} y_j\frac{\boldsymbol{J}_j^*}{cx_j}\right] \qquad 5.53$$

Extracting the N-th molar flux from the sum and applying the condition on the sum of the fluxes we obtain:

$$\begin{aligned}\boldsymbol{j}_i&=\frac{\rho}{c}y_i\left[\frac{\boldsymbol{J}_i^*}{x_i}-y_N\frac{\boldsymbol{J}_N^*}{x_N}-\sum_{j=1}^{N-1} y_j\frac{\boldsymbol{J}_j^*}{x_j}\right]=\frac{\rho}{c}y_i\left[\frac{\boldsymbol{J}_i^*}{x_i}+\frac{y_N}{x_N}\sum_{j=1}^{N-1}\boldsymbol{J}_j^*-\sum_{j=1}^{N-1} y_j\frac{\boldsymbol{J}_j^*}{x_j}\right]\\&=\frac{\rho}{c}y_i\left[\frac{\boldsymbol{J}_i^*}{x_i}+\sum_{j=1}^{N-1}\left(\frac{y_N}{x_N}-\frac{y_j}{x_j}\right)\boldsymbol{J}_j^*\right]\end{aligned} \qquad 5.54$$

Now, extracting the i-th element from the sum:

$$\begin{aligned}\boldsymbol{j}_i&=\frac{\rho}{c}y_i\left[\frac{\boldsymbol{J}_i^*}{x_i}+\left(\frac{y_N}{x_N}-\frac{y_i}{x_i}\right)\boldsymbol{J}_i^*+\sum_{\substack{j=1\\ j\neq i}}^{N-1}\left(\frac{y_N}{x_N}-\frac{y_j}{x_j}\right)\boldsymbol{J}_j^*\right]\\&=\frac{\rho}{c}y_i\left[\left(\frac{1-y_i}{x_i}+\frac{y_N}{x_N}\right)\boldsymbol{J}_i^*+\sum_{\substack{j=1\\ j\neq i}}^{N-1}\left(\frac{y_N}{x_N}-\frac{y_j}{x_j}\right)\boldsymbol{J}_j^*\right]\end{aligned} \qquad 5.55$$

Or, in a more contract form:

$$\boldsymbol{j}_i=\frac{\rho}{c}\sum_{j=1}^{N-1} y_i\left(\frac{y_N}{x_N}+\frac{\delta_{ij}-y_j}{x_j}\right)\boldsymbol{J}_j^* \qquad 5.56$$

So we obtain:

$$\boldsymbol{j}_i=\frac{\rho}{c}\sum_{j=1}^{N-1} B_{ij}^F\cdot\boldsymbol{J}_j^* \qquad 5.57$$

$$B_{ij}^{F} = y_i\left(\frac{y_N}{x_N} + \frac{\delta_{ij} - y_j}{x_j}\right) = \frac{y_j}{x_j}\left(\delta_{ij} - y_i\left(1 - \frac{y_N}{x_N}\frac{x_j}{y_j}\right)\right) \quad 5.58$$

As well as:

$$\frac{\boldsymbol{j}_i}{y_i} = \frac{\rho}{c}\sum_{j=1}^{N-1} B_{ij}^{F\prime} \cdot \boldsymbol{J}_j^* \quad 5.59$$

$$B_{ij}^{F\prime} = \frac{y_N}{x_N} + \frac{\delta_{ij} - y_j}{x_j} = \frac{B_{ij}^{F}}{y_i} \quad 5.60$$

Or, in matrix form:

$$[\boldsymbol{j}] = \frac{\rho}{c}[B^F][\boldsymbol{J}^*] \quad 5.61$$

$$\left[\frac{\boldsymbol{j}}{y}\right] = \frac{\rho}{c}[B^{F\prime}][\boldsymbol{J}^*] \quad 5.62$$

Combining equation 5.62 and 5.46 we obtain the following expression:

$$\left[\frac{\boldsymbol{j}}{y}\right] = -\rho[B^{F\prime}][D][\nabla x] \quad 5.63$$

So we obtained the transformation:

$$[D^*] = [B^{F\prime}][D] \quad 5.64$$

$$\left[\frac{\boldsymbol{j}}{y}\right] = -\rho[D^*][\nabla x] \quad 5.65$$

Which is the matrix form of equation 5.48.

To compute the matrix [D°], we first calculate the transformation from $[\nabla x]$ to $[\nabla y]$, knowing that:

$$x_i = \frac{\frac{y_i}{MW_i}}{\sum_j^N \frac{y_j}{MW_j}} \quad 5.66$$

Using the derivation rules:

$$\nabla x_i = MW^2\left(\frac{\nabla y_i}{MW \cdot MW_i} - \frac{y_i}{MW_i}\sum_{j=1}^{N}\frac{\nabla y_j}{MW_j}\right) = \frac{MW}{MW_i}\left(\nabla y_i - \sum_{j=1}^{N}\frac{MW}{MW_j}y_i\nabla y_j\right) \quad 5.67$$

Where the molecular weight of the mixture, MW, is defined as:

$$MW = \left(\sum_{j=1}^{N} \frac{y_j}{MW_j} \right)^{-1} \quad 5.68$$

We again extract the N-th element from the sum in equation:

$$\nabla x_i = \frac{MW}{MW_i} \left(\nabla y_i - \frac{MW}{MW_N} y_i \nabla y_N - \sum_{j=1}^{N-1} \frac{MW}{MW_j} y_i \nabla y_j \right) \quad 5.69$$

Then we use the relation:

$$\nabla y_N = \nabla \left(1 - \sum_{j=1}^{N-1} y_j \right) = - \sum_{j=1}^{N-1} \nabla y_j \quad 5.70$$

So that we get:

$$\nabla x_i = \frac{MW}{MW_i} \left(\nabla y_i + \sum_{j=1}^{N-1} MW\, y_i \left(\frac{1}{\mathrm{MW_N}} - \frac{1}{\mathrm{MW_j}} \right) \nabla y_j \right) \quad 5.71$$

Then, extracting the i-th element:

$$\nabla x_i = \frac{MW}{MW_i} \left(\left(1 + \mathrm{MW}\, y_i \left(\frac{1}{\mathrm{MW_N}} - \frac{1}{\mathrm{MW_i}} \right) \right) \nabla y_i + \sum_{\substack{j=1 \\ j \neq i}}^{N-1} MW\, y_i \left(\frac{1}{\mathrm{MW_N}} - \frac{1}{\mathrm{MW_j}} \right) \nabla y_j \right) \quad 5.72$$

$$\nabla x_i = \sum_{j=1}^{N-1} \frac{MW}{MW_i} \left[\delta_{ij} + MW y_i \left(\frac{1}{\mathrm{MW_N}} - \frac{1}{\mathrm{MW_j}} \right) \right] \nabla y_j \quad 5.73$$

Now we define the transformation matrix [B^{xy}] whose elements are given by:

$$B_{ij}^{xy} = \frac{MW}{MW_i} \left[\delta_{ij} + MW y_i \left(\frac{1}{\mathrm{MW_N}} - \frac{1}{\mathrm{MW_j}} \right) \right] = \frac{x_i}{y_i} \left(\delta_{ij} + y_i \left(\frac{x_N}{y_N} - \frac{x_j}{y_j} \right) \right) \quad 5.74$$

It is also possible to prove that B^F is the inverse of B^{xy}.

So the relationship between molar and mass gradients is:

$$\nabla x_i = \sum_{j=1}^{N-1} B_{ij}^{xy} \nabla y_j \quad 5.75$$

$$[\nabla x] = [\mathrm{B^{xy}}][\nabla \mathrm{y}] \quad 5.76$$

Finally we can combine equations 5.61, 5.46 and 5.76, so we obtain:

$$[\boldsymbol{j}] = \frac{\rho}{c} [B^F][\boldsymbol{J}^*] = -\rho [B^F][B]^{-1} [\nabla x] = -\rho [B^F][B]^{-1} [B^{xy}][\nabla y] \quad 5.77$$

That give us the formulation of the diffusivity matrix [D°]:

$$[D^{\circ}] = [B^F][B]^{-1}[B^{xy}] = [B^F][B]^{-1}[B^F]^{-1} \quad 5.78$$

$$[\boldsymbol{j}] = -\rho[D^{\circ}][\nabla y] \quad 5.79$$

This is the generalized Fick equation in terms of mass fluxes as a function of the gradients of the mass fractions.

5.3.1 From multicomponent to binary form

We can easily demonstrate that, if N = 2, we obtain the binary Fick law from the equations we just derived. The matrix [B], if N = 2 has only one component which is:

$$B_{11} = \frac{x_1}{Đ_{12}} + \delta_{11}\sum_{\substack{k=1\\k\neq 1}}^{2}\frac{x_k}{Đ_{ik}} + (\delta_{11}-1)\frac{x_1}{Đ_{11}} = \frac{x_1}{Đ_{12}} + \frac{x_2}{Đ_{12}} = \frac{x_1+x_2}{Đ_{12}} = \frac{1}{Đ_{12}} \quad 5.80$$

And so:

$$D_{11} = {B_{11}}^{-1} = Đ_{12} \quad 5.81$$

$$\boldsymbol{J}_1^* = -c\, Đ_{12}\nabla x_1 \quad 5.82$$

The matrix [B^F], has a single component as well, which is:

$$B_{11}^F = y_1\left(\frac{y_2}{x_2} + \frac{\delta_{11}-y_1}{x_1}\right) = y_1\left(\frac{y_2}{x_2}+\frac{y_2}{x_1}\right) = \frac{y_1y_2}{x_1x_2}(x_1+x_2) = \frac{y_1y_2}{x_1x_2} = \frac{x_1MW_1y_2MW_2}{MW^2x_1x_2} = \frac{MW_1MW_2}{MW^2} \quad 5.83$$

While the matrix [B^{xy}] is:

$$B_{11}^{xy} = \frac{MW}{MW_1}\left[\delta_{11} + MWy_1\left(\frac{1}{\mathrm{MW}_2}-\frac{1}{\mathrm{MW}_1}\right)\right] = \frac{MW}{MW_1}\left[\frac{MW_1MW_2 + y_1MWMW_1 - y_1MWMW_2}{MW_1MW_2}\right] = \frac{MW}{MW_1}\left[\frac{MW_1MW_2 + x_1MW_1^2 - x_1MW_1MW_2}{MW_1MW_2}\right] = \frac{MW}{MW_1}\left[\frac{x_1MW_1^2 + x_2MW_1MW_2}{MW_1MW_2}\right] = MW\left[\frac{x_1MW_1 + x_2MW_2}{MW_1MW_2}\right] = \frac{MW^2}{MW_1MW_2} \quad 5.84$$

So the matrix [D°] will be:

$$D_{11}^o = \frac{MW_1MW_2}{MW^2}\cdot Đ_{12}\cdot\frac{MW^2}{MW_1MW_2} = Đ_{12} \quad 5.85$$

$$\boldsymbol{j}_1 = -\rho Đ_{12}\nabla y_1 \quad 5.86$$

Finally, if one of the two species is very diluted with respect to the other one,

$$Đ_{12} = \frac{\mathfrak{D}_{12}}{\left(1 + \frac{\partial ln\gamma_1}{\partial ln x_1}\right)} = \mathfrak{D}_{12} \qquad 5.87$$

Because $\gamma_1 \rightarrow 1$ if $x_1 \rightarrow 0$ or $x_1 \rightarrow 1$.

Thus, we obtained the same forms as equations 5.23 and 5.24.

5.3.2 Alternative (direct) way to derive SM-equation in term of massive fluxes

It is possible to directly derive the matrix [D*] combining equations 5.33 and 5.20:

$$-\rho\nabla x_i = \sum_{j=1}^{N} \frac{x_i x_j}{Đ_{ij}}\left(\frac{\boldsymbol{j}_i}{y_i} - \frac{\boldsymbol{j}_j}{y_j}\right) = \frac{\boldsymbol{j}_i}{y_i}\sum_{j=1}^{N}\frac{x_i x_j}{Đ_{ij}} - \sum_{j=1}^{N}\frac{x_i x_j}{Đ_{ij}}\cdot\frac{\boldsymbol{j}_j}{y_j} \qquad 5.88$$

With the same logical rearrangements we obtain:

$$-\rho\nabla x_i = \sum_{j=1}^{N-1} B_{ij}^{*}\frac{\boldsymbol{j}_j}{y_j} \qquad 5.89$$

$$B_{ij}^{*} = x_i\left(\frac{y_j}{y_N}\frac{x_N}{Đ_{iN}} + \delta_{ij}\sum_{\substack{k=1\\k\neq i}}^{N}\frac{x_k}{Đ_{ik}} + \left(\delta_{ij} - 1\right)\frac{x_j}{Đ_{ij}}\right) \qquad 5.90$$

It's immediate to recognize that $[D^*] = [B^*]^{-1}$

5.4 Contribution of Knudsen diffusion

If the diffusion regime can be influenced by Knudsen diffusion, equation 5.42 can be corrected as reported in the literature [9], as follows:

$$\nabla x_i = -\frac{\boldsymbol{J}_i^{*}}{c\cdot D_i^{K}} - \sum_{j=1}^{N}\frac{x_i x_j}{Đ_{ij}}\left(\boldsymbol{v}_i - \boldsymbol{v}_j\right) \qquad 5.91$$

Where D_i^K is the Knudsen diffusion coefficient of i, which can be expressed by:

$$D_i^{K} = \frac{4}{3}K_0\sqrt{\frac{8R_gT}{\pi\cdot MW_i}} \qquad 5.92$$

Where K_0 is the Knudsen parameter, depending on the conformation of the solid medium. This extension adds a new term in the diagonal of the matrix [B], whose component will be:

$$B_{ij} = \frac{x_i}{Đ_{iN}} + \delta_{ij}\left(\frac{1}{D_i^K} + \sum_{\substack{k=1 \\ k\neq i}}^{N} \frac{x_k}{Đ_{ik}}\right) + (\delta_{ij} - 1)\frac{x_i}{Đ_{ij}} \qquad 5.93$$

Note that if D_i^K approaches to infinite, Knudsen diffusion is no longer important, and equation 5.93 returns to be in the form of equation 5.42.

5.5 Generalized Stefan-Maxwell for multiple driving forces and non ideal solutions

Thus far, we considered concentration differences as the only source of a diffusive flux, and for ideal mixtures. In general, diffusion can be generated by other non homogeneous properties in the system, such as:

a) Temperature gradients
b) Pressure gradients
c) External forces

In order to take into account all of these, the generalized Fick equation expressed by 5.47 has been extended into equation 5.94:

$$\boldsymbol{j}_i = -D_i^T \nabla \ln T - \rho y_i \sum_{j=1}^{N-1} D_{ij}^* \mathbf{d}_i \qquad 5.94$$

$$\boldsymbol{d}_i = x_i \nabla ln(a_i) + (\phi_i - y_i)\nabla lnP - \frac{1}{cRT}\left(\rho y_i \boldsymbol{g}_i - y_i \sum_{k=1}^{N} \rho y_k \boldsymbol{g}_k\right) \qquad 5.95$$

Where a_i is the activity of i, ϕ_i is the volumetric fraction of i, P is the pressure, T is the temperature, and g_i is the external force field applied to i. It may include, for example, gravity force, electric fields caused by ionic forces, permeability differences due to the presence of selective membranes. For more details about these ones, we remand to the literature [33]. D^T_i is the thermal diffusion coefficient of i, while D^*_{ij} is still calculated by the inversion of the matrix in eq. 5.90. It can be demonstrated that the sum of the driving forces of all the components must always be equal to zero:

$$\sum_{j=1}^{N} \boldsymbol{d}_j = 0 \qquad 5.96$$

Note that the contribution of the concentration gradient in this formulation is expressed by the first term of the right hand side of equation 5.95. For non ideal systems, $\mathscr{D}_{ij}$ and $Đ_{ij}$ are not interchangeable, and the

activity of i is different from its molar fraction. The comparison between the generalized form of the Stefan Maxwell equations and the Fick equation 5.23 gives the relationship between the two coefficients, already exposed in 5.34.

5.6 Simplified diffusion models: Mixture averaged model

The Stefan-Maxwell multicomponent diffusion is the most rigorous approach to describe the molar or massive diffusive fluxes in a system with more than two chemical species. It can be nevertheless quite annoying to use, because of its intrinsic implicit form, that requires the inversion of a matrix (B), whose components are different in any point of the system at any numerical iteration. This can result in a more expensive computational cost in the numerical solution of the material balances, particularly if N is very large. A simplified approach can be used, in order to have a fully explicit equation to calculate the diffusive fluxes, maintaining an approximate dependence on the composition of the system.

One widely used approach is to calculate a global diffusion coefficient, so that the diffusive flux of i is expressed in the form of the binary Fick law. For the molar flux:

$$\boldsymbol{J}_i^* = -cD_{im}\nabla x_i \tag{5.97}$$

Where D_{im} is the diffusion coefficient of i in the mixture. This diffusivity can be exactly calculated, comparing equations 5.97 and 5.35:

$$-c\nabla x_i = \frac{\boldsymbol{J}_i^*}{D_{im}} = \sum_{j=1}^{N} \frac{x_i x_j}{Đ_{ij}} \left(\frac{\boldsymbol{J}_i^*}{x_i} - \frac{\boldsymbol{J}_j^*}{x_j} \right) = \sum_{j=1}^{N} \frac{1}{Đ_{ij}} \left(x_j \boldsymbol{J}_i^* - x_i \boldsymbol{J}_j^* \right) = \boldsymbol{J}_i^* \sum_{\substack{j=1 \\ j\neq i}}^{N} \frac{x_j}{Đ_{ij}} - x_i \sum_{\substack{j=1 \\ j\neq i}}^{N} \frac{\boldsymbol{J}_j^*}{Đ_{ij}} \tag{5.98}$$

So we obtain:

$$D_{im} = \frac{\boldsymbol{J}_i^*}{\sum_{j=1}^{N} \frac{1}{Đ_{ij}} \left(x_j \boldsymbol{J}_i^* - x_i \boldsymbol{J}_j^* \right)} \tag{5.99}$$

Now using equations 5.16 and 5.18 into equation 5.99 we can express D_{im} as a function of the global molar fluxes:

$$D_{im} = \frac{\boldsymbol{N}_i - x_i \boldsymbol{N}}{\sum_{j=1}^{N} \frac{1}{Đ_{ij}} \left(x_j (\boldsymbol{N}_i - x_i \boldsymbol{N}) - x_i \left(\boldsymbol{N}_j - x_j \boldsymbol{N} \right) \right)} = \frac{\boldsymbol{N}_i - x_i \boldsymbol{N}}{\sum_{j=1}^{N} \frac{1}{Đ_{ij}} \left(x_j \boldsymbol{N}_i - x_i \boldsymbol{N}_j \right)} \tag{5.100}$$

Finally:

$$D_{im} = \frac{\boldsymbol{N}_i - x_i \boldsymbol{N}}{\boldsymbol{N}_i \sum_{\substack{j=1 \\ j\neq i}}^{N} \frac{x_j}{Đ_{ij}} - x_i \sum_{\substack{j=1 \\ j\neq i}}^{N} \frac{\boldsymbol{N}_j}{Đ_{ij}}} \tag{5.101}$$

Note that the combination of equations 5.101 and 5.97 is still another form of equation 5.33. If the molar flux of i is very large compared to the fluxes of the other species, then $N_i = N$, and $N_j = 0$, for j different from i. The diffusivity becomes:

$$D_{im} = \frac{1 - x_i}{\sum_{\substack{j=1 \\ j \neq i}}^{N} \frac{x_j}{Đ_{ij}}} \tag{5.102}$$

D_{im} still depends on the composition of the system (x) and on the multicomponent diffusivities, but not on the molar fluxes, so it's fully explicit.

5.6.1 Derivation of mass fluxes

Another common form of the mixture averaged model is through equation 5.103:

$$\boldsymbol{j}_i = -y_i \rho D_{im}^* \frac{\nabla x_i}{x_i} \tag{5.103}$$

Starting from equations 5.35 and 5.19:

$$-y_i \rho \frac{\nabla x_i}{x_i} = \frac{\boldsymbol{j}_i}{D_{im}^*} = \sum_{j=1}^{N} \frac{x_j}{Đ_{ij}} \left(\boldsymbol{j}_i - \frac{y_i}{y_j} \boldsymbol{j}_j \right) \tag{5.104}$$

$$D_{im}{}^* = \frac{\boldsymbol{j}_i}{\sum_{j=1}^{N} \frac{x_j}{Đ_{ij}} \left(\boldsymbol{j}_i - \frac{y_i}{y_j} \boldsymbol{j}_j \right)} \tag{5.105}$$

In terms of global massive fluxes:

$$D_{im}{}^* = \frac{\boldsymbol{n}_i - y_i \boldsymbol{n}}{\sum_{j=1}^{N} \frac{x_j}{Đ_{ij}} \left(\boldsymbol{n}_i - \frac{y_i}{y_j} \boldsymbol{n}_j \right)} = \frac{\boldsymbol{n}_i - y_i \boldsymbol{n}}{\boldsymbol{n}_i \sum_{\substack{j=1 \\ j \neq i}}^{N} \frac{x_j}{Đ_{ij}} - y_i \sum_{\substack{j=1 \\ j \neq i}}^{N} \frac{x_j}{y_j} \frac{\boldsymbol{n}_j}{Đ_{ij}}} \tag{5.106}$$

Again, if n_i is nearly equal to n:

$$D_{im}{}^* = \frac{1 - y_i}{\sum_{\substack{j=1 \\ j \neq i}}^{N} \frac{x_j}{Đ_{ij}}} \tag{5.107}$$

Equation 5.103 can be also expressed in terms of massive fraction as (Comsol MPh form):

$$\boldsymbol{j}_i = -\rho D_{im}^* \nabla y_i - y_i \rho D_{im}^* \frac{\nabla MW}{MW} \tag{5.108}$$

5.7 Effective diffusion coefficients

One final issue related to the correct description of diffusion phenomena regards effective diffusion coefficients. In the previous sections, diffusion models were described assuming that the gas species can diffuse in an open domain. In porous media, gas has to go through the pores and spaces present inside a solid matrix. The conventional diffusion models could be applied only if the pores domain was simulated, which implies the exact description of the local multiphase geometry inside the particle. This is almost never feasible, even if theoretical studies are made in this sense [35], [36]. A common approach implies the description of the gas-solid matrix as a continuum, with the properties of gas and solid species that can be calculated in any point. In order to describe diffusion, the same mathematical models presented before are used, but with effective diffusion coefficients scaled by local porosity ε and tortuosity τ. For instance, the diffusion coefficients of the generalized Fick's law for the molar diffusion fluxes (equation 5.47) become:

$$D_{ij}^{eff} = D_{ij}\frac{\varepsilon}{\tau} \qquad 5.109$$

The same approximation can be applied to the binary Fick's law and Mixture averaged models, both in molar and mass form. Porosity and tortuosity are properties of the solid matrix. Porosity can be calculated according to mass balances inside the particle, whereas tortuosity is much more difficult to quantify, and usually is considered as a parameter of the problem.

Notation

a_i	Activity of i
B_{ij}	Components of the inverse of Stefan-Maxwell diffusion matrix (s/cm^2)
B_{ij}^F, $B_{ij}^{F'}$	Matrices of transformation from molar diffusion fluxes to mass diffusion fluxes
B_{ij}^{xy}	Matrix of transformation from the gradients of y to the gradients of x
c	Total gas concentration (mol/cm^3)
$\mathfrak{D}_{ij}$	Binary Fick diffusion coefficient of i in j (cm^2/s)
$Ð_{ij}$	Multicomponent diffusion coefficient of i in j (cm^2/s)
D_{ij}	Components of the Stefan-Maxwell diffusion matrix (cm^2/s)
D_{ij}^{eff}	Effective Stefan-Maxwell diffusion coefficient (cm^2/s)
D_{ij}^*	Multicomponent diffusivities to express $\boldsymbol{j}_i$ as a function of the gradients of x (cm^2/s)
D_{ij}^0	Multicomponent diffusivities to express $\boldsymbol{j}_i$ as a function of the gradients of y (cm^2/s)
D_i^K	Knudsen diffusion coefficient of i (cm^2/s)
D_i^T	Thermal diffusion coefficient if i (cm^2/s)
D_{im}, D_{im}^*	Diffusion coefficients of i in the gas mixture, for the molar and mass fluxes (cm^2/s)
$\boldsymbol{g}_i$	External force field applied to i (J/g)
$\boldsymbol{j}_i$	Mass diffusive flux of i (g/cm^2/s)
$\boldsymbol{J}_i^*$	Molar diffusive flux of i (mol/cm^2/s)
K_0	Knudsen number
m_i	Mass of the i-th molecule or species (g)

MW	Molecular weight of gas phase (g/mol)
MW_i	Molecular weight of the i-th species (g/mol)
$\boldsymbol{n}, \boldsymbol{n_i}$	Total mass flux of the gas phase, of the gas i-th species (g/cm^2/s)
N, NG	Number of gas species in the system
$\boldsymbol{N}, \boldsymbol{N_i}$	Total molar flux of the gas phase, of the i-th gas species (mol/cm^2/s)
Nm_i	Number of molecules of the i-th species
Nm	Total number of gas molecules
P	Pressure (Pa)
$\boldsymbol{R}$	Position of the center of mass (cm)
$\boldsymbol{R}'$	Position of the molar center of mass (cm)
R_g	Universal gas constant (J/mol/K)
$\boldsymbol{r}_j$	Position of the j-th molecule (cm)
T	Absolute temperature (K)
$\boldsymbol{v}_i$	Velocity of the i-th species (cm/s)
$\mathbf{v}_{ij}$	Velocity of the j-th molecule of the i-th species (cm/s)
$\boldsymbol{v}$	Velocity of the gas center of mass (cm/s)
$\boldsymbol{v}^*$	Velocity of the gas molar center of mass (cm/s)
x_i	Molar fraction of the i-th gas species
y_i	Mass fraction of the i-th gas species

Greek letters

γ_i	Activity coefficient of i
ε	Porosity
ϕ_i	Volume fraction of i
ρ	Gas density (g/cm^3)
τ	Tortuosity

Chapter 6. Role of diffusion and convection in particle models

In the previous section, different approaches to describe gas diffusion were discussed. The multicomponent Stefan Maxwell model is the most correct when dealing with gas mixtures with more than two species involved. From a mathematical point of view, it is also the most difficult to implement, for two main reasons: first because the diffusive flux of one species depends on the concentration gradients of all the species in the system, so this model introduces other terms of coupling between the equations to solve; second but not less important, it introduces non linearities, in the calculation of the diffusion matrix. Even if the diffusion matrix usually depends weakly on the gas composition, a more complex numerical treatment is necessary to solve the problem. In many cases it can be convenient to use a simpler Fick's law, with constant diffusion coefficients, possibly scaled with the local porosity, or expressed as a function of the gas composition, like in the mixture averaged model.

All the simplifications may lead to inaccuracies in the description of gas diffusion, and in the model results. Several factors can affect these inaccuracies:

a) The importance of diffusion with respect to the other resistances: if diffusion is fast compared to chemical reaction (chemical regime) it is more likely that the choice of the diffusion model makes little or no difference in the estimated conversion results. On the contrary, if diffusion is the rate determining step it can be worth to be more accurate on the description of the gas transport inside the particle. The controlling regime can depend on many factors: the particle size may also play an important role.
b) The number of species in the gas mixture. It can be demonstrated that all the multicomponent diffusion models become identical to the binary Fick's law if only two species are present in the system. The more species, the more it is likely that a multicomponent model is necessary.
c) The values of the binary diffusion coefficients: it can be proved that the Stefan Maxwell model becomes identical to the binary Fick's law if all the binary diffusion coefficients are the same. On the contrary, major differences can arise if they are very different from each others. This happens for example if there are molecules with different volumes: a typical example of a critical mixture is when hydrogen is present, because of its higher diffusivity if compared to those of other gases.
d) The degree of dilution of the gas species. If the fraction of one species is very high if compared to the others, the multicomponent model becomes similar to the Fick's law, where the diffusion coefficients used are the diffusivities of the diluted species into the diluents.

6.1 Mathematical proof of model simplifications

In the following we provide mathematical proofs of the simplifications of SM to Fick's law for the four cases listed above. Let us consider the inverse of the multicomponent diffusion matrix as expressed in equation 5.42, and here reported again:

$$B_{ij} = \frac{x_i}{Đ_{iN}} + \delta_{ij} \sum_{\substack{k=1 \\ k \neq i}}^{N} \frac{x_k}{Đ_{ik}} + (\delta_{ij} - 1) \frac{x_i}{Đ_{ij}} \tag{6.1}$$

The limit case b) is related to the number of species: if only two species are present in the system, then N = 2 and the matrix is 1x1, and becomes:

$$B_{11} = \frac{x_1}{Đ_{12}} + 1 \frac{x_2}{Đ_{12}} + (1 - 1) \frac{x_1}{Đ_{11}} = \frac{1}{Đ_{12}} \tag{6.2}$$

Because the sum of x_1 and x_2 is equal to one. The inverse of B_{11} is $Đ_{12}$, and using this value in equation 5.47 we obtain the form of the binary Fick's law.

The limit case c) is when all of the binary coefficients have the same value. In such a case, $Đ_{ij} = Đ$, and can be collected in equation 6.1, obtaining:

$$B_{ij} = \frac{1}{Đ} \left(x_i + \delta_{ij} \sum_{\substack{k=1 \\ k \neq i}}^{N} x_k + (\delta_{ij} - 1) x_i \right) = \frac{1}{Đ} \left(\delta_{ij} \sum_{\substack{k=1 \\ k \neq i}}^{N} x_k + (\delta_{ij}) x_i \right) = \frac{\delta_{ij}}{Đ} \sum_{k=1}^{N} x_k = \frac{\delta_{ij}}{Đ} \tag{6.3}$$

So B becomes a diagonal matrix, whose inverse is a diagonal matrix with non zero values equal to Đ:

$$D_{ij} = \delta_{ij} Đ \tag{6.4}$$

Using this in equation 5.47 we obtain:

$$\boldsymbol{J}_i^* = -c Đ \sum_{j=1}^{N-1} \delta_{ij} \nabla x_j = -c \, Đ \, \nabla x_i \tag{6.5}$$

Which is Fick's law. The limit case d) is when the fraction of the N-th species tends to one, and the fractions of the other species tend to zero. We then consider the limit:

$$\lim_{x_N \to 1} B_{ij} = \frac{0}{Đ_{iN}} + \delta_{ij} \frac{1}{Đ_{iN}} + (\delta_{ij} - 1) \frac{0}{Đ_{ij}} = \frac{\delta_{ij}}{Đ_{iN}} \tag{6.6}$$

Again, the matrix D will be diagonal, as follows:

$$D_{ij} = \delta_{ij} Đ_{iN} \tag{6.7}$$

This time the elements in the diagonal are not all the same, but are the binary diffusion coefficients of the i-th species into the diluent. Equation 5.47 becomes:

$$\boldsymbol{J}_i^* = -c \sum_{j=1}^{N-1} \delta_{ij} Đ_{iN} \nabla x_j = -c\, Đ_{iN}\, \nabla x_i \qquad 6.8$$

Which is again the form of the Fick's law, but only the binary diffusivities of each species in the solvent are relevant. The same results can be obtained if the mixture averaged expression in equation 5.102 is considered. For a mixture of 2 species (hypothesis b), D_{im} for the 1st species becomes as follows:

$$D_{1m} = \frac{1 - x_1}{\sum_{\substack{j=1 \\ j \neq 1}}^{2} \frac{x_j}{Đ_{1j}}} = \frac{x_2}{\frac{x_2}{Đ_{12}}} = Đ_{12} \qquad 6.9$$

When all of the diffusion coefficients are the same (hypothesis c):

$$D_{im} = Đ \frac{1 - x_i}{\sum_{\substack{j=1 \\ j \neq i}}^{N} x_j} = Đ \frac{1 - 1 + \sum_{\substack{j=1 \\ j \neq i}}^{N} x_j}{\sum_{\substack{j=1 \\ j \neq i}}^{N} x_j} = Đ \qquad 6.10$$

Finally, when x_N tends to one (hypothesis d):

$$\lim_{x_N \to 1} D_{im} = \frac{1 - 0}{\frac{1}{Đ_{iN}}} = Đ_{iN} \qquad 6.11$$

Both in the cases of the mixture averaged and Stefan-Maxwell, in the limit cases the multicomponent diffusion coefficients no longer depend on the mixture composition.

6.2 Sensitivity analysis on diffusion models

The previous mathematical analysis is useful to identify the situations that allow an approximation in the diffusion model to use. It can be also useful to estimate which is the error made with simplified diffusion models, depending on how far away from the limit conditions the real system is. This can be done by carrying out sensitivity analyses.

This was done by solving the continuous model described in chapter 4. A number of simplifications were applied to the scheme of equations 4.37-4.41, in order to isolate the effect of the choice of the diffusion model on the results. In particular, a single irreversible reaction was chosen, involving one gas and one solid reagents and products, with unitary stoichiometric coefficients, in the form:

$$A(s) + B(g) \rightarrow C(s) + D(g) \qquad 6.12$$

It was assumed that no particle volume change occurs, and the solid species were supposed to have similar densities and molecular weights, so that the time variation of porosity as described by equation 4.45 is zero. Isothermal conditions were applied, which together with the former conditions also implied that no convective flux can be generated, according to equation 4.46. The reaction rate was chosen in the form of the simplified grain model, depending linearly on the concentration of B. Finally, no external mass transfer was considered. With these modifications, the continuous model of equations 4.37-4.41 becomes:

$$\frac{\varepsilon c^g \partial x_B^g}{\partial t} = -\frac{1}{r^2}\frac{\partial}{\partial r}(r^2 J_B^*) - c_B^g\,(1-X)^{2/3} \qquad 6.13$$

$$\frac{\varepsilon c^g \partial x_D^g}{\partial t} = -\frac{1}{r^2}\frac{\partial}{\partial r}(r^2 J_D^*) + c_B^g\,(1-X)^{2/3} \qquad 6.14$$

$$\frac{\partial c_A^S}{\partial t} = -c_B^g\,(1-X)^{2/3} \qquad 6.15$$

The boundary and initial conditions were considered constant in time and space, respectively:

$$\begin{aligned} &for\ r = r_0 && c_i^g = c_{i,bulk} \\ &for\ r = 0 && J_i^* = 0 \end{aligned} \qquad 6.16$$

$$\begin{aligned} &for\ \ t = 0 && c_i^g = c_i^{g\,0} \\ & && c_i^s = c_i^{s\,0} \end{aligned} \qquad 6.17$$

The simulated system involved a mixture of three gas components, B, D and an inert E. The model was solved considering three diffusion models: Multicomponent Stefan Maxwell (equations 5.42-5.47), mixture averaged (equations 5.97 and 5.102), and binary Fick (equation 5.24).

At each time step, the global particle conversion was calculated, by integrating the solid concentration in space, as follows:

$$\overline{c_A^S}(t) = \frac{\int_0^{r_0} 4\pi r^2 c_A^S(r,t)dr}{\frac{4}{3}\pi r_0^3} \qquad 6.18$$

$$\bar{X}(t) = 1 - \frac{\overline{c_A^S}(t)}{\overline{c_A^S}(0)} \qquad 6.19$$

A relative difference between the global particle conversion estimated with the Stefan Maxwell and Fick model can be defined as follows:

$$e_F(t) = \frac{\bar{X}_{Fick}(t) - \bar{X}_{SM}(t)}{\bar{X}_{SM}(t)} = \frac{\bar{X}_{Fick}(t)}{\bar{X}_{SM}(t)} - 1 \qquad 6.20$$

In the same way, an error of the mixture averaged model can be calculated, as follows:

$$e_{MA}(t) = \frac{\bar{X}_{MA}(t) - \bar{X}_{SM}(t)}{\bar{X}_{SM}(t)} = \frac{\bar{X}_{MA}(t)}{\bar{X}_{SM}(t)} - 1 \qquad 6.21$$

Different simulations were carried out to evaluate the errors at different conditions.

6.2.1 Effect of the fraction of inert

In this first set of simulations, the conversion was calculated for a large particle (1 cm radius), initially made of the reagent A, with a concentration of 0.025 mol/cm3 and a uniform constant porosity of 50%. The total gas concentration was calculated assuming temperature and pressure set to 1000K and 1 atm, respectively. The kinetic constant was fixed to 1000 s^{-1}. The binary diffusion coefficient of the gas reagent into the gas product was set to D_{BD} = 5 cm^2/s, whereas the binary diffusion coefficients of B and D into the inert were both set to 1/3 of D_{BD} (so D_{BE} = D_{DE} = $D_{BD}/3$). These ratios can be easily found in practice (for instance $D_{H2O,H2}/D_{H2O,N2}$ = 2.96).

In these conditions, a Thiele modulus associated to D_{BD} can be calculated as follows:

$$\Phi^2 = \frac{r_0^2 k}{D_{BD}} \qquad 6.22$$

With the chosen values of the parameters, Φ^2 = 200. This value is much higher than one, which means that diffusion is controlling over kinetics. So, this is a typical case when the accuracy of the diffusion model can be important.

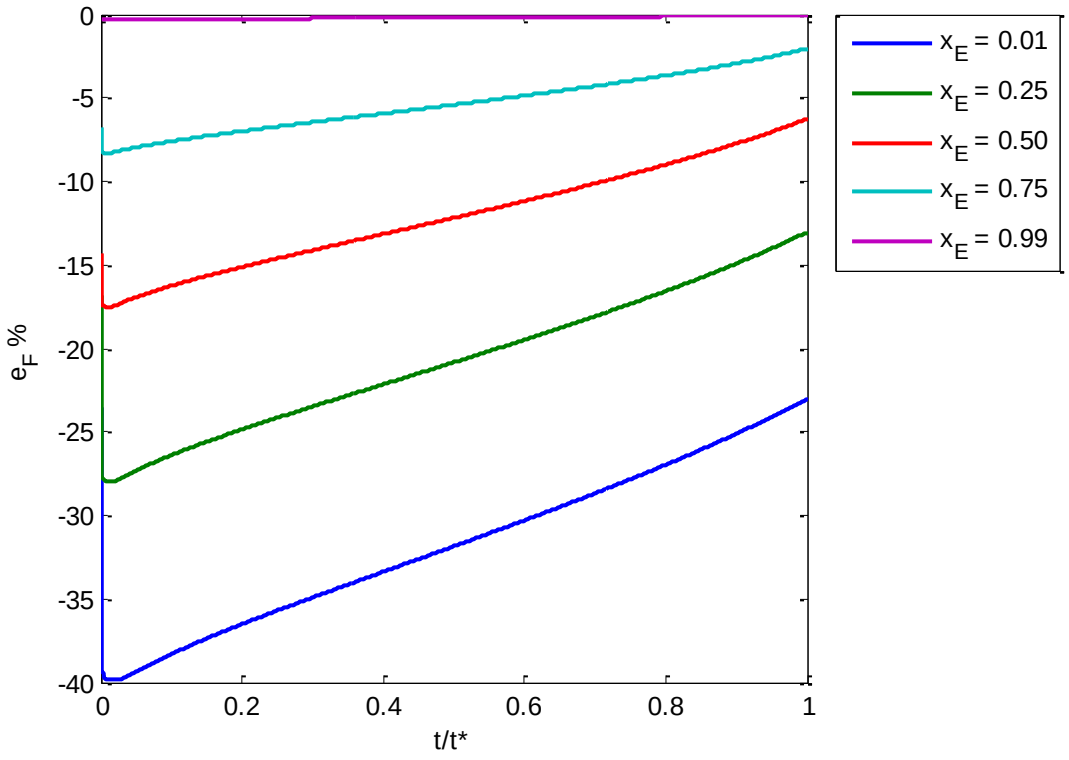

Figure 6.1: Relative difference between the particle conversion estimated with Fick's law (using D_{BE} as diffusion coefficient) and Stefan-Maxwell model, for Φ^2 = 200 and D_{BD} = 3 D_{BE}, for different values of inert molar fraction. In all cases $x_B^{bulk} = x_D^{bulk}$.

Different simulations were carried out, by changing the composition of the gas mixture outside the particle. In all of these, the fraction of inert E was changed. The fraction of B and D changed accordingly, but in all cases it was imposed that the fraction of B was equal to the fraction of D. The simulations were carried out with all three diffusion models and the errors of approximation of Fick and Mixture averaged models were calculated with respect to the solution of the Stefan Maxwell model. Figure 6.1 shows the results of the comparison Fick to Stefan Maxwell. The time coordinate was normalized with a factor t* which is the time for total conversion of the particle as simulated with the Stefan Maxwell model, and has a different value for each inert fraction considered. This normalization was made because the time scale of the conversion can change significantly for different boundary concentrations of the gas reagent.

Fick's law was simulated by using the diffusion coefficients of the gases into the inert species E. By doing this, it can be noticed that the error drops to zero when the fraction of inert approaches unity (x_E^{bulk} = 99%). This was expected, considering the mathematical proofs reported before. On the contrary, the error is maximum when the fraction of inert is minimum (x_E^{bulk} = 1%). In this situation, Fick's law is used with an incorrect value of the binary diffusion coefficient, because the actual mixture is made of B and D.

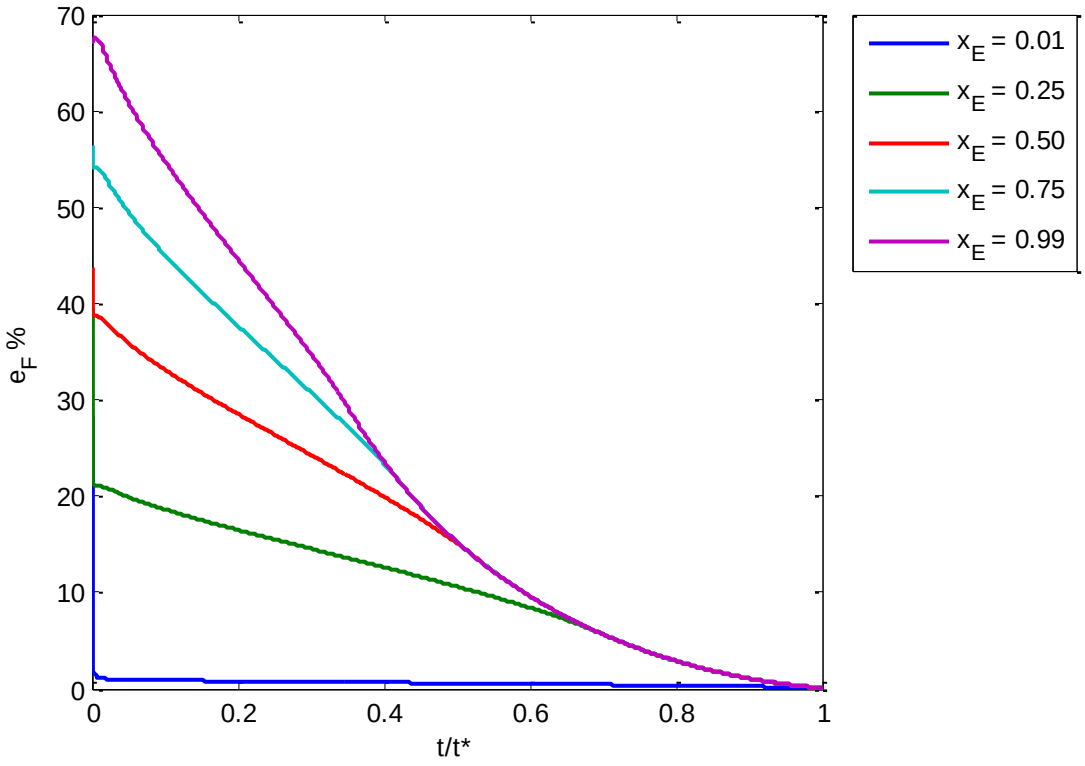

Figure 6.2: Relative difference between the particle conversion estimated with Fick's law (using D_{BD} as diffusion coefficient) and Stefan-Maxwell model, for Φ^2 = 200 and D_{BD} = 3 D_{BE}, for different values of inert molar fraction. In all cases $x_B^{bulk} = x_D^{bulk}$.

The same simulations can be done by using D_{BD} as a binary diffusion coefficient into Fick's law, instead of D_{BE} and D_{DE}. The resulting calculated errors are reported in figure 6.2. This situation is opposite to the one shown in figure 6.1: the error is minimum when the fraction of inert is minimum, because Fick's law correctly describes the binary mixture B-D with the correct diffusion coefficient. On the contrary, the error is maximum when the reagent and product are very diluted. Unlike the previous simulations, the errors are

positive in this case, because D_{BD} is higher than D_{BE}, and so the simplified model doesn't account for a more difficult diffusion into the inert, which results in an overestimation of the particle conversion. The error profiles seem to converge to a single line dropping to zero with time. This is just due to the fact that there is a time t < t* when Fick's law predicts full conversion of the particle, whereas for the Stefan Maxwell model the reaction is still going on. From that time on, the predicted conversion with Fick's law is always one, while the predicted conversion with Stefan Maxwell approaches one. As a result, the difference between the two models drops to zero. If the errors are negative this doesn't happen, because at t = t* the SM model predicts full conversion whereas according to the simplified model the reaction is still going on.

It can be noticed that the errors made with Fick's law can be very consistent for the considered cases (more than 50%). In general, the approximation using the diffusion coefficients related to the inert seems more accurate than the one using the binary coefficient of B in D, getting far away from the conditions of applicability of Fick's law.

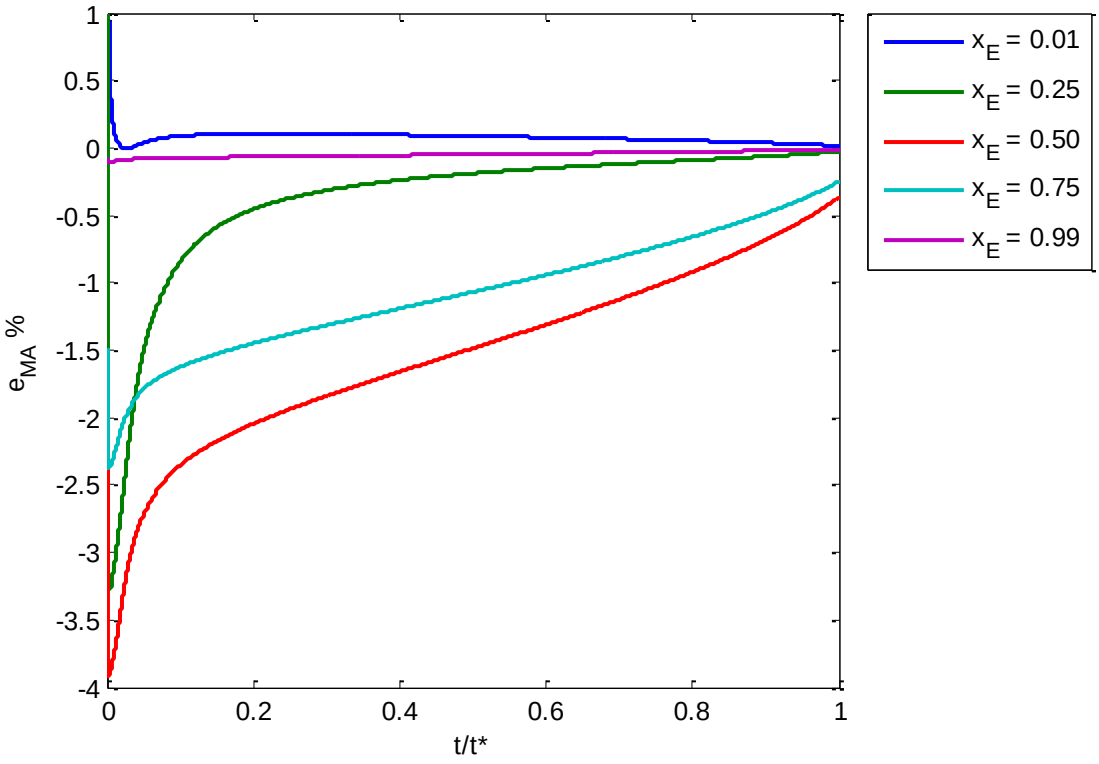

Figure 6.3: Relative difference between the particle conversion estimated with Mixture Averaged model and Stefan-Maxwell model, for Φ^2 = 200 and D_{BD} = 3 D_{BE}, for different values of inert molar fraction. In all cases $x_B^{bulk} = x_D^{bulk}$.

Figure 6.3 shows the comparison of the results obtained with Mixture averaged and Stefan Maxwell model. In this test, the estimated diffusion coefficients in the mixture (D_{im}) were calculated from the same set of binary diffusion coefficients as before. As expected, the Mixture averaged is much more accurate than Fick's law, because somehow it accounts for the effect of the local gas composition, even if not in the most rigorous way. The calculated errors are quite lower in this case. The errors drop to zero on both the limit cases (extreme dilution or no dilution of B and D). This is also consistent with what was proved in equations 6.2, 6.6 , 6.9 and 6.11. In this case the absolute error is maximum at intermediate conditions (50% of inert

and 50% of B-D mixture), where both the values of D_{BD} and D_{BE} are equally important. This error could also expected to grow if the diffusivities of the gas reagent and product in the inert are different.

6.2.2 Effect of the controlling regime

The previous results were obtained considering a fixed value for the Thiele modulus, corresponding to fixed kinetics, diffusion coefficients and particle size. The importance of the choice of the diffusion model can be different, depending on the importance of diffusion into the process itself. This can be quantified by doing simulations at different Thiele modulus.

This was made in a second sensitivity analysis. Again, the values of the parameters were kept constant as in the previous tests (k = 1000 s^{-1}, D_{BD} = 5 cm^2/s, D_{BE} = D_{DE} = 5/3 cm^2/s). This time the gas bulk composition was fixed: x_E^{bulk} = 0.75 x_B^{bulk} = x_D^{bulk} = 0.125. The value of the Thiele modulus was varied by simulating particles with different size, from 100 µm to 2.25 cm, corresponding to a range of Φ^2 = 0.02-1000.

The calculated errors for Fick's law (using D_{BE} as diffusion coefficient) are shown in figure 6.4.

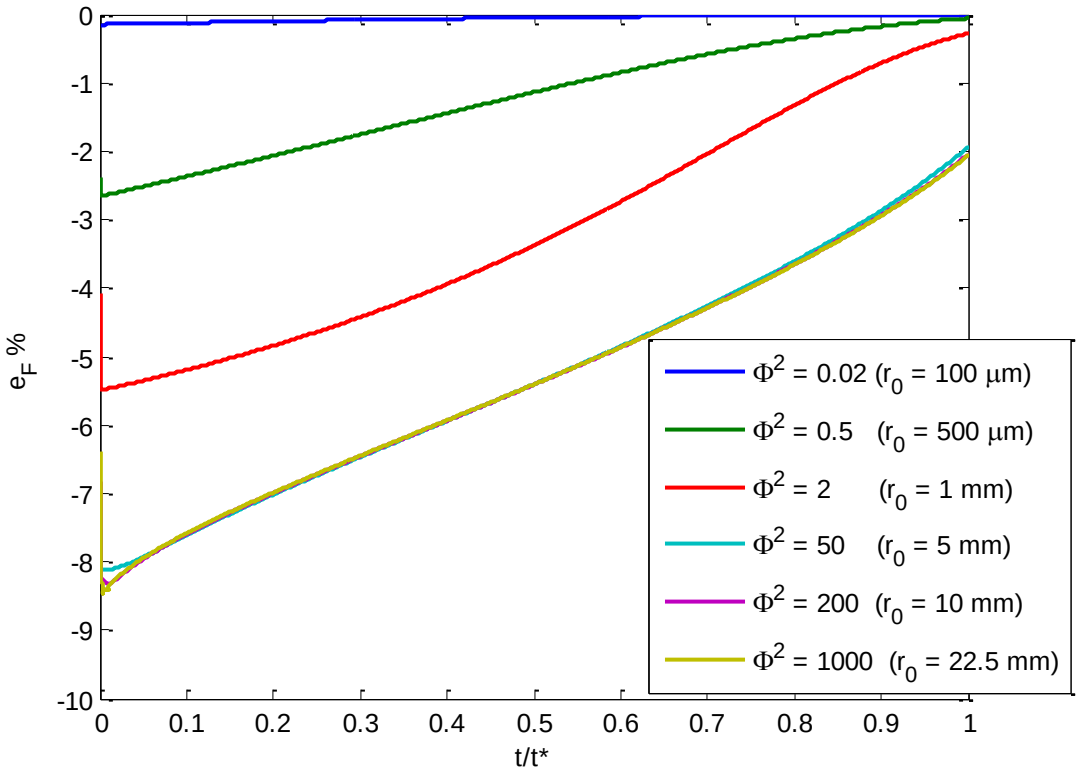

Figure 6.4: Relative difference between the particle conversion estimated with Fick's law (using D_{BE} as diffusion coefficient) and Stefan-Maxwell model, for x_E^{bulk} = 0.75, x_B^{bulk} = x_D^{bulk} = 0.125, D_{BD} = 3 D_{BE}, for different values of Thiele modulus.

For very small particles, the gas diffuses quickly into the solid matrix, and the whole process is controlled by the value of the kinetic rate. In these cases (Φ^2 = 0.02-0.5), the accuracy of the diffusion model is not important. As the Thiele modulus increases, the errors become more important.

The values of the errors of the mixture averaged model are reported in figure 6.5.

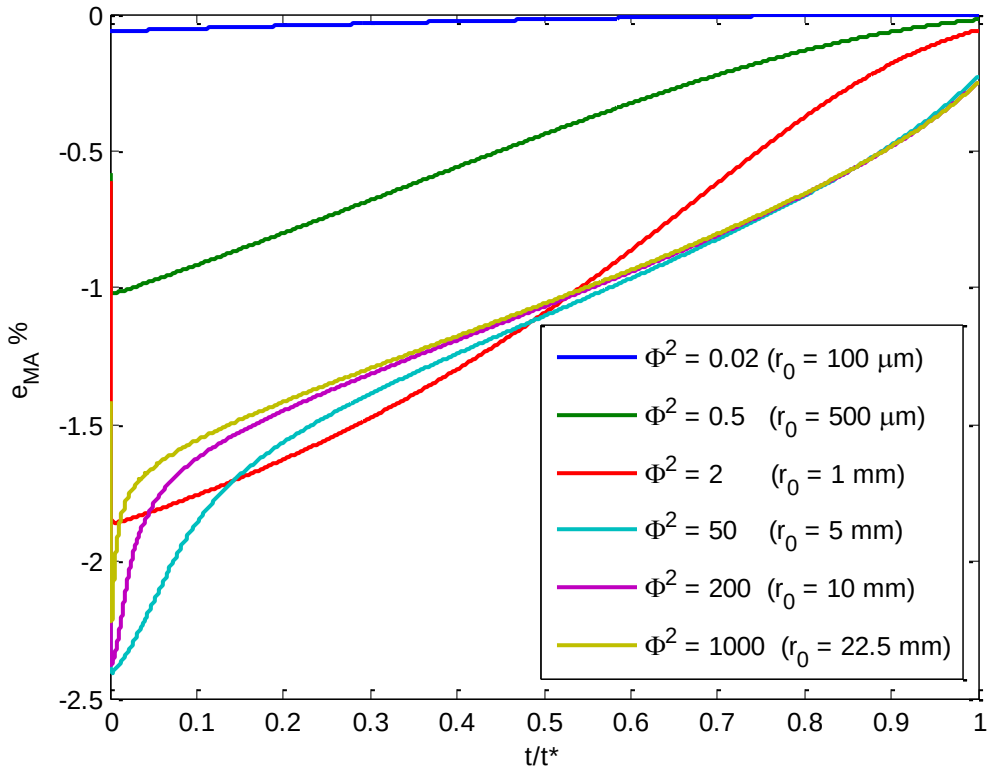

Figure 6.5: Relative difference between the particle conversion estimated with Mixture Averaged model and Stefan-Maxwell model, for x_E^{bulk} = 0.75, x_B^{bulk} = x_D^{bulk} = 0.125, D_{BD} = 3 D_{BE}, for different values of Thiele modulus.

Again, the mixture averaged model is a good approximation for all the considered cases. It can be noted that both for Fick and MA models, the error curves tend to an asymptotic profile for high values of Φ^2 (see cases for Φ^2 = 50, Φ^2 = 200 and Φ^2 = 1000).

6.2.3 Effect of non homogeneous diffusion matrix

In the previous simulations, the values of the binary diffusion coefficients D_{BD}, D_{BE} and D_{DE} were kept constant. The results of the diffusion models can be more or less divergent also depending on how much different the binary coefficients are from each others. With all of the other condition fixed, the errors are expected to reduce if the ratio between D_{BD} and D_{BE} approaches unity and to grow if the same ratio is much

higher or much lower than one. This is because all of the models become identical to Fick's law if the binary coefficients are the same, as it was proved before.

More simulations were carried out, fixing D_{BD} = 5 cm^2/s and changing D_{BE} (and consequently D_{DE}, which was imposed equal to D_{BE} for all the tests). The other parameters were fixed: k = 1000 s^{-1}, x_E^{bulk} = 0.75 x_B^{bulk} = x_D^{bulk} = 0.125 and r_0 = 1 cm. As in the first set of simulations, the value of the Thiele modulus for all of these runs is always equal to 200. Six D_{BD}/D_{BE} ratios were tested (D_{BD}/D_{BE} = 1, 2, 3, 5, 8, 10). The estimated errors for Fick's law (using D_{BE} as diffusion coefficient) are reported in figure 6.6.

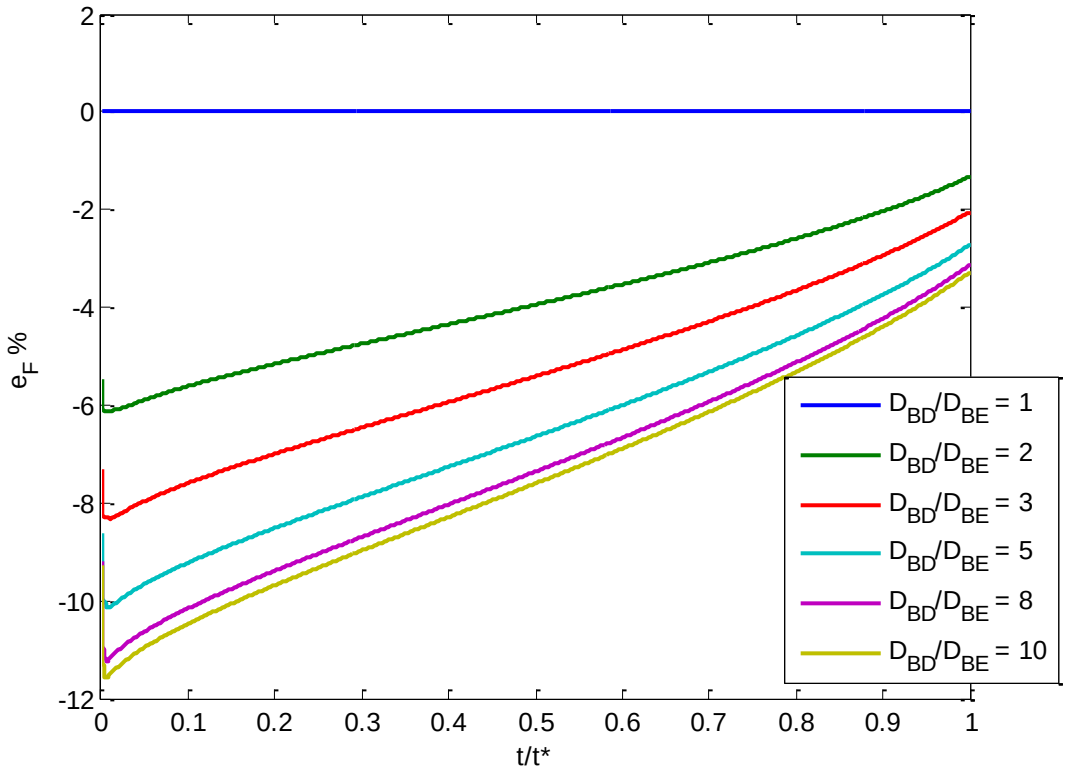

Figure 6.6: Relative difference between the particle conversion estimated with Fick's law (using D_{BE} as diffusion coefficient) and Stefan-Maxwell model, for x_E^{bulk} = 0.75, x_B^{bulk} = x_D^{bulk} = 0.125, Φ^2 = 200, and for different values of D_{BD}/D_{BE} ratios, and D_{DE} = D_{BE}.

As expected, if D_{BD} = D_{BE} = D_{DE} the estimated error is zero for any reaction time. If the diffusivity of B in D is higher that the diffusivity of B in the inert E, the error grows progressively with the D_{BD}/D_{BE} ratio, up to 5-10%. The relative difference also seems to decrease with time, in absolute value.

The corresponding errors of the Mixture averaged model are shown in figure 6.7. The trend of the profiles is the same as Fick's model errors, but errors are much lower (1-2 %). Again, MA models provide a good approximation of the rigorous multicomponent approach.

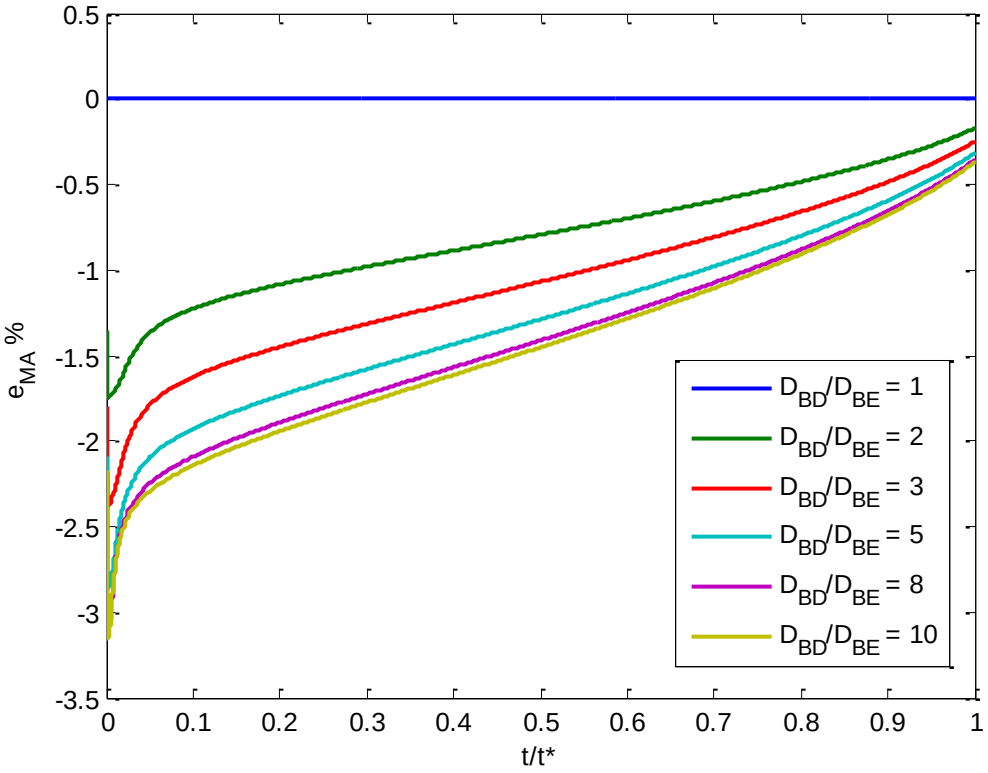

Figure 6.7: Relative difference between the particle conversion estimated with Mixture Averaged model and Stefan-Maxwell model, for $x_E^{bulk} = 0.75$, $x_B^{bulk} = x_D^{bulk} = 0.125$, $\Phi^2 = 200$, and for different values of D_{BD}/D_{BE} ratios.

In conclusion, the choice of the diffusion model to use in the description of the gas solid reaction particle can be very important or non influential, depending on a number of conditions that have been investigated. The degree of dilution of the binary reagent-product mixture into the inert species is certainly a key factor. Generally, using Fick's law can become dangerous, and it leads to serious inaccuracies that can eventually affect the identification of the kinetic parameters, if this is made for reacting solids where intra particle diffusion is important and the gas reagent is not very diluted.

This problem also affects the use of the shrinking core model, which is based on the use of Fick's law, thus propagating the errors deriving from the simplified approach. This is an important issue also because, in common gas-solid processes, the concentration of reacting gas is quite high, and it is rare to operate in diluted conditions, when Fick's law can acceptably approximate the multicomponent approaches.

6.3 Role of convection

In the previous section (§6.2), it was proven that the diffusion model used in the continuous particle model may play a role in the accuracy of the simulations results. Diffusion is not the only mass transfer mechanism into the particle. As stated in section §4, convection can also be present in the solid matrix. Unlike the reactor scale, inside the particle there is never a forced convection generated by an imposed pressure gradient. Nevertheless, according to equation 4.46, natural gas convection can be generated by porosity gradients, temperature gradients or a net production of number of gas moles due to reaction.

In continuous models, gas convection is often neglected, and in shrinking core models it is never included. The reason for this choice is that convection is always assumed to be of little importance with respect to diffusion within the pores. In this section, the effect of convection is evaluated for gas solid reactions, at different conditions.

A very large number of parameters is involved in the generation of convection. According to equation 4.46, they are:

- Total gas concentration (depending on gas temperature and pressure)
- The different molecular weights and intrinsic densities of the solid species.
- The different stoichiometric coefficients of the gas and solid phases.
- Kinetic parameters in the reaction rates.
- The heat capacities and conductivities of the gas and solid species.
- Heats of reactions.

Doing a sensitivity analysis is quite unfeasible, based on the number of possible variables. Instead, it can be more useful to consider some particular cases and try to get some insight into the problem by looking at the magnitude of the simulated convective fluxes.

One important issue that is often neglected is that the degree of approximation related to the simplification of the convective term can also depend on the form of the equations: if they are solved in terms of moles or mass, the relevance of the convective flux can be different. This can be seen by comparing the equations of the total molar gas flux (equation 4.46) and total mass gas flux (equation 4.83), that we report here, in a more compact way:

$$\frac{1}{r^2}\frac{\partial}{\partial r}(r^2 N^g) = -c^g \frac{\partial \varepsilon}{\partial t} + \frac{\varepsilon c^g}{T}\frac{\partial T}{\partial t} + \sum_{j=1}^{NG} s_j^g \qquad 6.23$$

$$\frac{1}{r^2}\frac{\partial}{\partial r}(r^2 n^g) = -\rho^g \frac{\partial \varepsilon}{\partial t} + \frac{\varepsilon \rho^g}{T}\frac{\partial T}{\partial t} + \varepsilon \rho^g \sum_{j=1}^{NG} \frac{\partial y_j}{\partial t}\frac{MW^g}{MW_j} + \sum_{j=1}^{NG} s_j^g MW_j \qquad 6.24$$

If the reaction is equimolar with respect to the gas species, the last term of the right hand side of equation 6.23 is zero, while it is not for the mass balance. In other words, a zero production of mole corresponds to a nonzero production of mass in gas phase, and this can have an effect on the two total fluxes. Another way to see this is by looking at the difference of the gas velocities associated with the mass and molar gas fluxes

(v and v*, according to equations 5.11-5.12). The mass and molar velocities can be related to each other, by combining equations 5.9 and 5.25, obtaining the following rule:

$$v = v^* + \sum_{j=1}^{NG} \frac{y_j J_j^*}{x_j c} \qquad 6.25$$

The difference between v and v* is often neglected for problems dominated by forced convection. In those cases, the diffusive fluxes are relatively small, and so the sum in equation 6.25 is small. Inside a porous medium, on the contrary, diffusion dominates, so that approximation is generally not valid, unless the molecular weights of the gas species are very similar to each other ($x_j \approx y_j$). If convection is neglected in the molar balance, that means that the flux of the i-th species is calculated considering the difference between the velocity of i and the molar velocity of gas (v*, as stated by equation 5.20), whereas if convection is neglected in the mass balance, the flux of i considers the difference between the velocity of i and the mass velocity (equation 5.19).

In order to see if this can make a difference in the predicted results, the model was solved on both molar and mass base, for two problems: reduction of FeO with CO (equimolar reaction), and oxidation of ZnS with oxygen (non equimolar in the gas phase). The results are reported in the next sections.

6.3.1 Gas equimolar reaction: reduction of wustite

In this first example, the reduction of wustite to metallic iron with carbon monoxide was simulated with the continuous model. The reaction stoichiometry is as follows:

$$FeO + CO \rightleftarrows Fe + CO_2 \qquad 6.26$$

This reaction is reversible, and moderately exothermic ($\Delta H°_{298}$ = -15.7 kJ/mol). The gas solid system was simulated considering a large particle (1 cm diameter), initially made of pure wustite with an apparent density (calculated on the total particle volume) of 3.5 g/cm^3. Considering the intrinsic density of FeO (5.7 g/cm^3), this corresponds to an initial particle porosity of 38.5%. Outside the particle an atmosphere of 40% CO in N_2 was assumed, constant in time. The grain model was used to express the reaction rate, including chemical equilibrium. The kinetic parameters were fixed according to the literature [9]. The gas temperature and pressure outside the pellet were assumed to be 800°C and 1 atm, respectively.

The reaction was simulated until complete FeO conversion, by using equations 4.37-4.41, with no changes in particle size (N^S= 0). It was also assumed that no external mass and energy transfer resistances are present (so the Dirichlet boundary conditions were in the form of equation 4.48). The results prove that, at these conditions (temperature, particle size, internal convection and external heat transfer conditions), the reaction is isothermal (the maximum simulated temperature rise was about 0.1 °C), which means that the generated heat is easily dispersed outside the particle. Figure 6.8 shows the radial composition profiles for the solid and gas phase at half of the reaction (at the time when the mean particle conversion is 50%).

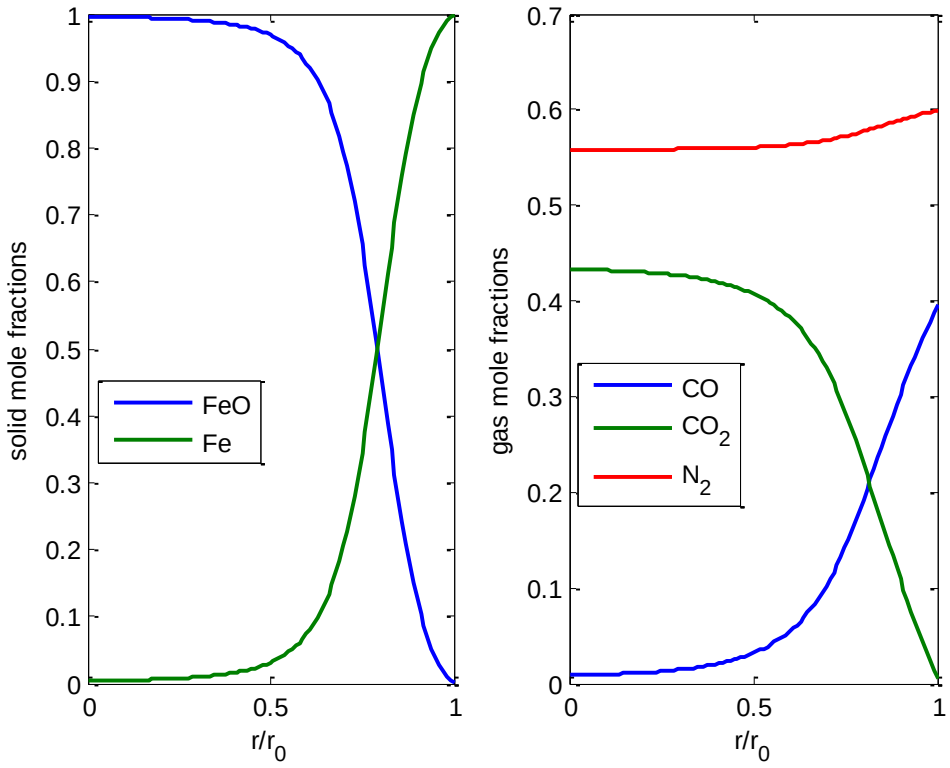

Figure 6.8: Estimated molar fractions of solid (left) and gas (right) species inside the particle when half of the wustite is converted (t = 102 s).

It can be noticed that in these conditions, the process is limited by the inner mass transport: in fact, important radial gradients are present in the profiles, and the concentration of CO drops to very low values in the core where FeO is not converted.

The same system was also simulated with the mass balances (equations 4.76-4.80), obtaining the same results, as the two models are identical. In both cases, the convective fluxes were correctly included. The importance of the convective part can be evaluated in the two cases, by comparing the profiles of the total (N_i, n_i) and diffusive (J_i*, j_i) fluxes of the gas species obtained with the molar and mass material balances. At half conversion time, such profiles are shown in figure 6.9 for CO.

The fluxes of carbon monoxide are negative, because CO moves from outside towards the centre of the particle, where it is consumed. A minimum of the diffusive flux is present, and this is due to a corresponding maximum CO concentration gradient that can be observed in figure 6.8.

It can be noticed that the calculated molar diffusive and total flux of CO are the same (figure 6.9, left side). At the same reaction time, the mass diffusive total flux of CO is different from its diffusive mass flux (figure 6.9, right side). The difference between n_{CO} and j_{CO} is given by the convective part of the mass flux, that is not visible when the equations are solved in terms of moles. From these results it looks clear that the simplification of the convective part in the balances will lead to higher errors if the mass equations are used instead of the molar ones. The contribution of convection can be also seen by comparing the simulated radial profiles of the mass and molar velocity (v and v*). They are shown for the same reaction time in figure 6.10, together with the velocity of CO.

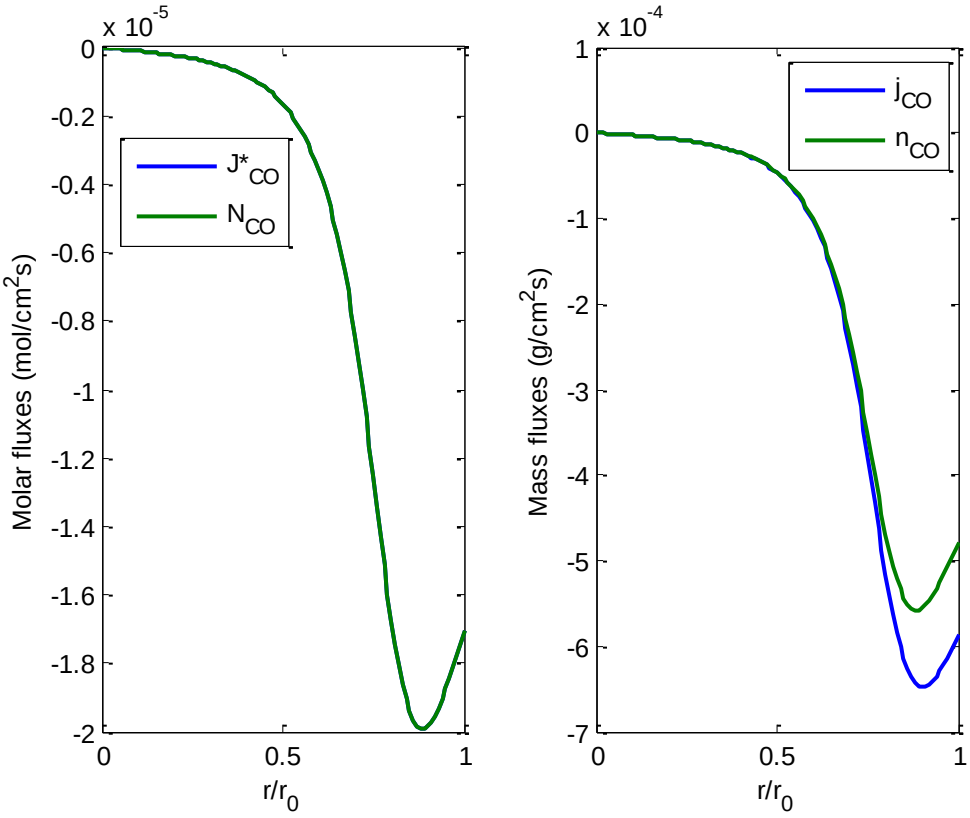

Figure 6.9: Diffusive and total (diffusive + convective) fluxes of CO at half conversion time (t = 102 s) inside the particle. Molar fluxes (left) and mass fluxes (right).

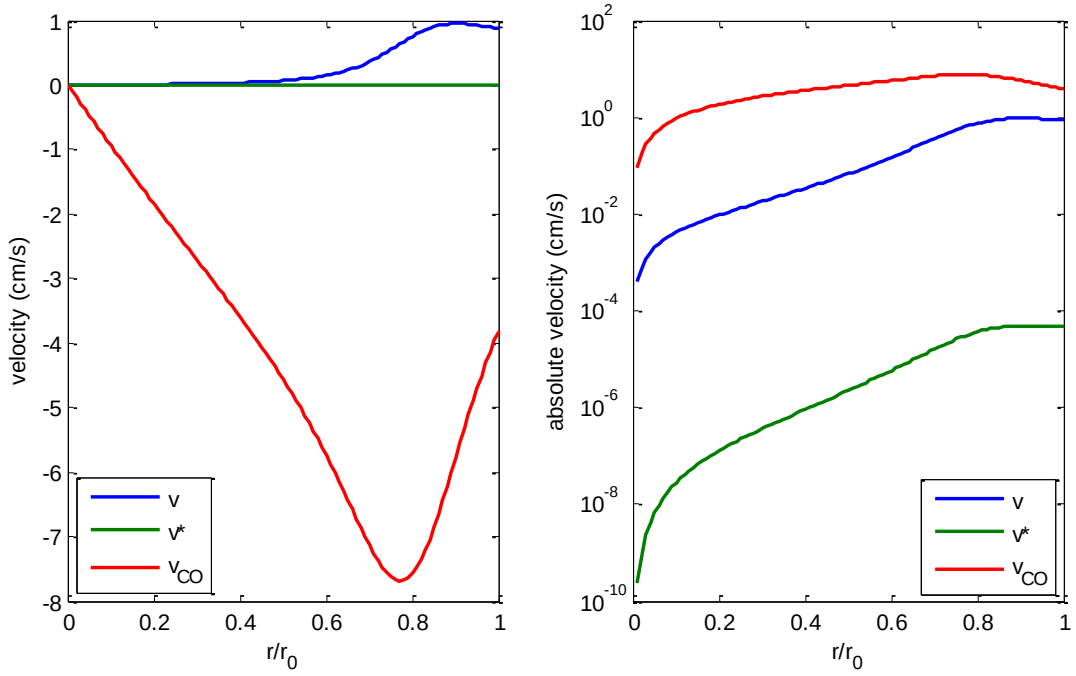

Figure 6.10: Radial profiles of the mass gas velocity (v), molar gas velocity (v*) and velocity of CO at half conversion time (t = 102 s). Results in linear scale (left), and logarithmic scale of their absolute values (right).

The mass velocity of gas is positive, because it reflects the production of mass in gas phase, due to the fact that oxygen is extracted from the solid phase, increasing the molecular weight of the gas mixture. The order of magnitude of v is more or less the same as that of the velocity of CO, which explains why convection has an influence on the mass flux of CO. In particular, the convective and diffusive mass fluxes of CO have opposite directions, and that is the reason why n_{CO} is less negative than j_{CO}. On the other hand, the profile of v* looks zero. Actually, the molar velocity is not zero, as it can be seen on the right of figure 9.10 where the same profiles are reported in logarithmic scale. It is just very small, compared to the other two velocities.

According to equation 6.23, in this particular case the molar velocity can be generated only by time variations of porosity, consistent with the hypothesis of constant particle volume (first term of the right hand side). In fact, no temperature gradients are present (the particle is isothermal), and no moles are generated or consumed. In this case, the particle porosity changes from the initial 38.5% (pure FeO), to 65.5% (pure iron), as a result of the loss of mass in the solid (the molecular weight of Fe is lower than that of FeO), and different intrinsic densities of the solid reagent and product (ρ_{FeO} = 5.7 g/cm^3, ρ_{FeO} = 7.9 g/cm^3). This is actually a large change of porosity, but in spite of that, a very low molar flux is generated. This proves that the porosity change term in equation 6.23 is not important at all.

This analysis seems to point out that the convective part can be easily cleared from the molar balances but not from the mass balances, for this particular case. The quantification of the errors due to this simplification can be evaluated by simulating the process, first including convection and then neglecting it in the equations. Two profiles for the mean particle conversion in time will be obtained, the correct one ($\bar{X}_{Correct}$) and the simplified one ($\bar{X}_{Simplified}$), i.e. neglecting convection. The error can be calculated as follows:

$$e(t) = \frac{\bar{X}_{Simplified}(t) - \bar{X}_{Correct}(t)}{\bar{X}_{Correct}(t)} \qquad 6.27$$

The mean particle conversion can be calculated by integrating in space the conversion profiles at any time, by using equations 6.18-6.19.

The errors were calculated for this simulation of FeO reduction, both using the molar balances (equations 4.37-4.41) and the mass balances (equations 4.76-4.80). In the first case, $\bar{X}_{Simplified}$ does not account for the molar convective fluxes of gas, while in the second case $\bar{X}_{Simplified}$ does not consider the mass convective fluxes of gas. The results are reported in figure 6.11. The errors are a function of the normalized time t/t*, where t* is again the time of full particle conversion, as calculated with the correct model.

As expected, the errors made by neglecting the molar convective fluxes are zero. The errors resulting from the simplification of the mass convective fluxes are 1-3%. It is quite a low error, and this is somehow unexpected, since the differences noticed between the diffusive and total mass flux of CO shown in figure 6.9 are locally much higher (also 25%). Since the simplified mass balance overestimates the particle conversion rate, it simulates complete conversion for t < t*, and from time on the error decreases up to zero.

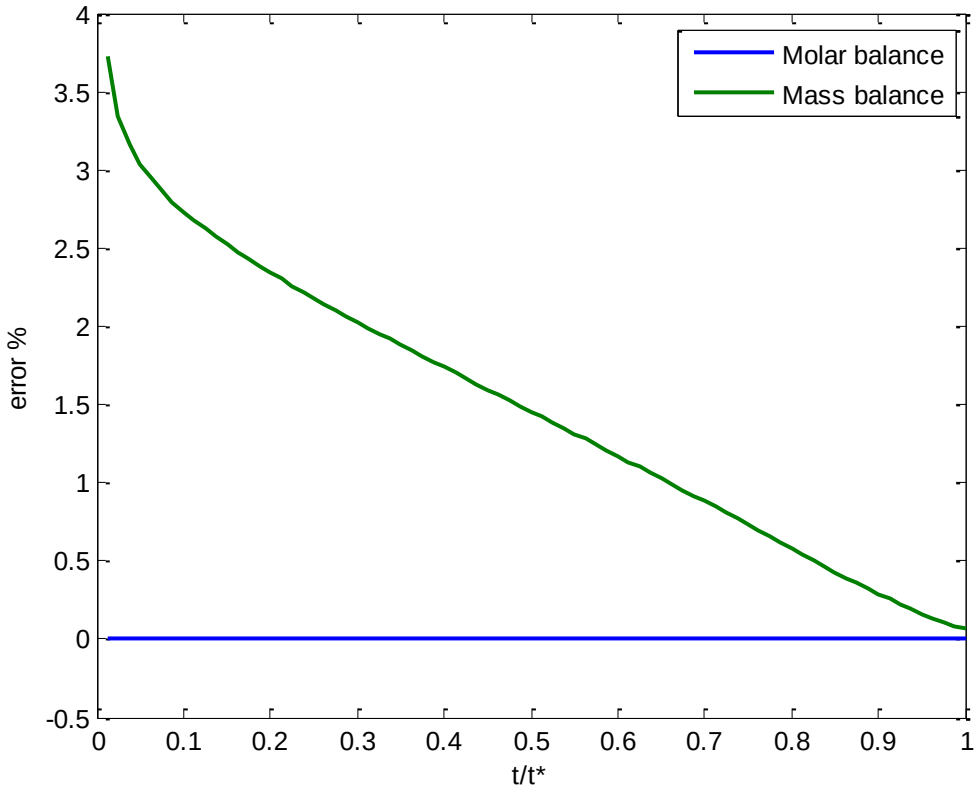

Figure 6.11: Estimated errors in the quantification of the particle conversion when the convective fluxes are neglected, solving the equations in terms of moles (blue line) and mass (green line). Case of the reduction of FeO with CO.

In this example, we conclude that the global error of neglecting natural convection is minimal. In general, for equimolar gas reactions this simplification can be more safely included when solving the molar equations. In mass balances, convection can still play an important role in the determination of the fluxes, even if in some cases the global results may not be significantly affected.

6.3.2 Gas non equimolar reaction: oxidation of zinc sulphide

The same analysis was repeated for the case of the oxidation of zinc sulphide with oxygen, to produce zinc oxide and SO_2, according to the following stoichiometry:

$$ZnS + \frac{3}{2}O_2 \rightarrow ZnO + SO_2 \qquad 6.28$$

This reaction occurs with consumption of number of gas moles (the reagent/product ratio is 1.5:1). It is highly exothermic (ΔH°_{298} = -442.09 kJ/mol) and it can be considered irreversible. Again, the simulations were carried out using the continuous model (in both mass and molar form). A large particle (1 cm diameter) was considered, initially made of pure ZnS with an apparent density of 2.1 g/cm^3, corresponding to an initial porosity of 50%. The grain model was used to express the form of the reaction rate, with the

kinetic parameters taken from the literature [8]. The reaction was simulated at atmospheric pressure, and the gas temperature outside the pellet was assumed to be 500°C. The bulk gas composition was set to 40% O_2 and 60% N_2.

Again, the continuous model was solved in molar base using equations 4.37-4.41 and in mass base using equations 4.76-4.80. No shrinking and swelling phenomena were assumed (N^S= 0, n^S= 0). No external mass and energy transfer resistances were considered. When half of the zinc sulphide in the particle is converted, the simulated radial profiles of the solid and gas species, according to both models, appear like in figure 6.12.

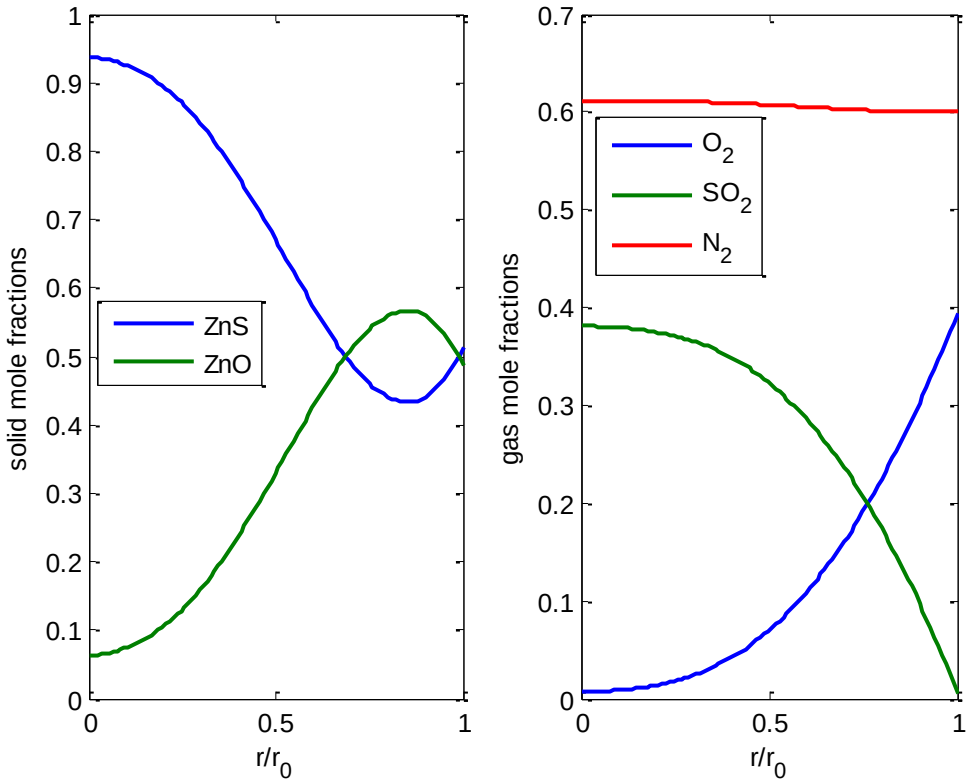

Figure 6.12: Estimated molar fractions of solid (left) and gas (right) species inside the particle when half of the zinc sulphide is converted (t = 140 s). Particle size = 1 cm.

Also in this case, the mass transfer phenomena inside the particle seem to be quite important, since high concentration gradients for the gas reagent and product are visible, and the particle does not react uniformly. In this system, energy transport is also important: very high temperature gradients are present inside the particle, as shown in figure 6.13.

The simulated temperature difference between the particle surface and centre at half conversion is about 500 K. This difference has a great influence on the reaction evolution. Temperature affects gas diffusion (through the diffusion coefficients dependency) and convection (because of the change of gas density). With respect to the reaction rate, it plays a double role: on the one hand, a higher temperature lowers the concentration of the reagent gas; on the other hand it raises the kinetic constant exponentially through the Arrhenius law. The combined effect of all these phenomena is visible in the solid composition profiles in figure 6.12, with a maximum in the local particle conversion which is not at the external particle surface,

but at an intermediate radial coordinate, where the concentration of oxygen is lower but temperature is higher than close to the surface.

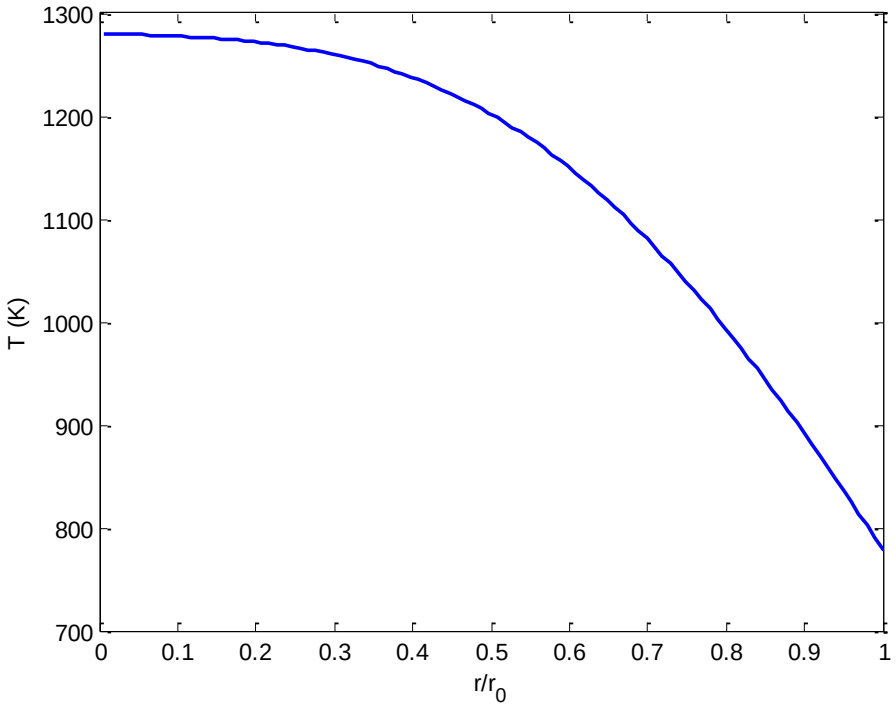

Figure 6.13: Simulated temperature profile inside the particle when half of the zinc sulphide is converted (t = 140 s). Case of the oxidation of 1 cm particles of ZnS

In this example, all three possible phenomena affecting the generation of molar convection are present: porosity change (50% to 65.5% as the solid conversion occurs), change of gas density due to temperature gradients and a high heat of reaction, and a consumption of number of moles due to the reaction stoichiometry.

The total and diffusive fluxes of reagent gas (O_2) calculated at half conversion time are shown in figure 6.14 for both molar and mass balances. As expected, the molar flux of the reagent gas deviates from its diffusion flux. In this case, molar convection is important, as well. Greater and yet moderate differences are still present for mass fluxes (right side of figure 6.14). One thing to notice is that N_{O2} is more negative than J^*_{O2}, whereas n_{O2} is less negative than j_{O2}. The reason for this is that the convective molar flux is negative, whereas the convective mass flux is positive.

This is also visible in figure 6.15, where the velocities are shown. The molar velocity v* is negative because the reaction reduces the number of moles. This means that the last sum in the right hand side of equation 6.23 is negative, and so the gradient of the flux must be negative as well. On the other hand, the mass velocity v is positive because the reaction produces mass in gas phase (1.5 moles of O_2 is equal to 48g and 1 mole of SO_2 is equal to 64g). This different behavior of the two velocities also proves that the term related to stoichiometry in equations 6.23-6.24 dominates over the term related to temperature change. As a matter of fact, the time change of total gas density (due to temperature increase) is negative, which gives a positive contribution to the gradient of the total molar flux. In spite of this fact, the total molar flux gradient is still negative.

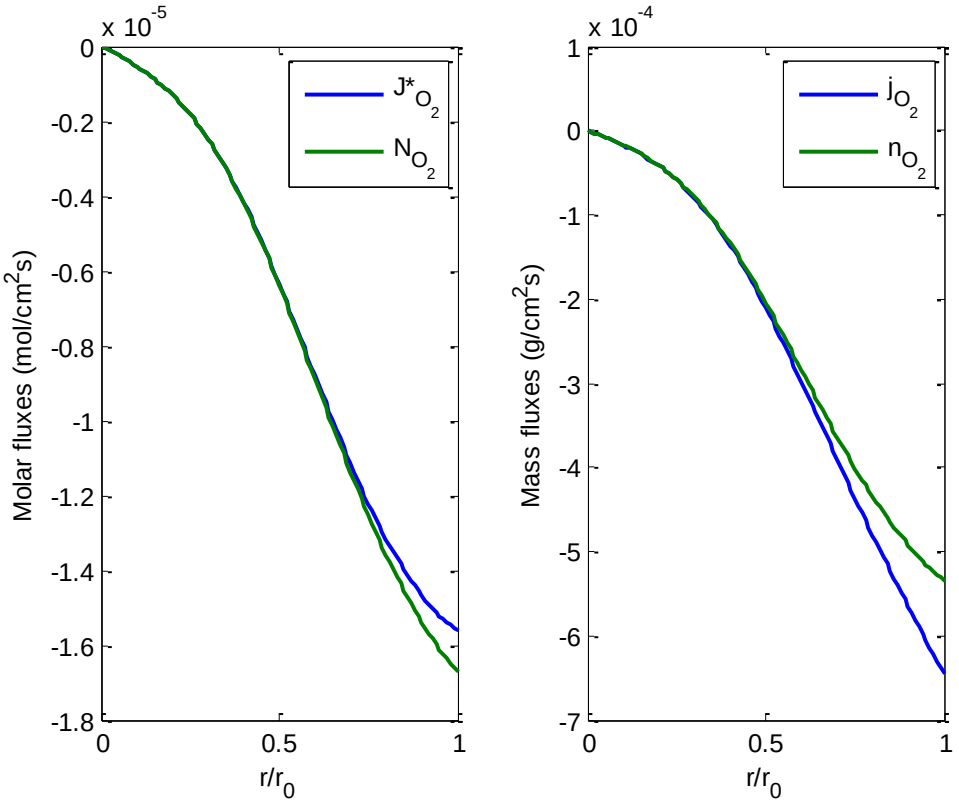

Figure 6.14: Diffusive and total (diffusive + convective) fluxes of O_2 at half conversion time inside the particle (t = 140 s). Molar fluxes (left) and mass fluxes (right). Case of the oxidation of 1 cm particles of ZnS

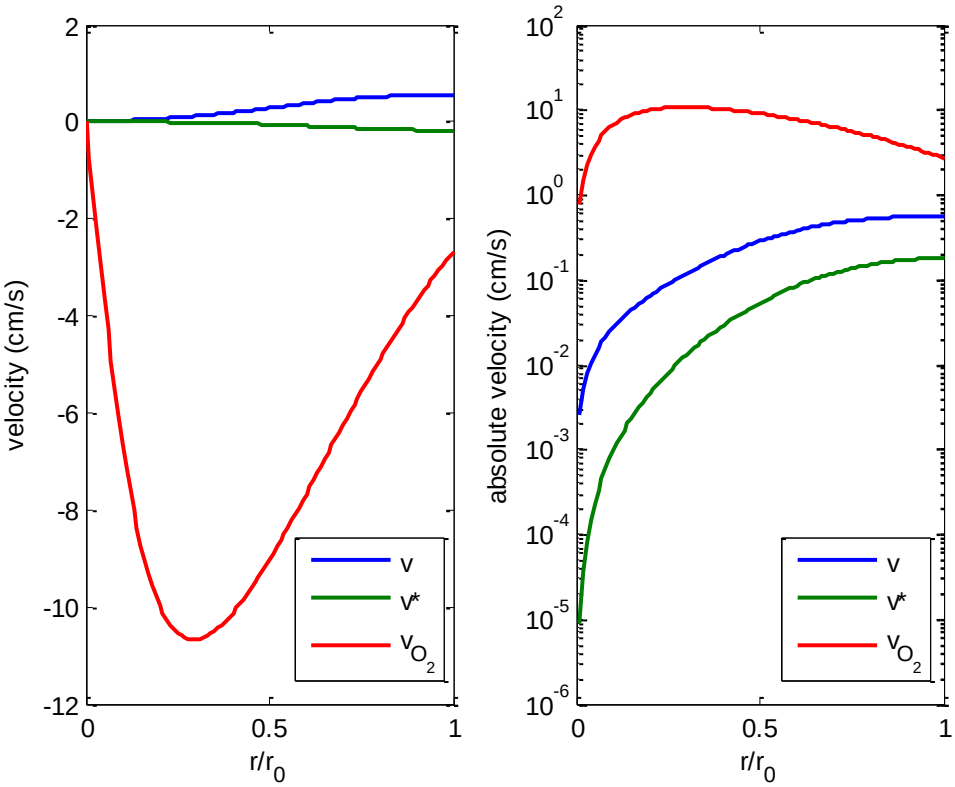

Figure 6.15: Radial profiles of the mass gas velocity (v), molar gas velocity (v*) and velocity of O_2 at t = 140 s. Results in linear scale (left), and logarithmic scale of their absolute values (right). Case of the oxidation of 1 cm particles of ZnS

For this reaction, convection seems to play a role in both mass and molar equations. An error of estimation of the particle conversion without considering the molar or mass total fluxes was calculated as before, by using equation 6.27. The resulting profiles in time are shown in figure 6.16.

Again, the simplification of the convective term has not a dramatic effect on the results: for the molar balance, the absolute error is below 2%. For the mass balance, the error can reach 7% for low conversion times. In this case it can be a good choice to include convection to have more accurate results.

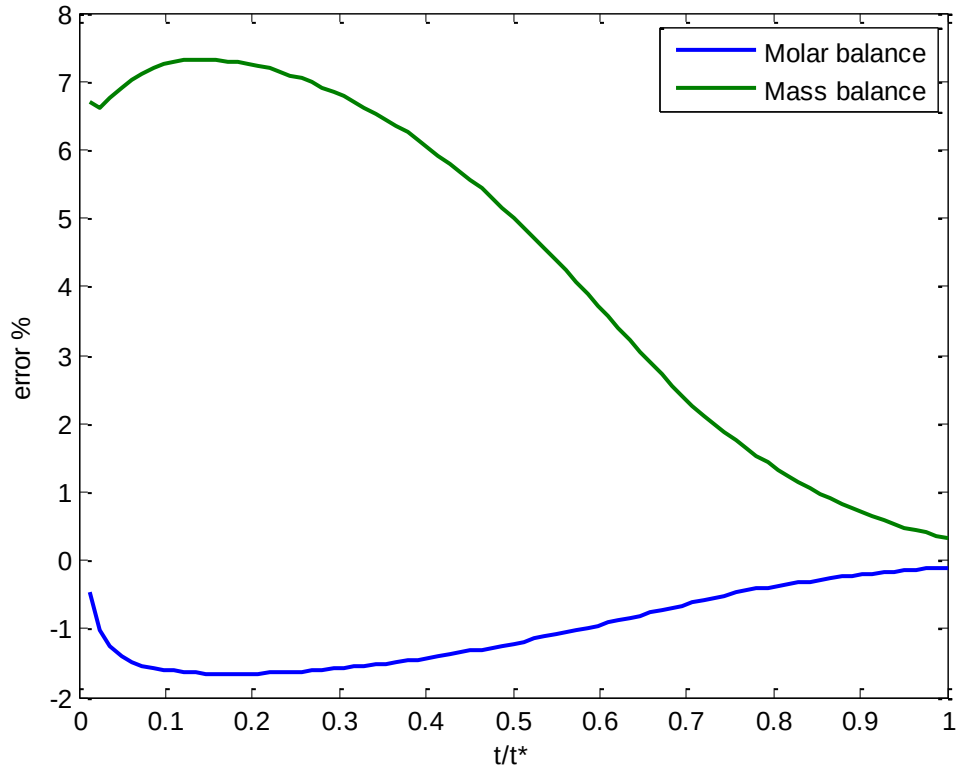

Figure 6.16: Estimated errors in the quantification of the particle conversion when the convective fluxes are neglected, solving the equations in terms of moles (blue line) and mass (green line). Case of the oxidation of 1 cm particles of ZnS.

It is interesting to notice that solving the balance in terms of moles without convection leads to an underestimation of the particle conversion, whereas solving the model in terms of mass neglecting convection leads to an overestimation. These different signs of the error values are also related to the opposite directions of v and v*.

One point that was not mentioned is that the importance of convection is related to the importance of diffusion. If the gas transport inside the particle does not play a role in the overall process, it is quite likely that convection can be neglected without losing any degree of accuracy in the calculated results. For this reason, more simulations were carried out to evaluate this issue, as shown in the next section.

6.3.3 Effect of convection in kinetic regime

In the previous examples, the conditions were set in such a way that reaction was very fast if compared to diffusion. Here, we present the results of the model where the effect of convection for kinetic regime is considered: the simulation of the oxidation of zinc sulfide (reaction 6.28) was carried out for a very small particle size (200 µm of diameter). All of the other reaction conditions were exactly the same as the previous example (bulk temperature 500°C, bulk composition 40% O_2 60% N_2, initial particle density 2.1 g/cm^3, same kinetic parameters and boundary conditions).

The change of particle size makes quite a difference in the results: first of all the heat of reaction is easily dispersed, and no temperature gradients are present inside the particle according to the continuous model (the maximum simulated temperature rise is about 0.3 °C, while in the previous case it was more than 500°C). So, the particle approaches uniform temperature in space and time. Besides this, diffusion is much faster compared to reaction, because now the gas has to be transported across a very short path to reach all the points of the porous matrix. The results of this is that the composition profiles of both gas and solid become flat along the radial coordinate, as it is shown in figure 6.17.

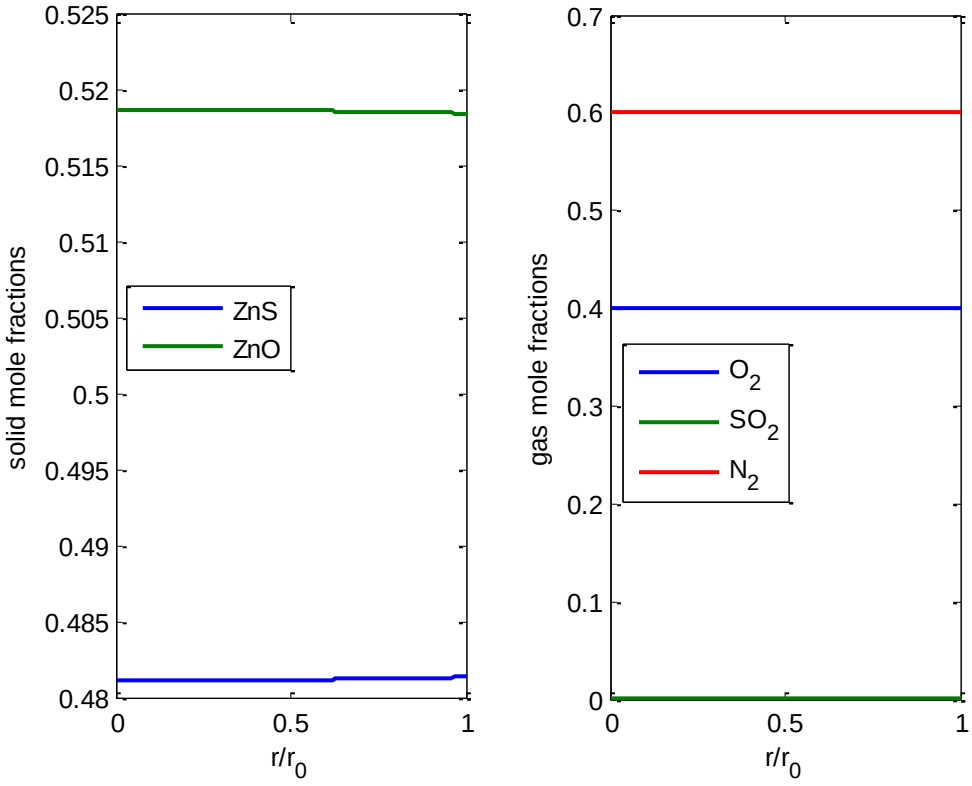

Figure 6.17: Estimated molar fractions of solid (left) and gas (right) species inside the particle when half of the zinc sulphide is converted. Particle size = 2 µm.

At these conditions, the calculated errors made by neglecting the convection term in the molar and mass balances are reported in figure 6.18. In both cases, the error is zero. In this situation, the model can be simplified without any consequence on the accuracy of results, as expected.

Comparing the results of the simulations of large particles (figure 6.18) with the errors for small particles (figure 6.16) it can be concluded that the importance of convection is not related just to the particular reaction, but also to the conditions at which the reaction is carried out.

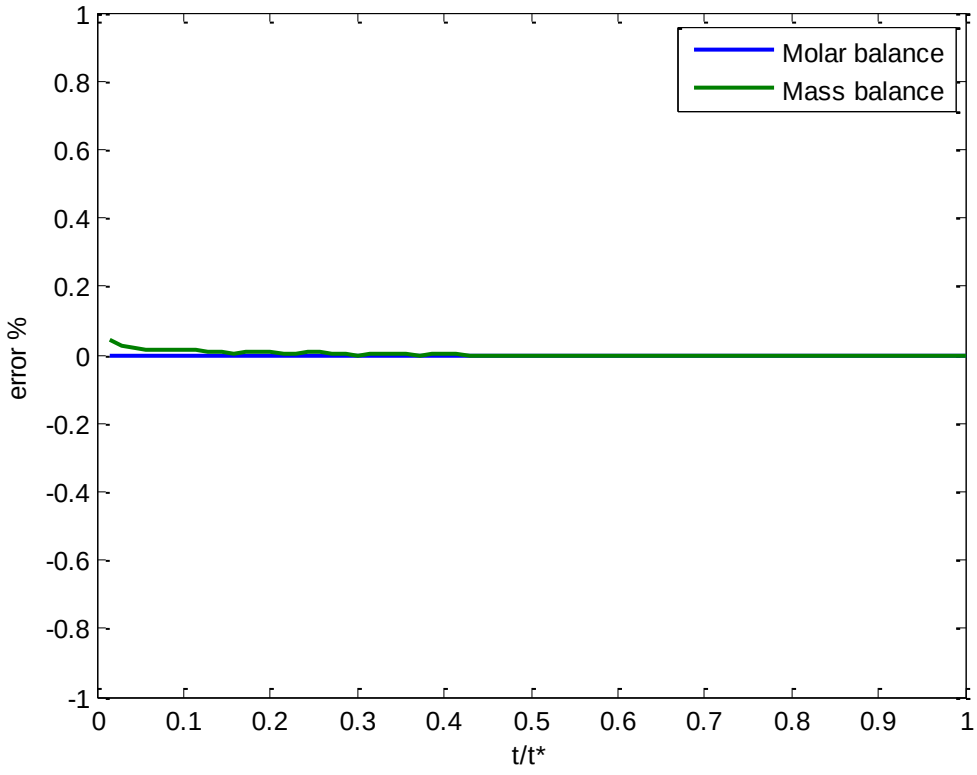

Figure 6.18: Estimated errors in the quantification of the particle conversion when the convective fluxes are neglected, solving the equations in terms of moles (blue line) and mass (green line). Case of the oxidation of 2 μm particles of ZnS.

In summary, the correct description of gas natural convection inside a reacting particle can improve the accuracy of the model if the system is controlled by inner gas transport, but at the same time, in most cases, no dramatic errors are made if convection is neglected. It was proven that the net production of moles or mass is the main factor responsible for the generation of a convective flux. The results prove that, if the no-convection simplification is applied, in many situations it can be recommendable to solve the model using the molar balances, particularly when the reaction is equimolar with respect to the gas species.

Notation

B_{ij}	Components of the inverse of Stefan-Maxwell diffusion matrix (s/cm^2)
c	Total gas concentration (mol/cm^3)
c_i^g, c_i^s	Molar concentration, of the i-th gas species, of the i-th solid species (mol/cm^3)
$\overline{c_i^s}$	Mean particle concentration of the solid i-th species (mol/cm^3)
$c_i^{g\,0}, c_i^{s\,0}$	Initial molar concentration, of the i-th gas species, of the i-th solid species (mol/cm^3)

$c_{i,bulk}$	Concentration of the i-th gas species outside the particle, in bulk phase (mol/cm^3)
c^g, c^s	Total concentration of gas phase, of solid phase (mol/cm^3)
$Đ_{ij}$	Multicomponent diffusion coefficient of i in j (cm^2/s)
D_{ij}	Components of the Stefan-Maxwell diffusion matrix (cm^2/s)
D_{im}	Diffusion coefficients of i in the gas mixture, for the molar fluxes (cm^2/s)
e	Relative error of estimation of the particle conversion neglecting gas convection
e_F	Relative error of estimation of the particle conversion with Fick's law
e_{MA}	Relative error of estimation of the particle conversion with Mixture averaged model
J_i^*	Molar diffusive flux of i (mol/cm^2/s)
k	volumetric kinetic constant (1/s)
MW_i	Molecular weight of the i-th species (g/mol)
MW^g	Molecular weight of gas phase (g/mol)
N	Number of gas species in the system
N^g	Total molar flux of the gas phase (mol/cm^2/s)
n^g	Total mass flux of the gas phase (g/cm^2/s)
P	Pressure (Pa)
r_0	Particle radius (cm)
r	Radial coordinate (cm)
s_i^g, s_i^s	Molar source term for the i-th gas species, for the i-th solid species (mol/cm^3/s)
T	Absolute temperature (K)
t	Time (s)
v_i	Velocity of the i-th species (cm/s)
v	Velocity of the gas center of mass (cm/s)
v^*	Velocity of the gas molar center of mass (cm/s)
X_i	Conversion of the i-th solid phase
$\bar{X}$	Mean particle conversion
$\bar{X}_{Fick}, \bar{X}_{MA}, \bar{X}_{SM}$	Mean particle conversion calculated with Fick, Mixture averaged, Stefan Maxwell models
$\bar{X}_{Correct}$	Mean particle conversion calculated including convection
$\bar{X}_{Simplified}$	Mean particle conversion calculated neglecting convection
x_i	Molar fraction of the i-th gas species
y_i	Mass fraction of the i-th gas species

Greek letters

ε	Porosity
Φ^2	Thiele modulus
ρ^g	Mass density of the gas phase (g/cm^3)

Chapter 7. Particle models for Chemical Looping Combustion

In the previous sections, continuous models have been studied in general, with respect to the contribution of the kinetic and intra particle mass transport phenomena. In practical applications, to achieve a reliable description of the evolution of the particle one of the key issues comes from correctly describing the influence of the particle morphology evolution (i.e. porosity field, superficial area) to the reaction and gas diffusion terms inside the balance equations. The evolution of particle morphology is often related to the particular process, and reaction conditions used, so it must be studied ad hoc. As a matter of fact, the available experimental data on the particle conversion in time can be usually explained with the same degree of accuracy by assuming different hypotheses, that need to be verified by carefully characterizing the solid particle.

In this section, this issue is discussed, by considering the application of the continuous model to chemical looping combustion processes. This has been possible thanks to the collaboration with the Technical University of Eindhoven (TU/e), in particular with the multiphase reactors research group.

7.1 Chemical Looping Combustion

Chemical looping combustion (CLC) derives from the interest in the control and treatment of emissions of gases in chemical processes. This is increasing more and more, and new sustainable technologies must be developed in order to accomplish this goal. In such a context, chemical looping combustion is a new process that can combine the need to get energy from conventional fossil fuels with the possibility of treating the produced gases in a better and more efficient way, also with respect to the coupling with CO_2 capture techniques. The main advantage of CLC is that the fuel and oxygen are never mixed up in a single gas phase: all the reactions involving oxygen actually occur via a solid oxygen carrier, which is constantly regenerated.

A general scheme of a chemical looping combustion process is shown in Figure 7.1. Two reactors are needed: in the first one, air is fluxed in a moving or fluidized bed where a metal compound is oxidized. The discharged gas is made of air, depleted of oxygen. This step is always exothermic, and provides the energy requested by the process. The oxidized solid is then moved to a second reactor, where it is in contact with the gas fuel. In this unit, the solid is reduced back to its original state and can be recycled to the first reactor. The outlet gas is generally composed of CO_2 and H_2O that can be easily separated by steam condensation, obtaining pure streams. The second step can be endothermic, with the heat of reaction that can be provided by the oxidation step. The global reaction of the whole process is the gas fuel oxidation, whereas the solid carrier is never consumed, theoretically. In synthesis, Chemical looping Combustion provides CO_2 separation in itself.

One of the main issues related to CLC is the reaction kinetics of the gas solid reactions. The oxidation step is usually quite fast, whereas the reduction can be affected by limitations. In this sense, one of the key features of CLC is the choice of the oxygen carrier, whose reactivity should be as good as possible in terms of reaction rate. At the same time its cost must not be very high. Redox activities of some metal oxides have been studied [37], the main ones being copper [38],[39],[40],[41], nickel[38],[42],[43], and manganese[44].

Also iron oxides have been proved to be quite suitable. In particular, ilmenite is a good compromise [45],[46],[13],[47],[48],[49]. Ilmenite is a mixed iron-titanium oxide ($FeTiO_3$), in which the active metal that can be oxidized is Fe, while Ti remains as inert in the form of TiO_2. In chemical looping processes, Fe^{2+} atoms in ilmenite are oxidized to Fe^{3+} to give pseudobrookite (Fe_2TiO_5), which can then be reduced again, back to ilmenite.

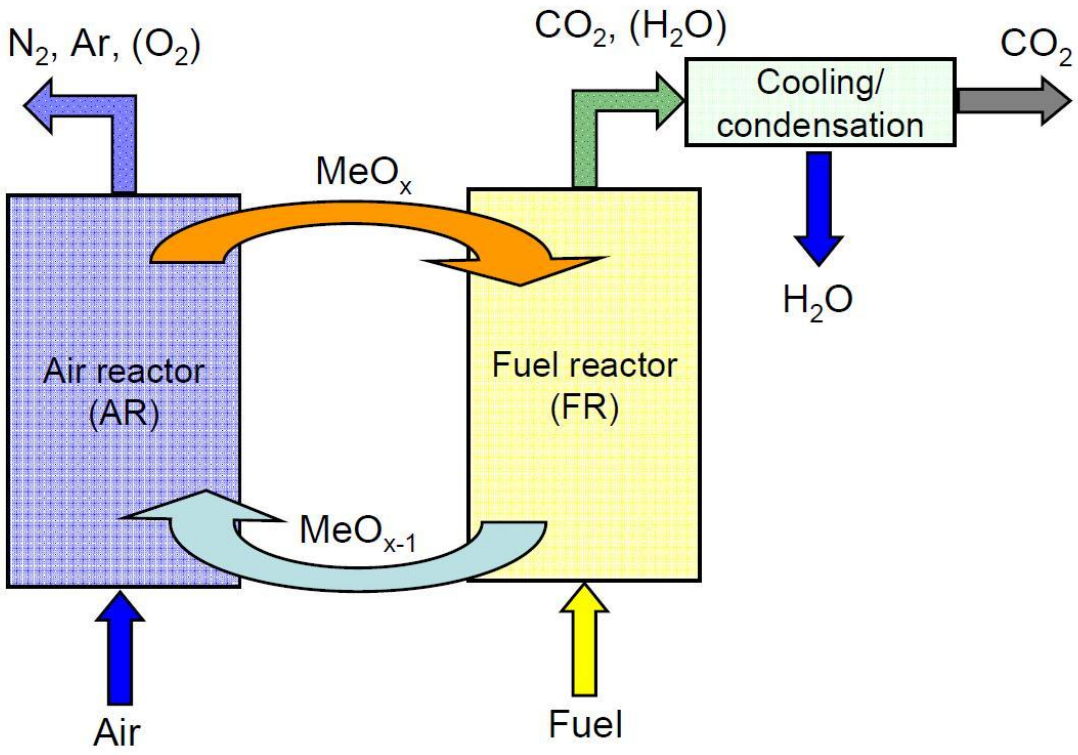

Figure 7.1: Scheme of a Chemical Looping Combustion process

The reaction system involved in chemical looping with iron oxides, using syngas as a fuel can be assumed to be the following:

$$2\,FeO + \frac{1}{2}\,O_2 \rightarrow\ Fe_2O_3 \qquad (oxydation\ step) \tag{7.1}$$

$$Fe_2O_3 + H_2 \rightarrow\ 2\,FeO + H_2O \qquad (reduction\ with\ H_2) \tag{7.2}$$

$$Fe_2O_3 + CO \rightarrow\ 2\,FeO + CO_2 \qquad (reduction\ with\ CO) \tag{7.3}$$

The sum of reactions 7.1 and 7.2 is the reaction of combustion of hydrogen, whereas the sum of 7.1 and 7.3 is the combustion of carbon monoxide:

$$H_2 + \frac{1}{2}O_2 \rightarrow H_2O \quad 7.4$$

$$CO + \frac{1}{2}O_2 \rightarrow CO_2 \quad 7.5$$

In CLC processes, the same solid pellets are involved in a high number of oxidation-reaction cycles, usually at high temperature. This may have an influence on the internal structure of the particles, that can change in time within a single cycle and along cycles.

Within CLC processes, both simple shrinking core models and continuous models are used in the literature. A shrinking-core model approach was followed by Abad et al. [13], to study the kinetics of the ilmenite-pseudobrookite system, for both oxidation and reduction steps. Noorman et al. [50] proposed a detailed model to describe Cu/CuO redox behavior in chemical looping, evaluating the contribution of internal and external mass transfer with respect to chemical reactions. Zhou et al. [51] developed a kinetic scheme for Ni/NiO CLC systems based on the grain model, and applied a continuous particle model to a fixed bed chemical looping reactor model [52].

7.2 Experimental estimation of carriers reactivity: TGA analysis

An important characteristic parameter of the solid species involved in CLC is the oxygen carrier capacity R_O, which defines the amount of oxygen that the carrier can transport due to the oxidation reduction loop, per unit of mass of oxidized sample:

$$R_O = \frac{m_{ox} - m_{red}}{m_{ox}} \quad 7.6$$

This quantity is fixed for any oxygen carrier, and it is related to the reaction stoichiometry of the single step, and also to the mass of non reacting solid phase (for instance rutile, in the case of the ilmenite-pseudobrookite system). The mass of the oxidized solid is always greater than that of the reduced one, and in general R_O should be as high as possible. At the same time, a solid conversion X can be related the mass of the solid sample $m(t)$ in any moment of the reaction. For the oxidation step it is as follows:

$$X_{ox}(t) = \frac{m(t) - m_{red}}{m_{ox} - m_{red}} \quad 7.7$$

In the same way, for the reduction step:

$$X_{red}(t) = \frac{m_{ox} - m(t)}{m_{ox} - m_{red}} \qquad 7.8$$

For a sample made of a single spherical particle, $m(t)$ can be calculated by the continuous model by considering the integrals in space of the solid species concentrations. With reference to the solution of the set of equations 4.37-4.41, the particle mass is:

$$m(t) = \sum_{j=1}^{NS} \left(MW_j \cdot \int_0^{r_0} 4\pi r^2 c_j^s(r,t) dr \right) \qquad 7.9$$

Consistently, m_{ox} and m_{red} can result from equation 7.9 for zero and infinite reaction times of the reduction step, respectively. If the system is made of more particles, all reacting in the same way (the gas composition outside each particle is the same), the calculated conversion of the group of particles is the same as the one calculated for a single particle.

This way of defining conversion is quite useful, because $m(t)$ can also be easily measured experimentally, by performing the gas solid reactions in thermo gravimetric (TGA) setups. Thermo gravimetric analysis is a technique that involves the accurate measurement of the weight of a sample, changing in time, corresponding to an assigned temperature profile. In this way, physical and or chemical modifications of the sample can be detected and quantified. The experimental setup is made of a balance, connected to a crucible where the sample is placed, which is inside a programmable furnace where the desired temperature is set. In many setups, the TGA apparatus can also be used as a reactor, with a gas being constantly fed into the furnace and reacting with the sample on the balance. In this sense the loss or gain in weight of the sample in time can be related to the kinetics of a chemical reaction.

In order to study chemical looping processes, TGA is quite useful, because the same sample of oxygen carrier can be used to evaluate the oxidation and reduction steps, by alternately feeding air and fuel to the balance where the carrier is placed. By knowing the weight of the fully reduced and fully oxidized sample, the conversions of equation 7.7 and 7.8 can then be measured. So TGA provides global quantitative data about the solid particle conversion, that can be easily compared with the results of a particle model.

Figure 7.2 shows an example of experimental data obtained by the laboratories of Tu\E by reducing particles of pseudobrookite (Fe_2TiO_5). A sample of about 100 mg of small particles (about 200 µm of diameter) was placed on the thermo balance crucible. In this example, CO is used as a reducing agent, and in all three cases the fed gas is composed of 15% CO and 20% CO_2 in nitrogen. A quite high gas flow rate was provided (about 500 mL/min) in order to avoid external mass transfer limitations as much as possible. The profiles show the experimental particles conversion at three fixed temperatures (600°C, 700°C and 800°C) and atmospheric pressure. The conversion profiles are the result of the reduction of iron oxide present in the particle, according to reaction 7.3.

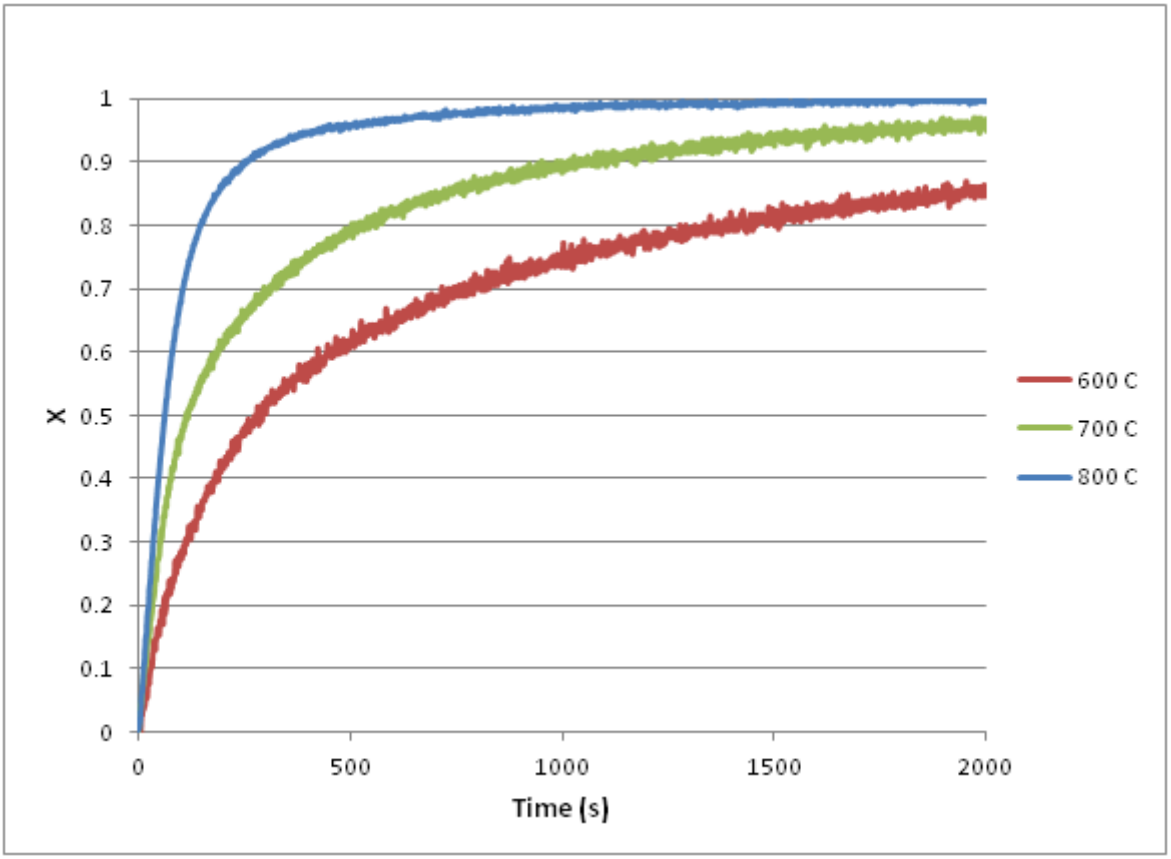

Figure 7.2: Experimental conversion of particles of pseudobrookite (200 µm diameter) measured by TGA at 600, 700 and 800°C. Composition of the reducing gas: 15% CO, 20% CO_2, 65% N_2

The experimental data show a change in the apparent reaction rate at high conversions, particularly sharp at 800°C, where a neat change of the slope of the conversion profile can be observed. These results are quite useful, but they also represent a very general description of the behavior of the solid particles.

Different particle models were used to reproduce the experimental conversion profiles obtained with TGA; in particular data from reduction of pseudobrookite (Fe_2TiO_5) to ilmenite ($FeTiO_3$) were considered. The model approaches used, and their results, are reported in the following subsections.

7.3 Application of the Shrinking Core Model

A common approach to simulate gas solid reactions in CLC systems is using Shrinking Core Model. This was widely discussed in section 2, together with its advantages and disadvantages with respect to more detailed approaches. In general, SCM can be a desired choice, particularly because it is very easy to couple with a reactor model. It is not assured, though, that it can be able to reliably reproduce any experimental data, because the core-shell structure assumptions are not always consistent with the real evolution of the particle.

In this case, SCM was used in an attempt to describe the conversion of Fe_2TiO_5 to $FeTiO_3$ by reduction with carbon monoxide. The experimental data used are related to TGA tests on small particles (100 mg of pseudobrookite particles with 200 µm of diameter, with a particle apparent density of 4.25 g/cm^3). Four tests were considered, the first three being the same previously reported in Figure 7.2. A fourth run was also included, in which the gas composition was different. The complete list of experimental conditions is shown in Table 7.1. At the beginning of the tests, a temperature ramp was set, while inert gas (N_2) was sent in the reactor. After the final temperature was reached, the feed was switched to the reducing gas.

Table 7.1: Experimental conditions for the TGA tests on reduction of Fe_2TiO_5. For all tests CO_2 is 20% and N_2 is the remaining fraction.

# test	Temperature [°C]	CO [%]
1	600	15
2	700	15
3	800	15
4	800	30

The data were simulated assuming that all of the particles react in the same way, and there is no effect of transport of gas between them. This is an important approximation, that was implied considering that the fed gas flow rate was quite high (500 mL/min) and the amount of particles in the crucible created a quite thin, coarse layer. In this case, the sample conversion is equivalent to the single particle conversion.

A single reaction step was first considered (in the form of equation 7.3). The equilibrium is totally shifted to the reaction products, so it can be assumed to be irreversible. In this case, the particle conversion $X_{red}(t)$ can be calculated according to the SCM equation (2.39), considering only kinetics and internal mass transfer resistances, and applying the correct stoichiometry, as follows:

$$X_{red}(t) = \frac{3}{c^0_{Fe2O3}} \cdot \frac{c_{CO,bulk}}{\frac{r_0}{k'}\left(1 - X_{red}(t)\right)^{-2/3} + \frac{r_0^2}{D_{CO}}\left(\left(1 - X_{red}(t)\right)^{-1/3} - 1\right)} \qquad 7.10$$

Where $c_{CO,bulk}$ is calculated by knowing temperature and pressure of the gas and the fraction of CO fed to the reactor, while c^0_{Fe2O3} is calculated by the initial density of the particles, and r_0 is known from the mean particle size. The equation can be solved once the parameters k' and D_{CO} are expressed. Also, k' depends on temperature through the Arrhenius law (equation 4.54) through the activation energy (Ea) and preexponential factor (A). This makes a total of three parameters to be identified.

These parameters were determined so that the results of the model were as close as possible to the experimental data. The objective function was defined based on the sum of the square errors, and it was minimized, thus finding the optimum values of A, Ea. Also D_{CO} was considered as a fitting parameter.

The results of the final simulations are shown in Figure 7.3.

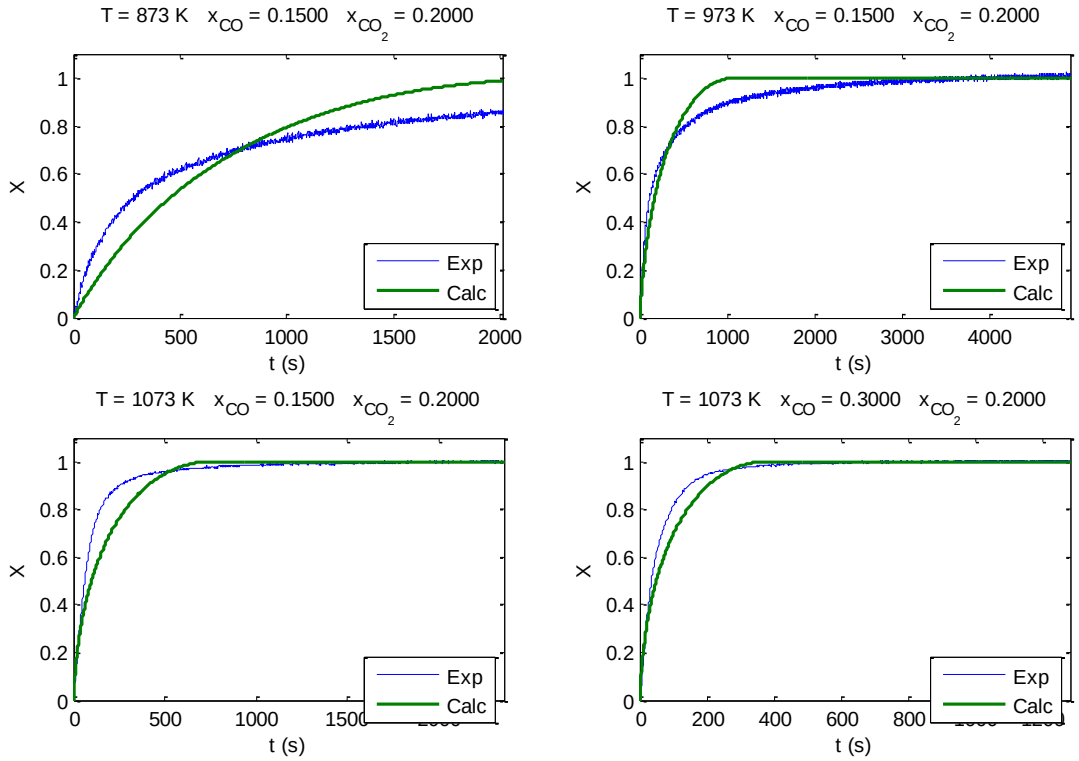

Figure 7.3: Comparison between experimental data and results of the SCM with one interface (single reaction), for the reduction of pseudobrookite to ilmenite with CO.

It can be noticed that the single interface Shrinking Core Model is not able to reasonably approximate the experimental results. In particular, the simulated global conversion rate is too high at high conversions. On the other hand, the model underestimates the conversion in the first stages of the reaction.

A second fit was made by using a two-interface Shrinking Core Model, assuming that the reduction of Fe2O3 to Fe occurs via an intermediate iron oxide, magnetite (Fe3O4). The reaction scheme of equation 7.3 was then modified as follows:

$$Fe_2O_3 + \frac{1}{3}CO \rightarrow \frac{2}{3}Fe_3O_4 + \frac{1}{3}CO_2 \qquad 7.11$$

$$Fe_3O_4 + CO \rightarrow 3\,FeO + CO_2 \qquad 7.12$$

The model of equation 2.93-2.94 and 2.111-2.227 was adapted to this scheme of reactions, obtaining the time profile of concentration of Hematite, Magnetite and Wustite in the particle. Then the global particle conversion was calculated through equation 7.8. Six parameters were identified for this model via a least square fitting of the experimental results: they are the pre exponential factors and activation energies of the two reactions (7.11 and 7.12) and the effective diffusion coefficient of CO in the magnetite and wustite layer.

The results of this second approximation are shown in Figure 7.4.

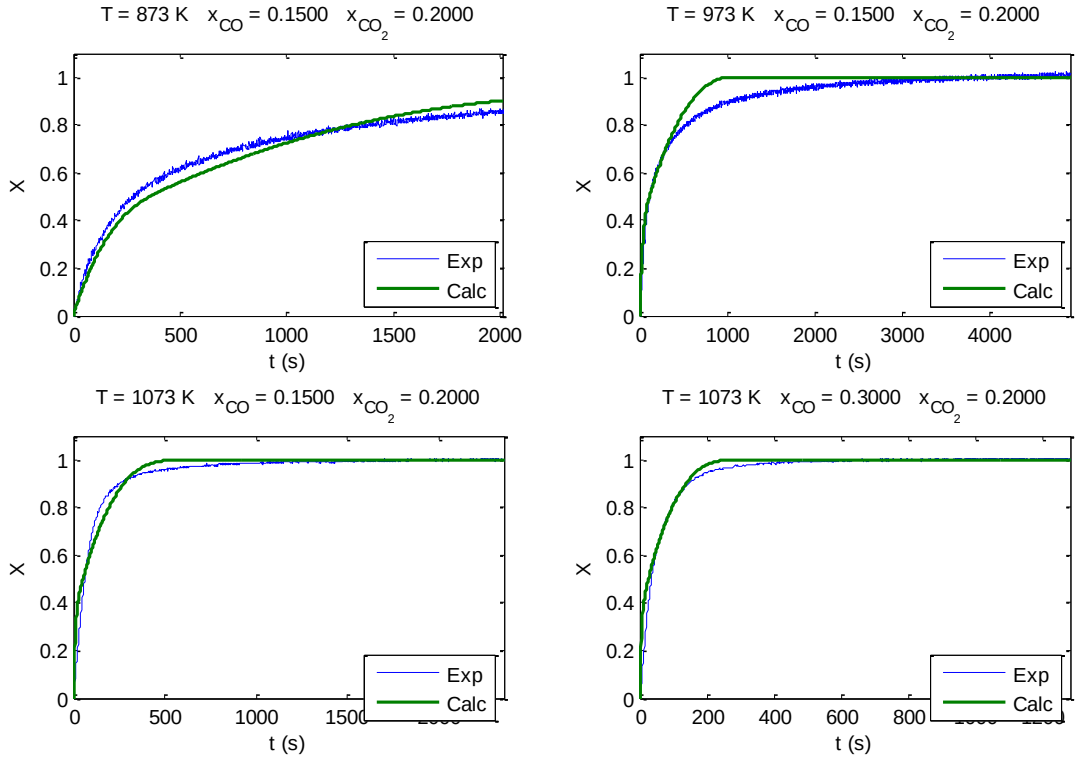

Figure 7.4: Comparison between experimental data and results of the SCM with two interfaces, for the reduction of pseudobrookite to ilmenite with CO.

Again, the results of the Shrinking Core Model are not completely satisfactory, particularly if the same set of parameters are required to apply to all the experimental data. Even doubling the number of parameters is not sufficient to accurately describe the available data. Better fitting results can be achieved by different sets of parameters for different conditions, but that is unacceptable. The results of the dual interface model show an early bending of the conversion profiles (quite visible for the test at 600°C). This tries to emulate a first faster step, followed by a slowdown in the global conversion. The model interprets this phenomenon by simulating a fast reaction of hematite to magnetite (7.11), followed by a slower reaction to wustite (7.12). When all of the Fe_2O_3 is consumed, the calculated profile bends. The difficulties appear to concentrate on the second step, which clearly cannot be described by a core shell approach. Again, the apparent reaction rate is too fast for high conversions.

7.4 Modified grain model

The same experimental data presented earlier were approximated using the continuous model. In particular, the set of equation 4.37-4.41 was implemented, assuming no particle size change (N^S = 0). The rigorous Stephan-Maxwell model was used to describe multicomponent diffusion (equations 5.42-5.47), with effective diffusion coefficients calculated as a function of the local porosity (equation 5.109). The

particle local porosity was calculated using equation 4.45. Details about the numerical implementation can be found in the appendices. The reaction rate in the source terms was first expressed by using the grain model in its simple form (equation 4.71), with a linear dependency on the concentration of gas reagent (equation 4.55, with β = 1). A single reaction step in the form of equation 7.3 was considered for the first calculation. With all of these assumptions, the equation of the reaction rate becomes as follows:

$$R = A \cdot \exp\left(-\frac{Ea}{R_g T}\right) \cdot c_{CO}^{g} \cdot (1 - X)^{2/3} \qquad 7.13$$

In this formulation, only two parameters are needed to fully characterize the model: the preexponential factor (A) and activation energy (Ea) of the reaction, whereas the effective diffusion coefficients were not fitted, differently from the SCM case presented earlier, but were calculated as already mentioned. Once again, these were determined by doing a least squares regression of the experimental data, by solving the model, calculating the estimated global conversion with equations 7.8-7.9 for each time corresponding to one experimental point, and finally calculating and minimizing the objective function by changing A and Ea.

The comparison of the data with the model results using the optimum values of the parameters can be seen in Figure 7.5. Also in this case, the model results are not very good. Curiously, comparing the results of Figure 7.5 with those obtained with the Shrinking Core Model and single reaction step (Figure 7.3), we can conclude that they are almost identical. So no improvement is achieved by using a more rigorous approach in this case. The reason for this is that in the simulated conditions, the reaction is controlled by kinetics (this is mainly due to the small particle size). It will be proven in the following section (§8) that in such a situation, the mathematical results of the grain model and SCM become the same.

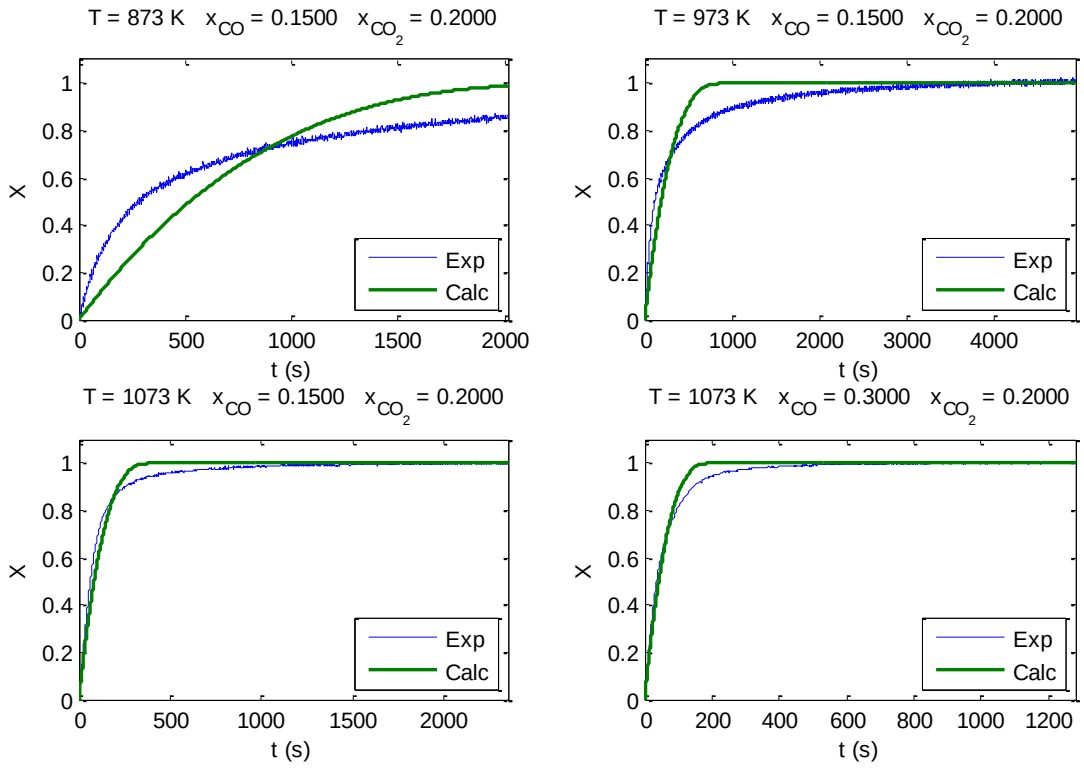

Figure 7.5: Comparison between experimental data and results of the CM using the grain model with single reaction step, for the reduction of pseudobrookite to ilmenite with CO.

So a different formulation for the continuous model must be expressed to better describe the data. The key issue is to be able to represent the reaction slowdown at high conversion degrees. One possible explanation of this phenomenon could be the restructuring of the solid matrix during the reaction, leading to a decrease of the available surface of solid reagent which is faster than that represented by the shrinking spherical surface considered by the grain model. As already pointed out in section §4, this evolution of the reagent solid surface with conversion is expressed by the function f(X) in equation 4.52.

For this reason, the shape of f(X) was changed in the continuous model. The grain model was replaced by its generalized form, also called the traditional model, where the 2/3 exponent characteristic of the spherical shape of the grains is replaced by an empirical value (equation 4.72). Keeping the single reaction step approach, the form of the reaction rate becomes as follows:

$$R = A \cdot \exp\left(-\frac{Ea}{R_g T}\right) \cdot c_{CO}^{g} \cdot (1 - X)^{\alpha} \qquad 7.14$$

This formulation of the continuous model also adds a parameter to the system, which is the so called sintering factor α. A new fitting was carried out on this model, and the final results are shown in Figure 7.6. This time, the agreement between calculated and experimental data is quite good for all the tests. The estimated parameters are reported in Table 7.2.

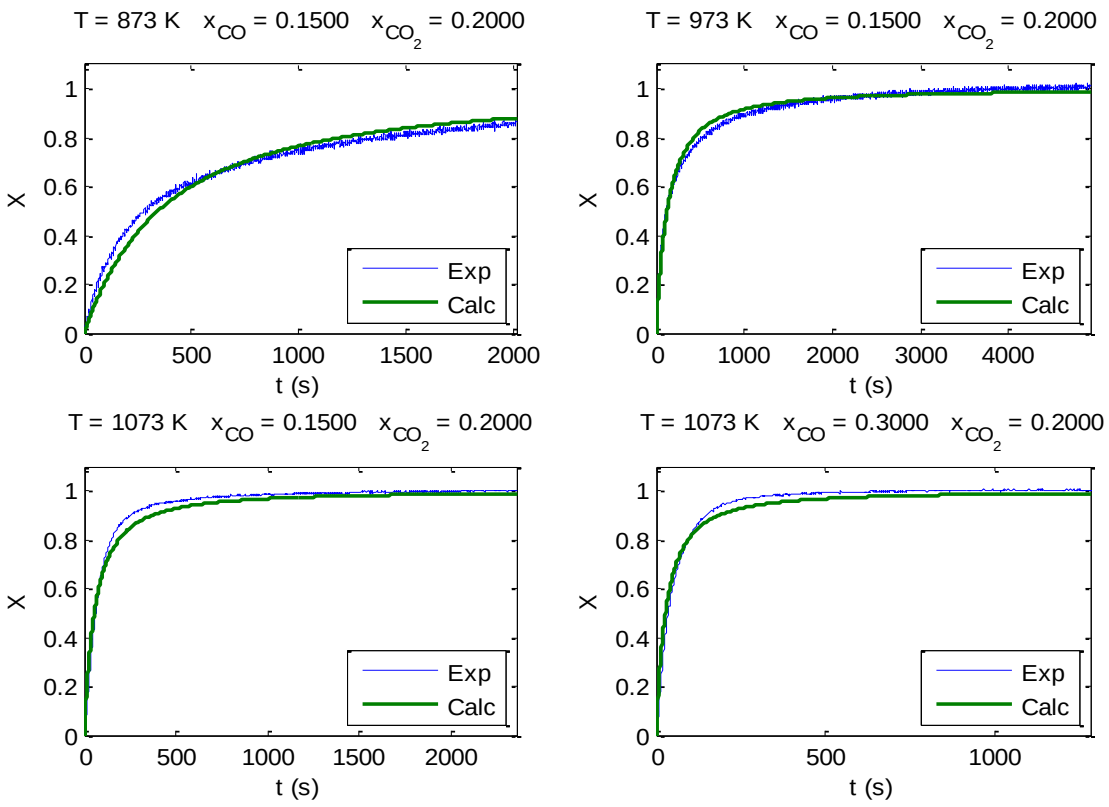

Figure 7.6: Comparison between experimental data and results of the CM using the modified model with single reaction step and fitted sintering exponent, for the reduction of pseudobrookite to ilmenite with CO.

In analogy with what was previously done with the Shrinking Core Model, a final simulation was carried out assuming two irreversible reaction steps instead of one, considering the kinetic scheme 7.11-7.12 (reduction via magnetite intermediate). With two reaction steps, using the modified grain model, the expressions for the reaction rates become as follows:

$$R_1 = A_1 \cdot \exp\left(-\frac{Ea_1}{R_g T}\right) \cdot c_{CO}^{g} \cdot (1 - X_{Fe2O3})^{\alpha_1} \qquad 7.15$$

$$R_2 = A_2 \cdot \exp\left(-\frac{Ea_2}{R_g T}\right) \cdot c_{CO}^{g} \cdot (1 - X_{Fe3O4})^{\alpha_2} \qquad 7.16$$

In this case, the number of parameters is twice that resulting from the single reaction approach (six instead that three). The quality of the fitting is expected to be naturally better. This is confirmed by the final results of the simulations, which are shown in Figure 7.7.

The agreement between the experimental data and model results are improved, particularly for the test at 600°C and for very high conversions for the tests at 800°C.

Table 7.2 reports the calculated values for the parameters for the three versions of the continuous model used to simulate the data. The right hand side column also reports the values of the minimum of the sum of square errors resulting from the three different fittings. Their relative difference can give an averall idea of the different qualities of the regressions, with the largest improvement determined by the introduction of the sintering parameter α.

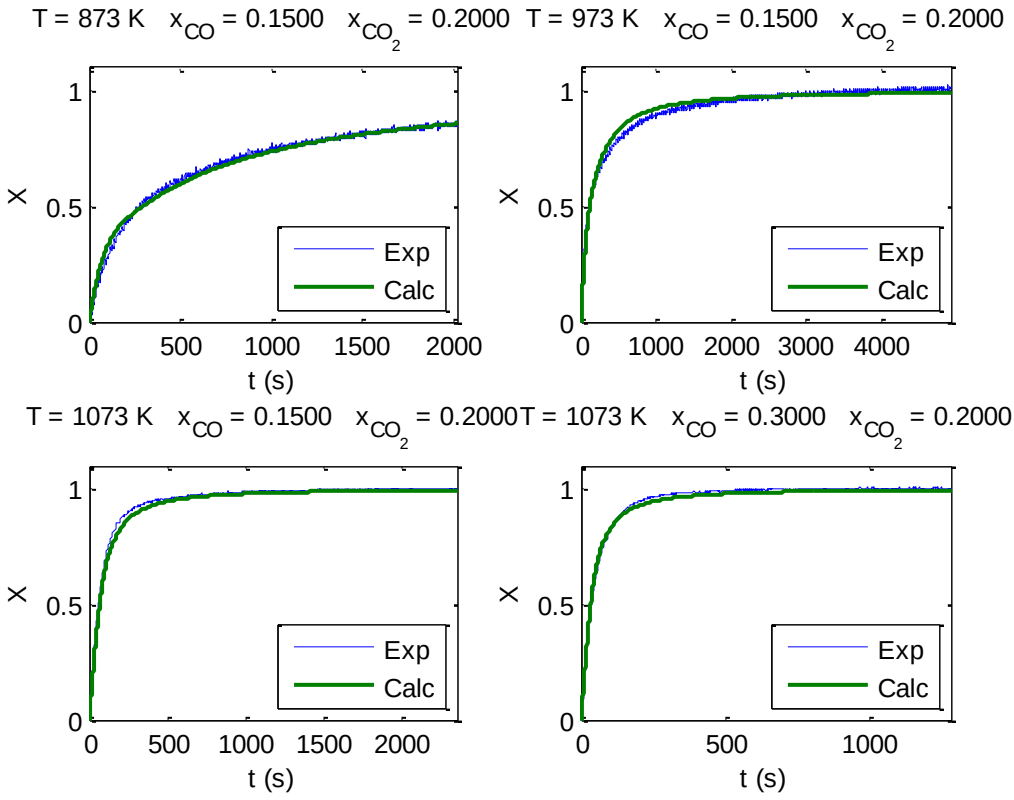

Figure 7.7: Comparison between experimental data and results of the CM using the modified model with two reaction steps and fitted sintering exponents, for the reduction of pseudobrookite to ilmenite with CO.

Table 7.2: Values of the parameters fitted for the continuous model for the three formulations considered

Model	A (1/s)		Ea (J/mol)		α		Figure	SSE
Grain Model 1 reaction	3.61e5		80029		2/3		Figure 7.5	7.17
Modified Grain Model 1 reaction	7.95e5		79934		1.76		Figure 7.6	2.49
Modified Grain model 2 reactions	A_1	1.47e3	Ea_1	29100	α_1	0.74	Figure 7.7	1.75
	A_2	3.14e6	Ea_2	97610	α_2	1.65		

When a single reaction is considered, the estimated activation energy is about 80 kJ/mol. The optimum value of α is 1.76 for the single reaction. As expected, it is higher than one, which corresponds to the situation when the solid reagent surface decrease is enhanced by the physical merging of grains and pores that can derive from sintering.

In conclusion, with only three parameters the continuous model can be able to describe the experimental data in a satisfactory way, much better than the shrinking core model with six parameters.

7.5 Effect of pore size distribution

In the previous section, the experimental data of reduction of iron oxides were interpreted with a continuous model, where the key issue was the description of the solid reactant surface available for the reaction, which has an effect on the estimation of the reaction rate. The effect of the change of the solid morphology can in fact have an influence on the kinetic part of the model, as already seen.

This is a possible explanation of the behavior of the experimental evidences, which is all based on the kinetic effects. Another possible reason for the decrease of the conversion rate at high conversions could be related to a change of the controlling regime, from kinetic to diffusive. At the same time, the size of the particles investigated is too small to actually lead to an influence of diffusion in the particle macro pores. Still, it could be possible, that, even if the gas can reach all the points of the solid particle quite easily through macro pores, for any radial coordinates there are lumps of solid reagent that are less easily accessible than others. This can be related to the presence of meso and micro pores with different sizes.

When the reacting gas is transported through sufficiently narrow pores, Knudsen diffusion becomes limiting with respect to molecular diffusion. This mechanism of diffusion is actually related to the pore size, which means that larger pores will transport the gas with higher fluxes than smaller pores. Correspondingly, the portions of solid where larger pores are present will react faster. This kind of diffusion

resistance occurs on a different scale than that of the radial transport of gas from the outside to the core of the particle. In fact, large or small micro pores can be present at any radial coordinate. If the transport through the macro pores is fast but the transport through micro pores is not, in comparison with the rate of reaction, the particle can still be converted homogeneously along the radial coordinate, but the reaction rate will decrease in time, as soon as the local portions of solid more easily accessed are consumed, and only those with smaller micro pores are remaining.

The effect of this decrease depends on the pore size distribution of the particle, that is on the fractions of solid occupied by any pore size. These can be actually measured for a porous solid, thanks to techniques based on gas adsorption quantification. This information can thus be translated into the quantification of the different diffusion resistances that can be present inside the pellets, with a model.

The continuous model presented so far is not able to represent this sub scale. If a single pore size is assumed, a single value of gas diffusivity is considered inside the particle, and the controlling regime is identified by the ratio between that diffusivity and the kinetic constant. So no important change of regime can be simulated. The introduction of multiple pore sizes also implies the introduction of a second coordinate inside the particle, because all the pore sizes will be present at any radial coordinate. One possible way to modify the model to account for this scale without significantly increasing its complexity is subdividing the single solid phase into a number of classes. Each class represents a fraction of the solid species crossed by a particular pore size. The initial concentration of each class is given by the pore size distribution of the particle, which can be assumed to be radially homogeneous if the particle is isotropic. This corresponds to assuming that small and large pores are present at any radial position.

So, instead of solving a single balance for the single i-th solid species, a balance will be solved for each j-th class and i-th species. This equation can be expressed as follows:

$$\frac{\partial c_{i,j}^{S}}{\partial t} = s_{i,j}^{S} \qquad i = 1,2 \dots NS, \quad j = 1,2 \dots nClass \tag{7.17}$$

Equation 7.17 was obtained by applying this approach to equation 4.43. The model has thus been transformed into a population balance equations system, discretized on single classes. $c_{i,j}^{S}$ is in fact the concentration of the i-th solid species having pores with j-th size. This is still a function of time, and particle radial coordinate. The total concentration of i at any time and position within the particle can easily be calculated by summing all the classes of $c_{i,j}^{S}$, as follows:

$$c_i^S(r,t) = \sum_{j=1}^{nClass} c_{i,j}^S(r,t) \tag{7.18}$$

In the formulation of equation 7.17, the PBE is written in a discrete form: instead of solving a single PDE in time and two dimensions (r and pore size d), this is transformed in a system of PDEs in time and one dimension (r). In this form the model can be more easily implemented numerically; also, a limited amount of classes should be employed to avoid an excessive increase of computational cost.

In equation 7.17, the source term $s_{i,j}^{S}$ also depends on the particular class j. This term must account for the diffusive resistance of gas transport into the pores with a specific size, so it not a purely kinetic term. In

section 4 we saw that the complete form of the grain model (equation 4.70) uses a similar approach. According to that, the reaction rate depends not only on the kinetic constant, and concentration of reagent gas, but also on the effective diffusion coefficient of gas into the grain.

This approach can be applied to the PBE formulation. The solid matrix can be ideally represented as locally made of grains, each one crossed by micro pores with a fixed size. The fraction of grains with a j-th pore size is again given by the pore size distribution. The reaction rate of the j-th solid lump (i.e. grain) can then be expressed with the grain model, with the intra grain diffusion coefficient of the gas calculated as a function of the characteristic dimension of the pores of the j-th class. By doing this, and considering a single irreversible reaction, the source term $s_{i,j}^{S}$ can be expressed as follows:

$$s_{i,j}^{S} = \nu_i^S \frac{3}{r_g} \cdot \frac{c_{react}^{g}}{\frac{1}{k'} \cdot \left(\frac{c_{i,j}^{S}}{c_i^{S0} \cdot f_j}\right)^{-2/3} + \frac{|\nu_{react}^{g}| r_g}{D_j^K} \cdot \left[\left(\frac{c_{i,j}^{S}}{c_i^{S0} \cdot f_j}\right)^{-1/3} - 1\right]} \qquad 7.19$$

Where ν_i^S is the stoichiometric coefficient of the solid i, ν_{react}^{g} is the stoichiometric coefficient of the reagent gas, r_g is the grain radius, c_i^{S0} is the initial concentration of the solid i, f_j is the fraction of solid occupied by the j-th class of pores (obtained by the pre size distribution), and c_{react}^{g} is the local concentration of the reagent gas in the macropores, outside the grains.

In equation 7.19, D_j^K is the Knudsen diffusion coefficient of the reagent gas into the pores of the j-th class, and can be expressed, according to the single pore model, as follows:

$$D_j^K = 4850 \cdot d_j \sqrt{\frac{T}{MW_{react}}} \qquad 7.20$$

Where d_j is the size of the pores in the j-th class, T is the temperature and MW_{react} is the molecular weight of the reagent gas.

The conservation equation for each gas species remains a single one, in the form of 4.37, where the source term is calculated on the sum of contributions of reaction rates in all the solid lumps. So it becomes, for the i-th gas species:

$$\frac{\partial \varepsilon c_i^g}{\partial t} = -\frac{1}{r^2}\frac{\partial}{\partial r}\left(r^2\left(x_i^g N^g + J_i^*\right)\right) + \nu_i^g \cdot \sum_{j=1}^{nClass} \frac{3}{r_g} \cdot \frac{c_{react}^{g}}{\frac{1}{k'} \cdot \left(\frac{c_{i,j}^{S}}{c_i^{S0} \cdot f_j}\right)^{-2/3} + \frac{|\nu_{react}^{g}| r_g}{D_j^K} \cdot \left[\left(\frac{c_{i,j}^{S}}{c_i^{S0} \cdot f_j}\right)^{-1/3} - 1\right]} \qquad 7.21$$

Note that one equations will be solved for the reagent gas (i = react). Analogously, the total gas concentration balance becomes as follows:

$$\frac{\partial \varepsilon c^g}{\partial t} = -\frac{1}{r^2}\frac{\partial}{\partial r}(r^2 N^g) + \sum_{i=1}^{NG} \nu_i^g \sum_{j=1}^{nClass} \frac{3}{r_g} \cdot \frac{c_{react}^{g}}{\frac{1}{k'} \cdot \left(\frac{c_{i,j}^{S}}{c_i^{S0} \cdot f_j}\right)^{-2/3} + \frac{|\nu_{react}^{g}| r_g}{D_j^K} \cdot \left[\left(\frac{c_{i,j}^{S}}{c_i^{S0} \cdot f_j}\right)^{-1/3} - 1\right]} \qquad 7.22$$

And the energy balance:

$$(cCp)\frac{\partial T}{\partial t} = -\frac{1}{r^2}\frac{\partial}{\partial r}\left(r^2\left(Cp^g N^g - k_t\frac{\partial T}{\partial r}\right)\right) - \Delta H^R \sum_{j=1}^{nClass}\frac{3}{r_g}\cdot\frac{c^g_{react}}{\frac{1}{k'}\cdot\left(\frac{c^S_{i,j}}{c^{S0}_i\cdot f_j}\right)^{-2/3} + \frac{|\nu^g_{react}|r_g}{D^K_j}\cdot\left[\left(\frac{c^S_{i,j}}{c^{S0}_i\cdot f_j}\right)^{-1/3} - 1\right]} \quad 7.23$$

The system is complete once the equation for the porosity is added:

$$\frac{\partial \varepsilon}{\partial t} = -\sum_{i=1}^{NS}\frac{MW_i}{\rho_i}\nu^S_i \sum_{j=1}^{nClass}\frac{3}{r_g}\cdot\frac{c^g_{react}}{\frac{1}{k'}\cdot\left(\frac{c^S_{i,j}}{c^{S0}_i\cdot f_j}\right)^{-2/3} + \frac{|\nu^g_{react}|r_g}{D^K_j}\cdot\left[\left(\frac{c^S_{i,j}}{c^{S0}_i\cdot f_j}\right)^{-1/3} - 1\right]} \quad 7.24$$

The model described by equations 7.17, 7.21-7.24 is made of NG + NS*nClass + 3 partial differential equations. They can be solved with the boundary conditions of equation 4.47 and 4.49. The initial conditions of equation 4.50 must be slightly modified to account for the initial concentration of each solid class for each solid species, as follows:

$$for\ t = 0 \qquad \begin{aligned} c^g_i &= c^{g0}_i \\ c^S_{i,j} &= c^{s0}_i\cdot f_j \\ T &= T^0 \end{aligned} \quad 7.25$$

The model can be solved once the pore size distribution is known, $f_j(d_j)$, and the grain radius r_g is known. The model should also consider that $f_j(d_j)$ can change in time and space because of reaction and physical phenomena of solid restructuring [53]. So far it was assumed that the pore size distribution remains constant.

7.5.1 Application to CLC experimental data: reduction of CuO

The PBE model was applied to describe the reduction of particles of CuO with CO, to compare its result with experimental data obtained by TGA analysis of chemical looping combustion using copper as an oxygen carrier. The considered reaction is:

$$CuO + CO \rightarrow Cu + CO_2 \quad 7.26$$

The reaction tests were carried out by the laboratories of Technical University of Eindhoven using spherical particles (1 mm diameter) of CuO supported by Al_2O_3, with initial density of 1 g/cm^3. In particular, one test was considered for the simulations: it was performed at 600°C and 1 atmosphere, with a composition of reducing gas of 20% CO in N_2. The CuO particles were previously characterized before reaction, in particular a pore size distribution was measured, and a SEM analysis was made to analyze the local microscopic

structure of the pellet. This information was processed to obtain the necessary parameters needed to solve the population balance equations model. This preliminary work is reported in the following sections.

7.5.1.1 Estimation of the mean grain size

On the left hand side of Figure 7.8 a SEM image of the copper oxide particle surface is shown. The particle is composed of an inert alumina matrix (dark phase), where small micro grains of CuO are visible (light gray regions). The shapes of the copper oxide grains are quite irregular, still they can be approximated with a spherical model, considering an equivalent diameter calculated by their volumes, or in this case by the area of their sections, since a two dimensional image is available. Then a mean grain size can be calculated and used in the model.

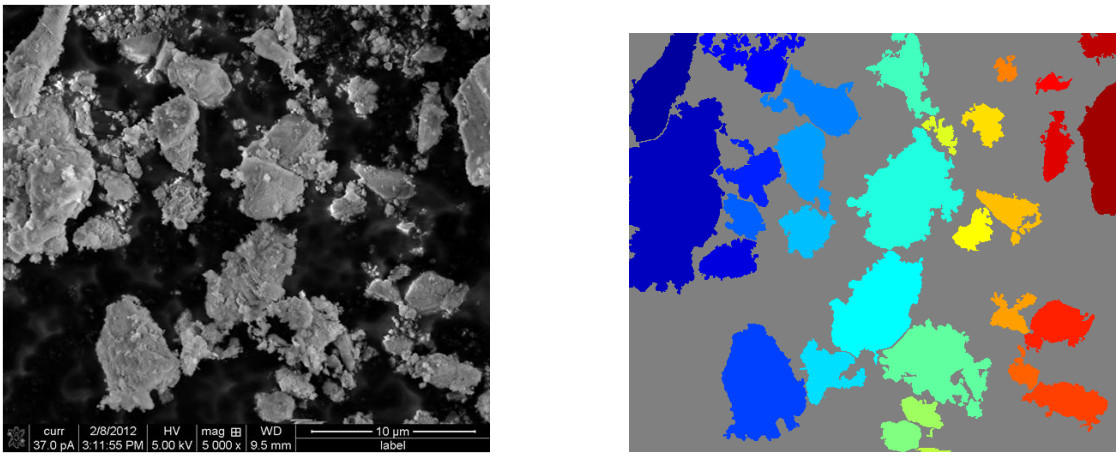

Figure 7.8: Identification of subgrains in the solid structure of CuO. Original SEM picture (left) and processed image (right)

First, the SEM image was processes, by some image analysis techniques, to clearly identify each grain and their extension. This was made thanks to the image processing toolbox in Matlab, that presents some dedicated routines that can be combined for the purpose. In particular, the following steps were followed:

- Separation of the dark and light phase by tuning the image contrast. The result of this is a binary (black and white) picture.
- Cleaning of the small fragments.
- Identification of the boundaries of each object.
- Identification of the objects, each one representing a single grain.

The result of this processing is shown on the right hand side of Figure 7.8. Once this was done, the area of each object was calculated by automatic pixel counting. The areas in pixel were converted in areas in square microns, using the scale given by SEM (on the bottom of the SEM image). Finally, the average area A_m was calculated, and the equivalent grain radius was estimated by using the inverse of the circle area formula:

$$r_g = \sqrt{\frac{A_m}{\pi}} \qquad 7.27$$

For the considered image, the approximated number found was r_g = 1.8 µm. Even if the approximation of spherical grains is quite ambitious, this image analysis can be useful just to have an order of magnitude of the scale to apply to the model.

7.5.1.2 Treatment of the PSD

Figure 7.9 shows the experimental pore size distribution obtained for the CuO particles through BET analysis. This technique allowed the quantification of macro and meso pores, up to a minimum size of 2 nm. The relative abundance of pores is expressed in terms of the pore area available for each pore size. This is just about the needed measure: since the reaction is superficial, the fraction of solid involved in each lump must be calculated from the areas occupied by each pore size, scaled by the total available area.

These results were also processed to be consistently used in the PBE model. The experimental profile was interpolated with a spline, because the available number of points was quite limited (14). Then the curve was normalized, dividing each value of the y-axis by the total area defined by the interpolated curve. This area was calculated as a numerical integral. The obtained profile is shown on the left hand side of Figure 7.10.

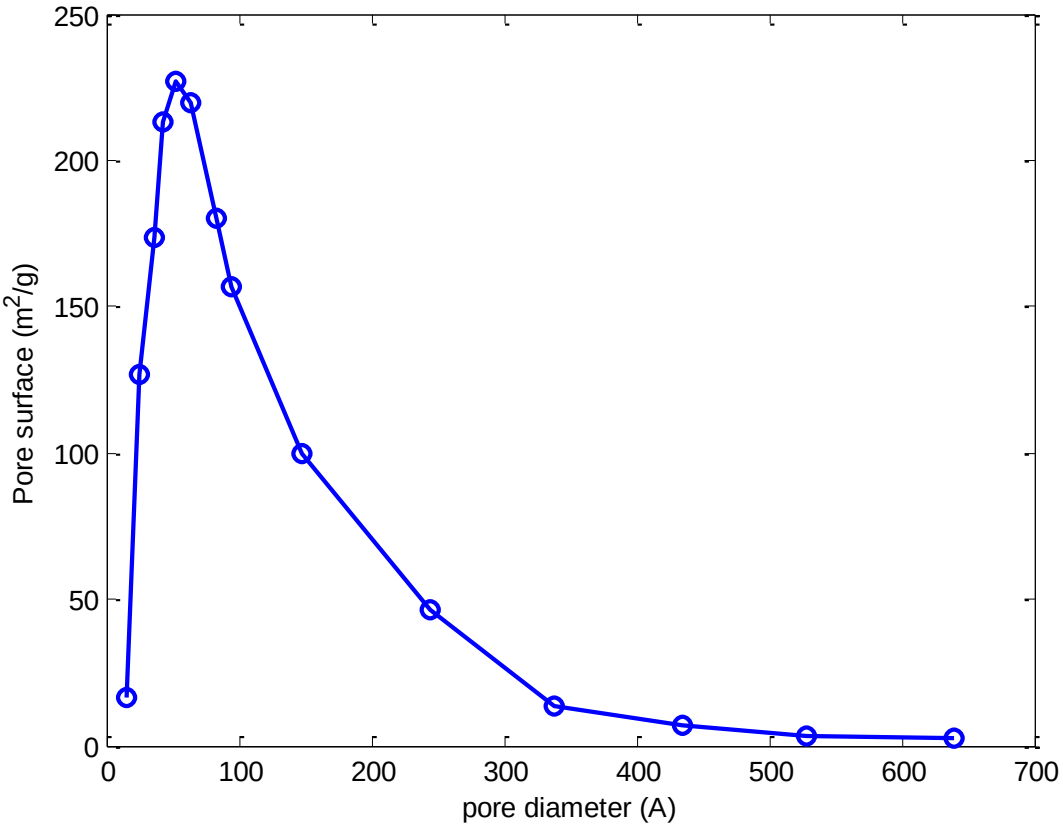

Figure 7.9: Measured BET pore size distribution of CuO particles

Since the PBE of equations 7.17-7.24 was expressed in a discrete form, the pore size distribution had also to be discretized. This was done, by choosing 20 pore classes. The surface underlined by the PSD was divided into 20 regions, and each of the subareas was divided by the total area, thus obtaining the normalized discrete pore size distribution, shown on the right hand side of Figure 7.10. The resulting values of pore diameters (d_j) to be used in the model can so be read on the x-axis, whereas their corresponding fractions (f_j) can be read on the y-axis. The classes were spaced uniformely on the x-axis, and the fraction corresponding to the j-th class was found by calculating the integral mean of the continuous distribution in a local interval of pore diameters, centered on d_j.

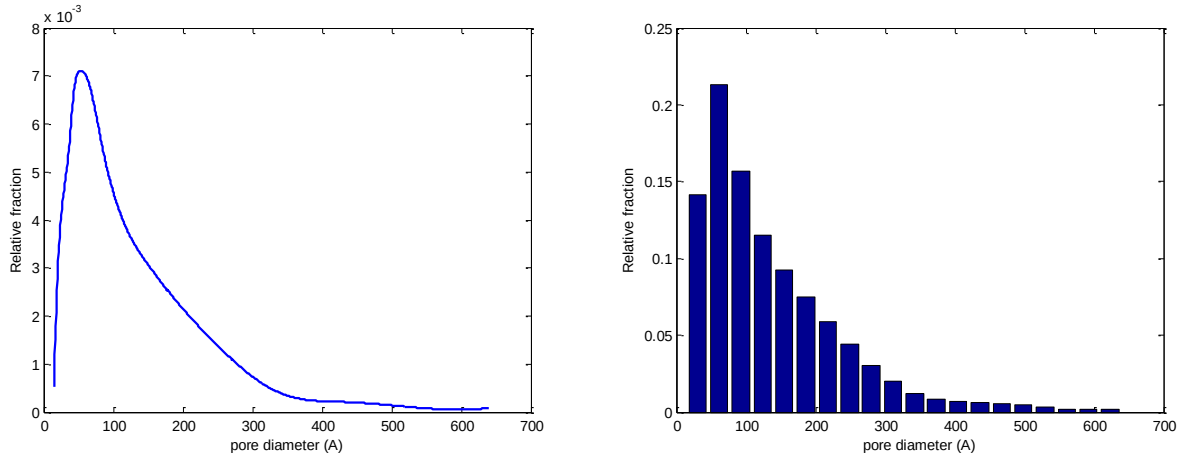

Figure 7.10: Processing of the experimental pore size distribution: interpolation and normalization (left). Discretization and renormalization (right).

In conclusion, the simulated system involved two gas species (CO and CO_2, the equation for N_2 is not solved), two solid species (CuO and Cu), and 20 pore classes, applied to both solid species, according to the pre processing carried out on the pore size distribution. This makes a total of 45 PDE that were solved.

7.5.2 Model results

The population balance equation system was solved to simulate the reduction of a 1 mm particle of CuO (made of grains with 1.8 µm diameter) with CO at 600°C and 1 atm. For the first simulation, the superficial kinetic constant of reaction 7.26 was arbitrarily fixed to k' = 0.5 cm/s.

Figure 7.11 shows the initial condition of the model at t = 0, for the concentration of CuO. The particle is assumed to be initially homogeneous, both in chemical composition and in the local pore size distribution, so no radial concentration gradients are present. For each radius, the class distribution of solid reagent resembles the shape of the pore size distribution imposed.

The evolution of the distribution of CuO is shown in Figure 7.12, for an intermediate conversion time. As the reaction proceeds, the concentration of copper oxide decreases, starting from the external particle surface (because of the gas radial diffusion resistance), and starting from the classes representing larger pores (because of the local diffusion resistance).

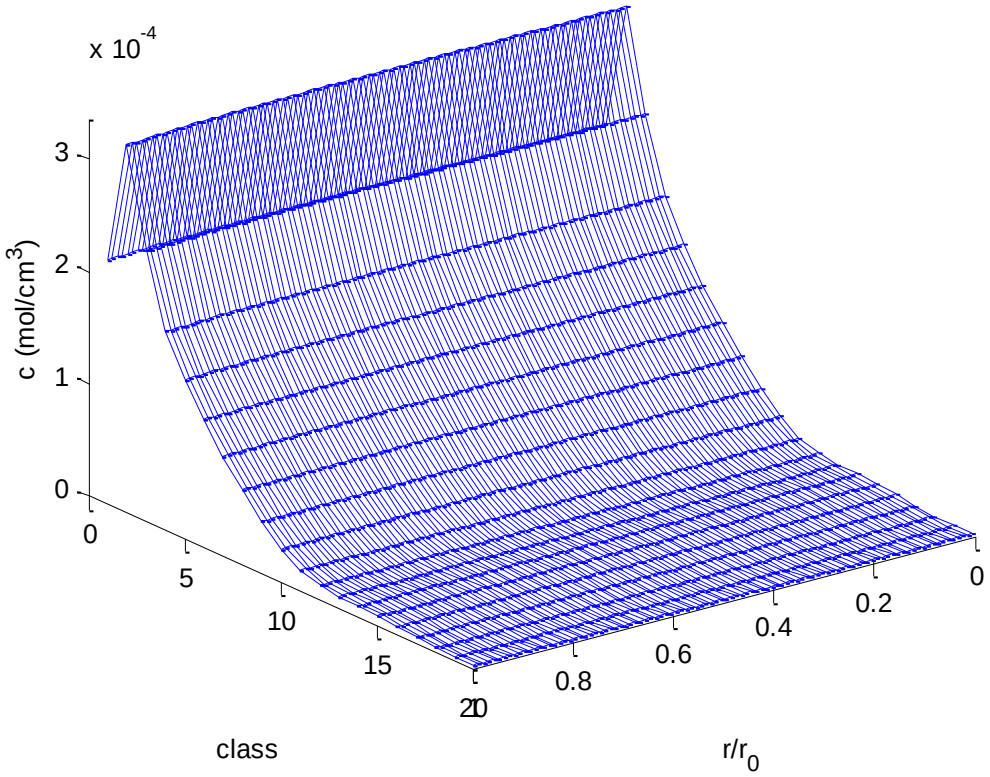

Figure 7.11: Initial distribution of concentration of CuO as a function of the radial coordinate and class number

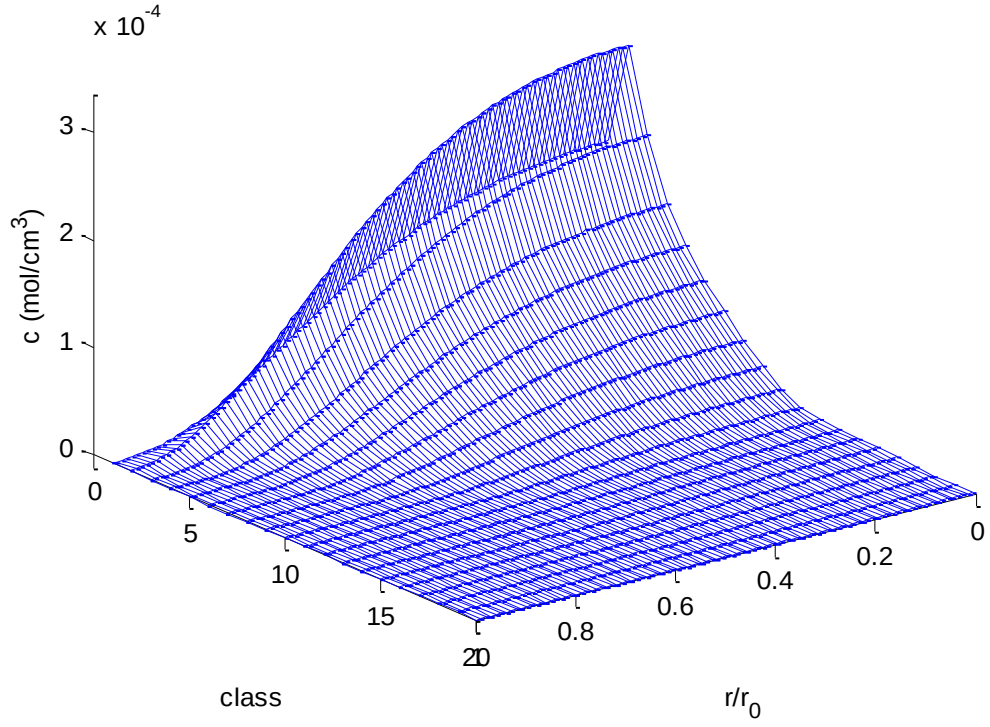

Figure 7.12: Distribution of concentration of CuO as a function of the radial coordinate and class number, as simulated by the model at an intermediate conversion time

In this situation, with the most important deformations of the distribution seem to be located along the radial coordinate, rather than in the class coordinate. This means that diffusion from the surface to the core seems to be important, whereas the difference of the diffusivities related to the different solid classes are not so evident.

Once again, the global particle conversion in time can be calculated from the model, by combining equations 7.18, 7.8 and 7.9. The comparison between the obtained conversion profile and the one measured by TGA tests is shown in Figure 7.13. The two profiles must be compared from a qualitative point of view, since an arbitrary kinetic parameter was used, and it is quite evident that the reaction rate is overestimated by the model. Nevertheless, it is quite clear that this model is not able to reproduce the experimental trend: despite the inclusion of different diffusion resistances, corresponding to large and narrow pores crossed by the reacting gas, this seems to have no effect on the global conversion profile.

In particular, there is no evident slowdown in the conversion, as it could be expected by an early reduction of the large pores classes, followed by a much slower reaction of the small pores classes. Yet, this situation does not happen, as it can be qualitatively observed in Figure 7.12. The used experimental pore size distribution covers more or less two orders of magnitude of pore diameters. This means, according to equation 7.20, that there are two orders of magnitude between the smallest and larger Knudsen diffusion coefficient within the classes. Despite this, the difference between the diffusive resistance of the first class and that of the last class is not large enough to explain a change of controlling regime. On the contrary, this change of regime seems to be quite evident in the experimental results, where the conversion rate becomes extremely small at about 50-60% of total particle conversion.

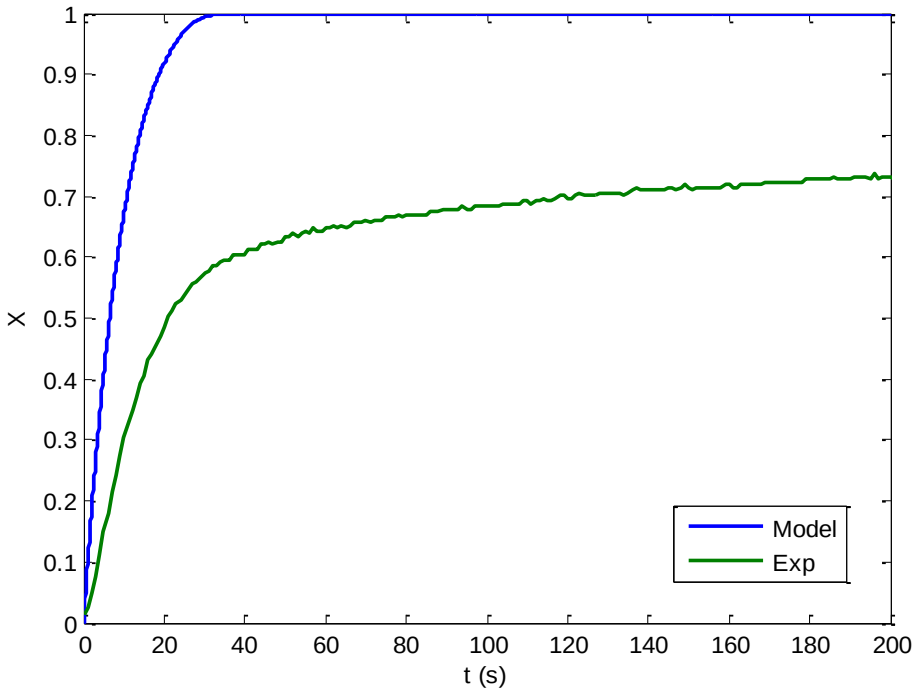

Figure 7.13: Comparison between experimental and calculated particle conversion using the experimental pore size distribution. No fitting of kinetic parameters.

One possible limitation of the model can be due to the fact that the distribution of small pores (< 2nm) was not measured, and so it was not included in the model, thus artificially reducing the pore range present in the particle. Yet, it seems quite unlikely that reducing the pore scale could solve the problem.

The main conclusion deriving from this analysis is that molecular and Knudsen diffusion cannot be responsible for a change of the controlling regime that can explain the experimental data for the considered reaction, particle conformation, and reaction conditions. Another diffusion mechanism must be assumed to achieve a good representation of the real process.

7.6 Effect of gas diffusion in non porous solid

In the previous section, a population balance equation model based on the grain model was developed and used, assuming that only molecular and Knudsen diffusion are the important mechanisms of gas transport inside the particle. A possibility that was not mentioned is that inside the particle there is a fraction of the solid reagent that is not directly accessible through pores. This can happen if a fraction of solid is completely covered by a layer of continuos, non porous solid product, or inert solid phase.

If this is the case, the reacting gas must also diffuse through the non porous solid in order to reach and convert all the solid reagent. On the microscopic scale, this is possible because the gas molecules can move across the empty sites that are commonly present as imperfections in the crystal structure of metals and metal oxides. The mechanism of gas diffusion into non porous solid can still be described through Fick's law. Commonly, the diffusion coefficients governing this transport mechanism are much smaller (usually several orders of magnitude) than Knudsen or effective molecular diffusivities of gases into pores. This issue was proven to be important in some gas-solid processes, and a possible model accounting for this diffusion resistance was proposed by Dam Johansen et al. [54].

The influence of gas tranport into non porous solid is strictly connected with the overall particle porosity. This is not the only parameter affecting this: in fact in a single particle there can be many small pores or few large pores, and the effect of diffusion into solid will be different in the two cases. It is possible to modify the PBE model presented earlier, in order to account for diffusion in solid. This was done by using again equations 7.17-7.24, but assuming that only two classes are present in the system. The first class represents the fraction of reagent solid that is accessible through the pores, where the gas transport is ruled by Knudsen diffusion, with a gas diffusivity calculated from the mean pore radius of the experimental pore size distribution. The second class represents the fraction of non porous solid, which can be crossed by the reducing gas only with a lower diffusivity.

The same system as the previous example was simulated (1 mm CuO particle reduced by a gas fed with a composition of 20% CO and 80% N_2, at 600°C and atmospheric pressure), using this new model. The fractions of the two classes were both assumed to be equal to 0.5. Different simulations were carried out, by assuming different values for the effective diffusion coefficient of CO into non porous solid (D_{CO}^{sol}). The results of this sensitivity analysis are shown in Figure 7.14, together with the experimental conversion profile.

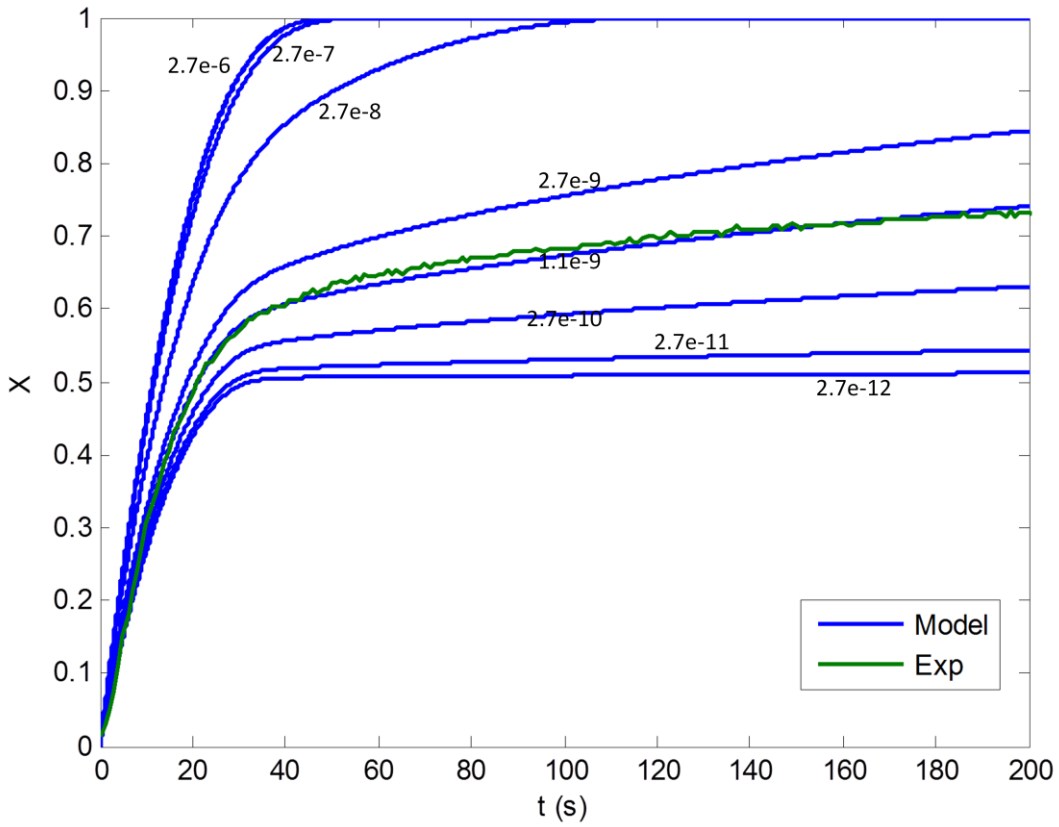

Figure 7.14: Estimated particle conversion profile calculated with the PBE model, changing the value of the gas diffusivity in solid (cm^2/s). Simulations with two classes ($f_1 = f_2 = 0.5$). Comparison with the experimental profile.

For high values of the solid diffusivity (10^{-6} cm^2/s), the model does not predict any change of the controlling regime: the process is mainly controlled by kinetics. When the value of D_{CO}^{sol} is decreased, the simulated profiles present a change in the slope at an intermediate conversion, and this change gets sharper for lower values ofD_{CO}^{sol}. In the limit condition, when the solid diffusivity tends to zero, only 50% of the solid particle reacts (this corresponds to the assumed fraction of porous solid, f_1 = 0.5). The global conversion velocity appears to be affected also in the first stages of the reaction, because the reaction of the two lumps occurs simultaneously.

It can be noticed that the model can predict the experimental data, only if a very small order of magnitude is assumed for the diffusivity controlling the gas transport into the second lump. This order of magnitude is about 10^{-9} cm^2/s, which is much lower than the orders of magnitude of molecular and Knudsen diffusion (which in this case are 10^{-5}-10^{-6} cm^2/s), that were used in the previous section, where only the effect of different pore sizes was considered. This confirms the conclusions of the previous section: if there is not a very large difference in the diffusion resistances in the different phases, it is not possible to explain the presence of two regimes in the TGA profiles. All the results presented in Figure 7.14 considered that the fraction of solid crossed by pores and the fraction of dense solid were equal to 0.5. A second sensitivity analysis was carried out, where D_{CO}^{sol} was fixed to the value of $1.1*10^{-9}$ cm^2/s, and f_1 was changed (and consequently f_2). These results are shown in Figure 7.15.

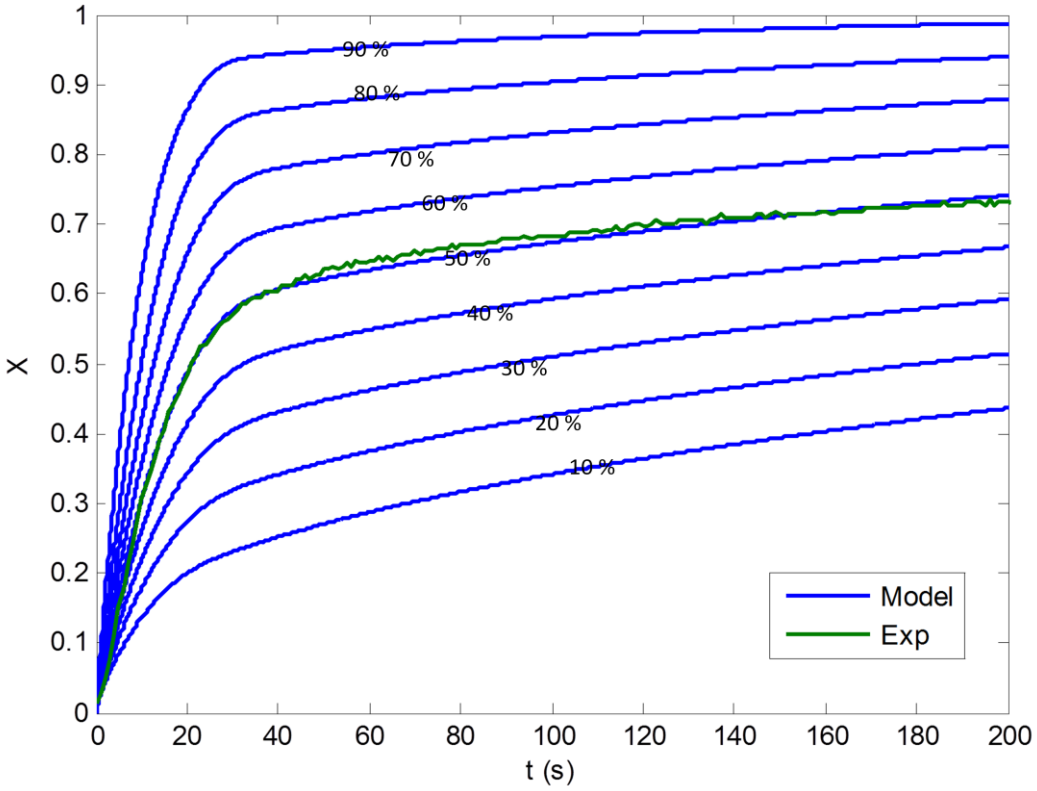

Figure 7.15: Estimated particle conversion profile calculated with the PBE model, assuming the value of the gas diffusivity in solid equal to 1.1*10^{-9} cm^2/s, for different values of fractions of porous solid f_1. Comparison with the experimental profile.

The different simulations show that the relative fractions of solid and dense material can have an important influence on the model results. The velocity of conversion in the second stage (identified by the slope of the profiles at long times) does not change, in fact this is identified by the value of D_{CO}^{sol} which is always the same. What is different is the conversion at which the simulated profile bends, which corresponds to the point when the fraction of porous material (f_1) has more or less completely converted, and only the dense solid reagent (f_2) remains. Also, the slope of the first stage can change, because of the presence of two combined resistances.

A final sensitivity test was made. This time, D_{CO}^{sol} was again fixed to the optimum value of 1.1*10^{-9} cm^2/s, and the fractions of porous and dense material were also fixed (f_1 = f_2 = 0.5). Different simulations were carried out, changing the kinetic constant k' of the model. The results are shown in Figure 7.16. The curves are parametric to a Thiele modulus Φ^2, calculated as follows:

$$\Phi^2 = \frac{k' r_0}{D_1^K} \qquad 7.28$$

In this formulation, D_1^K is the Knudsen diffusion coefficient of CO into the porous fraction, calculated from the average pore size and used to describe the gas reaction rate into the equation for the first class. It can be noticed that, for all the simulations, Φ^2 is well below unity, which means that for all the cases the early conversion step, corresponding to the reaction of the porous fraction of the particle, is controlled by

kinetics. The change of k' has an effect only on this stage, whereas after a certain time all of the simulated profiles converge to a single one: the reason for this is that, after the porous fraction is all converted, the process is controlled by solid state diffusion, and the value of k' is no longer important.

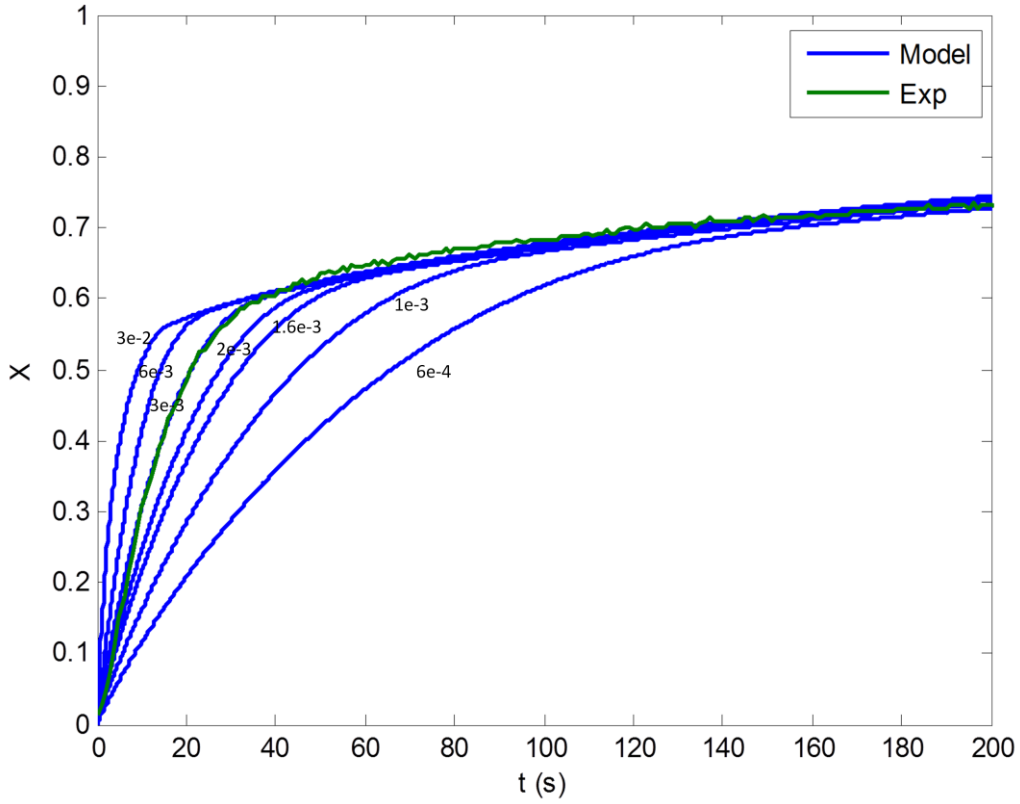

Figure 7.16: Estimated particle conversion profile calculated with the PBE model, assuming the value of the gas diffusivity in solid equal to $1.1*10^{-9}$ cm^2/s, and $f_1 = f_2 = 0.5$. Sensitivity for different values of Thiele modulus ϕ^2 (corresponding to different values of k'). Comparison with the experimental profile.

The sensitivity tests made with the PBE continuous model prove that gas diffusion in solid state may have an influence on the model results, and could be a key factor, explaining the behavior of the experimental data. Nevertheless, this kind of model relies on the quantification of some properties that can be difficult to measure in a real particle, for instance the fraction of dense and porous solid, and are more likely to be considered as model parameters.

7.7 Effect of solid phases segregation

In the previous sections, experimental data of reduction of oxygen carriers for CLC were tried to be interpreted through a particle model, by considering different possible phenomena affecting the results: solid sintering, influence of pores with different sizes, contribution of gas diffusion into dense solid. These

contributions can be generally present in any gas-solid reaction, but their influence on the process can be different, depending on the reaction conditions and particle conformation.

In Chemical Looping Combustion, further issues can originate, related to the fact that a single particle is reduced and oxidized a high number of times. In particular, some chemical and physical phenomena may accompany the reactions during the first cycles, and these may lead to an enhancement of the reactivity of the particles after a number of oxidation-reduction steps. Authors refer to this process as *particle activation*. For the ilmenite-pseudobrookite system, this phenomenon was studied by Adanez et al. [47], who proved that the activation is also the result of the restructuring of pseudobrookite, which can decompose to its primary oxides, that is hematite (Fe_2O_3) and rutile (TiO_2). Besides, hematite can migrate to the external layer of the particle, forming a shell with a different composition, enriched in iron. In Figure 7.17 we report their SEM analysis on activated ilmenite [47], clearly showing radial phase segregation within the solids.

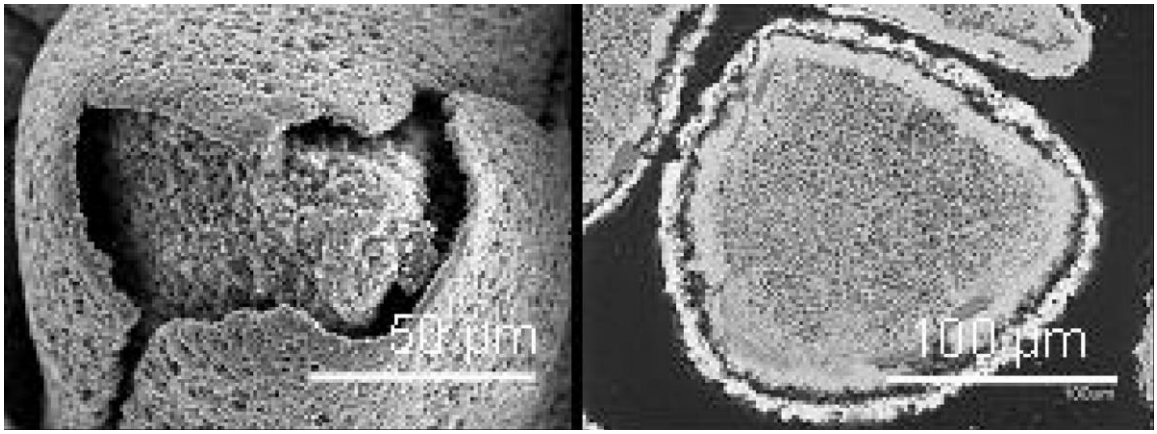

Figure 7.17: SEM observations of the conformation of activated ilmenite particle (reduced state) clearly showing phase segregation [47]

Making use of this information, our analysis was again focused on the description of the reduction step of the pseudobrookite/hematite system, which is the most critical one, because it is always much slower than the oxidation step. It is crucial to fully characterize and understand the phenomena controlling the kinetics, and the interaction between the gas and solid phases, particularly within the particle.

The continuous model presented in section §4 was again developed and modified, naturally accounting for continuous distribution of several species within the particle. The new model was applied to the understanding of the role of titanium-iron radial segregation in the particle conversion, in case ilmenite is chosen as oxygen carrier.

7.7.1 Model development

In the previous simulations, the reduction of Iron-Titanium oxides was described through a single step (equations 7.2-7.3), assuming that pseudobrookite can be expressed as an ideal mixture of hematite (the reacting phase), and rutile (the inert phase). The presence of both isolated hematite and pseudobrookite in

the activated particles, on the contrary, can suggest that both phases can react in parallel, possibly with a different kinetic rate.

A new reaction scheme was used, including both the reduction of hematite to wustite and the reduction of pseudobrookite to ilmenite. If hydrogen is the fuel, this is:

$$Fe_2O_3 + H_2 \rightarrow 2\,FeO + H_2O \quad 7.29$$

$$Fe_2TiO_5 + TiO_2 + H_2 \rightarrow 2\,FeTiO_3 + H_2O \quad 7.30$$

Analogously, for the reduction with CO:

$$Fe_2O_3 + CO \rightarrow 2\,FeO + CO_2 \quad 7.31$$

$$Fe_2TiO_5 + TiO_2 + CO \rightarrow 2\,FeTiO_3 + CO_2 \quad 7.32$$

More elaborated reaction systems could account for the presence of ulvospinel (Fe_2TiO_4), a reduced species which is thermodynamically unstable [55]. Interestingly, ilmenite and hematite can be perfectly miscible at high temperature, but not at lower ones. Given that the process cycles over the temperature, restructuring of the particle should be expected, leading to solid phase segregation. Note that two reactions sharing the same reagents are incompatible with the existence of two sharp reactions fronts within the particles, as assumed by the shrinking core model, where reactions need to be much faster than diffusion. The outermost interface is expected to consume all the reagent, i.e. CO or H_2, preventing its transport to the inner interface, to feed the other reaction.

To describe the evolution of the reactive particle with a continuous model, the conservation balances were solved assuming spherical geometry of the particles. Again, the continuous model in the form of equations 4.37-4.41 was used, considering no change of particle size. The Stefan-Maxwell model was used to describe the diffusive fluxes of the gas species (equations 5.43-5.47), including Knudsen diffusion (equation 5.93), whereas the evolution of local porosity was expressed through equation 4.45. The boundary and initial conditions used were in the form of equations 4.47, 4.48 and 4.50.

The reaction rates can be considered to be first order in the concentration of the gas reactant (H_2 or CO), and non linearly on the solid conversions X_i, with i=H(ematite) or i=P(seudobrookite), as follows:

$$R_1 = k_1 \cdot f(X_H) \cdot c^g{}_{H2} \quad 7.33$$

$$R_2 = k_2 \cdot f(X_P) \cdot c^g{}_{H2} \quad 7.34$$

$$R_3 = k_3 \cdot f(X_H) \cdot c^g{}_{CO} \quad 7.35$$

$$R_4 = k_4 \cdot f(X_P) \cdot c^g{}_{CO} \quad 7.36$$

In equations 7.33-7.36, the conversions of the single solid species are defined as follows:

$$X_H = 1 - \frac{c^S{}_{Fe2O3}}{c^{S0}_{Fe2O3}} \quad 7.37$$

$$X_P = 1 - \frac{c^S{}_{Fe2TiO5}}{c^{S0}_{Fe2TiO5}} \quad 7.38$$

The function f(X) was expressed through the grain model, according to equation 4.71.

A possible variation of the form of the reaction rates was also considered: in alternative to equations (7.33-7.36), the reaction rates can be also expressed by means of a Langmuir-type equation, which can take into account possible resistances due to a finite adsorption rate of the reagent gas:

$$R_1 = k_1 \cdot f(X_H) \cdot \frac{K_{H2}\, c^g{}_{H2}}{1 + K_{H2} c^g{}_{H2}} \quad 7.39$$

$$R_2 = k_2 \cdot f(X_P) \cdot \frac{K_{H2}\, c^g{}_{H2}}{1 + K_{H2} c^g{}_{H2}} \quad 7.40$$

$$R_3 = k_3 \cdot f(X_H) \cdot \frac{K_{CO}\, c^g{}_{CO}}{1 + K_{CO}\, c^g{}_{CO}} \quad 7.41$$

$$R_4 = k_4 \cdot f(X_P) \cdot \frac{K_{CO}\, c^g{}_{CO}}{1 + K_{CO}\, c^g{}_{CO}} \quad 7.42$$

In this formulation, four additional parameters K_1, K_2, K_3, K_4 must be provided, possibly depending on temperature. The Langmuir approach can be more suitable if the reaction dependency on the concentration of the reactant gas is apparently less than first order.

In any case, kinetic constants, k_1, k_2, k_3, k_4, must be specified as functions of temperature, by means of the Arrhenius law (eq. 4.54).

The model was solved using a finite difference method to discretize the space derivatives [56]. A centered differences scheme was used for the diffusion term, while first order upwind was chosen for the convective terms. The theta method was used to handle the time derivatives. In particular, Cranck-Nicholson scheme [57] was chosen (θ = ½). The problem was finally solved by linearizing the non linear (convection and reaction) terms with a Newton scheme, and thus solving iteratively the linear system obtained by introducing a Jacobian matrix that was calculated analytically.

From the model results, again the global particle conversion can be calculated through equations 7.8-7.9.

7.7.2 Model predictions and sensitivity to non uniform initial conditions

Before attempting any comparison of experimental data and model predictions, and subsequent parameter estimation, an investigation on the significance of the initial solids composition and the competition of the two reactions steps has been carried out.

Typically, simulations assume a uniform initial composition of the particles, i.e. constant radial concentration profiles for all the solid species in the pellet. If solid phase segregation is present at the beginning of the reaction, as shown in Figure 7.17 because of activation, the initial conditions must be modified accordingly. In addition, the solid migration phenomenon should be considered in a time dependent simulation, but this is quite slow if compared to the chemical reaction, and it has eventually no effect in activated particles. For this reason it can be neglected while simulating a single reduction step, but it might be important to include it while solving a high number of cycles, particularly during the first cycles that involve non activated solids. In this present work, the reaction was simulated for particles where migration has already occurred, and the oxidized phases are already segregated forming a core-shell structure. This mathematically is translated into non uniform initial solid radial concentration profiles.

The reaction of hematite and pseudobrookite can occur in series or in parallel. They take place in series if one of the two solid reagents is segregated in the outer region of the particle and the other one in the core, and also the reaction evolves like a shrinking core model. In this case, the reacting gas will first meet the outer solid phase, and eventually the inner phase, but only when the first one is completely oxidized. A shrinking core behavior is possible only if diffusion is controlling over the reaction rates, so in this case a different reactivity of Fe_2O_3 and Fe_2TiO_5 should not determine any change in the conversion rate. Yet, this could be the consequence of different effective diffusivities of the reagent gas in the two layers (for example if the porosities are very different from each others). A diffusive regime is usually possible for large particles, or particles with a quite dense solid matrix.

On the contrary, the two reaction steps take place in parallel if there is no phase segregation, or if there is segregation but the process is controlled by kinetics: in this case the reacting gas is always present throughout the particle, so both Fe_2O_3 and Fe_2TiO_5 react simultaneously even if one is in the core and the other in the shell of the particle. Nevertheless, if one of the two steps is much faster than the other, there will be a time when the fast reacting solid is completely reduced, while the second one is not. This could also cause a shift in the global conversion profiles.

In order to reproduce the initial core shell structure, and identify the initial composition profiles for the solid species inside the particle, some degrees of freedom must be fixed. They are:

- The radial position of the interface dividing the core and the shell.
- The relative composition of the core and the shell.

In the chemistry chosen here, three solid species are present before the reduction of the particles, namely hematite (Fe_2O_3), pseudobrookite (Fe_2TiO_5), and rutile (TiO_2). This makes a total of seven variables to set just to describe the initial conditions: they are the concentration of Fe_2O_3, Fe_2TiO_5 and TiO_2 in the core and in the shell, and the radial position of the core-shell interface.

Some constraints can also be set. First, if the global fraction of iron and titanium of the particle is known, it will be:

$$\frac{m_{Fe}}{m_{Fe} + m_{Ti}} = y_{Fe}^{set} \qquad 7.43$$

Where y_{Fe}^{set} is the set mass fraction of iron, while m_{Fe} and m_{Ti} are the total amount of iron and titanium in the particle. They are calculated from the solid concentration profiles as:

$$m_{Fe} = \int_0^{r0} 4\pi r^2 \cdot 2({c^s}_{Fe2O3} + {c^s}_{Fe2TiO5}) \cdot MW_{Fe} dr \quad 7.44$$

$$m_{Ti} = \int_0^{r0} 4\pi r^2 \cdot ({c^s}_{Fe2TiO5} + {c^s}_{TiO2}) \cdot MW_{Ti} dr \quad 7.45$$

The mass fraction of titanium and iron will remain constant, no matter how the solids are distributed, and how much pseudobrookite is dissociated into hematite and rutile.

Another constraint is related to the maximum density of the solid, which cannot exceed the intrinsic density of the dense material in any point of the particle. This density depends on the size of the molecule atoms and the crystal structure of the material. Mathematically:

$$\sum_{j=1}^{NS} {c^s}_j \cdot \frac{MW_j}{\rho_j} \leq 1 \quad 7.46$$

A further constraint is due to the reaction stoichiometry. In order to fully convert to ilmenite, pseudobrookite must combine with rutile (equations 7.30 and 7.32), which means that the concentration of rutile must be at least the same as the concentration of pseudobrookite in any point of the particle in order to achieve full conversion.

Uneven, stepwise changing initial solid profiles were set through a function that simulates the core-shell structure, smoothing the transition in the interface:

$${c^s}_i^0(r) = {c^s}_{i,c} + ({c^s}_{i,s} - {c^s}_{i,c}) \cdot \frac{1}{\sqrt{2\pi\sigma^2}} \int_0^r \exp\left(-\frac{(s-r_i)^2}{2\sigma^2}\right) ds \quad 7.47$$

In this equation, r_i is the radial position of the interface, ${c^s}_{i,c}$ and ${c^s}_{i,s}$ are the concentration of the species i in the core and in the shell, respectively. The parameter σ is related to the width of the transition region between the core and shell compositions. The function 7.47 is based on a scaled cumulated normal distribution function. Smoothing of the interface was introduced for the sake of numerical stability. In fact, continuous models can predict any radial profile, but they need the continuity of the solution and of the first derivative, too. Also, eq. 7.47 more realistically describes the actual initial distributions, since segregation is never abrupt at the core-shell interface. The value of σ was chosen arbitrarily in order approximate a fairly sharp transition at the interface, and it was kept constant during the sensitivity simulations.

7.7.2.1 Base case simulation

A small particle (200 μm diameter) was simulated in a reaction at 800°C and 1 atm, with a 30% mixture of CO in N_2. The gas properties (diffusivities, molecular weight and boundary composition) were calculated accordingly. The kinetic scheme of eq. (7.35-7.36) was chosen, with k_3 = 100 s^{-1} and k_4 = 10 s^{-1}. The position

of the interface is set at $r_i/r_0 = 0.8$, and complete segregation of hematite (in the shell) from pseudobrookite (in the core) was assumed, with the global mass fractions of solids being 30% hematite, 27% pseudobrookite and the remaining 43% rutile. The initial concentration profile of rutile was fixed by imposing uniform particle porosity, i.e.:

$$\sum_{j=1}^{NS} c^s{}_j \cdot \frac{MW_j}{\rho_j} = const \qquad 7.48$$

This condition is arbitrary, and implies initial non uniform density profiles. As a matter of fact, if in two spots the porosity of the solid is the same but the solid composition is different, according to equation 4.10 also the apparent density is different because the intrinsic densities of the species are, in general different. More simulations were carried out, considering constant radial density and non uniform porosity, leading to approximately the same results.

The results given by the model for such a base case is shown in Figure 7.18. The radial composition of the solid is reported at four different reaction times, corresponding to four points in the global particle conversion profile calculated, labeled A, B, C, D.

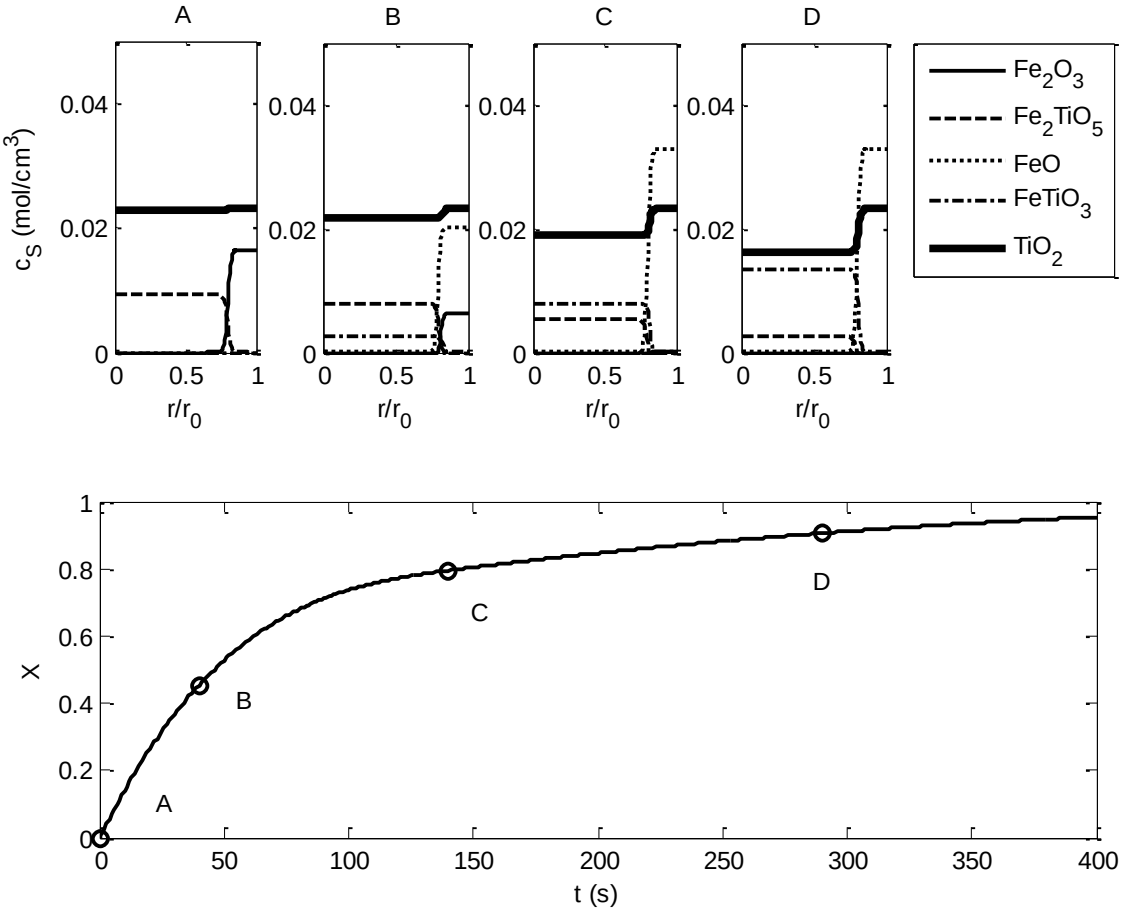

Figure 7.18: Simulated radial concentration profiles for the solid species at four different times (top). Predicted particle conversion profile in time (bottom). Initial core shell interface r/r0 = 0.8; kinetics ratio k3/k4 = 10.

In this simulation, the shell of the particle reacts more quickly, because hematite is present there, while the pseudobrookite in the core takes longer to be reduced. Inside the two regions, the reaction proceeds quite uniformly, which means that the gas diffusion resistance is less important than the kinetic one, and CO is available in any point of the particle. From point B to C the global conversion profile slows down, because all of the hematite in the shell is already converted and after a certain point only the slow reaction takes place.

Since the gas diffuses rather easily, we could conclude that the initial distribution of solid phases is not relevant, but only the total amount of solid species in the particle. This apparent conclusion was confuted by the results of a sensitivity analysis on the same reacting particle, changing the kinetics and the characteristics of the initial core shell distribution.

7.7.2.2 Sensitivity analysis - Kinetic constants

Starting from the base case simulation shown above, the effect of possible different reactivities of Fe_2O_3 and Fe_2TiO_5 was evaluated, considering the same initial conditions (see the profiles in Figure 7.18 A). Different kinetic constant ratios were tested (k_3/k_4 = 1, 4, 10, 100), keeping always k_3 =100 s^{-1} (so only the rate of reduction of Fe_2TiO_5 was changed).

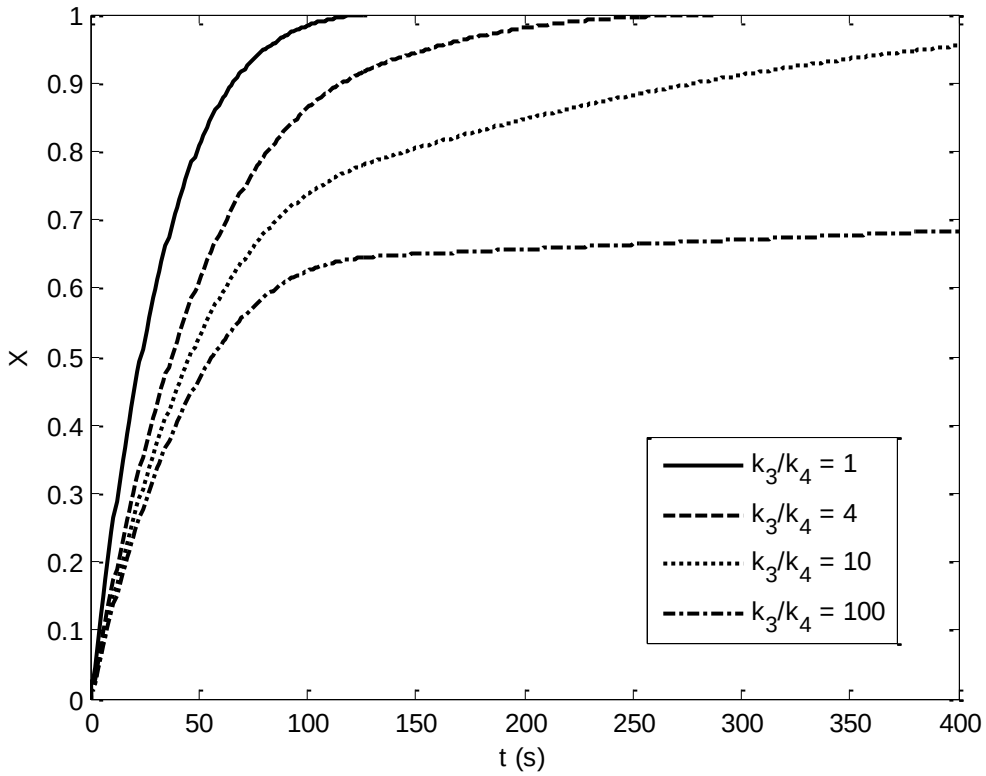

Figure 7.19: Simulated particle conversion starting from the same radial solid distributions as the base case, at different kinetics ratio for the two reactions.

Figure 7.19 shows the results of the simulations assuming different relative rates of hematite and pseudobrookite reduction. If the reduction of Fe_2TiO_5 is slower than the reduction of Fe_2O_3 (i.e. $k_3/k_4>1$), a progressively more pronounced change of slope in the global conversion profile can be observed, occurring earlier with larger k's differences. When the difference between the two rates is at least one order of magnitude, it is quite visible the point when the fast reacting phase is completely converted. From that moment on, only the remaining reagent is reduced. In the limit case, for a very slow conversion of pseudobrookite the profile is almost flat at 70% of total particle conversion. The conversion appears to be almost asymptotic, but actually it is slightly increasing with time and eventually 100% conversion is achieved, at long enough reaction times. For faster kinetics of pseudobrookite reduction, also the first section of the global conversion is faster, which proves again that in these conditions both reactions begin immediately, in parallel.

7.7.2.3 Sensitivity analysis - Position of the core/shell interface

The sensitivity of the model to the position of the interface was studied, assuming that complete segregation of Fe_2O_3 and Fe_2TiO_5 is present inside the particle. Again, all of the hematite was assumed to be located in the outer part of the particle, with the same global composition of the base case (30% hematite, 27% pseudobrookite and 43% rutile).

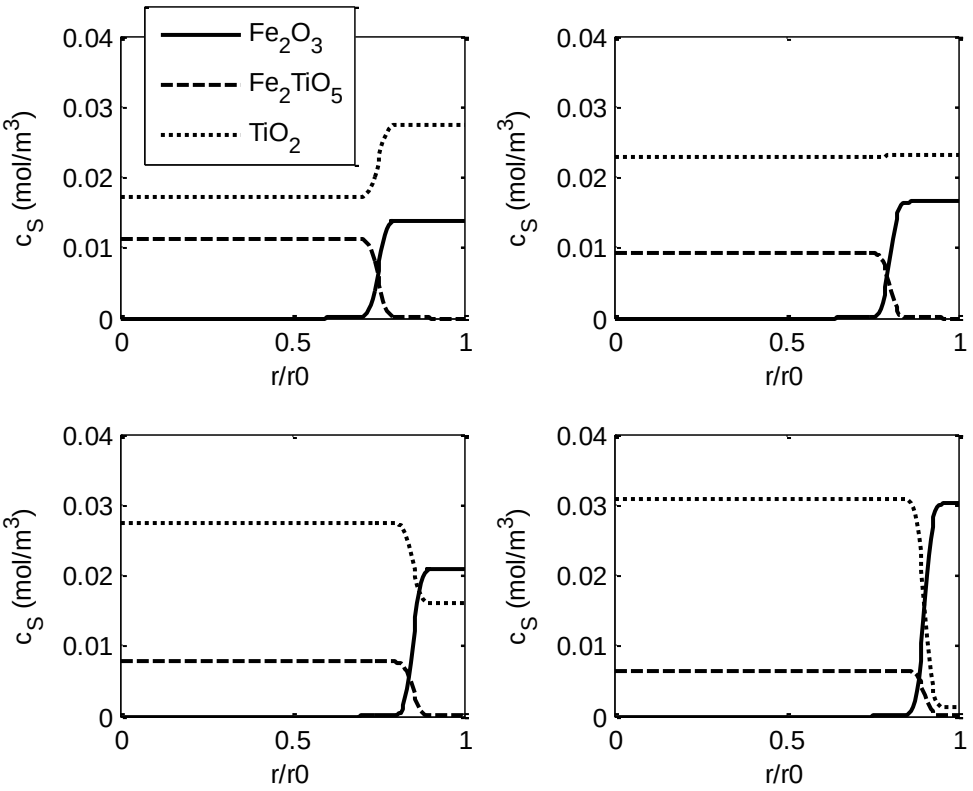

Figure 7.20: Initial solid distributions considered for the sensitivity analysis on the core shell interface position. ri/r0 = 0.75,0.90, 0.85, 0.90 from left to right and top to bottom

Now the effect of varying the position of the interface separating Fe_2O_3 and Fe_2TiO_5 is investigated, considering four different position of the core-shell interface (r_i/r_0 = 0.75, 0.80, 0.85, 0.90). The four initial profiles (molar concentrations) are shown in Figure 7.20; constrains on the total composition and porosity affect them beyond intuition. Note that the range of r_i/r_0 values is quite narrow, but it is fixed by the problem constraints. In fact the total amount of hematite is in the shell, whose thickness cannot be lower than a certain value, in order to keep the particle porosity uniform (this also means that the local density cannot be higher that the intrinsic density of hematite). On the other hand, the interface cannot be shifted too close to the particle center because a minimum amount of rutile is required in the core in order to have full conversion of pseudobrookite to ilmenite.

The resulting global particle conversion profiles simulated at different r_i/r_0 ratio are shown in Figure 7.21. For all of them, it was assumed k_3/k_4 = 10. Even for slight changes in the interface position, the change of shape of the conversion profile appears remarkable. Particularly, if the shell is thicker (small r_i/r_0) it becomes clearer the transition between the fast and slow reaction steps. Also, the time required for total conversion appears to be delayed, if the interface is closer to the center.

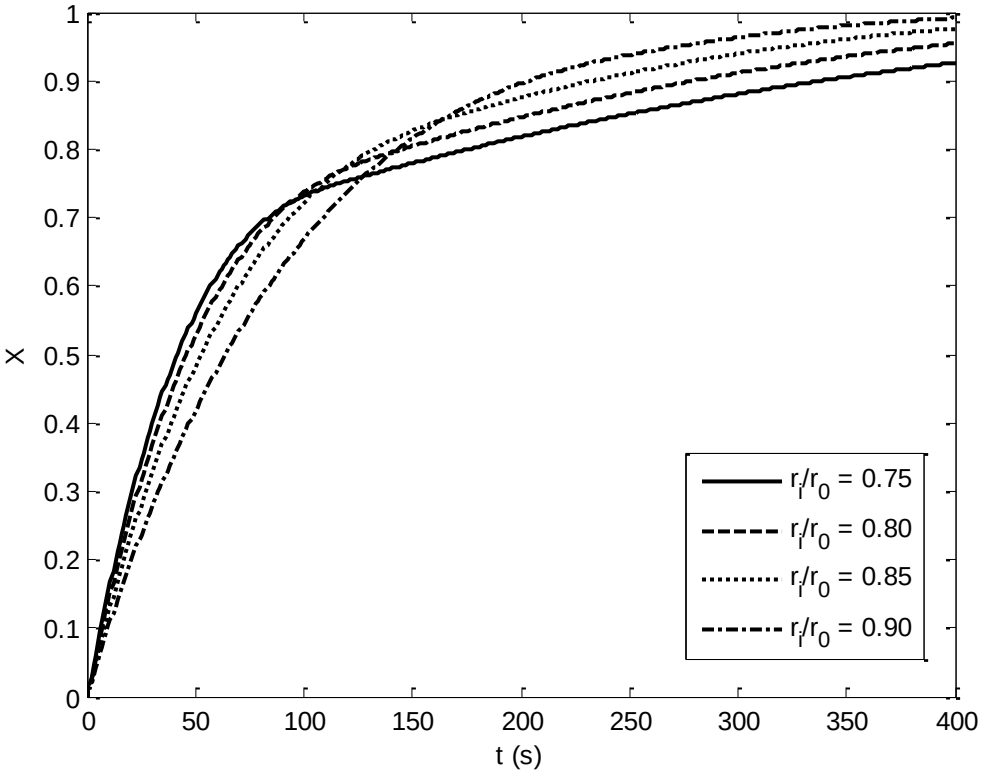

Figure 7.21: Simulation results for different core-shell interface positions, resulting from the initial profiles shown in Figure 7.20. Kinetics ratio k3/k4 = 10.

7.7.2.4 Sensitivity analysis - Composition of the core and the shell

Starting from the base case, we fixed $r_i/r_0 = 0.80$ and $k_3/k_4 = 10$, and the total amount of the three phases inside the particle (30% wt of Fe_2O_3, 27% wt of Fe_2TiO_5, 43% wt of TiO_2). All of the hematite was supposed to be in the shell, whereas the fraction of Fe in both the core and the shell was changed by changing the distribution of pseudobrookite, which could also be in the shell together with hematite. This affects the initial distributions of species, as shown in Figure 7.22. The four cases correspond to different Fe_2TiO_5/Fe_2O_3 concentration ratios in the shell (0%, 5%, 12%, and 21% respectively).

The corresponding model results are reported in Figure 7.23. Unlike the previous simulations, the initial reactivity is not affected by the different compositions; later, the conversion profiles progressively diverge, with the particle with mixed Fe_2O_3/Fe_2TiO_5 in the shell being reduced faster than the particle with only hematite in the shell. These differences may be explained by a non-negligible influence of diffusion, even if the controlling regime is apparently kinetic; that becomes clearer when the position of the solid reactant phases inside the particle is different. In particular, if more solid reagents are present in the outer part of the pellet (the cases with both Fe_2O_3 and Fe_2TiO_5 in the shell, and higher iron relative content), a larger amount of solid is in the section with higher reagent gas concentration (its profile decreases, moving from the particle surface to the center).

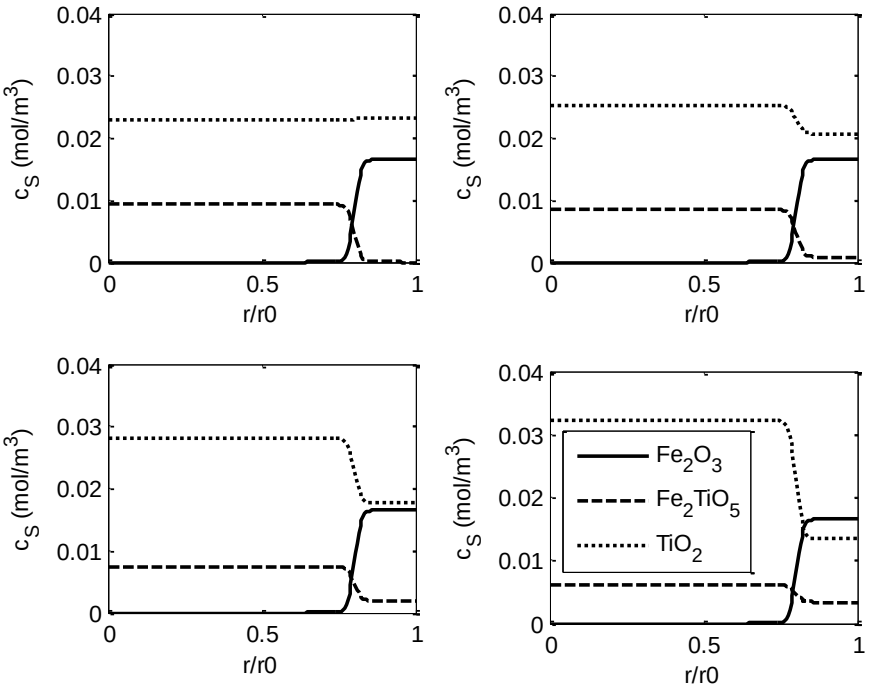

Figure 7.22: Initial solid distributions considered for the sensitivity analysis on the shell pseudobrookite/hematite concentration ratios. On top left: 0%. On top right: 5%. On bottom left: 12%. On bottom right: 21%.

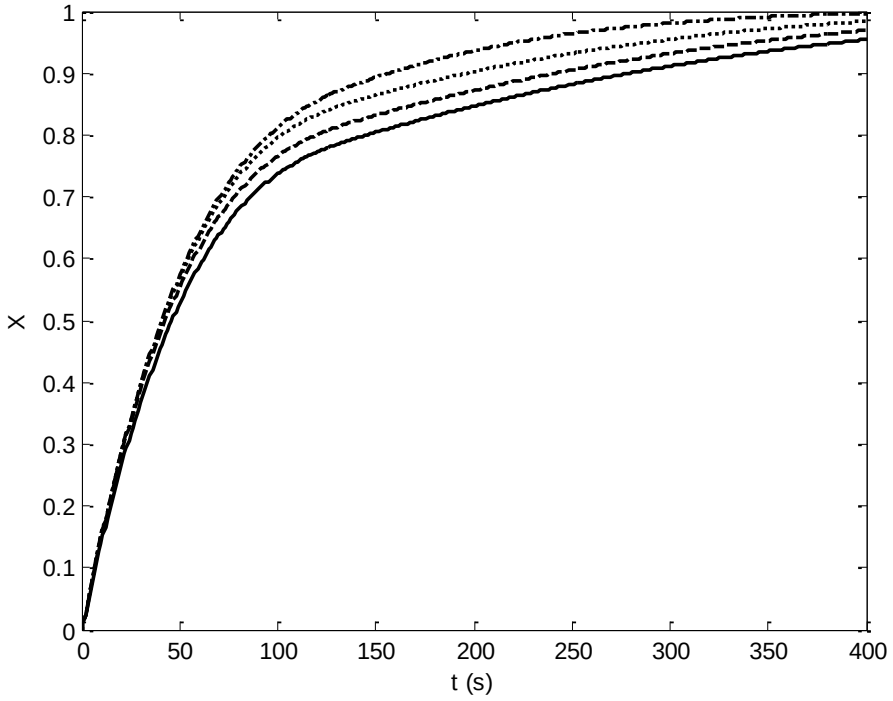

Figure 7.23: Simulation results for different initial pseudobrookite/hematite concentration ratios in the shell, resulting from the initial profiles shown in Figure 7.22. Case ($c_{Fe2TiO5}/c_{Fe2O3})_{shell}$ = 0.00 (–) ; ($c_{Fe2TiO5}/c_{Fe2O3})_{shell}$ = 0.05 (--); ($c_{Fe2TiO5}/c_{Fe2O3})_{shell}$ = 0.12 (..); ($c_{Fe2TiO5}/c_{Fe2O3})_{shell}$ = 0.21 (.-); Initial core shell interface r/r0 = 0.8; kinetics ratio k3/k4 = 10.

7.7.2.5 Sensitivity analysis - Global particle fraction of hematite

In the previous cases, we kept the same total initial fraction of hematite, pseudobrookite and rutile in the pellet. We just studied the effect of the solid phase distribution, assuming that they are separated, forming a core shell-structure in the particle. Now, we investigate how the total amount of components affect the global reactivity, while the degree of segregation of Fe_2O_3 and Fe_2TiO_5, as well as the core-shell interface position, remain the same. Precisely, all of the hematite was supposed to be located in the shell and all of the pseudobrookite in the core, with a core-shell interface at 80% of the particle radius (r_i/r_0 = 0.80). The total amount of Fe^{3+} inside the particle was fixed for all the simulations, so the constraint expressed by equation 7.43 is still valid. This is required to prevent misleading effects on the time scale of the particle conversion, due to a different amount of solid mass to be reduced. Like in the two previous sensitivity studies, the ratio between the kinetic of the fast and slow reactions was k_3/k_4 = 10.

Simulations were performed by considering different global fractions of hematite (20% wt, 27% wt, 33% wt, 40% wt). The corresponding profiles of pseudobrookite and rutile were set by using the constraints from equations 7.43 and 7.48; they are shown in Figure 7.24.

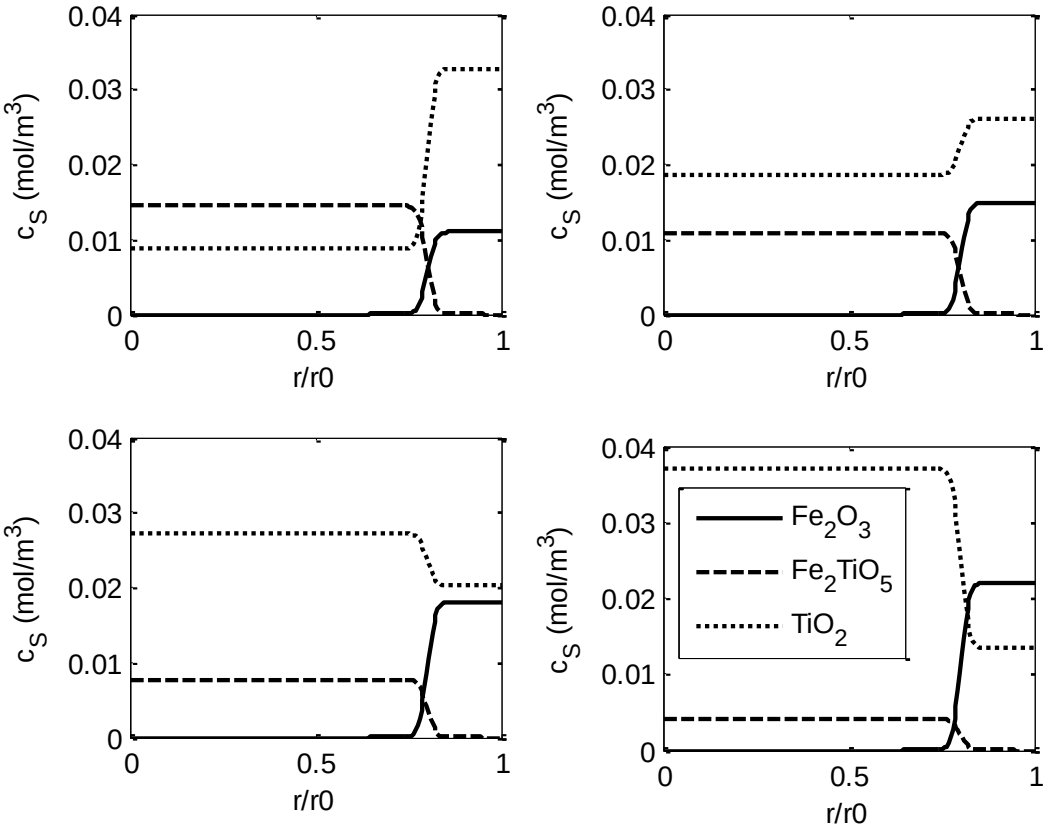

Figure 7.24: Initial solid distributions considered for the sensitivity analysis on the global phases mass content. From left to right, top to bottom: 20% hematite, 42% pseudobrookite; 27% hematite, 31% pseudobrookite; 33% hematite, 22% pseudobrookite; 40% hematite, 12% pseudobrookite.

Figure 7.25 shows the simulations results. Again, the initial reactivity is almost coincident for all cases. The relevant difference is the conversion at which a different regime establishes, indicated by a change of slope. In a particle with 40% of hematite (i.e. the smallest amount of pseudobrookite) its reduction, reaction 7.31, is predominant. Besides, the iron is more concentrated in the shell. For particles with lower concentration of hematite, the effect of the slow step (related to the reduction of Fe_2TiO_5) becomes more and more important, and consequently the change of slope of the global conversion profiles occurs at lower times and conversion degrees. It can be noticed that if the reactivity of the two phases is very different, even small changes in the initial particle composition can lead to large differences in the estimation of the particle conversion, after the first step.

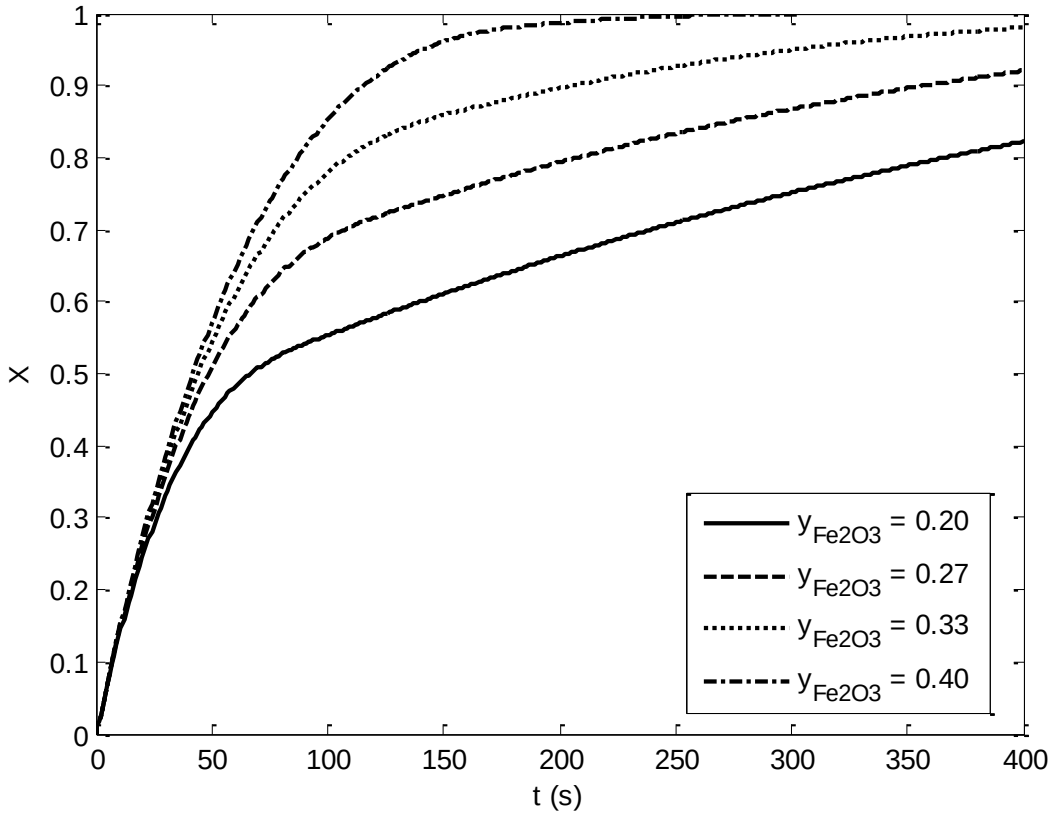

Figure 7.25: Simulation results for different total hematite amount in the particle, assumed completely segregated in the shell Initial core shell interface r/r0 = 0.8; kinetics ratio k3/k4 = 10.

Summarizing the indications of the sensitivity tests presented above, we can formulate some important general observations.

- The initial distribution of the solid reagents can be very important, but only if their reactivities are sufficiently different one from the other. Approximately an order of magnitude between the kinetic constants of the two reactions is needed to show a sharp change of the global conversion profile.
- In case of complete segregation of the reagents (one in the shell and one in the core of the particle), the radial position of the interface between the two plays an important role in the resulting conversion profile. Quite little variations of this position can lead to relatively large changes in the resulting curves, even if intraparticle diffusion is not dominant.
- The relative abundance of the reagents is important, both locally and globally. In particular, the global ratio between fast and slow reacting phases is the key factor affecting the change of reactivity experimentally observed.

7.7.3 Simulation of the experimental data

The simulations shown so far prove that information about the initial structure of the particle is needed to accurately describe its chemical evolution, given that quite different macroscopic behaviors could result. Only a detailed model as presented above can effectively exploit such a detail in the particle structure and evolution. The shrinking core model, including its modifications, cannot physically account for different reactions taking place in different points of the particle at different rates. If the solid phases actually show different reactivities, this can be an issue, because it is difficult to exactly know the position and local composition of the interface for every particle at the beginning of the reduction.

In this section we develop these concepts by comparison with original experimental data, questioning the detail required by a model to properly describe the measured data. We collected TGA experimental data on the reduction of activated pseudobrookite particles (200 μm diameter) with CO or H_2, at different temperatures in the range 600 to 800 °C and gas composition, at atmospheric pressure, as described above in Table 7.3. In all the experiments the gas phase contains 20%vol CO_2 and nitrogen up to 100%.

Table 7.3: Experimental conditions for the hematite reduction tests

Set	# test	Temperature [°C]	Reductant [%]
1 - CO	1	600	15
	2	700	15
	3	800	15
	4	800	30
2 - H2	5	600	15
	6	700	15
	7	800	15
	8	800	5

The experimental results are shown in Figure 7.26 and Figure 7.27, for CO and H_2, respectively, together with some simulations that will be soon commented.

The continuous model can additionally account for an initially uneven distribution of solids phases within the particle, which is likely when dealing with activated solids, as shown in Figure 7.17 and precisely the case of our experimental data. The initial solid phase distribution was not experimentally known, but in analogy with the measurements from the Abad research group [47], a core-shell structure was assumed, with the shell being enriched in iron and the core in titanium.

The initial distributions features were set first. We fit the experimental data by tuning the degree of pseudobrookite dissociation to hematite and rutile, in addition to the kinetic parameters. As demonstrated with the last sensitivity analysis, such a dissociation degree determines the time where the conversion rate drops (i.e. the 'knee' in the curves). Note that the model cannot fit the experimental profiles for all the temperatures, if the global amount of reagents is fixed, unless the degree of pseudobrookite dissociation is

adapted. The other initial composition parameters were kept constant, to avoid over parameterization. The interface was set at $r_i/r_0 = 0.80$, while complete segregation of hematite and pseudobrookite was assumed, with the first one being in the shell. Since all the features of the initial solids composition distribution have an impact on the model results, as shown by the sensitivity analysis, the numerical assumptions above arbitrarily determine the model predictions shown in the following. More realistic simulations require experimental information on the real initial distribution. The purpose of this work is just assessing which hypotheses about the initial conditions need to be verified to fully validate this model.

To describe the reaction rates, a Langmuir type expression was chosen (in the form of equations 7.39-7.42). For each of the two reaction schemes (reduction with CO and reduction with H_2), nine parameters were calculated: four kinetic parameters (preexponential factor and activation energy A, Ea for the reaction of hematite and pseudobrookite), two adsorption constants for the two reactions (they were assumed independent from the temperature) and an initial Fe_2O_3/Fe_2TiO_5 average particle concentration ratio for each temperature. Like the sensitivity tests, the global content of iron and titanium was fixed as a constraint, so equation 7.43 was used again.

The parameters were estimated by a least square minimization criterion, using the difference between calculated and estimated values of the particle conversions, at any time where an experimental measurement is available. Overall, we used about 10500 experimental points for the regression of the CO mechanism, and 7400 points for the regression of the hydrogen mechanism.

The results of the simulations are reported in Figure 7.26 for the tests of reduction with CO and Figure 7.27 for H_2.

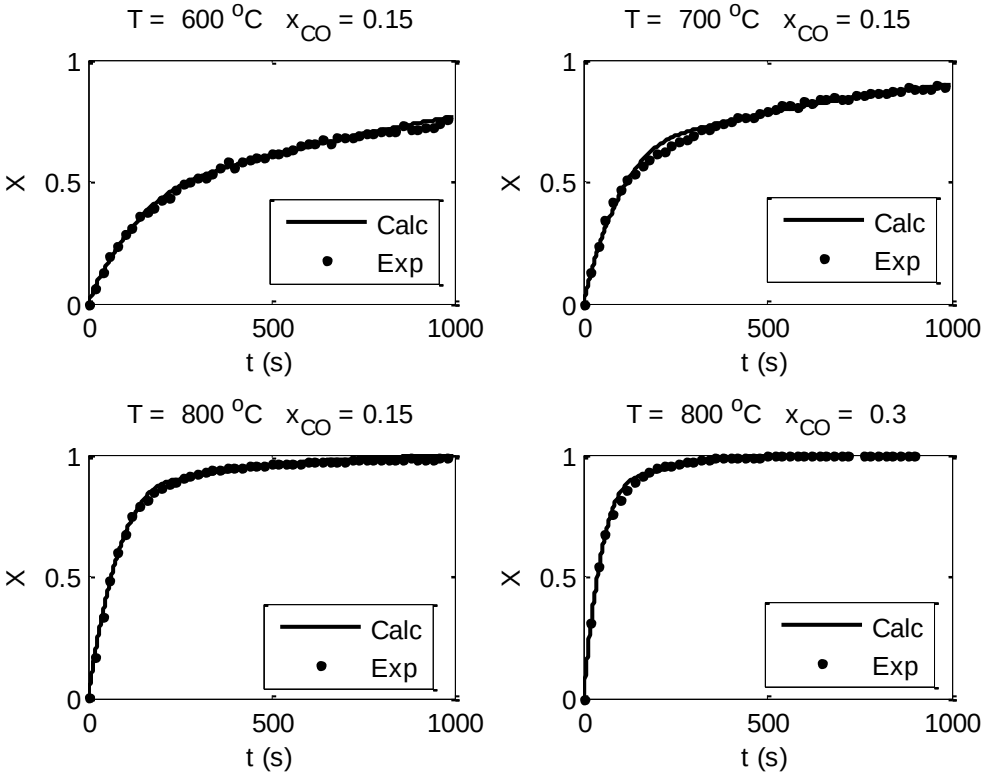

Figure 7.26: Experimental results for the reduction tests with CO, at different temperatures and gas compositions (symbols). continuous model (solid line). For all the sets, $x_{CO2} = 0.20$.

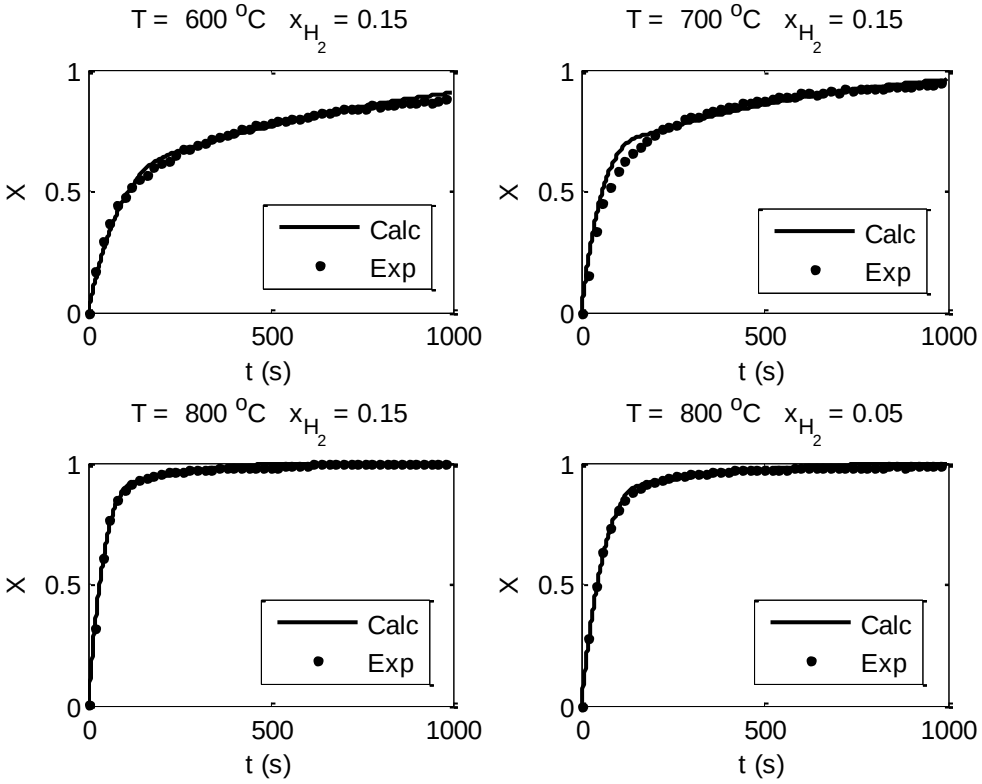

Figure 7.27: Experimental results for the reduction tests with H_2, at different temperatures and gas compositions (symbols). continuous model (solid line). For all the sets, x_{CO2} = 0.20.

The agreement between the calculated and experimental data looks good. Adsorption resistance had to be considered, in order to correctly describe the dependency of the conversion from the reacting gas concentration, particularly for the reduction with hydrogen. Still, some minor discrepancies are visible for the simulations with hydrogen at low temperature, particularly at 700°C where the model predicts a sharper transition between the fast and slow reaction than is not so apparent in the experimental data.

The fitted parameters are reported in Table 7.4. It should be underlined that these figures do not pretend to be intrinsic kinetics for this chemistry, because they are affected by the arbitrary assumptions on the initial distribution. Given that the continuous model accounting for uneven initial distribution of solids within the particle was proven able to properly describe the experimental data, actual kinetics should be determined once the effective initial particle composition is known.

Further to the kinetic parameters of Table 7.4, the Fe_2O_3 and Fe_2TiO_5 fractions used to describe the initial particle distributions were also estimated, for each experiment, given that they use always different solids samples. The resulting values are reported in Figure 7.28. Both for the reduction with CO and with H_2 the initial fraction of hematite has to be larger at higher temperatures to have a good prediction. This means that the solid dissociation of pseudobrookite that occurred during the previous cycles should have different results at different temperatures (the activation of the particles was made for every test at their corresponding temperature). In particular, the dissociation at higher temperature is expected to be larger. On the other hand, CO and H_2 yield fairly comparable results, with a closer match at higher temperatures.

Table 7.4: Values of the calculated kinetic parameters for the reduction with CO and H_2

Reduction with CO			
Reaction	A (mol, cm^3, s)	Ea (J/mol)	K (mol, cm^3)
Fe_2O_3 + CO	5.2e-1	55000	1.71e5
Fe_2TiO_5 + CO	2.3e-4	1000	3.1e4
Reduction with H_2			
Reaction	A (mol, cm^3, s)	Ea (J/mol)	K (mol, cm^3)
Fe_2O_3 + H_2	9.22e4	51000	2.54e6
Fe_2TiO_5 + H_2	7.97	2700	1.50e6

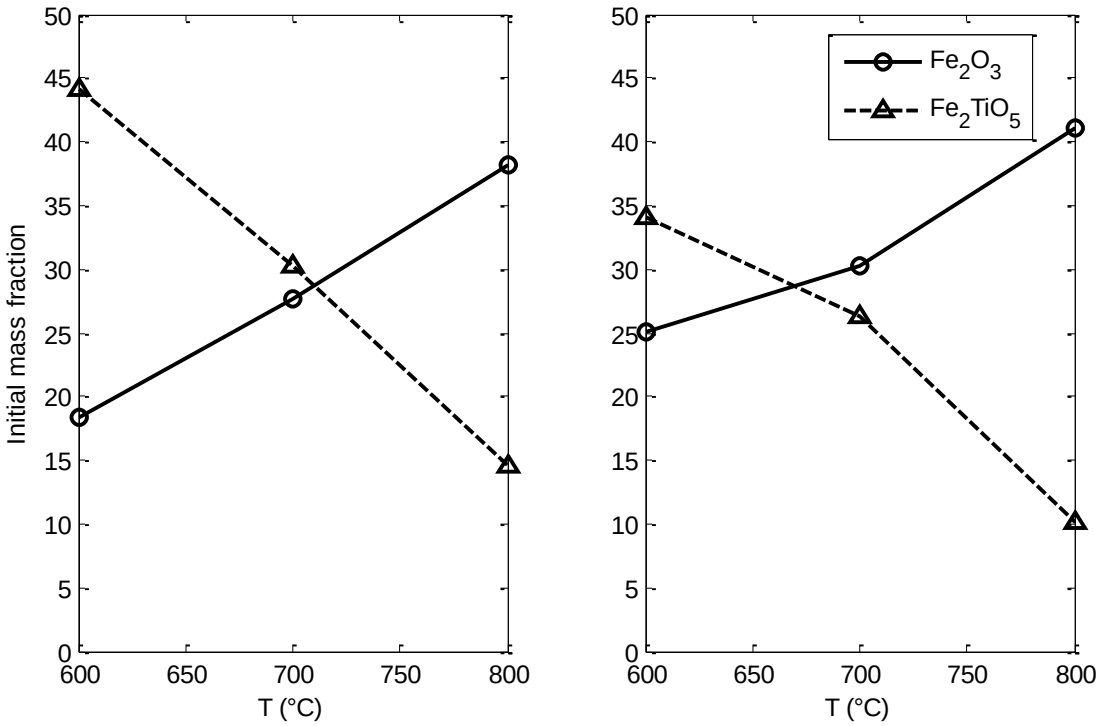

Figure 7.28: Estimated initial hematite and pseudobrookite fractions in the particle for the reduction simulations with CO (left) and H_2 (right)

The uncertainty on the arbitrarily chosen core-shell interface position was also discussed. We simulated the reduction with CO using the parameters estimated above, but changing the initial interface position from r_i/r_0 = 0.80 to r_i/r_0 = 0.85; results are shown in Figure 7.29. For a relatively small change of the initial condition, the results are still reasonable, but some inaccuracies are already clear. The 'knee' is clearly modified and the new results overestimate the solid conversion at long reaction times, at lower temperature.

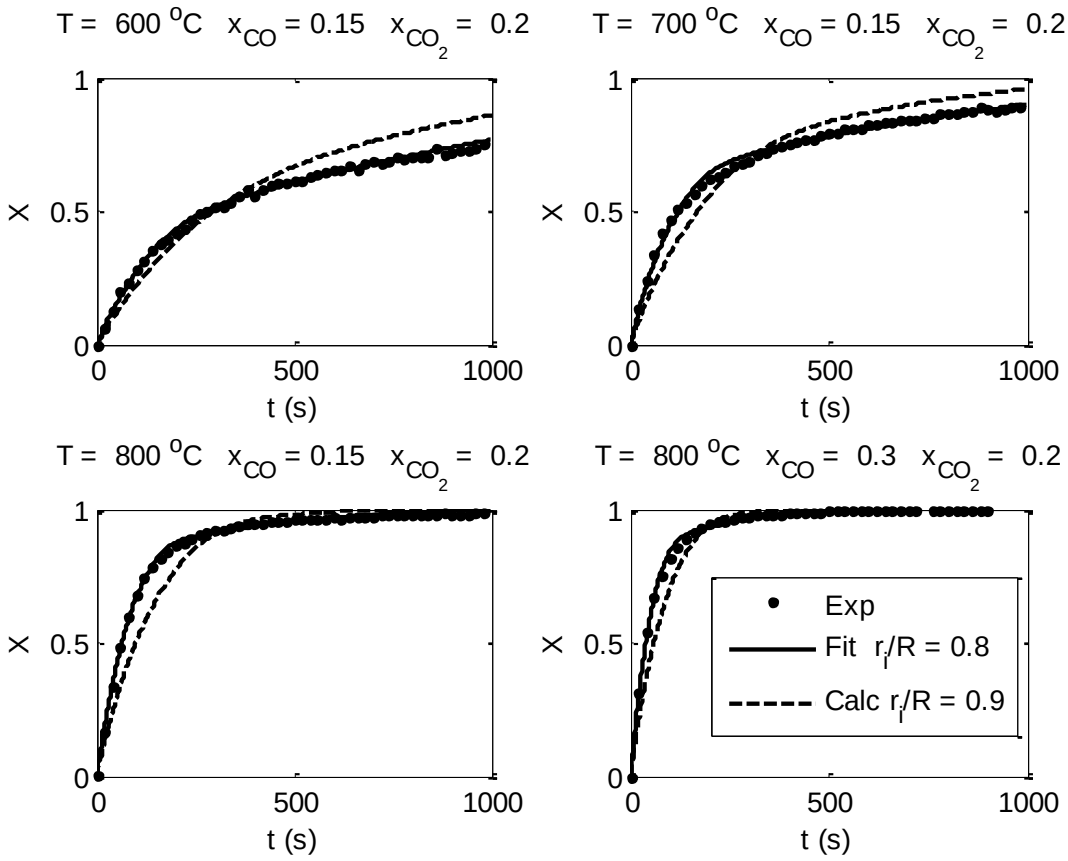

Figure 7.29: Simulation of the experimental data assuming two different positions for the core and shell interface.

In conclusion, the continuous model was reformulated to be able to account for multiple reactions in the porous solid phases and arbitrary composition of the initial particle.

The model was illustrated with reference to the reduction of activated iron-titanium oxides in porous particles used for chemical looping combustion. The model can be adapted to experimental evidences about solid segregation that may be present in activated particles.

The results of the sensitivity analyses prove that the initial solids distribution and composition may have a great influence on the resulting global conversion curve, particularly if the two kinetic constants are very different from each others. The conversion history is quite sensitive to small changes in the core-shell interface, and core-shell composition, but the most important parameter is the global relative abundance of the fast and slow reacting phases. In particular, this has a major impact on the point where the global conversion rate varies over time.

The results of the fitting of the continuous model on the experimental data suggest that a different initial pseudobrookite degree of dissociation is required to properly explain the conversion data at different temperatures. While that could be consistent with activation processes at different temperatures, it remains an indication calling for an experimental confirmation.

Summarizing, the results prove that a thorough investigation on the internal structure and composition of the particle is mandatory to correctly describe particles where solid state segregation occurs or solids with

different reactivities are present. Data about the conversion evolution in time are extremely useful to diagnose the global kinetics but must be supplemented by further internal characterization of the solids, to fully characterize the intrinsic kinetics.

Notation

A	Pre exponential factor of Arrhenius law (mol,cm,s)
c_i^g, c_i^s	Molar concentration, of the i-th gas species, of the i-th solid species (mol/cm^3)
$c^s{}_{i,c}$	Molar concentration of the solid i-th species in the core (mol/cm^3)
$c^s{}_{i,s}$	Molar concentration of the solid i-th species in the shell (mol/cm^3)
$c_i^{g\,0}, c_i^{s\,0}$	Initial molar concentration, of the i-th gas species, of the i-th solid species (mol/cm^3)
$c_{i,bulk}$	Concentration of the i-th gas species outside the particle, in bulk phase (mol/cm^3)
$c_{i,j}^s$	Concentration if the i-th solid species in the j-th pore class (mol/cm^3)
c_{react}^g	Local concentration of the reacting gas species (mol/cm^3)
c^g, c^s	Total concentration of gas phase, of solid phase (mol/cm^3)
cCp	Heat capacity of the medium (J/cm^3/K)
Cp^g	Heat capacity of the gas phase (J/mol/K)
d_i	Size of the pores if the i-th class (cm)
D_i	Effective diffusion coefficient of i used in SCM (cm^2/s)
D_i^K	Knudsen diffusion coefficient of the reacting gas into the pores of i-th class (cm^2/s)
Ea	Activation energy (J/mol)
f_i	Fraction of solid surface occupied by the pores if i-th class
J_i^*	Molar diffusive flux of i (mol/cm^2/s)
k'	Superficial kinetic constant used in SCM (cm/s)
k_i	Volumetric kinetic constant of the i-th reaction, used in CM (mol, cm, s)
k_t	Thermal conductivity of the medium (W/cm/K)
K_i	Adsorption equilibrium constant of the i-th gas species
m_{ox}, m_{red}	Mass of the sample in the oxidized form, in the reduced form (g)
m	Actual mass of the sample (g)
m_i	Mass of the i-th solid component into the particle (g)
MW_i	Molecular weight of the i-th species (g/mol)
MW_{react}	Molecular weight of the reacting gas species (g/mol)
N^g	Total molar flux of the gas phase (mol/cm^2/s)
$nClass$	Number of discretization classes of the pore size distribution
NG	Number of gas species in the system
NS	Number of solid species in the system
r	Radial coordinate (cm)
r_g	Grain radius (cm)
r_i	Coordinate of the core-shell interface (cm)
r_0	Particle radius (cm)
R	Molar reaction rate (mol/cm^3/s)
R_g	Universal gas constant (J/mol/K)
R_O	Oxygen carrier capacity
s_i^g, s_i^s	Molar source term for the i-th gas species, for the i-th solid species (mol/cm^3/s)
$s_{i,j}^s$	Molar source term for the i-th solid species in the j-th pore class (mol/cm^3/s)
T	Absolute temperature (K)
T^0	Initial local temperature (K)

t	Time (s)
x_i^g , x_i^s	Molar fraction of the i-th gas species, of the i-th solid species
X_i	Local conversion of the i-th solid phase
X_{ox}, X_{red}	Average particle conversion in the oxidation step, in the reduction step

Greek letters

α	Sintering exponent
ΔH^R	Heat of reaction, molar based (J/mol)
ε	Porosity
Φ^2	Thiele modulus
ν_i^g , ν_i^S	Stoichiometric coefficient of the i-th gas species, of the i-th solid species
ν_{react}^g	Stoichiometric coefficient of the reacting gas species
ρ_i	Intrinsic density of the i-th solid species (g/cm^3)

Chapter 8. Comparison between the Shrinking Core Model and the Continuous Model

In the previous sections, different approaches to the description of non catalytic gas-solid reactions were considered, also in comparison with real processes and experimental data. All of the presented results proved that the quantitative treatment of reactive solids must be related to a correct description of the actual physics, that can often be extremely complicated by:

1) The heterogeneous nature of the reaction, causing interference of chemical processes (reactions) and transport phenomena (internal diffusion)

2) The modification of the solids structure as a consequence of its reaction.

The most rigorous approach requires solving the microscopic conservation equations for the gas and the solid species within the single particle, with its actual texture. In practice, the porous phase is treated as pseudo-homogeneous continuous phase, with a given porosity (constant or locally variable), and a local concentration of accessible surface per unit volume.

Simplified approaches assume non-porous particles, or non-porous shrinking core model (SCM). The latter is extremely popular, notwithstanding its limitations. It assumes that the reaction takes place only on a surface, dividing the unreacted core by the product layer in the particle, and moving to the center as the reaction goes on. This situation is realistic if the core is not porous. If the particle is completely porous, SCM is still applicable if the reaction is fast compared to the inward diffusion of the gaseous reagent.

In the recent literature, many Authors claim the necessity to use the detailed approach [58-60], but several still choose the shrinking core model because of its simplicity [13, 15, 16, 18]. As already mentioned in section §2, it should be noticed that the physical description of the SCM only holds when the reaction is very fast compared to the diffusion of the gas. On the contrary, when diffusion is fast the gas tends to be uniformly distributed inside the particle (if the particle is initially porous), so the core-shell structure cannot be formed. Beside this, other inconsistencies can originate from the presence of equilibrium reactions, and multiple reaction steps.

In spite of this, the SCM can still be used, especially when an apparent value of the superficial kinetic constant can decently fit the available experimental data. It is possible that the SCM can reasonably approximate the same results as the continuous models, as discussed in this work and frequently stated in the literature [61]. A comparison was made by Ishida and Wen [62], who concluded that in most cases this approximation is good enough. In diffusive regime, Duong demonstrated [63] that the SCM and continuous models can become mathematically identical, no matter which is the chosen expression for the reaction rate.

Nevertheless, the limiting hypotheses implied by the shrinking core model should be a good reason not to use it for most applications (at least when the particle is fully porous, or diffusion is not dominant). Even if SCM can fit the experimental data, this doesn't mean that errors cannot arise when the fitted parameters are used to simulate conditions that are typically different from the available experimental data, if in reality

the particle reaction doesn't produce a core-shell structure. However, this warning is often neglected. In this section, we investigated more deeply into the different behavior of SCM and CM at different conditions, in order to gain more information about the safe applicability of SCM for applications involving porous particles.

Improvements in the quantitative description of reacting porous solids require developing sub-models accounting for the local porosity variations. Restructuring of the solids along the reaction course can affect both the rate of internal diffusion and the surface reaction rate. Sub-models of particle sintering and restructuring can be effectively exploited by particle models that properly describe both surface reactions and internal diffusion, improving on simpler particle models that occasionally and partially mimic the observed conversion evolution. In this section we started a systematic comparison of the models [64]. Here we consider the grain and the traditional models presented in section §4 as reference cases. The study was focused on their different behavior at different controlling regimes. The final aim was also assessing the reliability of the SCM in simulations far away from the experimental data used to establish the apparent kinetic constant, and the possible divergence of the SCM from the continuous model when used in non-diffusion controlled conditions.

8.1 Description of the compared models

8.1.1 Continuous model

For the present analysis, a generic reaction is considered, in which the solid species A and the gas species B yields a solid and a gas species through the irreversible reaction:

$$a\,A(s) + b\,B(g) \rightarrow c\,C(s) + d\,D(g) \qquad 8.1$$

Examples of this model chemistry are the direct reduction of iron oxides by H_2 or CO, calcinations of ZnS and FeS with O_2 to give metal oxides (ZnO, Fe_2O_3), combustion of coal to give CO_2 and ashes.

The conservation equations for the gas and solid species within a porous solid spherical particle, described as a pseudo homogeneous phase were reported in section §4 (equations 4.37-4.41).

In most applications, the gaseous reactants are highly concentrated in the gas phase, often the unique species (no diluents). Accordingly, the diffusive flux requires the generalized Fick law, presented in equations 5.42-5.47, possibly including Knudsen diffusion (equation 5.93) with the effective binary diffusion coefficients depending on the local porosity and tortuosity of the solid (equation 5.109).

Commonly, the tortuosity is considered as a parameter, whereas the porosity depends on the degree of conversion of the solid, due to the fact that the species A and C may have different densities, in general. If no variation of volume of the particle during the reaction is assumed, the porosity variations can be easily calculated, thanks to equations 4.10 and 4.45.

A common choice of the form of the reaction rate R is described assuming irreversibility and first order in the concentration of the gas reactant, but including a non linear function of the solid conversion X, as follows:

$$R = k \cdot f(X) \cdot {c^g}_B \qquad 8.2$$

$$X = 1 - \frac{{c^s}_A}{{c^{s\,0}}_A} \qquad 8.3$$

Where k is the kinetic constant. As already discussed in chapter 4, f(X) describes the local abundance of solid A per unit volume of porous solids. Being the reaction heterogeneous in nature, the relevant measure of abundance is the amount of superficial A per unit volume, which strongly depends on the local structure of the porous solids.

In the present work the traditional model in the form of equation 4.72 was considered. One advantage of using it is that it can be easily extended to non spherical grain geometries, with the parameter α that can take into account different shapes of the micrograins, and can also account for the reshaping phenomena occurring during the reaction, namely sintering of the solid due to high temperatures. If sintering occurs, α will become larger, because there will be a faster decrease of the superficial area at the beginning of the reaction.

The particle model can be solved with the initial and boundary conditions of equations 4.47-4.50.

The solutions of the model are the time and space dependent concentration profiles $c_i(r,t)$ of any species. From $c_i(r,t)$, the function $X(t)$ can be calculated by integration. Initial radial profiles must be provided to the model both for the gas and the solid species. These profiles can also be non uniform in r, for instance if the particle composition is not homogeneous before starting the reaction, as it was evidenced in section §7.

8.1.1.1 Possible simplifications to the continuous model

The model presented above can rigorously simulate the evolution of the conversion of the solid particle in isothermal conditions, provided the correct values for the parameters and the boundary and initial conditions. The model equations can also be somehow simplified, by considering the following assumptions:

a) The gas mixture is composed of only 2 components, B and D.
b) The molecular weights of solid species A and C are almost the same, as well as their intrinsic densities. This allows considering the porosity as a constant.
c) The reaction is equimolar with respect to the gas phase, which means that b = d.
d) The system is isothermal and isobaric.
e) The external mass transfer is very fast, so that the concentration at the particle surface is the same as the bulk of the gas.
f) No change of particle size occurs.

Hypothesis a), b) and d) have an effect on the diffusive flux. If only two components are present, a binary Fick law can be used, with a single diffusion coefficient D_{BD}. If pressure, temperature and porosity are constant, such a coefficient will be constant, and can be carried out of the derivative.

Hypothesis b), c) allow to neglect the convection term in the gas species conservation equations, so that the total concentration balance 4.38 doesn't need to be solved. In fact, the sum of the molar production rates of the gas is zero if the reaction is equimolar. Besides, there is no convection induced by a change in the porosity, which can change the volume occupied by the gas. Actually, the porosity time derivative in 4.37 is usually not important even if hypothesis b) is not verified.

In these conditions, we can write the equations for gas reagent B as:

$$\varepsilon \frac{\partial {c^g}_B}{\partial t} = D_{BD} \frac{1}{r^2} \frac{\partial}{\partial r}\left(r^2 \frac{\partial {c^g}_B}{\partial r} \right) - b\, k \cdot (1-X)^{\alpha} \cdot {c^g}_B \qquad 8.4$$

And for the solid reactant A:

$$\frac{\partial {c^s}_A}{\partial t} = -a\, k \cdot (1-X)^{\alpha} \cdot {c^g}_B \qquad 8.5$$

Also the boundary conditions can be simplified, by using condition e).

$$r = 0 \qquad \frac{\partial {c^g}_B}{\partial r} = 0 \qquad 8.6$$

$$r = r_0 \qquad {c^g}_B = c_{B,bulk} \qquad 8.7$$

$$t = 0 \qquad {c^g}_B = c_B^{g\,0} \qquad {c^s}_A = c_A^{s\,0} \qquad 8.8$$

Equations 8.4-8.5 can also be reformulated in non-dimensional form, as follows:

$$\beta \frac{\partial Y}{\partial \theta} = \frac{1}{\lambda^2} \frac{\partial}{\partial \lambda}\left(\lambda^2 \frac{\partial Y}{\partial \lambda} \right) - b\, \Phi^2 \cdot (1-X)^{\alpha} \cdot Y \qquad 8.9$$

$$\frac{\partial X}{\partial \theta} = a\, \gamma \cdot (1-X)^{\alpha} \cdot Y \qquad 8.10$$

Where the non-dimensional variables are defined as:

$$\theta = \frac{t}{t^*} \qquad \lambda = \frac{r}{r_0} \qquad Y = \frac{{c^g}_B}{c_{B,bulk}} \qquad X = 1 - \frac{{c^s}_A}{c_A^{s\,0}} \qquad 8.11$$

And the following non-dimensional numbers are introduced:

$$\Phi^2 = \frac{k \cdot r_0^2}{D_{BD}} \qquad \beta = \frac{\varepsilon\, r_0^2}{t^*\, D_{BD}} \qquad \gamma = k \cdot t^* \cdot \frac{c_{B,bulk}}{c_A^{s\,0}} \qquad 8.12$$

Where t* is the time for having full conversion of the particle. Φ^2 is the Thiele modulus, so its value quantifies the ratio between the kinetic and diffusive resistance. The boundary conditions in non dimensional form are:

$$\lambda = 0 \qquad \frac{\partial Y}{\partial \lambda} = 0 \tag{8.13}$$

$$\lambda = 1 \qquad Y = 1 \tag{8.14}$$

$$\theta = 0 \qquad Y = Y_0 \qquad X = 0 \tag{8.15}$$

This version of the continuous model was chosen to carry out a comparison with SCM. Although the simplifications introduced to derive such a simplified CM are quite relevant, our aim is comparing SCM and CM in the conditions where the two models are closer (same diffusion model, same transport phenomena, same effective diffusivities, same kinetic scheme). As shown below, differences in the numerical results can be dramatic.

8.1.2 Shrinking core model

The same gas solid reaction can be described with a shrinking core model. It assumes that the reaction is localized at an interface r*, moving from the external surface of the particle to its center as long as the reaction goes on. It is deduced by solving the equations for the gas reactant, where the reaction is a boundary condition at the core-shell interface, and only diffusion occurs in the layer between the reaction interface and the external particle surface. The model details are described in section §2.

For the considered stoichiometry (equation 8.1), the balance describing the evolution of the reagent solid A becomes as follows:

$$\frac{dC_A}{dt} = -a\frac{3\,{r_i}^2}{r_0^3}\cdot\frac{c_{B,bulk}}{\frac{1}{k'} + r_i\left(1-\frac{r_i}{r_0}\right)\frac{b}{D_{BD}}} \tag{8.16}$$

Or, in terms of conversion X:

$$\frac{dX}{dt} = \frac{3}{r_0}\cdot\frac{1}{\frac{1}{k'}\cdot(1-X)^{-2/3} + \frac{b\,r_0}{D_{BD}}\cdot(1-X)^{-1/3} - \frac{b\,r_0}{D_{BD}}}\cdot a\frac{c_{B,bulk}}{c_A^{s\,0}} \tag{8.17}$$

Note that equation 8.17 is very similar to the equation of the complete grain model (equation 4.70). The grain model is in fact an application of the shrinking core model to the grain scale, and the two models become eventually equivalent if $a_0 = 3/r_0$ (the initial surface-volume ratio of the solid in equal to the surface area of the particle), and $k = a_0 k'$. If the concentration of B at the pellet surface is constant in time, as well as the system temperature, the equation has an analytical solution, quite simple as *t(X)*:

$$t(X) = \tau_K \cdot \left[1 - (1-X)^{1/3}\right] + \tau_D \cdot 3\left[1 - (1-X)^{2/3} - 2/3 \cdot X\right] \quad 8.18$$

$$\tau_K = \frac{r_0}{a\, k'} \frac{c_A^{s\,0}}{c_{B,bulk}} \quad 8.19$$

$$\tau_D = \frac{b\, {r_0}^2}{6\, a\, D_{BD}} \frac{c_A^{s\,0}}{c_{B,bulk}} \quad 8.20$$

In this formulation, τ_K and τ_D quantify the importance of the kinetic and internal diffusion resistances respectively.

In non-dimensional form:

$$\theta(X) = \frac{\tau_K}{\tau_K + \tau_D} \cdot \left[1 - (1-X)^{1/3}\right] + \frac{\tau_D}{\tau_K + \tau_D} \cdot 3\left[1 - (1-X)^{2/3} - 2/3 \cdot X\right] \quad 8.21$$

A Thiele modulus can also be defined for the SCM, which is directly related to the ratio between the two characteristic times τ_K and τ_D:

$$\Phi^2 = \frac{3\, k' \cdot\, r_0}{D_{BD}} = \frac{18}{b} \frac{\tau_D}{\tau_K} \quad 8.22$$

Equation 8.21 for the two regimes becomes:

$$\theta(X) = \left[1 - (1-X)^{1/3}\right] \qquad (kinetic) \quad 8.23$$

$$\theta(X) = 3\left[1 - (1-X)^{2/3} - 2/3 \cdot X\right] \qquad (diffusive) \quad 8.24$$

These expressions are independent from the values of the parameters (τ_K and τ_D will have an effect on the actual non normalized time scale). They are also the two asymptotic profiles, in the sense that any other curve in the intermediate regime will lay in between the two.

In order to quantify how well a shrinking core model can numerically approximate a continuous model, the comparison with a simplified generalized grain model will be considered. It is true that some of the degree of detail that a fully rigorous continuous model can offer is lost in the simplified version (equations 8.9-8.10), and sometimes some of the hypothesis mentioned are not verified. Yet, this comparison is quite useful because it concerns the non analytical model closest to the shrinking core, and so it can be a good indication whether it is necessary or not to use a continuous model, instead of a shrinking core that could approximate its same solution. The effect of natural convection, change of porosity, temperature and external mass transfer can add further differences between the two approaches, and each of these should be analyzed individually, as it was proved in section §6.

Even more complications can originate when considering multiple reactions, possibly reversible. The present comparison is focused on the effect of sintering, expressed by the parameter α, and the effect of the controlling regime. Further, we aim at spotting those circumstances in which the two models may give

the same (or similar results) by coincidence, even if they almost always reflect very different physics of the reacting particle. Since a simplified version of the CM, sharing some assumption with SCM, was chosen for the analysis, we expect even larger errors using a more sophisticated CM, closer to the real behavior of some reacting porous solids.

8.2 Comparison of the two models

In Figure 8.1, the concentration profiles for the solid and the gas within the particle at X = 0.5 are shown, for different values of Φ^2 as given by both CM and SCM models.

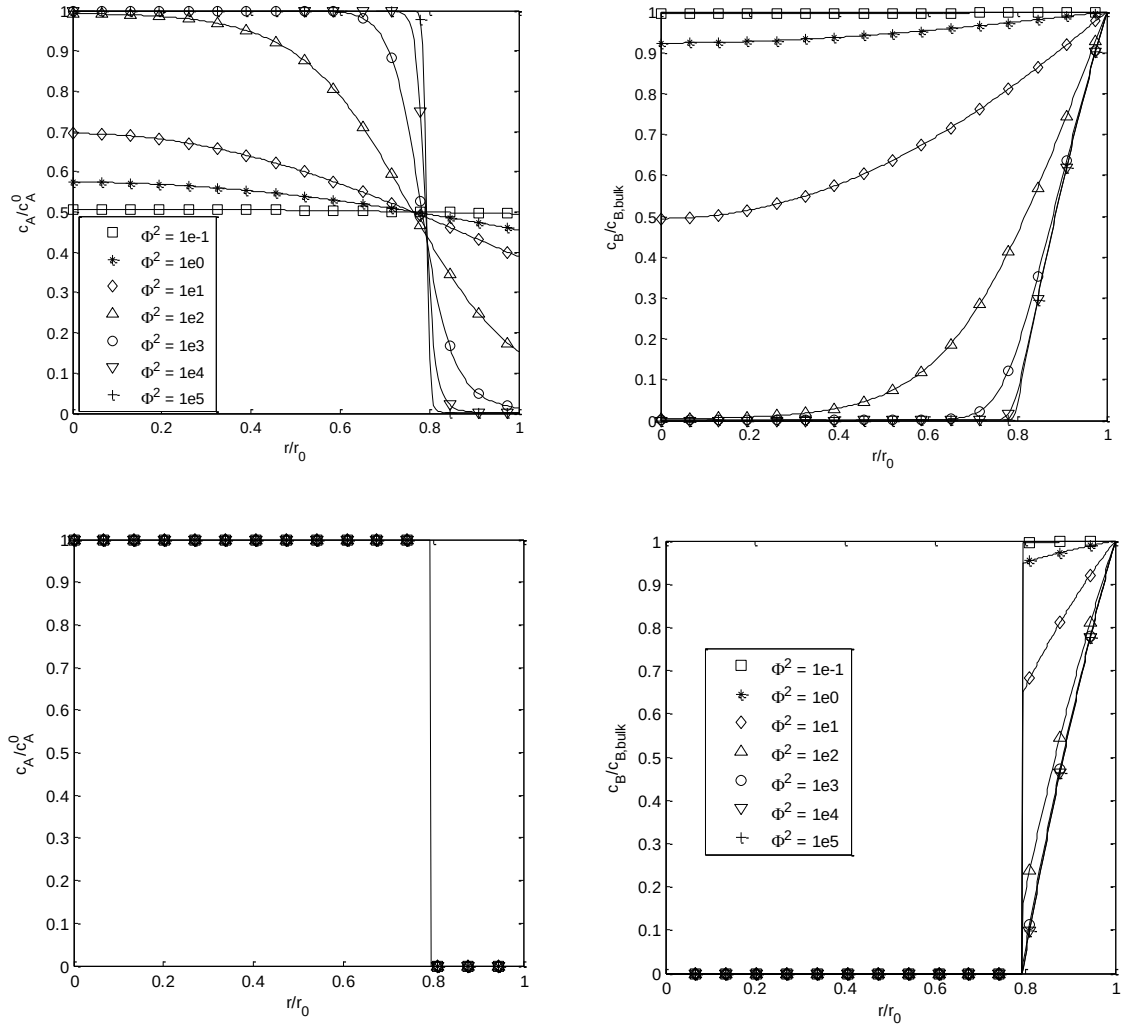

Figure 8.1: Simulated concentration profiles inside the particle for the solid (left) and the gas (right) at different values of Φ^2, at X = 0.5. Continuous model (top) and shrinking core model (bottom).

At low values of Φ^2 both models predict a uniform concentration profile of the gas across the particle (just the shell, for SCM), but while the grain model predicts a uniform concentration profile for the solid, the shrinking core still maintain a step profile corresponding to the reaction interface, which is present no matter what the regime is. At high values of Φ^2, the grain model converges to the step function for the solid concentration, and for the gases both models approach the same distribution, with the reactant concentration dropping to zero at the reaction interface.

Depending on the value of Φ^2, three regimes can be identified: diffusive (high Φ^2), kinetic (low Φ^2), and mixed (intermediate Φ^2). Figure 8.2 shows more intuitively how the continuous model describes the solid distribution inside the particle for the three regimes. At a fixed reaction time, these reflect the concentration profiles reported on the top left picture of Figure 8.1. On the other hand, the SCM can only represent the situation shown on the top of Figure 8.2.

In the following sections, the results of the two models have been quantitatively compared for the three regimes separately.

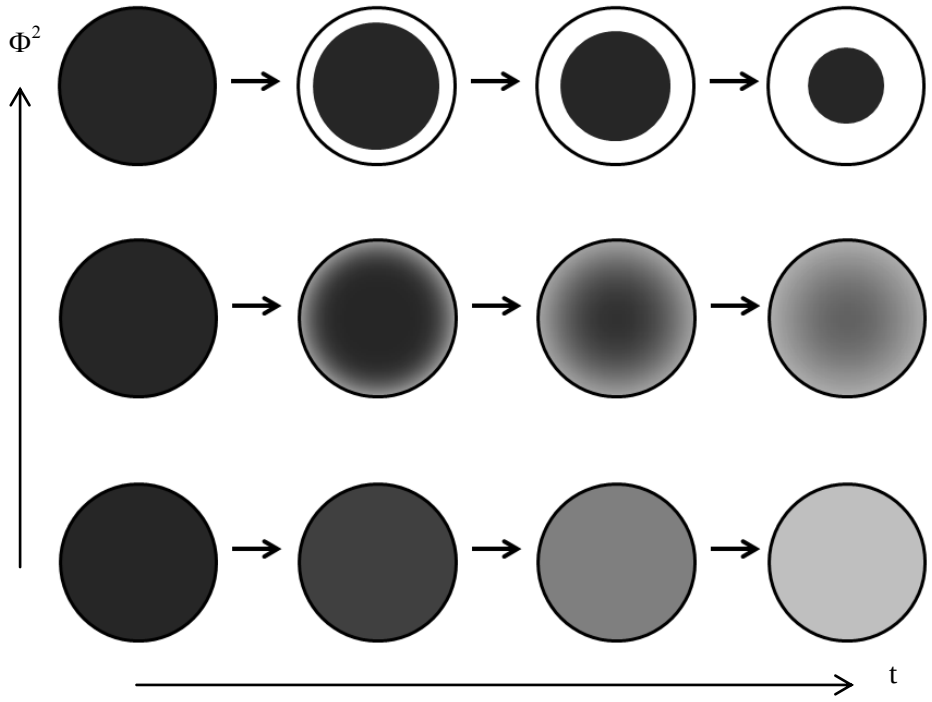

Figure 8.2: Description of the evolution of the solid particle with the CM for diffusive regime (top), mixed (middle), and kinetic (bottom).

8.2.1 Diffusive regime

In diffusive regime, the reaction rate is fast compared to the rate of transport of the gas within the solid. This is precisely the case when the shrinking core model correctly describes the same physics of the particle as the grain model does.

It can be demonstrated [63], that if Φ^2 is very large, equations 8.9 and 8.10 have the same solution as a shrinking core model like eq. 8.21where $\tau_K = 0$. In this case, the solution for the two models is the same:

$$t(X) = \frac{b\, r_0{}^2}{2\, a\, D} \frac{c_A^{s\,0}}{c_{B,bulk}} \cdot \left[1 - (1-X)^{2/3} - 2/3 \cdot X\right] \qquad 8.25$$

The convergence of the two solutions is also shown in Figure 8.1, for $\Phi^2 = 10^4$-10^5.

It is important to note that in diffusive regime the value of the kinetic constant is not important, and also the expression of the reaction rate. That's why the conversion profile will be independent from the value of α. This also means that it's not even necessary to fit any parameter for the shrinking core model in order that its solution matches the solution of the continuous model, it just suffices to use the same value for the diffusion coefficient of the gas in the solid matrix. The common solution of the two models is the same, as shown in Figure 8.3:

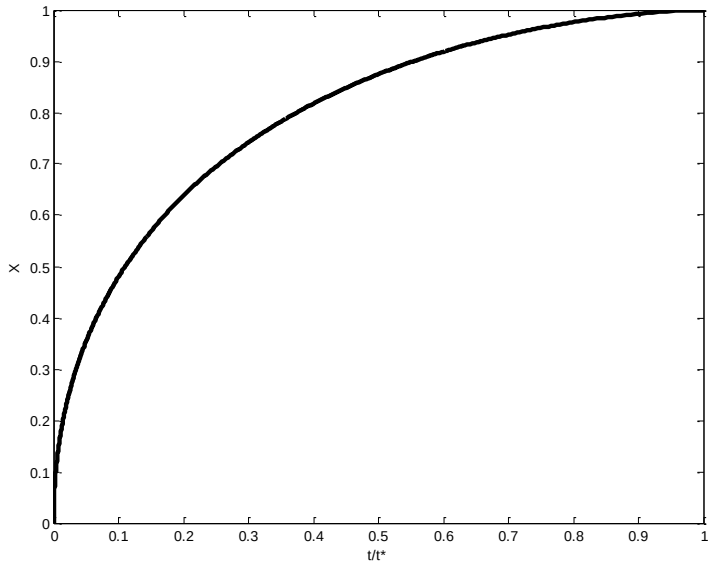

Figure 8.3: Simulated particle conversion profiles in total diffusion control. CM and SCM provide the same solution.

8.2.2 Kinetic regime

In kinetic regime, the transport of the gas within the solid particle is very fast, compared to the reaction rate. Kinetic regime is reached when the diffusion coefficient D_{BD} is very large, particularly compared to the kinetic constant. For the continuous model (§2.2), this is equal to assume that Φ^2 and β approach zero. In this case, the non dimensional mass balances of gaseous reagent B (8.9) becomes:

$$\frac{1}{\lambda^2}\frac{\partial}{\partial\lambda}\left(\lambda^2 \frac{\partial Y}{\partial\lambda}\right) = 0 \qquad 8.26$$

With the boundary conditions:

$$\frac{\partial Y}{\partial \lambda} = 0 \qquad \lambda = 0 \tag{8.27}$$

$$Y = 1 \qquad \lambda = 1 \tag{8.28}$$

The solution is Y = 1 for any normalized radius, λ. This means that the concentration of B is equal to the bulk concentration in any point of the pellet. In the case of a classical grain model (α = 2/3), the concentration balance for the solid reactant A becomes:

$$\frac{dc^{s}{}_{A}}{dt} = -a\,k \cdot (1-X)^{2/3} \cdot c_{B,bulk} \tag{8.29}$$

In terms of conversion:

$$\frac{dX}{dt} = a\,k \cdot (1-X)^{2/3} \cdot \frac{c_{B,bulk}}{c_A^{s\,0}} \tag{8.30}$$

So that the continuous model has analytical solution as well, if $c_{B,bulk}$ is constant in time:

$$t_{CM}(\mathrm{X}) = \frac{3}{a\,k} \cdot \frac{c_A^{s\,0}}{c_{B,bulk}} \cdot \left(1-(1-X)^{1/3}\right) \tag{8.31}$$

In kinetic regime, the SCM solution can be obtained by considering $\tau_D = 0$ in equation 8.21:

$$t_{SCM}(X) = \frac{r_0}{a\,k'} \frac{c_A^{s\,0}}{c_{B,bulk}} \cdot \left(1-(1-X)^{1/3}\right) \tag{8.32}$$

Comparing the results of equation 8.31 and 8.32, we see that they are identical when we set:

$$k' = k \cdot \frac{r_0}{3} \tag{8.33}$$

So the superficial kinetic constant for the shrinking core model is equal to the volumetric kinetic constant of the continuous model, divided by the surface-to-volume ratio of the whole particle. In other words, the product between the superficial constants of the two models and their respective initial superficial areas of the solid reacting phase is the same. Note that this is true only because the grain model is applied.

It is interesting to point out that the analogy of solutions is a coincidence. In fact the two models are physically describing two completely different situations: on the one hand, the shrinking core simulates a single macro particle, with the solid A converting from the external surface to the core. On the other one, the continuous model describes a particle reacting homogeneously along the radial coordinate. The numerical results of the two are, however, precisely the same. This is because the grain model is actually representing a number of micrograins, with all the same size and all reacting like shrinking cores with the same rate, because the concentration of the gas is the same in any point of the macro pellet.

8.2.2.1 Study for a generic value of α

We now investigate the extent of adaptation of SCM to the classical grain model (α = 2/3). If we consider a general expression of the superficial area of the reacting species as a function of the conversion within the continuous model:

$$R = k \cdot (1 - X)^{\alpha} \cdot c^{g}{}_{B} \qquad 8.34$$

We obtain the generalized grain model. In kinetic regime that leads to:

$$\frac{dX}{dt} = a\, k \cdot (1 - X)^{\alpha} \cdot \frac{c_{B,bulk}}{c_A^{s\,0}} \qquad 8.35$$

Which can be analytically integrated as well, giving:

$$t_{CM}(X) = \frac{1}{a\, k} \cdot \frac{c_A^{s\,0}}{c_{B,bulk}} \cdot \frac{1}{1 - \alpha} (1 - (1 - X)^{1-\alpha}) \qquad 8.36$$

We can evaluate how close the shrinking core model can approach the continuous model in a kinetic regime, depending on α, by considering the difference of the two *t(X)* analytical solutions, 8.32 and 8.36:

$$\Delta t(X) = t_{SCM} - t_{CM} = \frac{c_A^{s\,0}}{a\, c_{B,bulk}} \cdot \left(\left(\frac{r_0}{k'} - \frac{1}{k\,(1 - \alpha)} \right) - \frac{r_0}{k'} \cdot (1 - X)^{1/3} + \frac{1}{k\,(1 - \alpha)} \cdot (1 - X)^{1-\alpha} \right) \qquad 8.37$$

The kinetic constant k' by which the SCM best approximates the continuous model can be estimated by least squares criteria, requesting the best match between t_{CM} and t_{SCM} over the whole range of conversion:

$$\min_{k'} \int_0^1 \left(\Delta t\left(k', X\right) \right)^2 dX \qquad \rightarrow \qquad \frac{\partial}{\partial k'} \int_0^1 \left(\Delta t\left(k', X\right) \right)^2 dX = 0 \qquad 8.38$$

Substituting equation 8.37 into 8.38, calculating the derivative and solving the equation in k' we obtain:

$$k'_{opt} = k \cdot r_0 \cdot \frac{2(3\alpha - 7)(2 - \alpha)}{5(3\alpha - 10)} \qquad 8.39$$

It is trivial to see that, if α = 2/3, equation 8.39 reduces to equation 8.33. Note that k'_{opt} in the least squares sense does not imply a coincidence of *t(X)* for both models at any *X* value.

Note that, for α > 1, the function described by equation 8.36 diverges for X-->1, suggesting that the integral of equation 8.38 might not converge. However, carrying out the algebra we find that the error function given by the integral is finite, except for α=3/2, 2, 7/3:

$$E(k') = \int_0^1 \left(\Delta t(k', X) \right)^2 dX = \qquad 8.40$$

$$= \left(\frac{c_A^{s\,0}}{a\, c_{B,bulk}} \right)^2 \cdot \left(\left(\frac{r_0}{k'} \right)^2 \cdot \frac{1}{10} + \left(\frac{1}{k} \right)^2 \cdot \frac{2}{(3 - 2\alpha)(2 - \alpha)} + \frac{r_0}{k \cdot k'} \cdot \frac{3\alpha - 10}{2(2 - \alpha)(7 - 3\alpha)} \right)$$

Plotting the error function given by the integral as a function of k' results qualitatively in Figure 8.4. This suggests that the minimum is quite narrow. Departures from k'_{opt} leads to large divergence of predictions between the two models, much larger in case k' is underestimated.

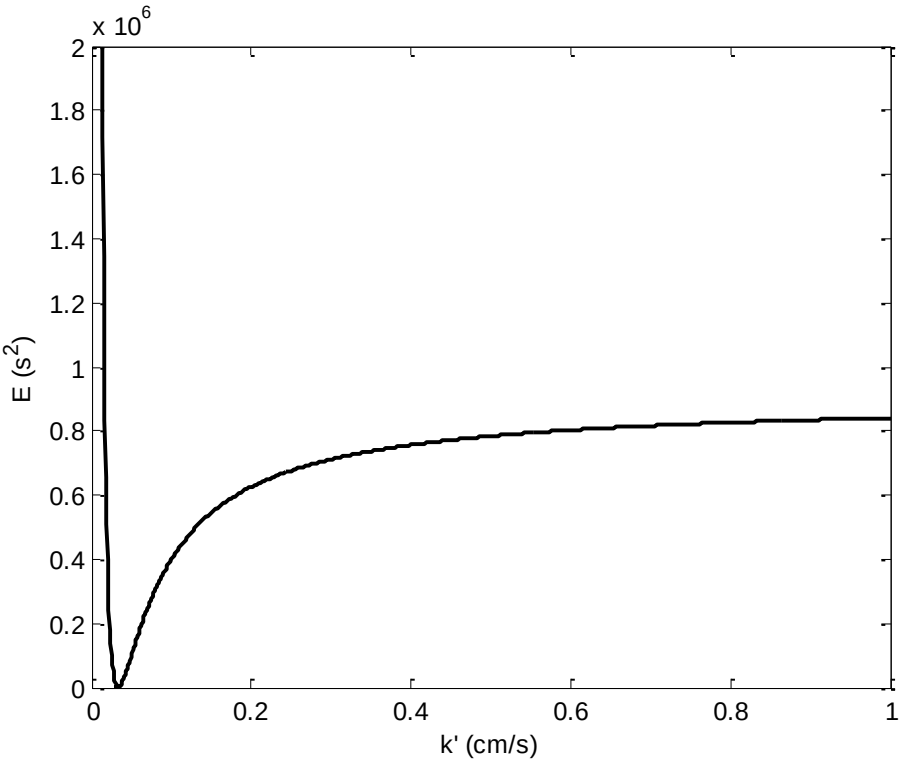

Figure 8.4: Calculated least squares error as a function of the fitted k' for the grain model (α = 2/3). Values of the parameters: r_0 = 100 µm, $c_A^{s\,0}$ = 10^{-2} mol/cm^3, $c_{A,bulk}$ = 1e^{-6} mol/cm^3, k = 10 s^{-1}, a = 1

By substituting k'_{opt} into the error function 8.40, we can study the locus of the minima as a function of alpha:

$$E_{opt} = \left(\frac{c_A^{s\,0}}{a\, c_{B,bulk} \cdot k}\right)^2 \cdot \frac{(6\alpha - 17)(3\alpha - 2)^2}{8(\alpha - 2)^2(3\alpha - 7)^2(2\alpha - 3)} \qquad 8.41$$

This function is nonnegative for any α<1 (when the integration is always possible), and has a single zero for α = 2/3. This is consistent with what we already obtained before. Figure 8.5 shows this curve as a function of α.

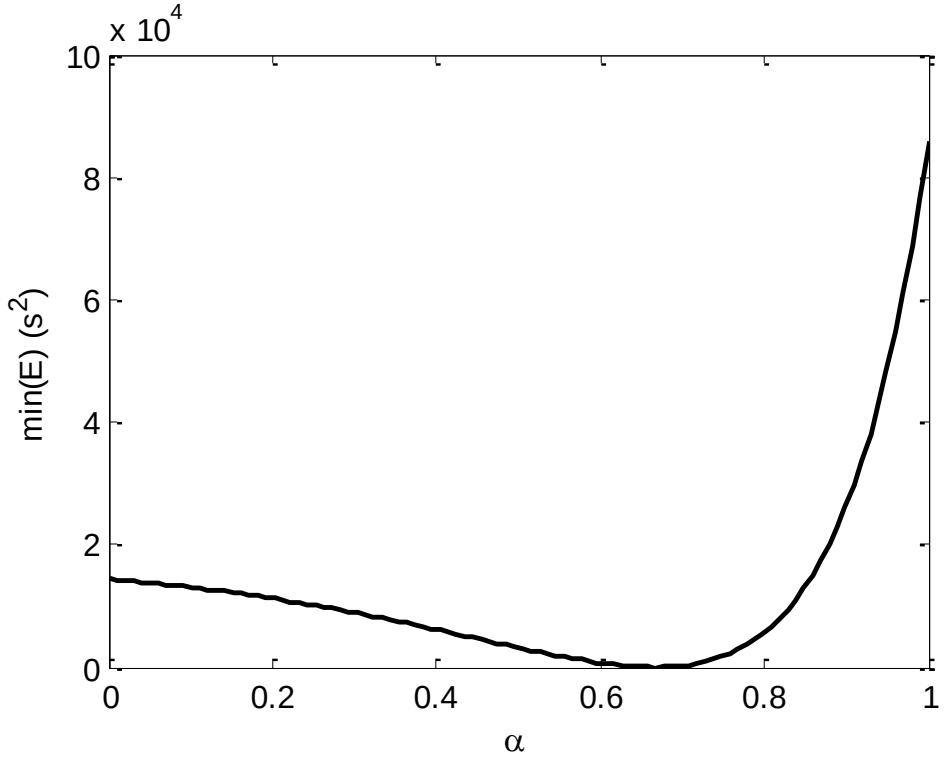

Figure 8.5: Minimum of the integral of square errors from fitting k' for the SCM to the conversion profiles of CM as a function of α

The error made with a shrinking core looks to be more important for α > 2/3 than for α < 2/3. However, it's not very clear how big the error is from this profile, since it represents the square of the difference of the two areas defined by the graphs of two conversion functions (8.32 and 8.36). Accordingly, relative errors have been calculated and reported in the main text.

We define the relative error of the shrinking core model with respect to the continuous model as:

$$e_r(X) = \frac{t_{SCM}(X) - t_{CM}(X)}{t_{CM}(X)} \qquad 8.42$$

By replacing t_{SCM} with equation 8.32 and t_{CM} with 8.36, and using the optimum value for k' as in eq. 8.39, we obtain:

$$e_r(X) = \frac{5\,(3\alpha - 10\,)(1-\alpha)}{2\,(3\alpha - 7)\,(2-\alpha)} \cdot \frac{\left[1-(1-X)^{1/3}\right]}{\left[1-(1-X)^{1-\alpha}\right]} - 1 \qquad 8.43$$

Which is a function of α and X alone. Other parameters like $c_A^{s\,0}$, $c_{B,bulk}$, k, r_0 are not relevant so that the indications of e_r are quite general. In Figure 8.6, e_r is plotted as a function of X for different values of α.

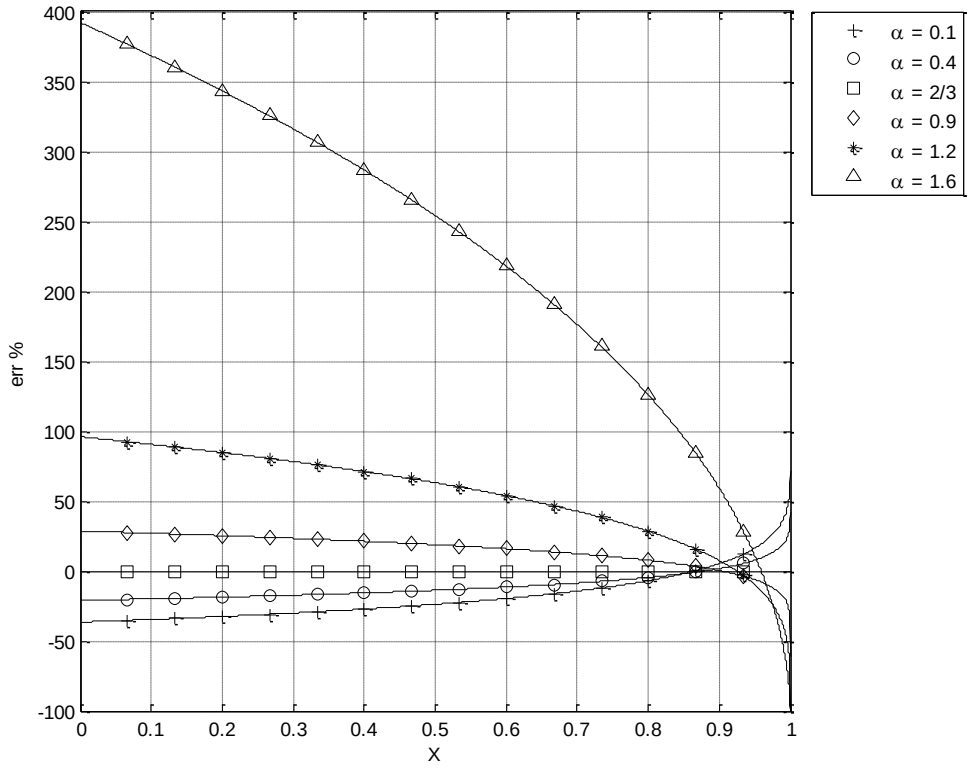

Figure 8.6: Relative difference (%) between the SCM and CM models as a function of the conversion and α, in the kinetic regime

The relative difference between the models can be quite important when α ≠ 2/3. It already rises up to 20-30% even for the two cases closest to the grain model (α = 0.4 and α = 0.9). For α > 1 the error increases dramatically. Low values of X amplify the error in any case (except α = 2/3). These observations can be somehow deceiving, because for low conversions, the absolute error also decreases down to zero. For this reason, it can be useful to examine the absolute error:

$$e_a(X) = \frac{t_{SCM}(X) - t_{CM}(X)}{t_{CM}(X = 0.99)} \qquad 8.44$$

In this case, the difference between the conversion times for the shrinking core and the generalized grain model is scaled on the calculated time for CM required to achieve 99% of conversion. This scaling is done in order to have comparable results, so the error is relative to one second of total reaction time (actually, it has been chosen X = 0.99 because the solution of the continuous model for α > 1 is asymptotic to X = 1).

The results are shown in Figure 8.7. At intermediate conversions, the error is limited (approx. < 10%) of the total reaction time. For conversion close to 1, the difference can easily exceed 30-40%.

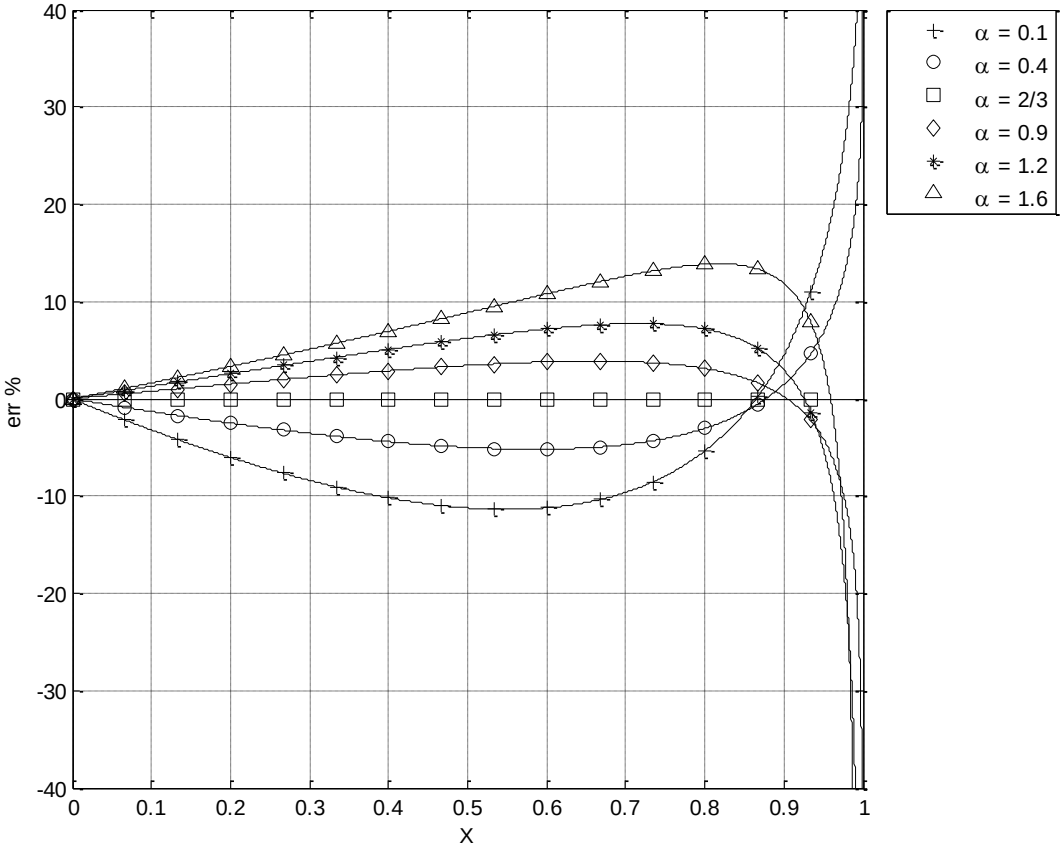

Figure 8.7: Absolute difference between the two models as a function of the conversion and α, scaled on the total conversion time, for kinetic regime (%)

The relative error between the two models can be averaged over *X*, by calculating the integral mean of the function 8.43:

$$\overline{e_r} = \int_0^1 \left| \frac{5\,(3\alpha - 10\,)(1-\alpha)}{2\,(3\alpha - 7)\,(2-\alpha)} \cdot \frac{\left[1-(1-X)^{1/3}\right]}{\left[1-(1-X)^{1-\alpha}\right]} - 1 \right| dX \qquad 8.45$$

The absolute value is to be used, in order to avoid cancelling negative and positive errors. This function is plotted in Figure 8.8.

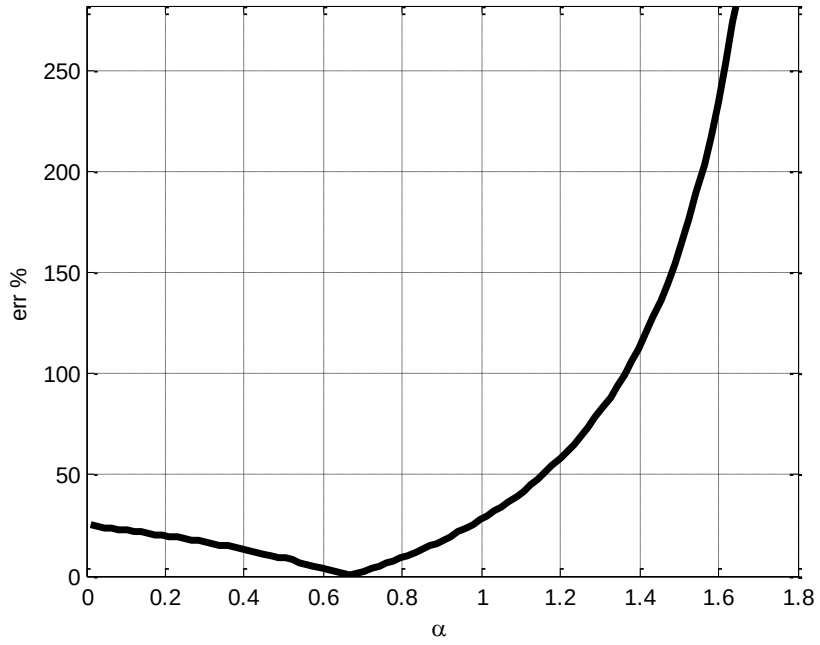

Figure 8.8: Mean relative difference (%) between the two models as a function of α. Kinetic regime

This qualitatively resembles the same as the integral of square errors as a function of α reported in Figure 8.5. Again, the error increases more quickly for α > 2/3 than for low α.

Finally, the comparison of the simulated conversion history obtained with the two models for the lowest and highest values of alpha (0.1 and 1.6) corresponding to the errors plots in Figure 8.6 and Figure 8.7 are shown in Figure 8.9 and Figure 8.10, respectively.

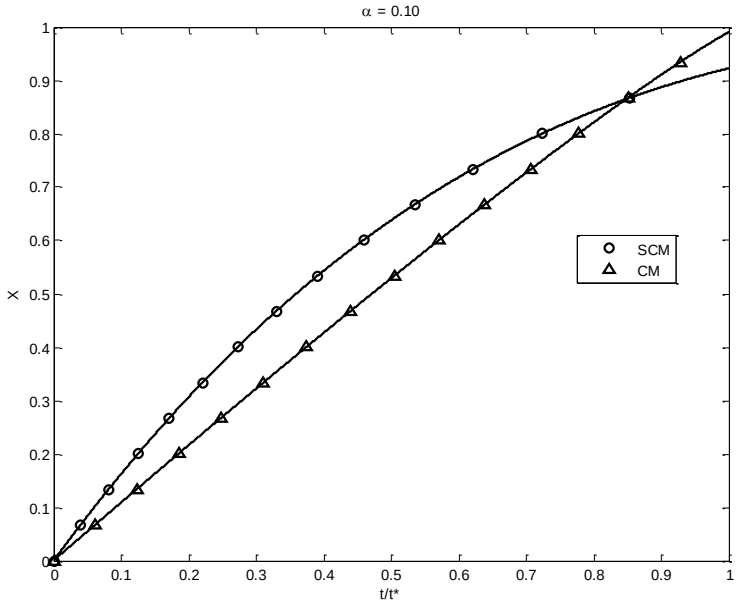

Figure 8.9: Conversion profiles of a single particle, simulated with CM (Δ) for α = 0.1, and comparison with the fitted profiles from SCM (o). Kinetic regime

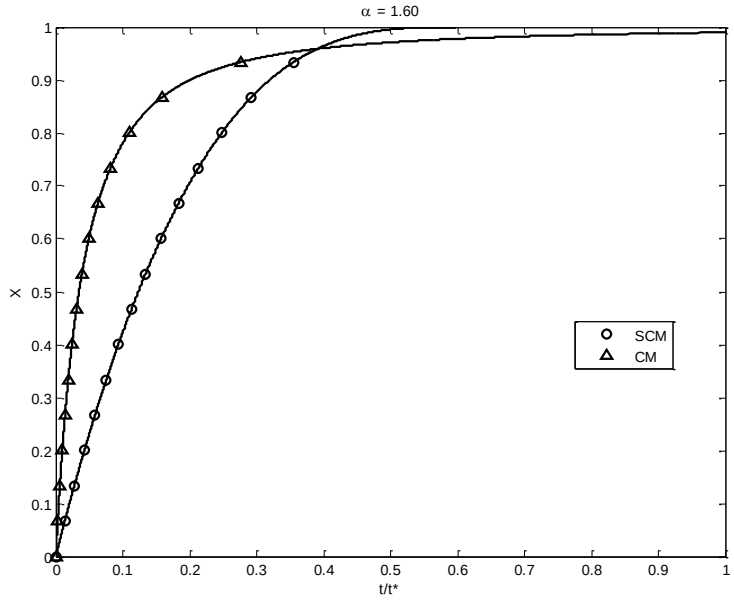

Figure 8.10: Conversion profiles of a single particle, simulated with CM (Δ) for α = 1.6, and comparison with the fitted profiles from SCM (o). Kinetic regime

A large value of α reflects solids where an important decrease of the reaction rate occurs when approaching to full particle conversion, whereas a low value of α can simulate a constant rate. The shrinking core model cannot discriminate these different behaviors.

In conclusion, in kinetic regime the shrinking core can perfectly simulate the results of the classical grain model (α = 2/3), but if α ≠ 2/3 the differences between the two models can be relevant.

8.2.3 Intermediate regime

It can be interesting to compare the behavior of the two models considering both resistances (kinetic and diffusive), i.e. intermediate values of the Thiele modulus. It has been demonstrated that in kinetic regime the kinetic constant for the SCM, *k'*, that best approximates the continuous model is given by equation 8.39, whereas in diffusive regime the same effective diffusion coefficient makes the two models identical, no matter what the value of α is.

This two pieces of information can be used together to fully characterize the values of the parameters in equations 8.18-8.20. The relative error between the two models can be calculated as in 8.42; now the t_{SCM} are calculated using both τ_K and τ_D. Simulations were carried on for different values of Φ^2 and α, and the results are synthetically shown in Figure 8.11 in terms of relative error averaged over the whole *X* range.

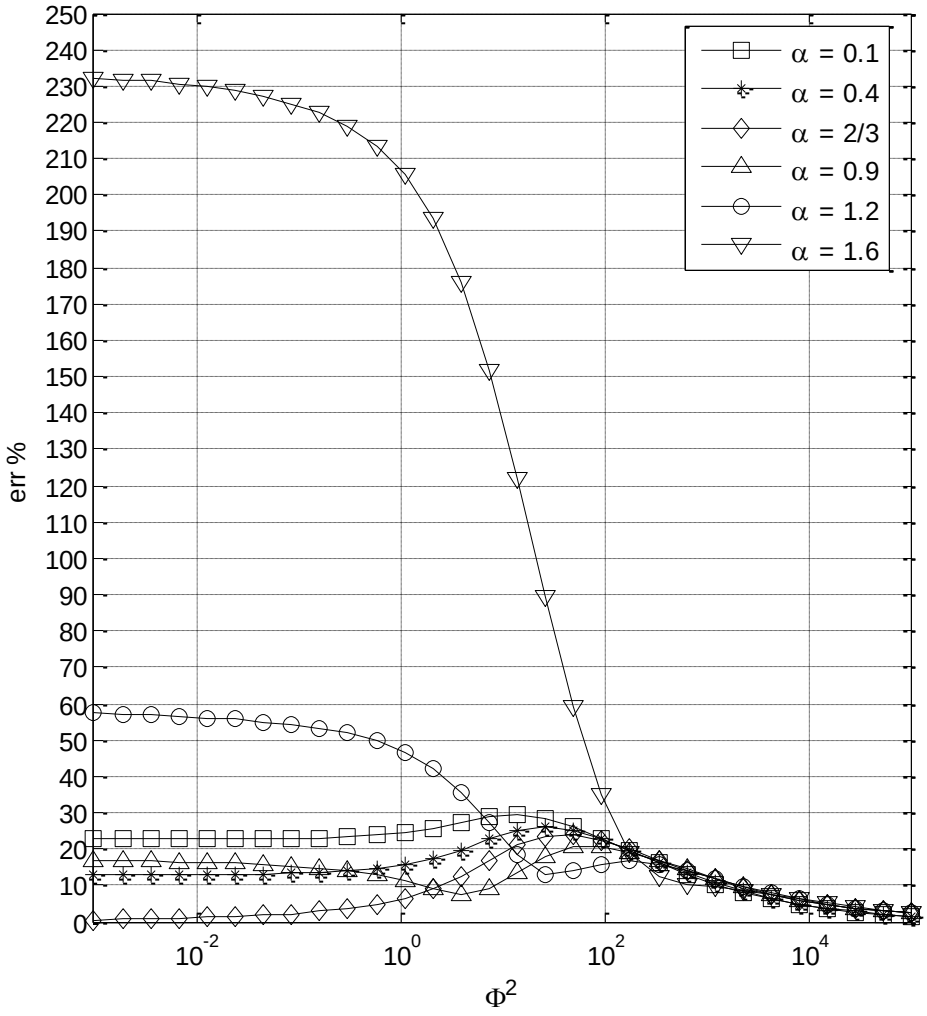

Figure 8.11: Mean relative difference (%) between the CM and SCM models, as a function of Φ^2 and α, after fitting *k'* in SCM for any different value of Φ^2 and α.

The behavior of the curves at extremely low and high Thiele modulus are in agreement with the results shown above for the kinetic and diffusive regimes, respectively. In particular, for low values of Φ^2, when diffusion is not important, the profiles are asymptotic to the errors shown in Figure 8.5 for the corresponding values of α. At the opposite side, for large Φ^2, when the values of k and the form of the kinetic rate expression no longer matter, the error drops to zero for any value of α. In between the two regimes there are unexpected variations of the error, depending on the value of α.

a) For α < 1 the error has a local maximum value in the intermediate regime, which is higher than the error in the kinetic regime. In the case of 2/3 < α < 1 there is also a local minimum. It can be noticed that, also for the grain model, which is the closest model to the SCM, the error can exceed 20% near the maximum. The values of the absolute maxima for α < 1 decrease with increasing α.
b) For α > 1 the error decreases at larger Φ^2. Local minimum and maximum are possible (e.g. α = 1.2), but in any case the error is always lower than the asymptotic value for $\Phi^2 \rightarrow 0$.

The first type of behavior is in agreement with the mathematical approach followed so far, according to which the values of the parameters used in the SCM are optimized for the limit cases. The second behavior is more consistent with the physical point of view: according to that, the more important the diffusion is, the closer the representation of the evolution of the particle according to the two models can get.

Unexpectedly, quite large deviations between the SCM and CM are observed also in the intermediate regime, and much larger than those observed in the kinetic regime, where the SCM is conceptually in error.

8.3 Particle size issues

The matching of the two models has been analyzed above, in the case of the kinetic regime, by fitting the kinetic constant of the SCM to the continuous model. As shown by equation 8.39, the optimum value of k' depends on the size of the particle, r_0, which is one of the variables that also affects the controlling regime (larger values of r_0 mean larger Φ^2); a larger particle implies a more important role of diffusion, at given k and D. Clearly, a 'kinetic constant' such as k' of the SCM, whose optimum value depends on the particle size, does not properly conveys purely chemical kinetic information. However, this issue is often neglected in practical applications, and this may lead to severe errors, when the proper scale factor is not applied to kinetic parameters from literature, if they were estimated by SCM. In the following, we quantify such an error of using estimates of k' based on SCM at a given particle size to simulate other sizes with SCM. The resulting errors should be compared to Figure 8.11, where k' has been adjusted at each new particles size.

Assuming that the generalized (any α) grain model correctly describes the reaction of the particle of any size, and so k is the intrinsic parameter ruling the reaction rate, the fitted value of k' that approximates the same conversion profiles will be, on the contrary, affected by the particular value of r_0. This means that changing the particle size while keeping the same values of k and k' may result in a divergence between the two models.

This can be a problem, particularly when the standard grain model (α = 2/3) can well describe the available experimental data, and so it is tempting to replace it by a simpler SCM, which will be equally in good agreement with them, as long as the size of the particles is kept constant. After a good fitting of k', this value could be used to simulate larger or smaller particles, wrongly thinking that the same calculated value of k' will be still correct. The error of using the same k' for any particle size can be evaluated, by simulating the SCM with a fixed k' at different particle sizes, and calculating the relative difference with the conversion profiles of the continuous model (also applied with a constant value of k) with equation 8.42. The results are shown in Figure 8.12. k' was calculated with r_0 = 10 μm, $c_{B,bulk}$ = 1e-6 mol/cm^3, c_A^{s0} = 1e-2 mol/cm^3 , D = 1 cm^2/s, k = 10^5 s^{-1}, a = b = 1. Under these conditions, Φ^2 = 0.1. As already shown in Figure 8.11, with these parameters the kinetic regime prevails. Note that this case also corresponds to the usual practice of attempting to identify the intrinsic kinetics by experiments on very small powders, expecting to prevent any diffusive limitations effects. Results of the continuous model (that we use as a substitute of a real experimental campaign) can be approximated by the SCM, calculating k' with equation 8.39. k' is calculated for each value of α, for r_0 = 10 μm. Then it is used to simulate the reacting particle with the SCM, varying the particle size from 1μm to 1 cm. This means that Φ^2 changes in the range 10^{-3}-10^5. A double x axis is

reported in Figure 8.12, to explain how the variation of Φ^2 is in this case related only to the variation of r_0, while all of the other parameters are kept constant during the simulations.

The calculated errors shown in Figure 8.12 are much larger than the ones from Figure 8.11, where k' was recalculated at each value of r_0, which led to a more close correspondence between the two models. For any α there is a maximum error in the intermediate regime (for $\Phi^2 \approx 10^1$-10^2). The value of the maximum increases with increasing α. For α = 2/3 the maximum error is about 700%! Since k' is not scaled with r_0, the value calculated at r_0 = 10 μm is too low for simulations at r_0 > 10 μm (that is Φ^2 > 0.1), which means that the SCM largely underestimates the expected conversion.

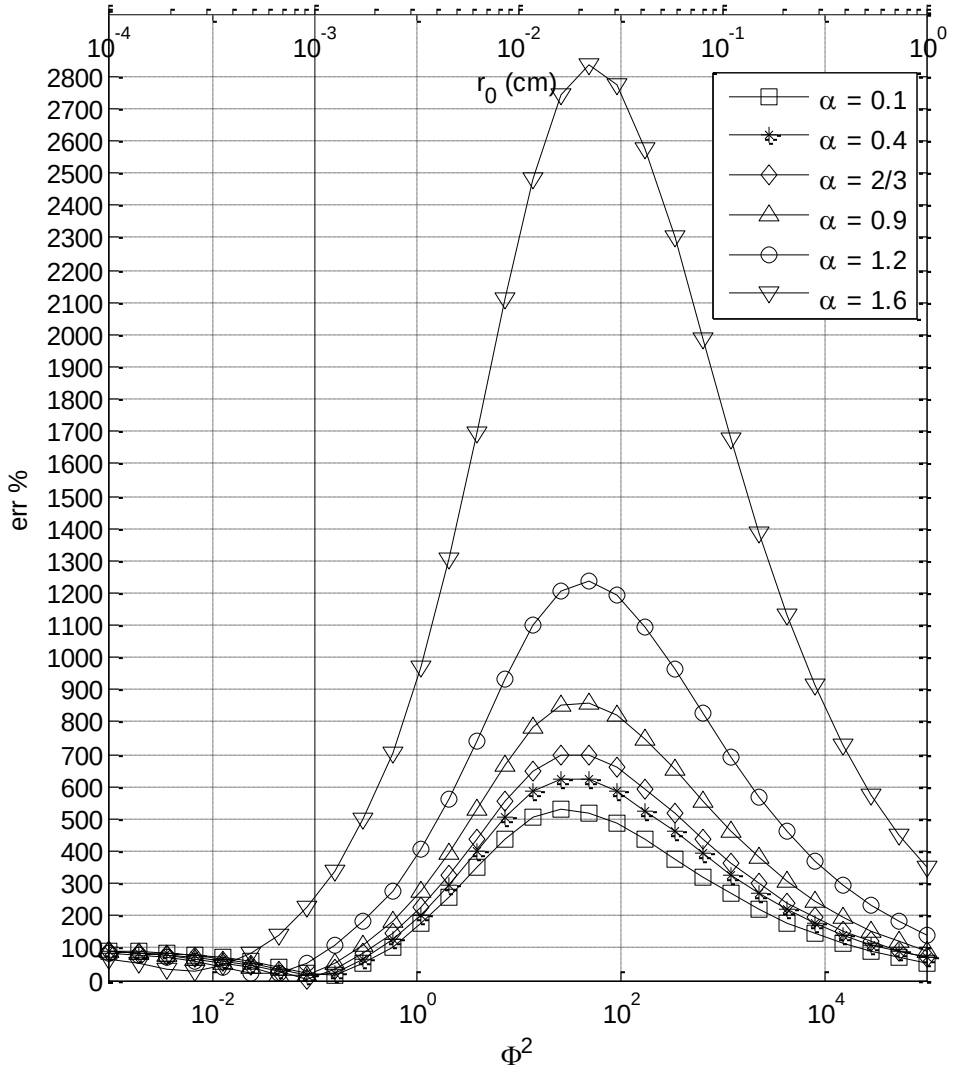

Figure 8.12: Mean relative error (%) between the SCM and CM calculated particle conversion, as a function of Φ^2 and α, when extrapolating k' estimated in the kinetic regime (Φ^2 = 0.1, r_0 = 10 μm, solid vertical line) to simulate the conversion at different values of Thiele modulus (i.e. different particle size; see scale on top)

This is evident in Figure 8.13, that compares the conversion history for the two models for different values of α. For Φ^2 = 0.1, which corresponds to the radius at which k' was estimated, the two models are still relatively close to each other (and eventually identical for α = 2/3). But using the same value of k' to

simulate a much larger particle (r_0 = 300 µm, Φ^2 = 100) results in a very important discrepancy between the two.

For very high values of Φ^2, getting closer to the diffusive regime the relative error decreases according to Figure 8.12, and eventually will drop to zero again; this is because in diffusive regime k' is no longer important, even if its value is wrong. However, it can be noticed in Figure 8.12 that for $\Phi^2 = 10^5$ the relative difference is still quite significant. This is because the calculated value of τ_K is still high compared to τ_D if k' is underestimated. In other words, the shrinking core model is actually simulating an intermediate regime, while the continuous model predicts a fully developed diffusive regime.

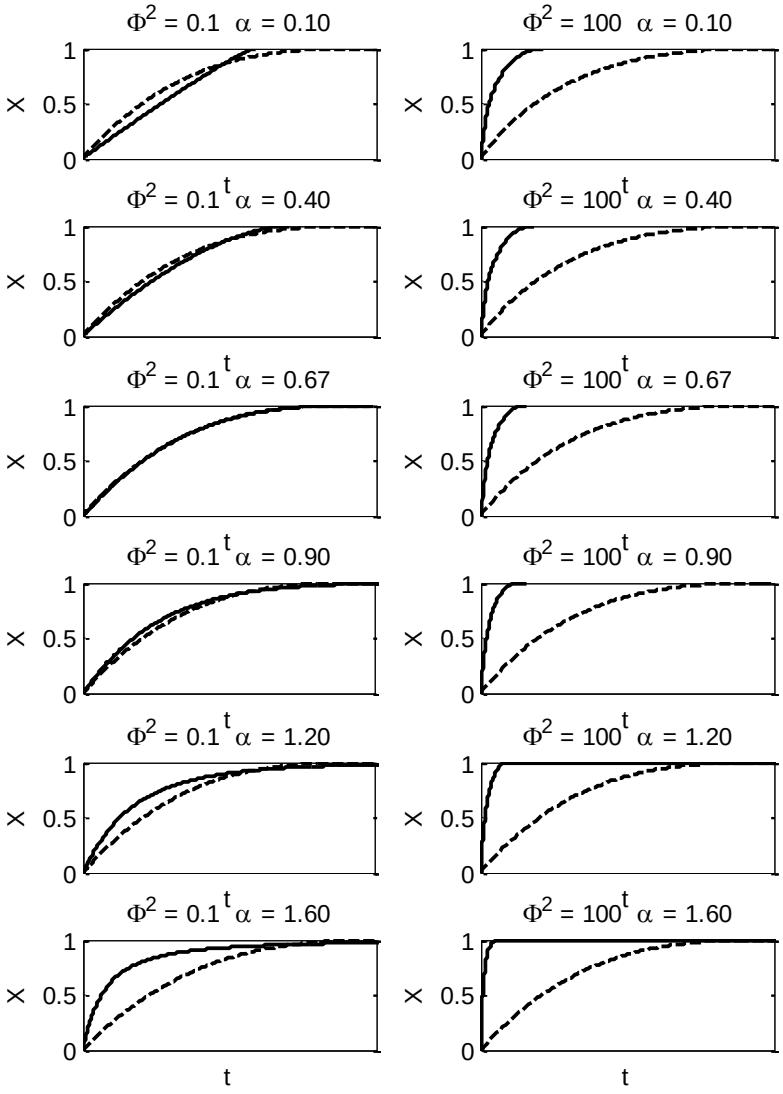

Figure 8.13: Comparison between the conversion profiles calculated with the SCM (dashed lines) and CM (continuous lines) when k' estimated at r_0 = 10 µm is used to simulate the conversion for r_0 = 10 µm (on the left), and when the k' estimated at r_0 = 10 µm is used to simulate the conversion at r_0 = 300 µm (on the right).

For $\Phi^2 < 0.1$ ($r_0 < 10$ μm), the value of k' fitted for $r_0 = 10$ μm is too high, and so the gap between the models increases again, even if both models are simulating a kinetic regime. For $\alpha = 2/3$, at $\Phi^2 = 0.001$ (i.e. $r_0 = 1$ μm) the error is about 90%. This is only apparently in contrast with what was previously stated: in kinetic regime, the SCM and CM become identical for $\alpha = 2/3$ only if k' is calculated for the same value of r_0 used for the simulations, otherwise large differences may arise even in this case.

It can be noticed that, for $\alpha \neq 2/3$, the minimum of the error in kinetic regime is not reached for $\Phi^2 = 0.1$. This may seem odd, but it's actually due to the fact that in our case the calculation of the optimum k' was made by minimizing the absolute difference, while the plot in Figure 8.12 shows the relative difference. By default, at low conversions the SCM overestimates the CM for $\alpha<2/3$ and underestimates it for $\alpha>2/3$ (see Figure 8.10). So if k' is lower than k'_{opt}, at $\alpha<2/3$ the SCM will be more accurate at low conversions, which results in a lower value of the integral mean of the relative error. The opposite happens for $\alpha>2/3$ if $k'>k'_{opt}$.

8.4 Conclusion

A comparison between the shrinking core model and the generalized grain model has been made. A simplified version of the continuous model was considered (Fickian diffusion, no natural convection of the gas, negligible effect of the variation of porosity), as well as a simple kinetics (a single irreversible reaction).

The study was focused on two aspects: the controlling regime, and the value of α, which is physically related to the shape of the micro grains and the effect of sintering. For spherical grains ($\alpha = 2/3$), the SCM can well approximate the continuous model, and the global pellet conversion profiles are mathematically equivalent in both kinetic and diffusive regime. The SCM does not represent the results of the CM if $\alpha \neq 2/3$, except in the full diffusion control.

The discrepancy between the two models was evaluated for different sintering behavior (values of α) and controlling regime (values of the Thiele modulus), after calculating the optimum value of the kinetic constant for the SCM to fit the conversion profile from the continuous model.

Finally, since outside of the diffusive regime the SCM incorrectly describes the physics of the evolution of the particle, it was proven that the value of the kinetic constant that fit the experimental data is not an intrinsic parameter, but is affected by the size of the particle itself. For this reason, it must be pointed out that the shrinking core model should be used very carefully, particularly when extrapolating the results at different conditions from those of the experimental data used to fit the kinetics. If k' was found in kinetic regime, it should be wise to linearly scale it with the particle size in order to avoid severe errors.

Finally, due to the simplifications introduced for the CM, the errors of approximation of SCM to CM shown by our work are quantified in the most optimistic situation, and in some cases they could be larger, if SCM is compared with a more detailed version of CM. Despite this, the calculations reported allow concluding that the classical assumption that SCM is a reasonable approximation of the reaction in any porous solids could be dramatically wrong under several circumstances. The reported results will hopefully help the practitioners to identify the most critical conditions in which the SCM leads to larger errors in simulating full scale reactors involving reacting porous solids, well beyond the intrinsic limitations of the SCM as a model.

Notation

a	Stoichiometric coefficient of the solid reagent
b	Stoichiometric coefficient of the gaseous reagent
c_i^g, c_i^s	Molar concentration, of the i-th gas species, of the i-th solid species (mol/cm^3)
$c_i^{g\,0}, c_i^{s\,0}$	Initial molar concentration, of the i-th gas species, of the i-th solid species (mol/cm^3)
$c_{i,bulk}$	Concentration of the i-th gas species outside the particle, in bulk phase (mol/cm^3)
C_i	Total concentration of i inside the particle (mol/cm^3)
D_{ij}	Effective diffusion coefficient of i in j (cm^2/s)
E	Integral of square errors
$e_r,\ e_a$	Relative and absolute error of calculated reaction times of SCM with respect to CM
$\overline{e_r}$	Mean relative error of calculated reaction times of SCM with respect to CM
k	Volumetric kinetic constant of CM (1/s)
k'	Superficial kinetic constant for SCM (cm/s)
r	Radial particle coordinate (cm)
r_i	Radius of the core-shell interface (cm)
r_0	Particle radius (cm)
R	Reaction rate per unit volume of porous solid (mol/cm^3/s)
t_{SCM}	Conversion time calculated for SCM
t_{CM}	Conversion time calculated for CM
t	Time (s)
t^*	Total conversion time (s)
T	Temperature (K)
X	Local solid conversion
Y	Non dimensional concentration of the reacting gas

Greek letters

α	Sintering factor
ε	Porosity
Φ^2	Thiele modulus
λ	Non dimensional radial coordinate
τ_K, τ_D	Characteristic times for reaction and diffusion for SCM (s)
θ	Non dimensional time coordinate

Chapter 9. Coupling of particle models with reactor models

In common applications, it is necessary to couple the single particle model with a more complex reactor model (2D or 3D). Like the 1D model, the evolution of the particle composition moving along a streamline must be simulated, once the velocity field of the solid phase is known. This is a so called Lagrangian approach. If the particle system in the reactor is modeled using a Lagrangian approach (for example using a Discrete Particle Model or a Discrete Element Model), the coupling is quite easy: one particle model will be solved for each particle in the system (this is very consuming from a computational point of view). In the CFD models, the velocity field for the solid is more easily calculated by using an Eulerian approach: according to this, the conservation equations are solved considering the single fixed coordinate points system, instead that considering the single lumps of fluid or particles moving through the system. It is still possible to convert the particle equations, written in a Lagrangian form, to their correspondent Eulerian form, using the equation of the substantial derivative:

$$\frac{Df(t,\boldsymbol{x})}{Dt} = \frac{\partial f(t,\boldsymbol{x})}{\partial t} + \boldsymbol{u}\cdot\nabla f(t,\boldsymbol{x}) \qquad 9.1$$

This equation says that the variation in time of the scalar quantity f that can be observed moving on a streamline (left hand side term) is equal in any fixed point of the system to the sum of the time derivative of f plus the scalar product of the space gradient of f and the Eulerian velocity field **u** associated to the scalar f (right hand side). In the coupled system, the variables describing the particle composition of the solid and the gas inside the solid become a function of t, the internal coordinate r, and the external coordinates associated to the position of the particle **x** ([x, y, z] for a 3D Cartesian system). Using equation 9.1 with the particle model described by equations 4.37-4.39 and 4.41 (with N^S=0), we obtain:

$$\frac{\partial \varepsilon c_i^g(t,\boldsymbol{x};r)}{\partial t} + \boldsymbol{u_s}(t,\boldsymbol{x})\cdot\nabla_{\mathrm{x}}\left(\varepsilon c_i^g(t,\boldsymbol{x};r)\right) = -\frac{1}{r^2}\frac{\partial}{\partial r}\left(r^2\left(x_i^g N^g(t,\boldsymbol{x};r) + J_i^*(t,\boldsymbol{x};r)\right)\right) + \sum_{j=1}^{NR} \nu_{ij}^g R_j\,(t,\boldsymbol{x};r) \qquad 9.2$$

$$\frac{\partial \varepsilon c^g(t,\boldsymbol{x};r)}{\partial t} + \boldsymbol{u_s}(t,\boldsymbol{x})\cdot\nabla_{\mathrm{x}}(\varepsilon c^g(t,\boldsymbol{x};r)) = -\frac{1}{r^2}\frac{\partial}{\partial r}(r^2 N^g(t,\boldsymbol{x};r)) + \sum_{i=1}^{NG}\sum_{j=1}^{NR} \nu_{ij}^g R_j\,(t,\boldsymbol{x};r) \qquad 9.3$$

$$\frac{\partial c_i^s(t,\boldsymbol{x};r)}{\partial t} + \boldsymbol{u_s}(t,\boldsymbol{x})\cdot\nabla_{\mathrm{x}}(c_i^s(t,\boldsymbol{x};r)) = \sum_{j=1}^{NR} \nu_{ij}^s R_j\,(t,\boldsymbol{x};r) \qquad 9.4$$

$$\rho C_p\left(\frac{\partial T(t,\boldsymbol{x};r)}{\partial t} + \boldsymbol{u_s}(t,\boldsymbol{x})\cdot\nabla_{\mathrm{x}}(T(t,\boldsymbol{x};r))\right) = -\frac{1}{r^2}\frac{\partial}{\partial r}\left(r^2(Cp^g N^g + q^t(t,\boldsymbol{x};r))\right) - \sum_{j=1}^{NR} R_j(t,\boldsymbol{x};r)\,\Delta H_j \qquad 9.5$$

In these equations, the gradient is written with the subscript x to indicate that is calculated only with reference to the "external" spatial coordinates (not including r). For instance, for a 3D Cartesian system it is:

$$\nabla_x(c_i(t,\boldsymbol{x};r)) = \begin{pmatrix} \dfrac{\partial c_i(t,\boldsymbol{x};r)}{\partial x} \\ \dfrac{\partial c_i(t,\boldsymbol{x};r)}{\partial y} \\ \dfrac{\partial c_i(t,\boldsymbol{x};r)}{\partial z} \end{pmatrix} \quad 9.6$$

The velocity field $\boldsymbol{u_s}$ is related to the solid particles phase. The time derivatives in equations 9.2-9.5 are present only if the system related to the corresponding quantity is not at steady state. The boundary conditions for the radial dimension are still valid, and they will be a function of time and **x**, in general:

$$for\ r = 0 \qquad \begin{aligned} J_i^*(t,\boldsymbol{x}) &= 0 \\ N^g(t,\boldsymbol{x}) &= 0 \\ q^t(t,\boldsymbol{x}) &= 0 \end{aligned} \quad 9.7$$

$$for\ r = r_0 \qquad \begin{aligned} x_i^g(t,\boldsymbol{x})N^g(t,\boldsymbol{x}) + J_i^*(t,\boldsymbol{x}) &= h_i\big(c_i^g(t,\boldsymbol{x};r_0) - c_{i,bulk}(t,\boldsymbol{x})\big) \\ N^g(t,\boldsymbol{x}) &= \sum_{i=1}^{NG} h_i\big(c_i^g(t,\boldsymbol{x};r_0) - c_{i,bulk}(t,\boldsymbol{x})\big) \\ q^t(t,\boldsymbol{x}) &= h_t(T(t,\boldsymbol{x};r_0) - T_{bulk}(t,\boldsymbol{x})) \end{aligned} \quad 9.8$$

Equations 9.8 are coupling terms: in fact, $c_{i,bulk}$ and T_{bulk} will be calculated by the conservation and energy balances of the gas species in the interparticle channels. In these equations there will be also some generation terms, due to the fact that there is mass and energy transfer at the surface of the particles. In particular, for the gas continuity equation:

$$s(t,\boldsymbol{x}) = 4\pi r_0^2 \cdot np(t,\boldsymbol{x}) \cdot \sum_{i=1}^{NG} h_i\big(c_i^g(t,\boldsymbol{x};r_0) - c_{i,bulk}(t,\boldsymbol{x})\big) \cdot MW_i \quad 9.9$$

For the single species concentration equation, the source term is:

$$s_i(t,\boldsymbol{x}) = 4\pi r_0^2 \cdot np(t,\boldsymbol{x}) \cdot h_i\big(c_i^g(t,\boldsymbol{x};r_0) - c_{i,bulk}(t,\boldsymbol{x})\big) \quad 9.10$$

For the energy balance, the source term is:

$$Q(t,\boldsymbol{x}) = 4\pi r_0^2 \cdot np(t,\boldsymbol{x}) \cdot h_t(T(t,\boldsymbol{x};r_0) - T_{bulk}(t,\boldsymbol{x})) \quad 9.11$$

These are also coupling terms between the particle and ractor models, because $c_i^g(t,\boldsymbol{x};r_0)$ and $T(t,\boldsymbol{x};r_0)$ result from the particle model, whereas $s_i(t,\boldsymbol{x})$ and $Q(t,\boldsymbol{x})$ need to be used in the reactor model. In equations 9.10-9.11, np is the number of particles per unit of volume. It can be calculated from:

$$np(t,\boldsymbol{x}) = \frac{1-\varepsilon_b(t,\boldsymbol{x})}{\frac{4}{3}\pi r_0^3} \quad 9.12$$

Where ε_b is the bed porosity (not to be confused with the intra particle porosity). In general, ε_b can be variable inside the reactor (this is true for example for fludized beds, whereas for fixed or moving beds it can be assumed as a constant paramter). Equations 9.2-9.5 add a good degree of complexity to the CFD model, because they include a new dimension, r, that need to be added do the discretization method. For instance, if the CFD reactor model is 3D ($\boldsymbol{x}$ = [x,y,z]), it will become even more computationally expensive once a fourth dimension is considered. Besides this, equations 9.2-9.5 may not be easily included in commercial CFD codes, that usually assume standard forms for the PDE. One solution to the problem can be treating the radial discretization separately. This can be done in a smart way, using a collocation method [65], [66]. With a good choice of the base functions that must describe the intra particle concentration profiles, even a low number of them can suffice. More details about collocation method in general are provided in Appendix B.

9.1 Solution for a simplified continuous model

In this section it is shown an example of the coupling of the particle model to CFD using a collocation method. The simplified continuous model shown in section 8 is considered (isothermal, Fick law, uniform particle porosity, no convection effect, steady state approximation for the gas, no external mass transfer resistance). It is considered a single irreversible gas solid reaction in the form:

a A(s) + b B(g) → c C(s) + d D(g)

The Lagrangian model for the gas and solid reagents is then:

$$0 = \frac{1}{\lambda^2}\frac{\partial}{\partial\lambda}\left(\lambda^2\frac{\partial Y}{\partial\lambda}\right) - b\,\Phi^2\cdot(1-X)^{\delta}\cdot Y \qquad 9.13$$

$$\frac{\partial X}{\partial t} = a\,\gamma\cdot(1-X)^{\delta}\cdot Y \qquad 9.14$$

Where λ is the non dimensional radial coordinate, Y is the normalized concentration of B and X is the conversion of A. The non dimensional numbers Φ^2 and γ are:

$$\Phi^2 = \frac{k\cdot r_0^2}{D_{BD}} \qquad 9.15$$

$$\gamma = k\cdot\frac{c_{B,bulk}}{c^{s\,0}{}_A} \qquad 9.16$$

The boundary conditions for the gas are:

$$\lambda = 0 \qquad \frac{\partial Y}{\partial\lambda} = 0 \qquad 9.17$$

$$\lambda = 1 \qquad Y = 1 \qquad 9.18$$

Using the Lagrangian-Eulerian conversion, equations 9.13-9.14 become:

$$0 = \frac{1}{\lambda^2}\frac{\partial}{\partial\lambda}\left(\lambda^2\frac{\partial Y(\boldsymbol{x};\lambda)}{\partial\lambda}\right) - b\,\Phi^2\cdot(1-X(\boldsymbol{x};\lambda))^{\delta}\cdot Y(\boldsymbol{x};\lambda) \qquad 9.19$$

$$\boldsymbol{u_s}(\boldsymbol{x})\cdot\nabla_{\mathrm{x}}(X(\boldsymbol{x};\lambda)) = a\,\gamma(\boldsymbol{x})\cdot(1-X(\boldsymbol{x};\lambda))^{\delta}\cdot Y(\boldsymbol{x};\lambda) \qquad 9.20$$

It assumed in equation 9.20 that the reactor model is solved at steady state. In this case, the "hystory" of the particle evolution is tracked by its position **x** inside the reactor. The parameter γ becomes a function of the particle position (the bulk reactant concentration $c_{B,bulk}$ will be in general different in any point of the reactor). Note that, since pseudo steady state assumption was made for the gas balance inside the particle, (eq. 9.14), its equation does not depend on the solid phase "external" velocity field, $\boldsymbol{u_s}$**.** Nevertheless, the inner gas profiles still depend on the particle position **x** through the term $X(\boldsymbol{x};\lambda)$, and implicitly $\gamma(\boldsymbol{x})$. Now, an approximation of the radial profiles of X and Y is introduced:

$$Y(\boldsymbol{x};\lambda) \approx \sum_{j=1}^{N}\alpha_j(\boldsymbol{x})\cdot\xi_j(\lambda) \qquad 9.21$$

$$X(\boldsymbol{x};\lambda) \approx \sum_{j=1}^{N}\beta_j(\boldsymbol{x})\cdot\varphi_j(\lambda) \qquad 9.22$$

In this formulation, N base functions are used to approximate Y and X. The dependency on the variables **x** and λ is separated: the base functions ξ_j and φ_j only depend on the radial coordinate, whereas the coefficients α_j and β_j only depend on the position of the particle in the reactor (they would also depend on time, if the reactor model was not at steady state). N collocation points in the radial particle domain are chosen for equation 9.19 and 9.20. The base functions are chosen arbitrarily form a subset of linearly independent functions, forming a base of the set of C^2 functions. According to the collocation method, the values of the coefficients α_j and β_j can be found by imposing the residue of equations 9.19-9.20 equal to zero at the chosen collocation points (λ_i). The resulting system is:

$$\sum_{j=1}^{N}\left[\alpha_j(\boldsymbol{x})\frac{1}{{\lambda_i}^2}\frac{\partial}{\partial\lambda}\left({\lambda_i}^2\frac{\partial\xi_j(\lambda_i)}{\partial\lambda}\right)\right] - b\,\Phi^2\cdot\left(1-\sum_{j=1}^{N}\beta_j(\boldsymbol{x})\cdot\varphi_j(\lambda_i)\right)^{\delta}\cdot\sum_{j=1}^{N}\alpha_j(\boldsymbol{x})\cdot\xi_j(\lambda_i) = 0 \quad i = 1,2\ldots N \qquad 9.23$$

$$\sum_{j=1}^{N}\left[\boldsymbol{u_s}(\boldsymbol{x})\cdot\nabla_{\mathrm{x}}\big(\beta_j(\boldsymbol{x})\big)\varphi_j(\lambda_i)\right] = a\,\gamma(\boldsymbol{x})\cdot\left(1-\sum_{j=1}^{N}\beta_j(\boldsymbol{x})\cdot\varphi_j(\lambda_i)\right)^{\delta}\cdot\sum_{j=1}^{N}\alpha_j(\boldsymbol{x})\cdot\xi_j(\lambda_i) \qquad i = 1,2\ldots N \qquad 9.24$$

The set of equations 9.23-9.24 is a system of partial differential equations in the variables α_j and β_j in **x** where the derivatives in λ are still present. These can be eliminated, once a base for ξ and φ is chosen, so that ξ_j and φ_j can be analytically differentiated. In equations 9.23-9.24, λ_i is the coordinate of the i-th collocation point. In this work we report the application of the collocation method when a polyomial approximation is used: as base functions, the powers of λ can be chosen ($1, \lambda, \lambda^2, \lambda^3 \ldots$). A modification of the chosen set can be found by applying the boundary conditions expressed in 9.17-9.18. By doing this, equation 9.21 becomes:

$$Y(\boldsymbol{x};\lambda) \approx 1 + \sum_{j=1}^{N} \alpha_j(\boldsymbol{x}) \cdot (\lambda^{j+1} - 1) \tag{9.25}$$

The approximation of the first derivative of Y in λ becomes:

$$\frac{\partial Y(\boldsymbol{x};\lambda)}{\partial \lambda} \approx \sum_{j=1}^{N} \alpha_j(\boldsymbol{x}) \cdot (j+1)\lambda^j \tag{9.26}$$

It is trivial to prove that the boundary conditions are always verified for any value of the set of coefficients α_j. Note that by doing this, the first order monomer λ is automatically excluded from the approximation of Y. This is coherent with the fact that the solution of the equation must be searched within a subspace of continuous and twice derivable functions that respect the boundary conditions, and for this reason some constraints are applied to the set of base functions. For the solution of the solid, X, no boundary conditions need to be imposed by the problem. Yet, a "natural" condition on the shape of the solution derives from the symmetry at $\lambda = 0$. So it is wise to choose a set of base functions for X so that the approximation of X is smooth at $\lambda = 0$. For instance:

$$X(\boldsymbol{x};\lambda) \approx \beta_1(\boldsymbol{x}) + \sum_{j=2}^{N} \beta_j(\boldsymbol{x}) \cdot \lambda^j \tag{9.27}$$

Applying equations 9.25-9.27 to the collocation formulation, equations 9.23-9.24 become:

$$\sum_{j=1}^{N} \left[\alpha_j(\boldsymbol{x})(j+1)(j+2)\lambda_i^{j-1}\right] - b\,\Phi^2 \cdot \left(1 - \beta_1(\boldsymbol{x}) - \sum_{j=2}^{N} \beta_j(\boldsymbol{x}) \cdot \lambda_i^j\right)^{\delta} \cdot \left(1 + \sum_{j=1}^{N} \alpha_j(\boldsymbol{x}) \cdot (\lambda_i^{j+1} - 1)\right) = 0 \tag{9.28}$$

$$\boldsymbol{u_s}(\boldsymbol{x}) \cdot \nabla_{\mathrm{x}}\left(\beta_1(\boldsymbol{x})\right) + \sum_{j=2}^{N} \left[\boldsymbol{u_s}(\boldsymbol{x}) \cdot \nabla_{\mathrm{x}}\left(\beta_j(\boldsymbol{x})\right)\lambda_i^j\right] = a\,\gamma(\boldsymbol{x}) \cdot \left(1 - \beta_1(\boldsymbol{x}) - \sum_{j=2}^{N} \beta_j(\boldsymbol{x}) \cdot \lambda_i^j\right)^{\delta} \cdot \left(1 + \sum_{j=1}^{N} \alpha_j(\boldsymbol{x}) \cdot (\lambda_i^{j+1} - 1)\right) \tag{9.29}$$

The resulting equations are non linear, so the source term has to be linearized and then the system can be solved iteratively. According to a Newton-Raphson scheme, the reaction term in equations 9.19-9.20 can be calculated at the n+1 iteration as follows:

$$(1 - X^{n+1})^{\delta} \cdot Y^{n+1} = (1 - X^n)^{\delta} \cdot Y^n - \delta(1 - X^n)^{\delta-1} \cdot Y^n \cdot (X^{n+1} - X^n) + (1 - X^n)^{\delta} \cdot (Y^{n+1} - Y^n) \tag{9.30}$$

The equations to solve, in the variables α^{n+1} and β^{n+1}, become in a matrix form:

$$A'' \cdot \alpha^{n+1}(\boldsymbol{x}) \; - b\, \Phi^2 \cdot \left[F^n(\boldsymbol{x}) + J_X^n(\boldsymbol{x}) \cdot B \cdot \beta^{n+1}(\boldsymbol{x}) + J_Y^n(\boldsymbol{x}) \cdot \left(diag(I) + A \cdot \alpha^{n+1}(\boldsymbol{x})\right)\right] = 0 \qquad 9.31$$

$$B \cdot \left(\boldsymbol{u_s}(\boldsymbol{x}) \cdot \nabla\beta^{n+1}(\boldsymbol{x})\right)^T = \; a\, \gamma(\boldsymbol{x}) \cdot \left[F^n(\boldsymbol{x}) + J_X^n(\boldsymbol{x}) \cdot B \cdot \beta^{n+1}(\boldsymbol{x}) + J_Y^n(\boldsymbol{x}) \cdot \left(diag(I) + A \cdot \alpha^{n+1}(\boldsymbol{x})\right)\right] \qquad 9.32$$

The matrices A, B, A'', J_X^n, J_Y^n and the vector F^n are defined from equations 9.33-9.38, whereas I is the identity matrix:

$$A_{ij} = \lambda_i^{j+1} - 1 \qquad 9.33$$

$$B_{i1} = 1 \qquad 9.34$$
$$B_{ij} = \lambda_i^j \quad (j > 1)$$

$$A''_{ij} = (j+1)(j+2)\lambda_i^{j-1} \qquad 9.35$$

$$\left(J_X^n(\boldsymbol{x})\right)_{ii} = -\delta\left(1 - \beta_1^n(\boldsymbol{x}) - \sum_{j=2}^{N} \beta_j^n(\boldsymbol{x}) \cdot \lambda_i^j\right)^{\delta-1} \cdot \left(1 + \sum_{j=1}^{N} \alpha_j^n(\boldsymbol{x}) \cdot (\lambda_i^{j+1} - 1)\right) \qquad 9.36$$
$$\left(J_X^n(\boldsymbol{x})\right)_{ij} = 0 \quad (j \neq i)$$

$$\left(J_Y^n(\boldsymbol{x})\right)_{ii} = \left(1 - \beta_1^n(\boldsymbol{x}) - \sum_{j=2}^{N} \beta_j^n(\boldsymbol{x}) \cdot \lambda_i^j\right)^{\delta} \qquad 9.37$$
$$\left(J_Y^n(\boldsymbol{x})\right)_{ij} = 0 \quad (j \neq i)$$

$$\left(F^n(\boldsymbol{x})\right)_i = \delta\left(1 - \beta_1^n(\boldsymbol{x}) - \sum_{j=2}^{N} \beta_j^n(\boldsymbol{x}) \cdot \lambda_i^j\right)^{\delta-1} \cdot \left(1 + \sum_{j=1}^{N} \alpha_j^n(\boldsymbol{x}) \cdot (\lambda_i^{j+1} - 1)\right) \cdot \left(\beta_1^n(\boldsymbol{x}) + \sum_{j=2}^{N} \beta_j^n(\boldsymbol{x}) \cdot \lambda_i^j\right) \qquad 9.38$$

Note that A, B, A'' are constant, so they can be calculated once the number and position of the collocation points are chosen. On the contrary, J_X^n, J_Y^n and F^n depend on the values of the variables calculated at the previous iteration. Equation 9.31 is linear algebraic, while 9.32 is differential with respect to the variables **x**. They must be solved iteratively until convergence (this will imply that equation 9.32 must be integrated and equation 9.31 must be solved using the matrices calculated at the n-th iteration, until the solution at n+1 is equal to the solution at n). The gradient $\nabla\beta^{n+1}(\boldsymbol{x})$ is defined as:

$$\left(\nabla\beta^{n+1}(x)\right)_{ij} = \frac{\partial {\beta_j}^{n+1}(\boldsymbol{x})}{\partial x_i} \qquad 9.39$$

Once the solution in $\alpha_j(\boldsymbol{x})$ and $\beta_j(\boldsymbol{x})$ is obtained, the mean particle solid conversion can be found in any point of the reactor by calculating the following integral:

$$\bar{X}(\boldsymbol{x}) = \frac{\int_0^1 4\pi\lambda^2 X(\boldsymbol{x};\lambda)d\lambda}{\frac{4}{3}\pi} = \beta_1(\boldsymbol{x}) + \sum_{j=2}^{N}\left(\beta_j(\boldsymbol{x}) \cdot \frac{3}{j+3}\right) \qquad 9.40$$

The source term for the bulk gas composition for the reactant B becomes:

$$s_B = 4\pi r_0^2 \cdot np \cdot J_B^*(r_0) = -4\pi r_0^2 \cdot np \cdot \frac{D_{BD}\, c_{B,bulk}}{r_0} \sum_{j=1}^{N} \left(\alpha_j(\boldsymbol{x}) \cdot (j+1)\right) \qquad 9.41$$

The computational cost added to the problem with the particle model is strictly related to the chosen number of collocation points. For the considered simplified particle model and reaction mechanism, one PDE and one algebraic equation are added to the problem for every collocation point. Few collocation points can also mean a low accuracy in the approximation of the intra particle profiles, and high errors in the solution. An optimum value must be chosen, depending on the problem to solve. It is also important to point out that, for a fixed number of collocation points, the accuracy of the approximated solution can easily depend on the form of the base functions (in this example, polynomials were used). If the analytical shapes of the base functions are more similar to the real solution profile, it is more likely that a low number of them can suffice to obtain a good result. This "efficiency" cannot be evaluated a priori, but depends on the considered problem, and specific numerical tests are needed to identify the best choice.

9.2 Coupling with 1D moving bed reactor model

The mathematical approach described by equations 9.2-9.5 can be easily applied to a one dimension reactor model. In this section the example of a moving bed reactor is considered. The reactor is assumed to be cylindrical, with a stream of reacting gas flowing from the bottom to the top. At the same time, a counter current flow rate of solid particles is fed at the top of the reactor. The reacting gas flows in the spaces between the particles, and diffuses inside them converting the solid species. If all the characteristics of the solid and gas phases are assumed to be uniform along the reactor radial coordinate, a one dimension reactor model can be used.

The solid particles are supposed to flow along the axial coordinate along parallel streamlines at a constant velocity. The entire reactor works at steady state. If these assumptions are correct, the particle model expressed by equations 9.2-9.5 becomes:

$$u_s \cdot \frac{\partial \varepsilon c_i^g(z,r)}{\partial \mathrm{z}} = -\frac{1}{r^2}\frac{\partial}{\partial r}\left(r^2\left(x_i^g N^g(z,r) + J_i^*(z,r)\right)\right) + \sum_{j=1}^{NR} \nu_{ij}^g R_j(z,r) \qquad i = 1{,}2 \ldots NS\ gas \qquad 9.42$$

$$u_s \cdot \frac{\partial \varepsilon c^g(z,r)}{\partial \mathrm{z}} = -\frac{1}{r^2}\frac{\partial}{\partial r}\left(r^2 N^g(z,r)\right) + \sum_{i=1}^{NG}\sum_{j=1}^{NR} \nu_{ij}^g R_j(z,r) \qquad 9.43$$

$$u_s \cdot \frac{\partial c_i^s(z,r)}{\partial \mathrm{z}} = \sum_{j=1}^{NR} \nu_{ij}^s R_j\,(z,r) \qquad i = 1{,}2 \ldots NS\ solid \qquad 9.44$$

$$\rho C_p u_s \cdot \frac{\partial T(z,r)}{\partial \mathrm{z}} = -\frac{1}{r^2}\frac{\partial}{\partial r}\left(r^2\left(Cp^g N^g(z,r) + q^t(z,r)\right)\right) - \sum_{j=1}^{NR} R_j(z,r)\,\Delta H_j \qquad 9.45$$

Equations 9.42-9.45 are the equations for the concentration of gas species, total gas concentration, concentration of solid species and energy inside the particle, respectively. In this formulation, u_s is a

parameter. The boundary conditions for the gas inside the particle are the same reported by equations 9.7-9.8. The gas species concentration balances in the channels between particles are in the form:

$$\frac{\partial c_{i,bulk}(z) u_g(z)}{\partial z} = -\frac{\partial J_i^*(c_{i,bulk}(z))}{\partial z} + s_i(z) \qquad 9.46$$

Equation 9.46 considers convection, diffusion and a source term due to the mass transfer of the gas i from the bulk to the particles or vice versa. The source term is again expressed through equation 9.10, i.e. the species flux of the i-th species from the particle external surface to the gas, as given by the particle model. A total concentration balance must be added to evaluate the axial gas velocity profile:

$$\frac{\partial c_{bulk}(z) u_g(z)}{\partial z} = \sum_{j=1}^{NG} s_j(z) \qquad 9.47$$

The energy balance for the bulk gas phase is:

$$\rho C_p u_g(z) \cdot \frac{\partial T_{bulk}(z)}{\partial z} = \frac{\partial}{\partial z}\left(k_c \frac{\partial T_{bulk}(z)}{\partial z}\right) + Q(z) \qquad 9.48$$

Where the source term Q is expressed through equation 9.11, i.e. the heat flux from the particle external surface to the gas, as given by the particle model. Boundary conditions bust be also added at the reactor gas inlet and solid inlet. Assuming that z = 0 is the solid inlet and the gas outlet, and z = L is the gas inlet and solid outlet, the boundary conditions are:

$$z = 0 \qquad \begin{array}{ll} c_i^s(0,r) = c_i^0 & i = 1,2 \dots NS\ solid \\ \dfrac{\partial c_{i,bulk}(0)}{\partial z} = 0 & i = 1,2 \dots NS\ gas \end{array} \qquad 9.49$$

$$z = L \qquad \begin{array}{ll} c_{i,bulk}(L) = c_{i,bulk}^L & i = 1,2 \dots NS\ gas \\ u_g(L) = u_g^L & \\ T_{bulk}(L) = T_{bulk}^L & \end{array} \qquad 9.50$$

The numerical treatment of the problem expressed by equations 9.42-9.48 is relatively simple. Once a discretization scheme is applied to the radial particle dimension in equations 9.42-9.45, the resulting system is only made of ordinary differential equations in z. The only further difficulty is related to the fact that the boundary conditions are both at z = 0 and z = L, so the system cannot be treated as an initial value problem but as a boundary value problem.

Figure 9.1 shows an example of solution obtained for the moving bed reactor model, for an isothermal case (equations 9.42-9.44 and 9.46-9.47). The model has been implemented in Matlab [23], using a finite volume method to express the radial derivative and then using a BVP solver to solve the resulting ODE system. The reaction mechanism considered is the reduction of Hematite to Metallic Iron with CO, in three steps:

$Fe_2O_3 + CO \rightarrow Fe_3O_4 + CO_2$

$Fe_3O_4 + CO \rightarrow FeO + CO_2$

$FeO + CO \rightarrow Fe + CO_2$

The kinetic parameters used were taken from the literature [4]. A 10m high and 1m wide reactor was simulated, considering large particles (1.2 cm diameter) of pure hematite continuously fed from the top with a solid velocity of 0.002 m/s. A gas flowrate of 10 kg/s at 800°C and 7.5 atm was fed from the bottom, with an inlet gas composition of 40% CO and 60% N_2.

Figure 9.1 shows on the left the predicted radial concentration profiles for the solid species inside the particles at three different axial coordinates (at the top inlet, at mid height and at the bottom solid outlet). The right hand plot shows the corresponding gas concentration profiles outside the particles. The gas reagent, CO, is consumed from the bottom of the reactor, where it is fed, up to the top. An equimolar production of CO_2 is observed.

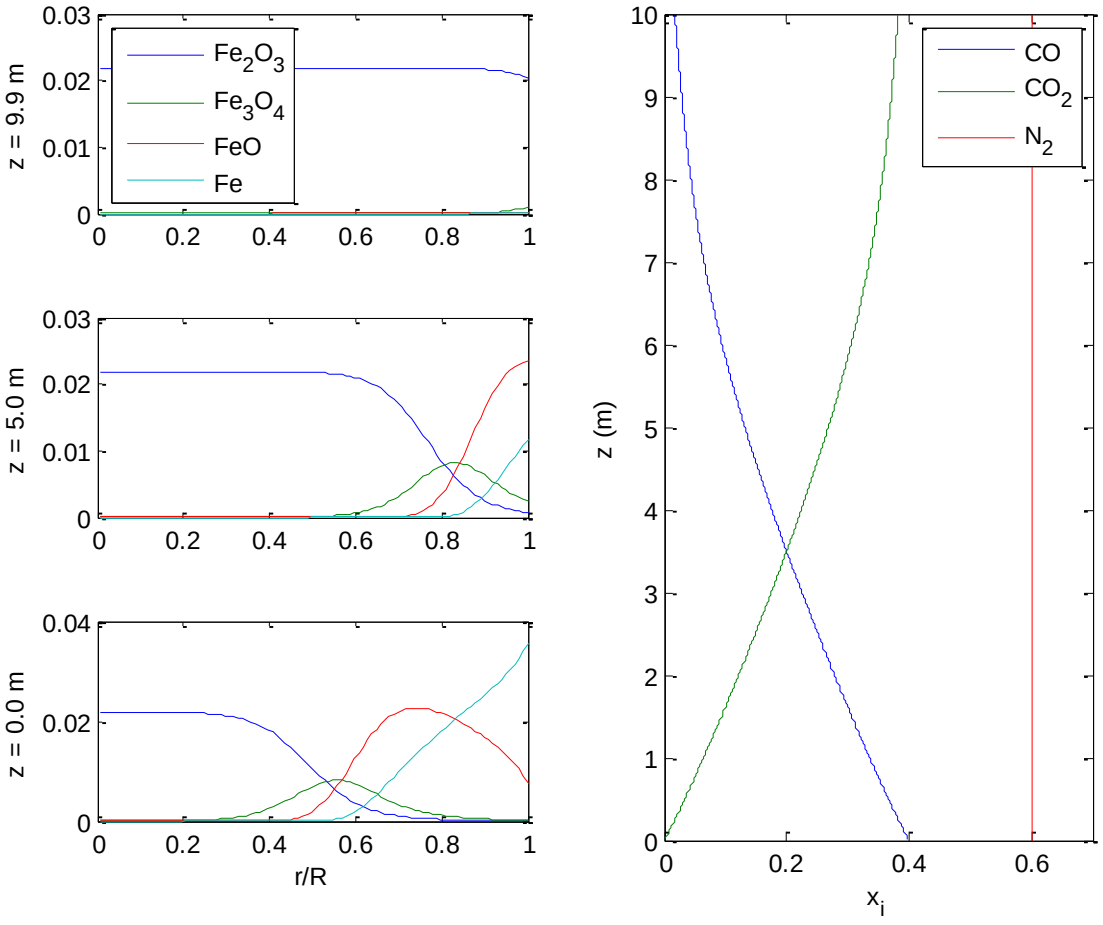

Figure 9.1: Results of the 1D moving bed reactor coupled with the particle model from the Iron ore reduction process with CO

Notation

c_i^g, c_i^s	Molar concentration, of the i-th gas species, of the i-th solid species (mol/cm^3)
$c_i^{g\,0}, c_i^{s\,0}$	Initial molar concentration, of the i-th gas species, of the i-th solid species (mol/cm^3)
c_i^0	Concentration of the i-th solid species at the particles inlet (mol/cm^3)
c^g, c^s	Total concentration of gas phase, of solid phase (mol/cm^3)
$c_{i,bulk}$	Concentration of the i-th gas species outside the particle, in bulk phase (mol/cm^3)
$c_{i,bulk}^L$	Concentration of the i-th gas species in bulk phase, at the gas reactor inlet (mol/cm^3)
cCp	Heat capacity of the medium (J/cm^3/K)
Cp^g, Cp^s	Heat capacity of the gas phase, of the solid phase (J/mol/K)
D_{ij}	Effective diffusion coefficient of i in j (cm^2/s)
h_i	Mass transfer coefficient of i (cm/s)
h_t	Heat transfer coefficient (W/cm^2/K)
J_i^*	Molar diffusive flux of i (mol/cm^2/s)
k	Volumetric kinetic constant of CM (1/s)
MW_i	Molecular weight of the i-th species (g/mol)
np	Number of particles per unit of reactor volume (1/cm^3)
N	Number of base functions
N^g	Total molar flux of the gas phase (mol/cm^2/s)
NG	Number of gas species in the system
NR	Number of reactions
NS	Number of solid species in the system
q^t	Conductive flux (W/cm^2)
Q	Source term for the energy balance for the gas in bulk phase (W/cm^3)
r	Radial particle coordinate (cm)
r_0	Particle radius (cm)
s	Source term for the continuity equation of the gas bulk phase (g/cm^3/s)
s_i	Source term for the concentration balance of the i-th gas in bulk phase (mol/cm^3/s)
R_i	Rate of the i-th reaction (mol/cm^3/s)
t	Time (s)
T, T_{bulk}	Absolute temperature, local, outside the particle in bulk phase (K)
T_{bulk}^L	Absolute temperature of gas in bulk phase at the gas reactor inlet (K)
u_g	Velocity of the gas in bulk phase (cm/s)
u_g^L	Velocity of the gas in bulk phase at the gas reactor inlet (cm/s)
$\boldsymbol{u_s}$	Velocity field of the solid particles medium (cm/s)
$\boldsymbol{x}$	Vector of spatial coordinates (cm)
x_i	i-th spatial coordinate in the reactor reference system
x_i^g , x_i^s	Molar fraction of the i-th gas species, of the i-th solid species
X	Local solid conversion
$\bar{X}$	Mean particle conversion
Y	Non dimensional concentration of the reacting gas

Greek letters

α_i	Coefficient of the i-th base function approximating Y
β_j	Coefficient of the i-th base function approximating X
δ	Sintering factor
ΔH_j^R	Heat of the j-th reaction, molar based (J/mol)
ε	Particle porosity
ε_b	Bed porosity

Φ^2	Thiele modulus
λ	Non dimensional radial coordinate
λ_i	Coordinate of the i-th collocation point
ν_{ij}^g	Stoichiometric coefficient of the i-th gas species in the j-th reaction
ν_{ij}^s	Stoichiometric coefficient of the i-th solid species in the j-th reaction
ξ_i	i-th base function approximating Y
φ_i	i-th base function approximating X

Chapter 10. Conclusions

The aim of this thesis was to evaluate the reliability of the different approaches that can be used while modeling non catalytic gas-solid reactions, with particular interest in single particle models. This study was carried out both by theoretical analyses of the models results, and by comparison with experimental data from different processes. The final goal was to understand the importance of using detailed continuous models, instead of the simpler core-shell reaction rate.

The first base case considered was the application of the Shrinking Core Model to the reduction of hematite to metallic iron with syngas. A CFD model was developed to simulate the process in shaft furnaces, with a flux of reacting spherical particles in countercurrent with a stream of gas at high temperature and pressure. The model allowed solving the velocity fields, compositions and temperatures of both solid and gas phases. After a fitting of the kinetic parameters of SCM to experimental data, the model was able to predict the solid conversions of the two phases both in the full scale plants and in the pilot plants, that were realized within the industrial project to study the particle reaction rates. The simulated particles in this process are quite large (about 2 cm diameter), which results in an important contribution of the diffusion resistance in the overall mechanism of particle conversion: this is the situation when a core-shell structure is really formed, and the SCM is able to correctly describe the heterogeneous process. This explains the good predictivity of the model, in comparison with the available evidences. The choice of SCM in the simulation of industrial processes is often dictated by its straightforward applicability to CFD, yet it is sometimes proven to work because it can still consider both kinetic and intra particle diffusion phenomena.

A good agreement with the experimental data is not always a guarantee that the model is good per se. As a matter of fact, the data regression can dissimulate the incorrect or approximated description of mass transport phenomena, by discharging these errors into the quantification of the unknown parameters. For this reason, an analysis of more detailed particle models (continuous models) was performed.

The sensitivity tests on the accuracy of the diffusion model proved that the use of a rigorous Stefan-Maxwell approach can be necessary in most of the cases where intraparticle diffusion is important. This is particularly true when the concentration of gas reagent into the mixture is high. The simplified mixture averaged model, with an effective coefficient calculated on the composition of the mixture is proved to be a very good alternative, with resulting errors that are quite low (below 5%) even for heterogeneous gas mixtures with species with very different diffusivities. On the contrary, the binary Fick's Law with a constant diffusion coefficient can lead to severe discrepancies in the prediction of the global particle conversion for high Thiele modulus (also 10-50% for the most difficult cases). This issue should be really taken into consideration, because it is common practice to simplify the form of the diffusion fluxes to be used in the continuous model, also to obtain a more direct and easy numerical implementation.

A detailed investigation was carried out on the role of natural convection as a mechanism of mass transport into the porous matrix. This is in most cases neglected in the literature, because diffusion is assumed to be largely dominant. In our analysis, three different sources of natural convection into the reacting particle were identified: the effect of changing porosity (which reflects on the changing gas volume due to the change of the molar density of the solid during the reaction), the effect of temperature gradients (and so different density of the gas in different points of the particle), and the net production or consumption of

number of gas moles related to the reaction stoichiometry. The first two contributions were proven to be negligible, whereas it was shown that the presence of a non equimolar reaction in gas phase could imply the inclusion of convection into the model for a more correct description of the process. Nevertheless, the performed simulations for the considered examples showed limited errors in the determination of the global particle conversion, when convection is not considered (maximum 5-8% for the non equimolar reaction of oxidation of zinc sulphide).

The continuous model was applied to describe the reduction of metal oxides with syngas, considering solid particles used as oxygen carriers for chemical looping combustion. Chemical looping is a classical example of process where the evolution of the porous solid matrix due to physical and chemical phenomena is expected to have a great influence on the reacting system, because of the high number of reaction cycles involving the same particles. This is evident from experimental data that show an improvement of the solid reactivity with increasing number of cycles. Another characteristic of the oxygen carriers reactivity is that it greatly decreases for high conversions, and this is largely documented by TGA analyses. Different hypotheses were made to try to describe the particle conversion profiles with the continuous model. Namely, solid sintering, the effect of pore size distribution, the effect of gas diffusion in dense solid, and the effect of solid phase segregation were considered. These phenomena were independently implemented into different formulations of the particle model. All these versions were able to explain the TGA data, except for the model including the experimental pore size distribution. This proved that, for the considered example, the effect of different effective diffusivities in pores with different size cannot be responsible for a change of the controlling regime during the particle conversion. On the other hand, the reactivity slowdown could be either the result of one of the following phenomena:

- An important decrease of the superficial area of the reacting solid with time due to sintering of micrograins at high temperature.
- The presence of fractions of solid matrix that are not reached by pores, where the diffusion resistance of gas transportation plays an important role.
- The presence in activated particles of segregated solid phases with different reactivities, that can lead to two kinetic steps (fast and slow reaction).

The first two results are just a consequence of preliminary assumptions, whereas the third one is confirmed in the case of the ilmenite-pseudobrookite system by an experimental characterization of the solid activated particles, that really shows the existence of different solid phases, and a slow process of their redistribution within the core and an outer layer of the particle during the activation steps. The sensitivity analysis made on the new implemented model also shows that a different reactivity of these solid phases could explain both the conversion rate decrease of the particles during a single cycle, and the reactivity increase with increasing number of cycles, due to the fact that the more reactive phase (hematite) separates from the slow reacting one (pseudobrookite) in the first loops. This interpretation must be further validated in the future, for the considered system. In particular, the results of the fitting of the continuous model suggest that a different initial pseudobrookite degree of dissociation is required at different temperatures to explain the experimental behavior, and this must be still demonstrated.

Two important conclusions can be made from the results of the work on chemical looping combustion: first, it is quite easy that, for gas-solid reaction processes, the particle reactivity can be successfully described only if a non trivial interaction phenomenon between the evolution of the solid morphology and the process is considered and included into the particle model, and this cannot be done through the

shrinking core model, but a more detailed approach is necessary; second, the results show that an experimental quantification of the global solid reactivity is surely necessary but not sufficient to fully understand all the chemical-physical phenomena controlling the process. A thorough characterization of the properties of the solid matrix, possibly obtained at several conversion steps, can be the key factor to discriminate through different possible explanations of the same TGA profiles.

The importance of using a detailed approach was also assessed with the final comparison between the Shrinking Core Model and a simplified version of the Continuous Model. The study was carried out by considering different controlling regimes, and different forms of the gas-solid reaction rate used in the continuous particle model. On the one hand, the results prove that the SCM can in several cases well approximate the results of the CM, not only in diffusive regime as it is already stated in the literature, but also for a kinetic controlled process, in the case of the grain model. A mathematical function was derived, that relates the kinetic constant of the shrinking core model to that of the continuous model, that minimizes the difference between the results of the two. On the other hand, the quantification of the kinetic constant used in the shrinking core model was proved to be affected by the particle size. Very high errors (> 100!) can arise if the SCM is used to simulate particles with very different sizes from those corresponding to the conditions of the kinetic fitting. This highly limits the possibility of extrapolating the results of the SCM in gas-solid simulations.

In conclusion, this thesis provides some insight into the modeling of gas-solid reaction problems, providing some tools to more wisely evaluate the importance of several degrees of detail to be included when choosing a single particle model.

Appendix A: Numerical discretization of the continuous model by Finite Differences

In this section, the numerical implementation if the continuous model described in chapter §4 is presented. In particular, it is considered the case of the model for an isothermal spherical particle, with unchanging size. This is described by equations 4.37-4.39, with N^S = 0. First of all, the conservation equations for the gas species (4.37) can be manipulated as follows:

$$\frac{\partial x_g}{\partial t} = \frac{1}{c \cdot \varepsilon(c_s)} \cdot \left(\frac{1}{r^2} \frac{\partial}{\partial r} \left(r^2 \cdot \left(-N^g x_g + cD(x_g, \varepsilon(c_s)) \frac{\partial x_g}{\partial r} \right) \right) - c x_g \frac{\partial \varepsilon(c_s)}{\partial t} + s_g \right) \quad \text{A.1}$$

Where x_g is the vector of all x_i^g, c_s is the vector of all c_i^s and s_g is the vector of all the source terms s_i^g. Equation A.1 is written by explicating the molar fractions of the gas phase, which are the variables of the equation to solve. In this formulation, $D(x_g, \varepsilon(c_s))$ is a matrix that results from the chosen diffusion model, and generally depends on the gas composition and local porosity. A new term is present, coming from the separation of the time derivative of $cx_g\varepsilon$. The time derivative of porosity is calculated using equation 4.45.

The equations for the solid species are:

$$\frac{\partial c_s}{\partial t} = s_s \quad \text{A.2}$$

The equation of total gas concentration has to be solved in terms of the total molar flux of gas, and is written as follows:

$$\frac{1}{r^2} \frac{\partial}{\partial r} (r^2 \cdot N^g) = \sum_{i=1}^{NG} s_{g,i} - c \frac{\partial \varepsilon(c_s)}{\partial t} \quad \text{A.3}$$

The problem can be solved using the method of lines. By applying a space discretization, the system of equations becomes:

$$\frac{\partial U}{\partial t} = EC(U) \cdot \left[\left(-C(N^g) + A(U) + E(U) \right) \cdot U + S(U) \right] \quad \text{A.4}$$

$$C^* \cdot N^g = S^*(U) + E^*(U) \quad \text{A.5}$$

In equations A.4 and A.5, U is the vector containing the discretized variables x_g and c_s. Its structure is explicated in equation A.6, where ${x^g}_{i,j}$ is the value of the mole fraction of the gas species i at the node j, and analogously for the solid concentrations ${c^s}_{i,j}$. Here, nn nodes are assumed for the spatial domain.

$$U = \begin{bmatrix} \begin{pmatrix} {x^g}_{1,1} \\ {x^g}_{2,1} \\ \dots \\ {x^g}_{NG,1} \end{pmatrix} \\ \dots \\ \begin{pmatrix} {x^g}_{1,nn} \\ {x^g}_{2,nn} \\ \dots \\ {x^g}_{NG,nn} \end{pmatrix} \\ \begin{pmatrix} {c^s}_{1,1} \\ {c^s}_{2,1} \\ \dots \\ {c^s}_{NS,1} \end{pmatrix} \\ \dots \\ \begin{pmatrix} {c^s}_{1,nn} \\ {c^s}_{2,nn} \\ \dots \\ {c^s}_{NS,nn} \end{pmatrix} \end{bmatrix} \quad \text{A.6}$$

The system of PDE becomes a mixed system of ordinary differential equations (A.4) and algebraic equations (A.5). The time derivatives can be also discretized, using the θ method (either an implicit or an explicit scheme). Using the Crank-Nicholson method (θ = ½), we obtain:

$$\frac{U^{n+1} - U^n}{\Delta t} = \frac{EC^{n+1}}{2} \cdot [(-C^{n+1} + A^{n+1} + E^{n+1}) \cdot U^{n+1} + S^{n+1}] + \frac{EC^n}{2} \cdot [(-C^n + A^n + E^n) \cdot U^n + S^n] \quad \text{A.7}$$

Where the superscripts indicate the value of the matrices and vectors at the time step n or n+1. In equation A.7, the vectors S^n and S^{n+1} are still a nonlinear function of U^n and U^{n+1}, respectively. Those terms can be linearized, by using a Newton-Raphson scheme, as follows:

$$S(U^{n+1}) = S\left(U^{\hat{n}}\right) + J\left(U^{\hat{n}}\right) \cdot (U^{\hat{n}+1} - U^{\hat{n}}) \quad \text{A.8}$$

Where $J\left(U^{\hat{n}}\right)$ is the Jacobian matrix, containing the partial derivatives of S with respect of all the terms of $U^{\hat{n}}$. Applying equation A.8 into equation A.7 we obtain the final forms of the linear systems to solve:

$$\left[I - \frac{\Delta t}{2} EC^{\hat{n}} \cdot \left(-C^{\hat{n}} + A^{\hat{n}} + E^{\hat{n}} + J^{\hat{n}}\right)\right] \cdot U^{\hat{n}+1} = \left[I + \frac{\Delta t}{2} EC^n \cdot (-C^n + A^n + E^n)\right] \cdot U^n + \frac{\Delta t}{2} EC^n \cdot S^n + \frac{\Delta t}{2} EC^{\hat{n}} \cdot \left(S^{\hat{n}} - J^{\hat{n}} \cdot U^{\hat{n}}\right) \quad \text{A.9}$$

$$C^* \cdot N^{g\,\hat{n}+1} = S^{*\hat{n}} + E^{*\hat{n}} \quad \text{A.10}$$

Systems A.9 and A.10 are solved in the variables $U^{\hat{n}+1}$ and $N^{g\,\hat{n}+1}$. Since a linearization was applied, they must be solved iteratively until $U^{\hat{n}+1}$ gets equal to $U^{\hat{n}}$ and $N^{g\,\hat{n}+1}$ is equal to $N^{g\,\hat{n}}$, for each time step. The two systems are coupled, because the matrix C depends on N^g and the matrix S* depends on U. They can also be solved iteratively, using the solution of the first into the second and then the solution of the second into the first, until convergence. This procedure must be repeated for each time step.

A scheme of the algorithm used is reported below:

Initialize matrices and vectors

For any time step:

Until convergence:

Compute matrices $EC^{\hat{n}}$ $C^{\hat{n}}$ $A^{\hat{n}}$ $E^{\hat{n}}$ $J^{\hat{n}}$ *(Fortran)*

Compute the vectors $S^{\hat{n}}$ $S^{*\hat{n}}$ $E^{*\hat{n}}$ *(Fortran)*

Solve the two sparse linear systems in $U^{\hat{n}+1}$ $N^{g\,\hat{n}+1}$ *(Matlab)*

Update $U^{\hat{n}} = U^{\hat{n}+1}$ $N^{g\hat{n}} = N^{g\hat{n}+1}$

Loop until $U^{\hat{n}+1} \cong U^{\hat{n}}$ $N^{g\hat{n}+1} \cong N^{g\hat{n}}$

Change time step:

Update matrices $EC^n = EC^{\hat{n}}$ $C^n = C^{\hat{n}}$ $A^n = A^{\hat{n}}$ $E^n = E^{\hat{n}}$

Update vectors $S^n = S^{\hat{n}}$ $S^{*n} = S^{*\hat{n}}$ $E^{*n} = E^{*\hat{n}}$

Update solutions $U^n = U^{\hat{n}+1}$ $N^{gn} = N^{g\hat{n}+1}$ *(after saving solutions)*

Loop until final integration time

Calculation of the matrices

A finite difference discretization was applied to the space coordinate derivatives. In this section, the formulation of the matrices deriving for equation A.9 is discussed. Analogous forms can be easily found for the matrices in equation A.10.

Diffusive term

A centered differences scheme was applied to express the divergence of the diffusive fluxes. At the i-th node, we have that:

$$\left[\frac{1}{r^2}\frac{\partial}{\partial r}\left(r^2\cdot\left(cD(x,\varepsilon)\frac{\partial x}{\partial r}\right)\right)\right]_i = \frac{c}{2r_i^2(\Delta r)^2} \cdot\left[x_{i-1}\cdot\left(r_{i-1/2}^2\cdot(D_i+D_{i-1})\right)-x_i \cdot\left(r_{i-1/2}^2\cdot D_{i-1}+\left(r_{i-1/2}^2+r_{i+1/2}^2\right)\cdot D_i+r_{i+1/2}^2\cdot D_{i+1}\right)+x_{i+1} \cdot\left(r_{i+1/2}^2\cdot(D_i+D_{i+1})\right)\right] \quad \text{A.11}$$

Where the indicated terms are:

$$r_{i-1/2}=\frac{r_{i-1}+r_i}{2} \quad \text{A.12}$$

$$r_{i+1/2}=\frac{r_{i+1}+r_i}{2} \quad \text{A.13}$$

$$D_i = D(x_i,\varepsilon_i) \quad \text{A.14}$$

$$x_i=\begin{bmatrix}x_1\\x_2\\\dots\\x_N\end{bmatrix}_i \quad \text{A.15}$$

In order to build the global diffusion matrix A, it will be necessary to calculate the diffusion matrices D for any r_i. These will be assembled in the global matrix.

For any cell node three matrices NGxNG can be created:

$$A_{i-1}=\frac{c}{2r_i^2(\Delta r)^2}\left[\left(r_{i-1/2}^2\cdot(D_i+D_{i-1})\right)\right] \quad \text{A.16}$$

$$A_i=\frac{c}{2r_i^2(\Delta r)^2}\left[\left(r_{i-1/2}^2\cdot D_{i-1}+\left(r_{i-1/2}^2+r_{i+1/2}^2\right)\cdot D_i+r_{i+1/2}^2\cdot D_{i+1}\right)\right] \quad \text{A.17}$$

$$A_{i+1}=\frac{c}{2r_i^2(\Delta r)^2}\left[\left(r_{i+1/2}^2\cdot(D_i+D_{i+1})\right)\right] \quad \text{A.18}$$

Matrices A.16-A.18 are built up into the global diffusion matrix in order to calculate the divergence of the diffusive fluxes in any point of the domain, as follows:

$$-\begin{bmatrix} [\cdots] \\ [\cdots] \\ [\cdots] \\ [\,div(J)_i\,] \\ [\cdots] \\ [\cdots] \\ [\cdots] \end{bmatrix} = \begin{bmatrix} [\cdots] & [\cdots] & [\cdots] & & & & \\ & [\cdots] & [\cdots] & [\cdots] & & & \\ & & [A_{i-1}] & [\boldsymbol{A_i}] & [A_{i+1}] & & \\ & & & [\cdots] & [\cdots] & [\cdots] & \\ & & & & [\cdots] & [\cdots] & [\cdots] \end{bmatrix} \cdot \begin{bmatrix} [\cdots] \\ [\cdots] \\ [x_{i-1}] \\ [\,x_i\,] \\ [x_{i+1}] \\ [\cdots] \\ [\cdots] \end{bmatrix} \qquad \text{A.19}$$

The global matrix A has 3(2NG-1) non zero diagonals in general, if the diffusion model used is Stefan-Maxwell. If the diffusion model is Fick, or Mixture Averaged, A becomes tri-diagonal. Note that A depends on x, unless the diffusion is Fickian. This means that A must be calculated iteratively while solving the system in x. This is not too much of a problem, since the dependence of A on x is quite "weak", which means that the quadratic convergence using a Newton method is not slowed down too much.

Generalization of the diffusion matrix D

We discussed how to calculate the diffusion matrix $D(x_i, \varepsilon_i)$ for Stefan-Maxwell diffusion. A D matrix can be also calculated from the other diffusion models. The generalized D matrix, for Mixture averaged of Fick diffusion will be a diagonal matrix, since the diffusive flux of the i-th species depends only on the related composition gradient of the i-th species. Considering both molecular and Knudsen diffusion, in general D will be the inverse of a B matrix, which can be calculated as follows:

Stefan-Maxwell + Knudsen

$$B_{ij} = \left[\frac{x_i}{Đ_{iN}} + \delta_{ij}\left(\frac{1}{D_i^K} + \sum_{\substack{k=1 \\ k\neq i}}^{N} \frac{x_k}{Đ_{ik}}\right) + (\delta_{ij} - 1)\frac{x_i}{Đ_{ij}}\right] \cdot \frac{1}{\left(\frac{\varepsilon}{\tau}\right)} \qquad \text{A.20}$$

Mixture Averaged + Knudsen

$$B_{ij} = \delta_{ij}\left(\frac{1}{D_i^K} + \frac{1}{1 - x_i} \cdot \sum_{\substack{k=1 \\ k\neq i}}^{N} \frac{x_k}{Đ_{ik}}\right) \cdot \frac{1}{\left(\frac{\varepsilon}{\tau}\right)} \qquad \text{A.21}$$

Binary Fick + Knudsen

$$B_{ij} = \delta_{ij}\left(\frac{1}{D_i^K} + \frac{1}{Đ_{iN}}\right)\cdot\frac{1}{\left(\frac{\varepsilon}{\tau}\right)} \qquad \text{A.22}$$

Considering the species N as the inert one. Note that if all of the species are infinitely diluted into the species N, (x_i = 0 for i = 1,2…N-1 and x_N = 1), then the matrix expression for the Mixture averaged and Stefan Maxwell model become identical to the binary Fick B matrix.

Convection term

Using a 1st order upwind, the divergence of the convective flux becomes:

$$\left[\frac{1}{r^2}\frac{\partial}{\partial r}(r^2\cdot N^g x)\right]_i = -\left(\frac{N^g{}_i}{\Delta r}\right)\cdot x_i + \left(\frac{N^g{}_{i+1}\cdot r_{i+1}^2}{\Delta r\cdot r_i^2}\right)\cdot x_{i+1} \qquad N^g < 0 \qquad \text{A.23}$$

$$\left[\frac{1}{r^2}\frac{\partial}{\partial r}(r^2\cdot N^g x)\right]_i = +\left(\frac{N^g{}_i}{\Delta r}\right)\cdot x_i - \left(\frac{N^g{}_{i-1}\cdot r_{i-1}^2}{\Delta r\cdot r_i^2}\right)\cdot x_{i-1} \qquad N^g > 0 \qquad \text{A.24}$$

Extracting the vector of gas compositions, we obtain:

$$\begin{bmatrix} [\cdots] \\ [\cdots] \\ [\cdots] \\ [\,div(N^g x)_i\,] \\ [\cdots] \\ [\cdots] \\ [\cdots] \end{bmatrix} = \begin{bmatrix} [\cdots] & [\cdots] & [\cdots] & & & & \\ & [\cdots] & [\cdots] & [\cdots] & & & \\ & & [0] & \left[-\left(\frac{N^g{}_i}{\Delta r}\right)\right] & \left[\left(\frac{N^g{}_{i+1}\cdot r_{i+1}^2}{\Delta r\cdot r_i^2}\right)\right] & & \\ & & & [\cdots] & [\cdots] & [\cdots] & \\ & & & & [\cdots] & [\cdots] & [\cdots] \end{bmatrix}\cdot\begin{bmatrix} [\cdots] \\ [\cdots] \\ [x_{i-1}] \\ [\,x_i\,] \\ [x_{i+1}] \\ [\cdots] \\ [\cdots] \end{bmatrix} \qquad N^g < 0 \qquad \text{A.25}$$

$$\begin{bmatrix} [\cdots] \\ [\cdots] \\ [\cdots] \\ [\,div(N^g x)_i\,] \\ [\cdots] \\ [\cdots] \\ [\cdots] \end{bmatrix} = \begin{bmatrix} [\cdots] & [\cdots] & [\cdots] & & & & \\ & [\cdots] & [\cdots] & [\cdots] & & & \\ & & \left[-\left(\frac{N^g{}_{i-1}\cdot r_{i-1}^2}{\Delta r\cdot r_i^2}\right)\right] & \left[\left(\frac{N^g{}_i}{\Delta r}\right)\right] & [0] & & \\ & & & [\cdots] & [\cdots] & [\cdots] & \\ & & & & [\cdots] & [\cdots] & [\cdots] \end{bmatrix}\cdot\begin{bmatrix} [\cdots] \\ [\cdots] \\ [x_{i-1}] \\ [\,x_i\,] \\ [x_{i+1}] \\ [\cdots] \\ [\cdots] \end{bmatrix} \qquad N^g > 0 \qquad \text{A.26}$$

Commonly, the sign of N^g is known before solving the model, and one of the two forms can be chosen accordingly.

Jacobian matrix and source term

The global Jacobian matrix is obtained calculating the local matrices J_j, one for any j-th point of the grid. For a general mechanism, the local Jacobian can be obtained as:

$$J_j = \nu \cdot \begin{bmatrix} \frac{\partial R_1}{\partial x^g{}_{1,j}} & \cdots & \frac{\partial R_1}{\partial x^g{}_{NG,j}} & \frac{\partial R_1}{\partial c^s_{1,j}} & \cdots & \frac{\partial R_1}{\partial c^s_{NS,j}} \\ \cdots & \cdots & \cdots & \cdots & \cdots & \cdots \\ \frac{\partial R_{NR}}{\partial x^g{}_{1,j}} & \cdots & \frac{\partial R_{NR}}{\partial x^g{}_{NG,j}} & \frac{\partial R_{NR}}{\partial c^s_{1,j}} & \cdots & \frac{\partial R_{NR}}{\partial c^s_{NS,j}} \end{bmatrix} \quad \text{A.27}$$

In this formulation, ν is the global stoichiometric matrix, extended to both gas and solid species.

At the same way, the local source term will be:

$$s_j = \nu \cdot \begin{bmatrix} R_1(x_j^g, c_j^s) \\ \cdots \\ R_{NR}(x_j^g, c_j^s) \end{bmatrix} \quad \text{A.28}$$

Equations A.27-A.28 can be more completely explicated once the reaction mechanism is defined, and also the form of the reaction rates has been chosen. Here we report the case for the reaction mechanism of reduction of Pseudobrookite in two steps:

Fe2O3 + H2 → 2 FeO + H2O (R_1)

Fe2TiO5 + TiO2 + H2 → 2 FeTiO3 + H2O (R_2)

The two gas species and five solid species are ordered like this: H_2 H_2O Fe_2O_3 Fe_2TiO_5 FeO $FeTiO_3$ TiO_2. So the global stoichiometric matrix for the mechanism will be:

$$\nu = \begin{pmatrix} -1 & -1 \\ 1 & 1 \\ -1 & 0 \\ 0 & -1 \\ 1 & 0 \\ 0 & 1 \\ 0 & -1 \end{pmatrix} \quad \text{A.29}$$

If the reaction rates are expressed as first order in gas reactant, irreversible, and using the traditional model, grain model, we have:

$$R_1 = k_1 \cdot c \cdot x_{H2} \cdot \left(\frac{c_{Fe2O3}}{c_{Fe2O3}{}^0} \right)^{\alpha} \quad \text{A.30}$$

$$R_2 = k_2 \cdot c \cdot x_{H2} \cdot \left(\frac{c_{Fe2TiO5}}{c_{Fe2TiO5}{}^0} \right)^{\alpha} \quad \text{A.31}$$

So the local source term and Jacobian matrix are expressed respectively from equation A.32 and A.33:

$$s_j = \nu \cdot \begin{bmatrix} k_1 \cdot c \cdot x_{H2,j} \cdot \left(\frac{c_{Fe2O3,j}}{{c_{Fe2O3,j}}^0} \right)^{\alpha} \\ k_2 \cdot c \cdot x_{H2,j} \cdot \left(\frac{c_{Fe2TiO5,j}}{{c_{Fe2TiO5,j}}^0} \right)^{\alpha} \end{bmatrix} \quad \text{A.32}$$

$$J_j = \nu \cdot \begin{bmatrix} \left(k_1 \cdot c \cdot \left(\frac{c_{Fe2O3,j}}{{c_{Fe2O3,j}}^0} \right)^{\alpha} \right) & 0 & \left(k_1 \cdot c \cdot x_{H2,j} \cdot \frac{\alpha \cdot \left(c_{Fe2O3,j} \right)^{\alpha-1}}{\left({c_{Fe2O3,j}}^0 \right)^{\alpha}} \right) & 0 & 0 & 0 & 0 \\ \left(k_2 \cdot c \cdot \left(\frac{c_{Fe2TiO5,j}}{{c_{Fe2TiO5,j}}^0} \right)^{\alpha} \right) & 0 & 0 & \left(k_2 \cdot c \cdot x_{H2,j} \cdot \frac{\alpha \cdot \left(c_{Fe2TiO5,j} \right)^{\alpha-1}}{\left({c_{Fe2TiO5,j}}^0 \right)^{\alpha}} \right) & 0 & 0 & 0 \end{bmatrix} \quad \text{A.33}$$

Once the local matrices are calculated for any grid point, they are assembled into the global matrices, consistently with the ordering of the variables in the vector U of equation A.6.

More details about the numerical implementation, with the definition of all the problem matrices, can be found in the source codes reported in appendix C.

Appendix B: Basics of Weighted Residual Methods

Let us consider a generic partial differential equation, and defined as follows:

$D(u(x)) = f$ A.34

Where u(x) is the unknown function, defined in the domain Ω, D is a generic differential operator, and f is a known function. An approximation ũ(x) of the exact solution can be defined, as a linear combination of N continuous base functionsξ, linearly independent from each other:

$$\tilde{u}(x) = \sum_{j=1}^{N} a_j \xi_j(x) \quad \text{A.35}$$

It can be mathematically proved that if N→∞, there is a set of coefficients a_j such that ũ = u. In practical applications, a finite number of coefficients a_j must be found, such that ũ approximates u as well as possible. In order to define a criterion of "good approximation", the residual R of ũ is defined, as a function of the set of coefficients a = [a_1, a_2,… a_N]:

$$R(a, x) = f - D(a, x) \quad \text{A.36}$$

The residual is a function of x, once the coefficients are defined. It should be noticed that the residual cal be analytically calculated, if the derivatives of the base functions can be calculated. The Weighted Residual Method allows calculating the set of coefficients a, by solving the system of equations defined by the following expression:

$$\int_{\Omega} R(a, x) w_i(x) dx = 0 \qquad for\ i = 1,2 \dots N \quad \text{A.37}$$

In equation B.4, $w_i(x)$ are weight functions, that are orthogonalized to the residual. A wise choice of the weight functions must be done, in order to obtain a good approximation with few base functions. Different numerical methods are defined, based on the form of $w_i(x)$. The main ones are reported in the next lines:

a) Collocation method.

According to this, the weight functions are defined as follows:

$$w_i(x) = \delta(x - x_i) \quad \text{A.38}$$

Here, δ is the Dirac delta, which is equal to infinite if $x = x_i$ and is equal to zero otherwise, and its integral over the whole domain is equal to one. The nodes x_i are chosen points of the domain. By choosing these base functions, the system to solve becomes:

$$R(a, x_i) = 0 \qquad for\ i = 1,2 \dots N \tag{A.39}$$

This is equal to impose that the residual must be zero in the chosen nodes x_i inside the domain.

b) Method of subdomains.

The domain is divided into a number of subregions Ω_i. For each one of these, a weight function is defined, as follows:

$$w_i(x) = 1 \quad if\ x \in \Omega_i \tag{A.40}$$

$$w_i(x) = 0 \quad if\ x \notin \Omega_i$$

The system to solve is:

$$\int_{\Omega_i} R(a, x)dx = 0 \qquad for\ i = 1,2 \dots N \tag{A.41}$$

This is equal to assume that the integral of the residual is locally zero, in each subdomain.

c) Least squares method.

The weight functions are in the form of equation B.9:

$$w_i(x) = \frac{\partial R(a, x)}{\partial a_i} \tag{A.42}$$

Even if it is not straight forward, if this method is applied this is equal to find a set of coefficients a_i such that the integral of the square of the residual is minimum:

$$min \int_{\Omega} \big(R(a, x)\big)^2 dx \tag{A.43}$$

d) Galerkin method.

According to this, the weight functions are equal to the base functions:

$$w_i(x) = \xi_i \tag{A.44}$$

So the residual must be orthogonal to each of the base functions:

$$\int_{\Omega} R(a,x)\xi_i dx = 0 \qquad for\ i = 1,2 \dots N \tag{A.45}$$

In general, there is not a quality hierarchy of the different methods. The Galerkin method has become very popular, because is the base of the Finite Element Methods (an application of WRM, that also imply the choice of piecewise base functions). The Least Squares Method assures that the residual of the approximate solution is minimum, but it must be noticed that minimum residual does not imply minimum error, in general. The collocation method is the easiest to use, because it does not need the solution of integrals to calculate the coefficients of the resulting discretization matrices. Besides, it offers flexibility because the collocation points can be arbitrarily chosen, which means that the approximation of the solution can be more accurate in a fixed part of the domain, once the number of collocation points is set. For these reasons, collocation methods have also become popular.

WRM for unsteady state problems

The Weighted Residual Methods are usually applied to discretize the space derivatives. If the function also depends on time, a different approach is used.

Let us consider a problem defined by the following differential equation:

$$\frac{\partial u(x,t)}{\partial t} = -D(u(x,t)) + f \tag{A.46}$$

Where D is a linear differential operator, involving only space derivatives (in the x variables). The numerical method can still be applied. In this case, the approximation of the solution is defined by considering time dependent coefficients $a_j(t)$, as follows:

$$\tilde{u}(x,t) = \sum_{j=1}^{N} a_j(t)\xi_j(x) \tag{A.47}$$

It is interesting to notice that this approach is similar to the principle of separation of variables, when an exact solution of a PDE is calculated. As a matter of fact, $a_j(t)$ only depend on time, but not on space, and $\xi_j(x)$ only depend on space but are constant in time. By applying the weighted residual methods, we obtain:

$$\int_{\Omega} \left(\frac{\partial}{\partial t} \sum_{j=1}^{N} a_j(t)\xi_j(x) \right) w_i(x) dx = \int_{\Omega} \left(-D\left(\sum_{j=1}^{N} a_j(t)\xi_j(x) \right) + f \right) w_i(x) dx \tag{A.48}$$

By inverting the derivation and integration operators, thanks to the properties of integrals and derivatives, equation B.15 becomes:

$$\sum_{j=1}^{N} \frac{\partial a_j(t)}{\partial t} \int_{\Omega} \xi_j(x) w_i(x) dx = \int_{\Omega} \left(-D\left(\sum_{j=1}^{N} a_j(t) \xi_j(x) \right) + f \right) w_i(x) dx \quad \text{A.49}$$

Equation B.16 can be written on a matrix form, as follows:

$$M \frac{\partial a(t)}{\partial t} = A \cdot a(t) - b \quad \text{A.50}$$

In this form, A and b can be calculated as in the steady state problem. Their general form is expressed by the following equations:

$$A_{ij} = -\int_{\Omega} \left(D\left(\xi_j(x)\right) \right) w_i(x) dx \quad \text{A.51}$$

$$b_i = \int_{\Omega} f(x) w_i(x) dx \quad \text{A.52}$$

The matrix M is called mass matrix, and its coefficients are calculated from the following integrals:

$$M_{ij} = \int_{\Omega} \xi_j(x) w_i(x) dx \quad \text{A.53}$$

In particular, for the collocation method, equations B.18-B20 become:

$$A_{ij} = -D\left(\xi_j(x_i)\right) \quad \text{A.54}$$

$$b_i = f(x_i) \quad \text{A.55}$$

$$M_{ij} = \xi_j(x_i) \quad \text{A.56}$$

Whereas, for the Galerkin method:

$$A_{ij} = -\int_{\Omega} \left(D\left(\xi_j(x)\right) \right) \xi_i(x) dx \quad \text{A.57}$$

$$b_i = \int_{\Omega} f(x) \xi_i(x) dx \quad \text{A.58}$$

$$M_{ij} = \int_{\Omega} \xi_i(x)\xi_j(x)dx \quad \text{A.59}$$

The matrices M, A and b do not depend on time, so they can be calculated once the method and set of base functions have been chosen. By applying the WRM, the initial PDE equation is transformed in a system of ODE, that can be easily solved. In common practice, the time derivatives are discretized using finite differences. For instance, using the generalized Euler method:

$$M\frac{a^{n+1} - a^n}{\Delta t} = \theta(Aa^{n+1} - b) + (1-\theta)(Aa^n - b) \quad \text{A.60}$$

The resulting linear system is:

$$(M - \Delta t\theta A)a^{n+1} = (M + \Delta t(1-\theta)A)a^n - \Delta tb \quad \text{A.61}$$

At each time step, it is sufficient to solve the system B.28 in the variables a^{n+1}. These are the set of coefficients that approximate the solution at the n+1 time step. The system can be solved, once the solution at time n is known.

Boundary and initial conditions

The boundary conditions are imposed a priori, while defining the base functions. The set of $\xi_j(x)$ is chosen, so that the approximated solution satisfies the boundary conditions for any set of coefficients $a(t)$.

The initial conditions are defined by finding a set of coefficients a_j that best approximates the form of the function u, at the initial time, which is usually known analytically. In order to do so, a least squares fitting can be performed on the function u(x,0). Note that the values of the coefficients generally don't have a physical meaning, but are just defined by the numerical method used.

Appendix C: Matlab codes

In this section, the main versions of the codes used to implement the presented models are shown.

Solution of SCM for one, two or three interfaces (reaction rate subroutine)

```
function dydt = scm(t,c,k,K,D,r0,cb,nus,nug,na,n,ceq,iseq)


ci  = c.*na;
cr  = zeros(n+1,1);
for i = 1:n+1
    cr(i) = sum(ci(1:i));
end
r = r0*(cr(1:end-1)/cr(end).*(cr(1:end-1)>1e-16)+1e-16*(cr(1:end-1)<=1e-16)).^(1/3);

R = rates(r,cb,ceq,k,K,D,r0,n,iseq);
if n==2
    R = R.*[(c(1)>0); (c(2)>0)];
end

dydt = nus*R;

% Velocità di reazione per SCM a 1, 2 o 3 interfacce
function R = rates(r,cb,ceq,k,K,D,r0,n,iseq)

switch n
    case 1                  % 1 interfaccia
        x  = (r(1)/r0);
        A1 = 1/x^2/(k(1)*(1+1/K(1)));
        B1 = (1-x)/x*r0/D(1);
        F  = 0;
        W  = A1+B1+F;
        R  = 3/r0/W*(cb(1)-ceq(1));
    case 2                  % 2 interfacce
        x  = (r(1)/r0);
        y  = (r(2)/r0);
        A1 = 1/x^2/(k(1)*(1+1/K(1)*iseq));
        A2 = 1/y^2/(k(2)*(1+1/K(2)*iseq));
        B1 = (y-x)/x/y*r0/D(1);
        B2 = (1-y)/y*r0/D(2);
        F  = 0;
        W  = (A1+B1)*(A2+B2+F)+A2*(B2+F);
        R  = [3/r0/W*(A2+B2+F)*(cb(1)-ceq(1))+   ...
              -(B2+F)*(cb(1)-ceq(2))
              3/r0/W*(-(B2+F)*(cb(1)-ceq(1))+    ...
              +(A1+B1+B2+F)*(cb(1)-ceq(2)))];
        R = R.*[(x>0)*(x<=1); (y>0)*(y<=1)*(y>x)];
    case 3                  % 3 interfacce
        x  = (r(1)/r0);
        y  = (r(2)/r0);
        z  = (r(3)/r0);
        A1 = 1/x^2/(k(1)*(1+1/K(1)));
        A2 = 1/y^2/(k(2)*(1+1/K(2)));
        A3 = 1/z^2/(k(3)*(1+1/K(3)));
```

```
        B1 = (y-x)/x/y*r0/D(1);
        B2 = (z-y)/y/z*r0/D(2);
        B3 = (1-z)/z*r0/D(3);
        F  = 0;
        W  = (A1+B1)*(A3*(A2+B2+B3+F)+(A2+B2)*(B3+F))+A2*(A3*(B2+B3+F))+B2*(B3+F);

        R = [3/r0/W*((A3*(A2+B2+B3+F)+(A2+B2)*(B3+F))*(cb(1)-ceq(1))+   ...
            -(A3*(B2+B3+F)+B2*(B3+F))*(cb(1)-ceq(2))+                   ...
            -A2*(B3+F)*(cb(1)-ceq(3)))
             3/r0/W*(-(B2*(A3+B3+F)+A3*(B3+F))*(cb(1)-ceq(1))+          ...
            +((A1+B1+B2)*(A3+B3+F)+A3*(B3+F))*(cb(1)-ceq(2))+           ...
            -(A1+B1)*(B3+F)*(cb(1)-ceq(3)))
             3/r0/W*(-A2*(B3+F)*(cb(1)-ceq(1))+                         ...
            -(A1+B1)*(B3+F)*(cb(1)-ceq(2))+                             ...
            ((A1+B1)*(A2+B2+B3+F)+A2*(B2+B1+F))*(cb(1)-ceq(3)))];
end
```

Application of SCM to the reduction of iron process, for the system Hematite-Magnetite-Wustite-Iron

```
function [t c] = SCM(t,r0,Xb,T,par)
% Struttura input
% t:    vettore colonna dei tempi
% r0:   raggio della particella (scalare)
% Xb:   matrice delle condizioni al contorno [cri cpi]
% T:    temperatura della particella
%clc
%close all
if nargin==0
    close all
    clc
    r0 = 0.675;                 % Raggio del pellet (cm)
    T = 1073;
    Xb = [0.3783e-4    0.0420e-4  0.0219   0    0   0  0.2049 0.0056 0.7895];
    t = 0:1:3600;
    par = [27.0e4       113859 0.25e4       73674 0.17e4       69488];
end

% === Parametri ===
MWi = [55.845 15.9994];         % Pesi molecolari atomici Fe - O (g/mol)
MWs = [MWi(1)*2+MWi(2)*3        % Peso molecolare Fe2O3 (g/mol)
       MWi(1)*3+MWi(2)*4        % Peso molecolare Fe3O4 (g/mol)
       MWi(1)*1+MWi(2)*1        % Peso molecolare FeO   (g/mol)
       MWi(1)*1+MWi(2)*0];      % Peso molecolare Fe    (g/mol)
ncg = 2;                        % Numero di componenti della fase gas
ncs = 4;                        % Numero di componenti della fase solida
P = 750000;                     % Pressione (Pa)
rho0 = 3.50;                    % Densità del solido iniziale (g/cm3)

% Matrice stechiometrica delle specie gas (-)
nug = [  -1  -1  -1             % CO
          1   1   1];           % CO2
% Matrice stechiometrica delle specie solide (-)
nus = [ -3   0   0              % Fe2O3
         2  -1   0              % Fe3O4
         0   3  -1              % FeO
         0   0   1];            % Fe
% Parametri cinetici (cm/s - J/mol)
k = [par(1:2)                   % 3 Fe2O3 + CO = 2 Fe3O4 + CO2
     par(3:4)                   %   Fe3O4 + CO = 3 FeO   + CO2
```

```
     par(5:6) ];                % FeO   + CO =   Fe    + CO2
% Parametri termodinamici (K)
K = [ 3.940      3968.37        % 3 Fe2O3 + CO = 2 Fe3O4 + CO2
      8.980     -3585.64        %   Fe3O4 + CO = 3 FeO   + CO2
     -2.946      2744.63];      %   FeO   + CO =   Fe    + CO2
% Matrice delle diffusività a 1 atm, 1073 K (cm2/s)
D = [1.0 1.5 1.8                % CO-CO   CO-CO2   CO-N2
     1.5 1.0 1.5                % CO2-CO  CO2-CO2  CO2-N2
     1.8 1.5 1.0];              % N2-CO   N2-CO2   N2-N2
h = 30.0;                       % Coefficiente scambio materia (cm/s)% Conducibilità dei
gas (W/mK)

por0 = [0.3396; 0.3431; 0.4475; 0.6890];

kd = k(:,1).*exp(-k(:,2)/T/8.314);
cd  = 101325./P.*(T./1073).^1.75.*(1/2.*por0.*(1+por0));
Dif = D(1,2).*cd;
Keq = exp(K(:,1)+K(:,2)./T);
cg0 = Xb(1:2);
cs0 = Xb(3:6);
xb = Xb(7:end);
Di = (1-xb)./(xb*(1./D)-xb./diag(D,0)');
cFeMax = sum(cs0.*[2 3 1 1]);

[t c] = ode45(@scm,t,cs0,[],kd,Keq,Dif,cFeMax,r0,cg0,nus);
%plot(t,c)
cH = c(:,1);
cM = c(:,2);
cW = c(:,3);
cF = c(:,4);
r3 = r0*(1-cF./cFeMax).^(1/3);
r2 = r0*((2*cH+3*cM)./cFeMax).^(1/3);
r1 = r0*(2*cH./cFeMax).^(1/3);
x = r1/r0;
y = r2/r0;
z = r3/r0;
plot(t,x,t,y,t,z),legend('r_1/r_0','r_2/r_0','r_3/r_0'),xlabel('t')
figure
plot(t,cH,t,cM,t,cW,t,cF),legend('Fe_2O_3','Fe_3O_4','FeO','Fe'),xlabel('t')
xlim([0 t(end)]),ylim([0 0.04])



function dcdt = scm(t,c,kd,Keq,Dif,cFeMax,r0,cgb,nus)

cH = c(1);
cM = c(2);
cW = c(3);
cF = c(4);
r3 = r0*((1-cF/cFeMax)*(cF<cFeMax)+1e-16*(cF>=cFeMax))^(1/3);
r2 = r0*((2*cH+3*cM)/cFeMax*(2*cH+3*cM>0)+1e-16*(2*cH+3*cM<0))^(1/3);
r1 = r0*(2*cH/cFeMax*(cH>0)+1e-16*(cH<=0))^(1/3);
x = (r1/r0);
y = (r2/r0);
z = (r3/r0);
A1 = 1/x^2/(kd(1)*(1+1/Keq(1)));
A2 = 1/y^2/(kd(2)*(1+1/Keq(2)));
A3 = 1/z^2/(kd(3)*(1+1/Keq(3)));
B1 = (y-x)/x/y*r0/Dif(2);
B2 = (z-y)/y/z*r0/Dif(3);
B3 = (1-z)/z*r0/Dif(4);
F = 0;
W = (A1+B1)*(A3*(A2+B2+B3+F)+(A2+B2)*(B3+F))+A2*(A3*(B2+B3+F))+B2*(B3+F);
ceq1 = (cgb(1)+cgb(2))/(1+Keq(1));
ceq2 = (cgb(1)+cgb(2))/(1+Keq(2));
ceq3 = (cgb(1)+cgb(2))/(1+Keq(3));

R1 = 3/r0/W*((A3*(A2+B2+B3+F)+(A2+B2)*(B3+F))*(cgb(1)-ceq1)+...
```

```
            -(A3*(B2+B3+F)+B2*(B3+F))*(cgb(1)-ceq2)+...
            -A2*(B3+F)*(cgb(1)-ceq3));
R2 = 3/r0/W*(-(B2*(A3+B3+F)+A3*(B3+F))*(cgb(1)-ceq1)+...
            +((A1+B1+B2)*(A3+B3+F)+A3*(B3+F))*(cgb(1)-ceq2)+...
            -(A1+B1)*(B3+F)*(cgb(1)-ceq3));
R3 = 3/r0/W*(-A2*(B3+F)*(cgb(1)-ceq1)+...
            -(A1+B1)*(B3+F)*(cgb(1)-ceq2)+...
            ((A1+B1)*(A2+B2+B3+F)+A2*(B2+B1+F))*(cgb(1)-ceq3));
dcdt = (nus*[R1*(R1>0); R2*(R2>0); R3*(R3>0)]);
```

Application of the continuous model applied to the process reduction of iron. Single particle model, coupled with moving bed reactor model.

```
function PelletFullPFRDiff
clc
close all
global p
global m
global bc
global ic
global solve

% === Parametri ===
p.MWs  = [159.6882; 231.5326; 71.8444; 55.8450];                    % Pesi
molecolari dei solidi (g/mol)
p.MWg  = [28.01010; 44.00950; 28.01340];                            % Pesi
molecolari dei gas (g/mol)
p.r0   = 0.675;                                                     % Raggio del
pellet (cm)
p.ncg  = 2;                                                         % Numero di
reagenti della fase gas
p.ncs  = 4;                                                         % Numero di
componenti della fase solida
% p.rho0 = 3.50;                                                      % Densità
del solido iniziale (g/cm3)
p.rho0 = 5.29;                                                      % Densità del
solido iniziale (g/cm3)
p.rhoi = [5.30; 5.15; 5.70; 7.87];                                  % Densità
intrinseche dei solidi (g/cm3)
p.a0   = [10.0; 2.96; 0.65; 0.40]*10^4*p.rho0;                      % Rapporto
superficie/volume per i solidi puri (1/cm)
p.ps   = [1.72 1.56 2.00 1.50];                                     % Costanti di
sinterizzazione
p.kg   = [0.0240; 0.0146; 0.0240];                                  %
Conducibilità dei gas (W/mK)
p.ks   = [80.2; 80.2; 80.2; 80.2];                                  %
Conducibilità dei solidi (W/mK)
p.Cpg  = [1.185; 1.234; 1.185];                                     % Calori
specifici dei gas (J/gK)
p.Cps  = [1.07; 1.07; 0.82; 0.83];                                  % Calori
specifici dei solidi (J/gK)
p.h    = 30.0;                                                      %
Coefficiente scambio materia (cm/s)
p.ht   = 0.20*4.18;                                                 %
Coefficiente di scambio termico alla parete (W/cm2K)
p.L    = 10;                                                        % Altezza del
reattore (m)
p.d    = 1;                                                         % Diametro
del reattore (m)
p.us   = 0.002;                                                      % Velocità
di discesa del solido (m/s)
```

```
p.m0   = 2;                                                          % Portata
massiva di gas alimentato (kg/s)
p.porx = 0.47;                                                       % Porosità
del letto
p.Np   = (1-p.porx)/(4/3*pi*(p.r0*1e-2)^3);                          % Numero di
pellet per unità di volume (1/m3tot)
p.rhod = 4.23;
p.MWd  = 79.866;
p.yd   = 0.46;

% Matrice stechiometrica delle specie gas (-)
p.nug = [ -1  -1  -1            % CO
           1   1   1];          % CO2
% Matrice stechiometrica delle specie solide (-)
p.nus = [ -3   0   0            % Fe2O3
           2  -1   0            % Fe3O4
           0   3  -1            % FeO
           0   0   1];          % Fe
% Parametri cinetici (cm/s - J/mol)
p.k = [221.82e-4  5514.7*8.314  % 3 Fe2O3 + CO = 2 Fe3O4 + CO2
       704.03e-4  6098.6*8.314  %   Fe3O4 + CO = 3 FeO   + CO2
       916.20e-4  2036.5*8.314];%   FeO   + CO =   Fe    + CO2
% Parametri termodinamici (K)
p.K = [3.940      3968.37       % 3 Fe2O3 + CO = 2 Fe3O4 + CO2
       8.980     -3585.64       %   Fe3O4 + CO = 3 FeO   + CO2
      -2.946      2744.63];     %   FeO   + CO =   Fe    + CO2
% Matrice delle diffusività a 1 atm, 1073 K (cm2/s)
p.D = [1.0  1.5  1.8            % CO-CO   CO-CO2   CO-N2
       1.5  1.0  1.5            % CO2-CO  CO2-CO2  CO2-N2
       1.8  1.5  1.0];          % N2-CO   N2-CO2   N2-N2
% Parametri per la viscosità
p.mu0 = [118  518.67  0.01720   % CO
         240  527.67  0.01480   % CO2
         111  540.99  0.01781]; % N2
% Parametri per i calori di reazione dH = a + b*(T-c)
p.dH =  [-3000  -3.18  1023     % 3 Fe2O3 + CO = 2 Fe3O4 + CO2
         13500   0     0        %   Fe3O4 + CO = 3 FeO   + CO2
         -3975  -0.90  673];    %   FeO   + CO =   Fe    + CO2

% === Creazione mesh ===
m.ns = 100;                                                           % Numero di
celle
m.nt = 100;                                                          % Numero di
tempi
m.rb = linspace(0,p.r0,m.ns+1)';                                     % Coordinate
dei bordi delle celle nel pellet (cm)
m.r  = (m.rb(2:end)+m.rb(1:end-1))/2;                                % Coordinate
dei nodi nel pellet (cm)
m.z  = linspace(0,p.L,m.nt);                                         %
Discretizzazione spaziale del reattore (m)
m.t  = m.z/p.us;                                                     %
Discretizzazione del tempo (s)

% === Condizioni al contorno ===
bc.Tb   = 1073;                                                      % Temperatura
di bulk (K)
bc.Pb   = 750000;                                                    % Pressione
di bulk (Pa)
bc.cb   = bc.Pb/8.314/bc.Tb*10^-6;                                   %
Concentrazione totale di bulk (mol/cm3)
bc.xend = [0.4 0.0 0.6];
bc.cgb  = bc.xend(1:end-1)*bc.cb;                                    %
Concentrazioni dei gas di bulk (mol/cm3)
bc.cs0  = [p.rho0/p.MWs(1) 0 0 0];                                   %
Concenrazioni dei solidi (mol/cm3)
bc.rhouend = -p.m0/(p.d^2/4*pi);  %kg/m2tot/s

% === Condizioni iniziali ===
```

```
ic.cg0    = repmat([0.0 0.0],m.ns,1)*bc.cb;                                  %
Composizione fase gas nel pellet (mol/cm3)
ic.cs0    = repmat(bc.cs0,m.ns,1);                                           %
Composizione fase solida nel pellet (mol/cm3)
ic.T0     = ones(m.ns,1)*bc.Tb;                                              % Temperature
iniziali (K)
ic.por0   = epps(ic.cs0,[],p.MWs,p.rhoi,m.ns,p.ncs);                         % Porosità
iniziale
ic.cgpor0 = ic.cg0.*repmat(ic.por0,1,p.ncg);                                 % Prodotto
concentrazioni-porosità iniziale

% === Setting modello ===
solve.pfr = false;
% Modello di diffusione
% F:        Fick, diffusività binaria
% MA:       Fick, diffusività Mixture-Averaged
% SM:       Stefan-Maxwell
modelD = 'SM';

% Modello termico
% ISOT:     Isotermo, temperatura omogenea, uguale a quella di bulk
% ADIAB:    Adiabatico, scambio termico nullo alla parete
% BT:       Temperatura fissa alla parete, uguale a quella di bulk
% FLUX:     Flusso termico alla parere, secondo la legge q = ht*(Tb-T)
modelT = 'FLUX';

% Esecuzione del calcolo
% true:  Esegue l'integrazione temporale e post processing
% false: Carica i risultati ed esegue post processing e bilanci di materia
docalc = true;
doplot = true;

% === Inizializzazioni ===
m.Afv = 3*[-m.rb(1:end-1)./(m.rb(2:end).^3-m.rb(1:end-1).^3)...              % Diagonale -
1 della matrice dei volumi finiti
           m.rb(2:end)./(m.rb(2:end).^3-m.rb(1:end-1).^3)];                  % Diagonale
0 della matrice dei volumi finiti
m.Afv = spdiags(m.Afv,[1 0],m.ns,m.ns)';                                     % Matrice
sparsa dei volumi finiti per divergenza in geometria sferica

X0   = [reshape(ic.cgpor0,[],1)                                              % Condizioni
iniziali per il bilancio fase gas
        reshape(ic.cs0,[],1)                                                 % Condizioni
iniziali per il bilancio fase solida
        reshape(ic.T0,[],1)];                                                % Condizioni
iniziali per il bilancio termico
Xend = [bc.rhouend                                                           % Condizioni
finali per l'equazione di continuità di bulk
        bc.xend(1:end-1)'];                                                  % Condizioni
finali per il bilancio in fase gas di bulk

% === Calcolo ===
if docalc==true
    if solve.pfr
        omega = 0.05;                                                        % Fattore di
rilassamento
        nmax  = 100;                                                         % Numero
massimo di iterazioni
        toll  = 1e-4;                                                        % Tolleranza
        x     = Xend;                                                        % Inizializza
le condizioni iniziali non note
        %x     = [-15.510;  0.0176; 0.3822];
        err   = 1;                                                           % Inizializza
l'errore
        n     = 1;                                                           % Inizializza
il numero di iterazioni
        tic
        while err>toll && n<nmax
```

```
            fprintf('\n N. iterazione: %3.0f \n',n)
            R   = res(x,m.t,X0,Xend,modelD,modelT);                          % Risolve ai
valori iniziali e calcola il residuo
            err = norm(R);                                                   % Funzione
errore
            x   = x+omega*R;                                                 % Valore
delle incognite alla nuova iterazione
            n   = n+1;                                                       %
Aggiornamento del contatore
        end
        x        = [x; 1-sum(x(end-p.ncg+1:end)); zeros(p.ncg+1,1)];        %
Composizione della soluzione
        [~, X]   = ode15s(@DAEfun,m.t,[X0; x],[],modelD,modelT,false);      % Risoluzione
dei bilanci con i valori al contorno corretti
        etime    = toc;                                                      % Tempo di
calcolo (s)
        fprintf('\n Tempo di calcolo: %3.2f s\n',etime)
    else
        x = Xend;
        x        = [x; 1-sum(x(end-p.ncg+1:end)); zeros(p.ncg+1,1)];        %
Composizione della soluzione
        [~, X]   = ode15s(@DAEfun,m.t,[X0; x],[],modelD,modelT,false);
    end
    save('pelletPFRDiffArt.mat','X','X0','x','p','m','bc')                     % Salva le
soluzioni
else
    load 'pelletPFRDiffArt.mat'                                                 % Carica
le soluzioni
end

% === Post Processing ===
rhou  = -flipud(X(:,m.ns*(p.ncg+p.ncs+1)+1));
xbulk = flipud(X(:,m.ns*(p.ncg+p.ncs+1)+2:m.ns*(p.ncg+p.ncs+1)+2+p.ncg));
j     = flipud(X(:,m.ns*(p.ncg+p.ncs+1)+1+(p.ncg+1)+1:end));
rho   = xbulk*p.MWg*bc.cb*1e3;
u     = rhou./rho;
cs    = X(:,m.ns*p.ncg+1:m.ns*(p.ncg+p.ncs));

%n(m.t(1),X(1,:)',modelD,modelT,doplot)
subplot(3,2,[2 4 6])
plot(xbulk,m.z),xlabel('x_i'),ylabel('z (m)'),legend('CO','CO_2','N_2'),xlim([0 0.7])
csI = reshape(cs(round(1/100*m.nt),:),m.ns,p.ncs);
subplot(3,2,1)
plot(m.r/m.r(end),csI),ylabel(sprintf('z = %3.1f m',m.z(round(99/100*m.nt))))
legend('Fe_2O_3','Fe_3O_4','FeO','Fe','Location','NorthWest')
csI = reshape(cs(round(1/2*m.nt),:),m.ns,p.ncs);
subplot(3,2,3)
plot(m.r/m.r(end),csI),ylabel(sprintf('z = %3.1f m',m.z(round(1/2*m.nt))))
csI = reshape(cs(round(1/1*m.nt),:),m.ns,p.ncs);
subplot(3,2,5)
plot(m.r/m.r(end),csI),ylabel(sprintf('z = %3.1f m',m.z(1))),xlabel('r/R')

figure
plot(m.z,j)

figure
plot(m.z,u)
m.t
% cs0 = reshape(cs(1,:),[],4);
% m0 = trapz(m.r,4*pi*m.r.^2.*(cs0*p.MWs));
% mend = trapz(m.r,4*pi*m.r.^2.*(csI*p.MWs));
% % u(end)*(D^2/4*pi)*cbulk(end)*1e6*xbulk(1,2).*16*1e-3
% mpin = p.us*(p.d^2/4*pi).*p.Np*m0*1e-3
% mpout = p.us*(p.d^2/4*pi).*p.Np*mend*1e-3
% mpin-mpout
%
% mgin = rhou(1)*pi*p.d^2/4
% mgout = rhou(end)*pi*p.d^2/4
```

```
% mgout-mgin
% figure
% plot(m.z,j)


% ========================================================================
% Costruzione dei bilanci di materia ed energia
% ========================================================================
function B = DAEfun(t,X,modelD,modelT,doplot)
global p
global m
global bc
global solve

% Estrazione delle variabili dipendenti
cgpor = reshape(X(1:m.ns*p.ncg),m.ns,p.ncg);                                % Matrice
delle concentrazioni in fase gas (mol/cm3tot)
cs    = reshape(X(m.ns*p.ncg+1:m.ns*(p.ncg+p.ncs)),m.ns,p.ncs);             % Matrice
delle concentrazioni in fase solida (mol/cm3tot)
T     = X(m.ns*(p.ncg+p.ncs)+1:m.ns*(p.ncg+p.ncs+1));                       % Vettore
delle temperature (K)
rhou  = X(m.ns*(p.ncg+p.ncs+1)+1);                                          % Flusso
massivo di bulk (kg/m2tot/s)
xbulk = X(m.ns*(p.ncg+p.ncs+1)+2:m.ns*(p.ncg+p.ncs+1)+2+p.ncg)';            % Frazioni
massive dei gas di bulk
jbulk = X(m.ns*(p.ncg+p.ncs+1)+1+(p.ncg+1)+1:end);                          % Flussi
diffusivi massivi dei gas di bulk (kg/m2tot/s)

xbulk = xbulk.*(xbulk>0)+ones(1,p.ncg+1)*1e-10.*(xbulk<=0);                 % Porta a
zero le frazioni negative
xbulk = xbulk/sum(xbulk);                                                   %
Rinormalizza sulla somma a 1
ybulk = xbulk.*p.MWg'/(xbulk*p.MWg);                                        % Frazioni
massive dei gas di bulk

% Variabili ai nodi
[por rho] = epps(cs,[],p.MWs,p.rhoi,m.ns,p.ncs);                            % Campo di
porosità (-) e densità apparente (g/cm3)
c   = bc.Pb/8.314./T*10^-6;                                                 % Matrice
della concentrazione totale di gas (mol/cm3gas)
cg  = cgpor./repmat(por,1,p.ncg);                                           % Matrice
delle concentrazioni in fase gas (mol/cm3gas)
xg  = [cg./repmat(c,1,p.ncg) 1-sum(cg./repmat(c,1,p.ncg),2)];               % Frazioni
molari dei gas
xs  = cs./repmat(sum(cs,2),1,p.ncs);                                        % Frazioni
molari dei solidi
P   = c*1e6*8.314.*T;                                                       % Campo di
pressione (Pa)
ktg = xg*p.kg/100;                                                          %
Conducibilità della fase gas (W/cm/K)
kts = xs*p.ks/100;                                                          %
Conducibilità della fase solida (W/cm/K)
kt  = ktg.*por+kts.*(1-por);                                                %
Conducibilità del medium (W/cm/K)
Cpg = xg*p.Cpg;                                                             % Cp della
fase gas (J/gK)
Cps = xs*p.Cps;                                                             % Cp della
fase solida (J/gK)
Cp  = Cpg.*por+Cps.*(1-por);                                                % Cp del
medium (J/gK)
DH  = (repmat(p.dH(:,1)',m.ns,1)+repmat(p.dH(:,2)',m.ns,1).*...             % Calori di
reazione (J/mol)
      (repmat(T,1,size(p.dH,1))-repmat(p.dH(:,3)',m.ns,1)))*4.18;

% Estrapolazioni al contorno
nfit = 3;                                                                   % Grado del
polinomio da utilizzare
```

```
pb  = polyval(polyfit(m.r(end-nfit:end),por(end-nfit:end),nfit),m.rb(end)); % Porosità a
r = R (-)
kb  = polyval(polyfit(m.r(end-nfit:end),kt(end-nfit:end),nfit),m.rb(end));  %
Conducibilità a r = R (W/cm/K)

% Variabili ai bordi delle celle
porb = [por(1); Davg(por(1:end-1),por(2:end)); pb];                         % Porosità
ktb  = [kt(1); Davg(kt(1:end-1),kt(2:end)); kb];                            %
Conducibilità (W/cm/K)
[T0 x0] = BC(bc.Tb,bc.Pb,xbulk,m.rb(end)-m.r(end),p.ncg,...                 % Temperatura
e composizione alla parete
           modelT,modelD,T(end),xg(end,:),ktb(end),porb(end),p.D,p.ht,p.h);
xgb  = [xg(1,:); Davg(xg(1:end-1,:),xg(2:end,:)); x0];                      % Frazioni
molari dei gas
xgb  = xgb./repmat(sum(xgb,2),1,p.ncg+1);                                   % Normalizza
le frazioni molari interpolate
MWgb = xgb*p.MWg;                                                           % Peso
molecolare della fase gas (g/mol)
ygb  = xgb.*repmat(p.MWg',m.ns+1,1)./repmat(MWgb,1,p.ncg+1);                % Frazioni
massive dei gas
Tb   = [T(1); Davg(T(1:end-1),T(2:end)); T0];                               % Temperature
(K)
Pb   = [P(1); Davg(P(1:end-1),P(2:end)); bc.Pb];                            % Pressione
(Pa)
cb   = [c(1); Davg(c(1:end-1),c(2:end)); bc.Pb/8.314/T0*10^-6];             %
Concentrazione totale di gas (mol/cm3gas)
cD   = 101325./Pb.*(Tb./1073).^1.75.*(1/2.*porb.*(1+porb));                 % Correzione
diffusività in base a T, P, porosità

% Gradienti ai bordi delle celle
gradT = [0;                                                                 % Gradiente
di temperatura a r = 0
        (T(2:end)-T(1:end-1))./(m.r(2:end)-m.r(1:end-1));                   % Gradiente
di temperatura a 0<r<R
        (Tb(end)-T(end))/(m.rb(end)-m.r(end))];                             % Gradiente
di temperatura a r = R
gradx = [zeros(1,p.ncg+1);                                                  % Gradiente
delle x a r = 0
        (xg(2:end,:)-xg(1:end-1,:))./repmat(m.r(2:end)-m.r(1:end-1),1,p.ncg+1);   %
Gradiente delle x a 0<r<R
        (xgb(end,:)-xg(end,:))./(m.rb(end)-m.r(end))];                      % Gradiente
delle x a r = R

% Termini di generazione
R   = Rrate(p.k,p.K,cg,cs,T,m.ns,p.a0,p.ps);                                % Velocità di
reazione (mol/cm3/s)
rpg = (p.nug*R')';                                                          % Velocità di
produzione dei gas (mol/cm3/s)
rps = (p.nus*R')';                                                          % Velocità di
produzione dei solidi (mol/cm3/s)
Q   = -sum(DH.*R,2);                                                        % Produzione
di calore (W/cm3)

% Bilancio termico
q    = thfluxes(gradT,ktb);                                                 % Flusso
conduttivo (W/cm2)
divq = divf(q,m.rb,1);                                                      % Divergenza
del flusso conduttivo (W/cm3)
dTdt = (-divq+Q)./(rho.*Cp)*(strcmp(modelT,'ISOT')==0);                     % Derivata
della temperatura (K/s)

% Bilancio di concentrazione totale
[~, ~, dpordt] = epps(cs,rps,p.MWs,p.rhoi,m.ns,p.ncs);                      % Derivata
della porosità (1/s)
dPdt    = zeros(m.ns,1);                                                    % Derivata
della pressione (Pa/s)
dcdt    = 1/8.314./T.^2.*(T.*dPdt-P.*dTdt)*1e-6;                            % Derivata
della concentrazione totale di gas (mol/cm3gas/s)
```

```
dcpordt = dpordt.*c+por.*dcdt;                                          % Derivata
della concentrazione totale di gas (mol/cm3tot/s)
Nt      = [0; m.Afv\(-dcpordt+sum(rpg,2))];                             % Flusso
molare totale di gas (mol/cm2/s)

% Bilanci di specie chimica
J = fluxes(modelD,xgb,gradx(:,1:end-1),repmat(cb,1,p.ncg),p.D,cD,m.ns+1,p.ncg+1);   %
Flussi diffusivi molari di gas (mol/cm2/s)
N     = repmat(Nt,1,p.ncg+1).*xgb+J;                                    % Flussi
molari totali delle singole specie gas (mol/cm2/s)
divN  = divf(N(:,1:end-1),m.rb,p.ncg);                                  % Divergenza
dei flussi molari delle specie gas (mol/cm3/s)
dcgdt = -divN+rpg;                                                      % Derivate
delle concentrazioni delle specie gas (mol/cm3/s)
dcsdt = rps;                                                            % Derivate
delle concentrazioni delle specie solide (mol/cm3/s)

% Campi di velocità nel pellet
vstar = Nt./cb;                                                         % Velocità
molare del gas (cm/s)
v     = vstar+sum(ygb./xgb.*J./repmat(cb,1,p.ncg+1),2);                 % Velocità
del gas (cm/s)

if solve.pfr
    % Bilanci di bulk
    rbulk   = N(end,:)'.*p.MWg*4*pi*m.rb(end)^2*1e-3*p.Np;              % Produzione
massiva delle specie gas di bulk (kg/m3tot/s)
    MWbulk  = xbulk*p.MWg;                                              % Peso
molecolare del gas di bulk (kg/kmol)
    rhobulk = cb(end)*MWbulk*1e3;                                       % Densità del
gas di bulk (kg/m3)
    Db      = p.D*1e-4*101325/bc.Pb*(bc.Tb/1073)^1.75;                  % Matrice
delle diffusività di bulk (m2/s)
    Bj      = SM('j',Db,p.ncg+1,xbulk,ybulk);                           % Matrice S-M
per i flussi massivi (s/m2)
    dxdz    = -1/rhobulk*Bj*jbulk(1:end-1);                             % Gradienti
di x bulk (1/m)
    dxdz    = [dxdz; -sum(dxdz)];                                       % Completa la
matrice dei gradienti di x bulk
    Bxy     = xy('xy',p.ncg+1,p.MWg,MWbulk,xbulk,ybulk);                % Matrice di
conversione da gradienti molari a massivi
    dydz    = [Bxy*dxdz(1:end-1); -sum(Bxy*dxdz(1:end-1))];             % Gradienti
di y bulk (1/m)
    drhoudt   = p.us*sum(rbulk);                                        % Derivata
temporale del flusso massivo totale (kg/m2tot/s2)
    dxdt      = p.us*dxdz;                                              % Derivate
temporali di x bulk (1/s)
    djdt      = p.us*(rbulk-rhou*dydz-ybulk'*sum(rbulk));               % Derivate
temporali dei flussi diffusivi massivi (kg/m2tot/s2)
    djdt(end) = -sum(djdt(1:end-1));                                    % Impone
nulla la somma delle derivate dei flussi siffusivi

    % Composizione dei bilanci
    B = [reshape(dcgdt,[],1);                                           % Bilanci di
concentrazione in fase gas (mol/cm3/s)
         reshape(dcsdt,[],1);                                           % Bilanci di
concentrazione in fase solida (mol/cm3/s)
         dTdt                                                           % Bilancio
termico (K/s)
         drhoudt                                                        % Equazione
di continuità di bulk (kg/m2tot/s2)
         dxdt                                                           % Bilancio
delle frazioni massive di bulk (1/s)
         djdt];                                                         % Bilancio
dei flussi diffusivi massivi di bulk (kg/m2tot/s2)
else
    B = [reshape(dcgdt,[],1);                                           % Bilanci di
concentrazione in fase gas (mol/cm3/s)
```

```
        reshape(dcsdt,[],1);                                                % Bilanci di
concentrazione in fase solida (mol/cm3/s)
        dTdt;                                                               % Bilancio
termico (K/s)
        zeros(2*length(xbulk)+1,1)];
end

% Progresso del calcolo
H = waitbar(t/m.t(end));                                                    % Crea la
barra
waitbar(t/m.t(end),H,sprintf('%2.1f %%',t/m.t(end)*100));                   % Segnala il
progresso
if t == m.t(end)
    close(H)                                                                % Chiude la
barra alla fine
end

% Plotting dei profili
if doplot
    subplot(241)
    plot(m.rb/m.rb(end),xgb)
    ylabel('X gas'),legend('CO','CO_2','N_2')
    subplot(242)
    plot(m.r/m.rb(end),cs)
    ylabel('c solidi (mol/cm3)'),legend('Hem','Mag','Wus','Fe')
    subplot(243)
    plot(m.rb/m.rb(end),Tb)
    ylabel('T (K)')
    subplot(244)
    plot(m.rb/m.rb(end),Nt)
    ylabel('Flusso molare totale (mol/cm2/s)')
    subplot(245)
    plot(m.rb/m.rb(end),porb)
    ylabel('porosità')
    subplot(246)
    plot(m.rb/m.rb(end),cb)
    ylabel('c totale gas (mol/cm3)')
    subplot(247)
    plot(m.rb/m.rb(end),J(:,1),m.rb/m.rb(end),N(:,1),m.rb/m.rb(end),Nt)
    ylabel('Flussi molari CO (mol/cm2/s)'),legend('J*','N','N_t')
    subplot(248)
    plot(m.rb/m.rb(end),v,m.rb/m.rb(end),vstar)
    ylabel('velocità del gas (cm/s)'),legend('v','v*')
    drawnow
end
%plot(m.rb,xgb,m.rb(end),xbulk,'o'),title(sprintf('progress = %3.2g
%%',t/m.t(end)*100)),drawnow

% ========================================================================
% Calcolo delle variabili al contorno
% ========================================================================
function [T0 x0] = BC(Tbulk,Pbulk,xbulk,dr,ncg,modelT,modelD,Tend,xend,k,por,D,ht,h)

T0   = Tbulk*(strcmp(modelT,'TB')+strcmp(modelT,'ISOT'))+      ...          % Temperatura
di parete: Caso temperatura fissa alla parete
       (Tend+Tbulk*dr*ht/k)/(1+dr*ht/k)*strcmp(modelT,'FLUX')+ ...          % Temperatura
di parete: Caso flusso termico alla parete
       Tend*strcmp(modelT,'ADIAB');                                         % Temperatura
di parete: Caso senza scambio termico alla parete

c0   = Pbulk/8.314/T0*10^-6;                                                %
Concentrazione totale di gas alla parete (mol/cm3gas)
cD   = 101325/Pbulk*(T0/1073)^1.75*(1/2*por*(1+por));                       % Correzione
diffusività in base a T, P, porosità alla parete
x0   = xbulk;                                                               %
Composizione alla parete di primo tentativo
err  = 1;                                                                   % Inizializza
il calcolo iterativo della composizione alla parete
```

```
while err>1e-5
    gradx0 = (x0(1:end-1)-xend(1:end-1))/dr;                                % Gradiente
di composizione alla parete
    Jb     = fluxes(modelD,x0,gradx0,repmat(c0,1,ncg),D,cD,1,ncg+1);        % Flussi
diffusivi alla parete
    x0new  = xbulk+Jb./h./c0;                                               %
Composizione alla parete uguagliando i flussi diffusivi ai flussi esterni
    err    = norm((x0new-x0)./x0);                                          % Calcolo
dell'errore
    x0     = (x0new+x0)/2;                                                  %
Aggiornamento delle composizioni alla parete
end

% ========================================================================
% Calcolo del campo di porosità
% ========================================================================
function [por rhoa dpordt] = epps(c,dcdt,MW,rhoi,ns,nc)

rhoa = c*MW;                                                                % Densità
apparente (g/cm3)
y    = c.*repmat(MW',ns,1)./repmat(rhoa,1,nc);                              % Frazioni
massive di solido
rhot = 1./(y*(1./rhoi));                                                    % Densità
teorica (g/cm3)
por  = 1-rhoa./rhot;                                                        % Campo di
porosità

if nargout==3
    sdcMWdt = dcdt*MW;                                                      % Derivata
della densità apparente (g/cm3/s)
    dydt    = zeros(ns,nc);                                                 % Inizializza
le derivate delle frazioni massive
    for i=1:nc
        dydt(:,i)=(dcdt(:,i).*MW(i).*rhoa-c(:,i).*MW(i).*sdcMWdt)./rhoa.^2; % Derivate
delle frazioni massive (1/s)
    end
    drhotdt = -(dydt*(1./rhoi)).*rhot.^2;                                   % Derivata
della densità teorica (g/cm3/s)
    drhoadt = sdcMWdt;                                                      % Derivata
della densità apparente (g/cm3/s)
    dpordt  = -(drhoadt.*rhot-rhoa.*drhotdt)./rhot.^2;                      % Derivata
della porosità (1/s)
end

% ========================================================================
% Calcolo delle velocità di reazione --> Meccanismo cinetico
% ========================================================================
function R = Rrate(k,K,cg,cs,T,ns,a0,p)

xs = repmat([2 3 1 1],ns,1).*cs./repmat(cs*[2 3 1 1]',1,4);                 % Conversioni
locali delle specie solide (-)
a  = repmat(a0',ns,1).*xs.^repmat(p,ns,1);                                  % Aree
superficiali per le fasi solide (1/cm)
kr = repmat(k(:,1)',ns,1).*exp(-repmat(k(:,2)',ns,1)/8.314./repmat(T,1,3)); % Costanti
cinetiche (cm/s)

% Velocità di reazione (mol/cm3/s)
R(:,1) = kr(:,1).*(a(:,1).*cg(:,1)-a(:,2).*cg(:,2)./exp(K(1,1)+K(1,2)./T)); % Hematite  -
-> Magnetite
R(:,2) = kr(:,2).*(a(:,2).*cg(:,1)-a(:,3).*cg(:,2)./exp(K(2,1)+K(2,2)./T)); % Magnetite -
-> Wustite
R(:,3) = kr(:,3).*(a(:,3).*cg(:,1)-a(:,4).*cg(:,2)./exp(K(3,1)+K(3,2)./T)); % Wustite   -
-> Ferro
R = real(R);                                                                % Pulisce
eventuali parti immaginarie

% ========================================================================
% Calcolo dei flussi diffusivi
```

```
% ========================================================================
function J = fluxes(model,x,gradx,c,D,cD,ns,n)

J = zeros(ns,n);                                                        % Inizializza
i flussi
switch model
    % Diffusione Fickiana, binaria
    case 'F'
        Df = D(1,2)*repmat(cD,1,n-1);                                   % Correzione
P, T, por
        J(:,1:end-1) = -c.*Df.*gradx;                                   % Legge di
Fick
    % Diffusione Fickiana, diffusività Mixture-Averaged
    case 'MA'
        D0  = (1-x)./(x*(1./D)-x./repmat(diag(D,0)',ns,1));             % Regola di
miscela
        Dma = D0(:,1:end-1).*repmat(cD,1,n-1);                          % Correzione
P, T, por
        J(:,1:end-1) = -c.*Dma.*gradx;                                  % Legge di
Fick
    % Diffusione Stefan-Maxwell
    case 'SM'
        for k=1:ns
            Dk  = D*cD(k);                                              % Correzione
P, T, por
            xk  = x(k,:);                                               % Estrae la
composizione al raggio rk
            Bk  = SM('J',Dk,n,xk);                                      % Calcolo
della matrice B
            Dsm = Bk^-1;                                                % Inversione
della matrice B
            J(k,1:end-1) = -(c(k,:)'.*(Dsm*gradx(k,:)'))';              % Legge di
Fick generalizzata
        end
end
J(:,end) = -sum(J(:,1:end-1),2);                                        % Calcola i
flussi dell'ultima specie per differenza a zero

% ========================================================================
% Matrici di diffusività Stefan-Maxwell
% ========================================================================
function B = SM(flux,D,n,x,y)

B = zeros(n-1,n-1);                                                     % Inizializza
switch flux
    case 'J'                                                            % Matrice per
i flussi molari
        for i=1:n-1
            for j=1:n-1
                B(i,j) = x(i)/D(i,n)+                           ...     % Termini
comuni
                         (sum(x./D(i,:))-x(i)/D(i,i))*(i==j)+ ...       % Termini
della diagonale
                         -x(i)/D(i,j)*(i~=j);                           % Termini
fuori dalla diagonale
            end
        end
    case 'j'                                                            % Matrice per
i flussi massivi
        for i=1:n-1
            for j=1:n-1
                B(i,j) = x(i)/y(j)*(y(j)/D(i,n)*x(n)/y(n)+      ...     % Termini
comuni
                         (sum(x./D(i,:))-x(i)/D(i,i))*(i==j)+ ...       % Termini
della diagonale
                         -x(j)/D(i,j)*(i~=j));                          % Termini
fuori dalla diagonale
            end
```

```
        end
end

% ========================================================================
% Matrici di conversione dei gradienti di frazioni
% ========================================================================
function Bxy = xy(dir,n,MWi,MW,x,y)

Bxy = zeros(n-1,n-1);                                                   % Inizializza
switch dir
    case 'xy'
        for i=1:n-1
            for j=1:n-1
                Bxy(i,j) = MWi(i)/MW*((i==j)+x(i)/MW*(MWi(n)-MWi(j)));      % Matrice per
passare dai gradienti di x ai gradienti di y
            end
        end
    case 'yx'
        for i=1:n-1
            for j=1:n-1
                Bxy(i,j) = MW/MWi(i)*((1==j)+y(i)*MW*(1/MWi(n)-1/MWi(j)));  % Matrice per
passare dai gradienti di y ai gradienti di x
            end
        end
end
% ========================================================================
% Calcolo dei flussi conduttivi
% ========================================================================
function q = thfluxes(gradT,k)

q = -k.*gradT;                                                          % Legge di
Fourier

% ========================================================================
% Calcolo delle divergenze dei flussi
% ========================================================================
function df = divf(f,r,nb)

% Estensione della matrice dei raggi in base al numero di bilanci
r  = repmat(r,1,nb);                                                    % Matrice
delle coordinate dei bordi (cm)
% Applicazione dei volumi finiti
df = 3*(r(2:end,:).^2.*f(2:end,:)-r(1:end-1,:).^2.*f(1:end-1,:))./ ...      % Differenza
dei flussi
    (r(2:end,:).^3-r(1:end-1,:).^3);                                    % Divide per
il volume

% ========================================================================
% Calcolo delle variabili ai bordi
% ========================================================================
function D = Davg(D1,D2)
model = 'armonica';                                                     % Modello
utilizzato
switch model
    case 'aritmetica'
        D = (D1+D2)./2;                                                 % Media
aritmetica
    case 'armonica'
        D = 2./(1./D1+1./D2);                                           % Media
armonica
end

% ========================================================================
% Calcolo dei residui
% ========================================================================
function res = bcfun(ya,yb,modelD,modelT,doplot)
global bc
```

```
X0  = [reshape(ic.cgpor0,[],1)                                                  %
Condizioni iniziali per il bilancio fase gas
       reshape(ic.cs0,[],1)                                                     %
Condizioni iniziali per il bilancio fase solida
       reshape(ic.T0,[],1)];                                                    %
Condizioni iniziali per il bilancio termico

Xend = [bc.rhouend
        bc.xend(1:end-1)'];

res = [ya(1:ns*(ncg+ncs+1))-X0
       yb(ns*(ncg+ncs+1)+1:end-ncg-1)-Xend
       ya(end-ncg:end)                      ];

function myres = res(x,t,X0,Xend,modelD,modelT)
global p

x        = [x; 1-sum(x(end-p.ncg+1:end)); zeros(p.ncg+1,1)];
[~, X]   = ode15s(@DAEfun,t,[X0; x],[],modelD,modelT,false);
Xendc = X(end,end-2*(p.ncg+1):end)';
myres    = Xend(1:3)-Xendc(1:3);
fprintf('          |    IN    |   END    |   OBJ    |  \n')
fprintf(' Flux     | % 3.3f  | % 3.3f  | % 3.3f  | \n',x(1),Xendc(1),Xend(1))
fprintf(' x CO     |  %3.4f  | % 3.4f  | % 3.4f  | \n',x(2),Xendc(2),Xend(2))
fprintf(' x CO2    |  %3.4f  | % 3.4f  | % 3.4f  | \n',x(3),Xendc(3),Xend(3))
fprintf(' x N2     |  %3.4f  | % 3.4f  | % 3.4f  | \n\n',1-x(2)-x(3),1-Xendc(2)-
Xendc(3),1-Xend(2)-Xend(3))
```

Continuous particle model with implemented finite differences. Isothermal model

```
function [t, C] = PelletF(par,msh,bc)
clc
close all
% Parameters

N  = par.ng;
NS = par.ns;

P = par.P;
T = par.T;
c = P/8.314/T*1e-6;

MWg = par.MWg;
D   = par.D*(T/1073)^1.75;
Dk  = 4850*par.dp*sqrt(T./MWg);
tau = par.tau;
cst = par.cst;

nr    = par.nr;
kall  = par.k;
k     = kall(1:nr).*exp(-kall(nr+1:end)/8.314/T);
nu    = par.nu;
alpha = par.a;
kin   = {k, nu, c, alpha};


% Mesh
L   = msh.r0;
m   = 2;
nx  = msh.nx;
```

```
dx  = L/nx;

x   = (0:dx:L);
xh  = (x(1:end-1)+x(2:end))/2;
xm  = x.^m;
xhm = xh.^m;
ig  = 1:N*(nx+1);
is  = N*(nx+1)+1:(N+NS)*(nx+1);

t  = msh.t;

% Boundary Conditions
bc1 = [ones(N,1) zeros(N,2)];
bc2 = [zeros(N,1) ones(N,1) -bc.x0];

b1  = [2*bc1(:,1)/dx./(3*bc1(:,1)/2/dx-bc1(:,2)) ...
      -bc1(:,1)/2/dx./(3*bc1(:,1)/2/dx-bc1(:,2)) ...
            bc1(:,3)./(3*bc1(:,1)/2/dx-bc1(:,2)) ];
b2  = [2*bc2(:,1)/dx./(3*bc2(:,1)/2/dx-bc2(:,2)) ...
      -bc2(:,1)/2/dx./(3*bc2(:,1)/2/dx-bc2(:,2)) ...
            bc2(:,3)./(3*bc2(:,1)/2/dx-bc2(:,2)) ];
bcc = 0;
a   = -1;

% Initial Conditions
x0  = repmat(zeros(N,1),1,nx+1);
cv  = zeros(nx+1,1);
cs0 = bc.cs0;

Uold = [reshape(x0,[],1); cs0];

% Processing
docalc = true;
modelD = 'S';
if docalc
    tic
    % Inizializzazione
    niter = length(t);
    dt    = t(2)-t(1);
    [Ab, B ] = boundary(N,NS,nx,b1,b2);
    [Cc, Bc] = makeCc(nx,dx,xm,bcc,a);
    I = speye((N+NS)*(nx+1),(N+NS)*(nx+1));
    I(1:N,1:N) = 0;
    I(ig(end)-N+1:ig(end),ig(end)-N+1:ig(end)) = 0;
    Ucap = Uold;
    S = makeS(N,NS,nx,nr,kin,Uold(ig),Uold(is),cs0);
    [e, E, ES] = por(N,NS,nx,Uold(is),S(is),cst,c);
    A = makeA(N,NS,nx,dx,xm,xhm,D,Dk,Uold(ig),c,modelD,e/tau);
    C = makeC(N,NS,nx,dx,xm,cv,a);
    bold = (I+dt/2*E*(A-C+ES))*Uold+dt/2*E*S;
    solg = zeros(nx+1,N,niter+1);
    sols = zeros(nx+1,NS,niter+1);
    solg(:,:,1) = (reshape(Uold(ig),N,[]))';
    sols(:,:,1) = (reshape(Uold(is),NS,[]))';

    % Time step iteration
    for i=2:niter
        dt  = t(i)-t(i-1);
        err = 1;
        while err>1e-6
            Jcap = makeJ(N,NS,nx,nr,kin,Ucap(ig),Ucap(is),cs0);             % Jacobian of
the source term
            Scap = makeS(N,NS,nx,nr,kin,Ucap(ig),Ucap(is),cs0);             % Source term
(reactions)
            [e, Ecap, EScap, ESc] = por(N,NS,nx,Ucap(is),Scap(is),cst,c);   % Porosity
field
            Acap = makeA(N,NS,nx,dx,xm,xhm,D,Dk,Ucap(ig),c,modelD,e/tau);   % Matrice di
diffusione
```

```
            Ccap = makeC(N,NS,nx,dx,xm,cv,a);                                   % Matrice di
convezione
            AA = (I-dt/2*Ecap*(Acap+Jcap-Ccap+EScap))+Ab;                       % Compone la
matrice del sistema
            b  = bold+dt/2*Ecap*(Scap-Jcap*Ucap)+B;                             % Compone il
termine noto del sistema
            Unew = AA\b;                                                        % Risolve le
composizioni

            Sc = (sum(reshape(Scap(1:ig(end)),N,[]),1))'+Bc;                    % Source term
per l'equazione di continuità
            cv = Cc\(Sc+ESc);                                                   % Risolve
l'equazione di continuità
            err  = norm(Unew-Ucap)/((N+NS)*(nx+1));                             % Calcola
convergenza
            Ucap = Unew;                                                        % Aggiorna
vettore delle incognite
        end
        Uold = Unew;
        Ucap = Uold;
        A = Acap;
        C = Ccap;
        S = Scap;
        E = Ecap;
        ES = EScap;
        bold = (I+dt/2*E*(A-C+ES))*Uold+dt/2*E*S;

        solg(:,:,i) = (reshape(Uold(ig),N,[]))';
        sols(:,:,i) = (reshape(Uold(is),NS,[]))';
        %plot(x,cv),drawnow,pause(.5)
        %waitbar(i/niter)
    end
    %etime = toc
    %save('PelletRedux.mat','x','t','solg','sols')
else
    %load 'PelletRedux.mat'
end

% Post processing
% for i=1:length(t)
%     subplot(121)
%     plot(x/x(end),sols(:,:,i))
%     ylim([0 5e-2])
%     subplot(122)
%     plot(x/x(end),solg(:,:,i))
%     ylim([0 0.5])
%     drawnow%,pause(0.5)
% end
ni = zeros(length(t),NS);
for i=1:length(t)
    for j=1:NS
        ni(i,j) = trapz(x,4*pi*x.^2.*(sols(:,j,i)'));
    end
end
mi = ni.*repmat(par.MWs',length(t),1);
cox = ni(1,:);
cred = [0 0 2*cox(1) 2*cox(2) cox(5)-cox(2)];
mred = cred*par.MWs;
mox  = cox*par.MWs;
R0   = mox-mred;
C = sum(mi,2);
C = (C(1)-C)/R0;
figure
plot(t,C),ylim([0 1])

% -------------------------------------------------------------------------
% MATRICI
% -------------------------------------------------------------------------
```

```
% Boundary conditions
function [Ab, Bb] = boundary(N,NS,nx,bc1,bc2)

[T, Bb] = BoundaryMat(N,nx,bc1,bc2);
Ab = sparse(T(:,1),T(:,2),T(:,3),(N+NS)*(nx+1),(N+NS)*(nx+1));
Bb = [Bb; zeros(NS*(nx+1),1)];


% Matrice di diffusione
function A = makeA(N,NS,nx,dx,x,xh,D,Dk,U,c,model,etau)

T = DiffusionMat(dx,x,xh,D,Dk,U(1:(nx+1)*N),c,model,etau);
A = sparse(T(:,1),T(:,2),T(:,3),(N+NS)*(nx+1),(N+NS)*(nx+1));


% Matrice di convezione
function C = makeC(N,NS,nx,dx,x,U,a)

T = ConvectionMat(N,nx,dx,x,U,a);
C = sparse(T(:,1),T(:,2),T(:,3),(N+NS)*(nx+1),(N+NS)*(nx+1));


% Equazione di continuità
function [Cc, Bc] = makeCc(nx,dx,x,bc,a)

T  = ContinuityMat(nx,dx,x,a);
Cc = sparse(T(:,1),T(:,2),T(:,3),(nx+1),(nx+1));
Bc = zeros(nx+1,1);
Bc(1) = bc;


% Source term
function S = makeS(N,NS,nx,nr,pars,cg,cs,cs0)

S = SourceMat(N,NS,nx,nr,pars{1},pars{2},pars{3},cg,cs,cs0,pars{4});


% Jacobian of the source term
function J = makeJ(N,NS,nx,nr,pars,U,cs,cs0)

T = JacobianMat(N,NS,nx,nr,pars{1},pars{2},pars{3},U,cs,cs0,pars{4});
J = sparse(T(:,1),T(:,2),T(:,3),(N+NS)*(nx+1),(N+NS)*(nx+1));


% Porosity field
function [e, E, ES, ESc] = por(N,NS,nx,cs,rs,cst,c)

[e, ed, esd, ESc] = PorosityMat(N,NS,nx,cs,rs,cst,c);
E  = spdiags(ed,0,(N+NS)*(nx+1),(N+NS)*(nx+1));
ES = spdiags(esd,0,(N+NS)*(nx+1),(N+NS)*(nx+1));
```

Appendix D: Fortran codes

In this section, we report the Fortran codes used to calculate the discretization finite different matrices used to implement the single particle model. These codes were compiled as Mex-files and used as Matlab functions.

```
!-------------------------------------------------------------------------
!     Boundary condition matrices
!-------------------------------------------------------------------------
      SUBROUTINE boundary(n,nx,bc1,bc2,T,BB)

      INTEGER n, nx

      DOUBLE PRECISION bc1(n,3), bc2(n,3)
      DOUBLE PRECISION T(6*n,3), BB(n*(nx+1))

      ! Boundary 1
      T(1:3*n,1:2) = RESHAPE(SOURCE = (/ (/1:n/), (/1:n/), (/1:n/),
     +                  (/1:3*n/) /), SHAPE = (/3*n,2/))
      T(1:n,3) = 1
      T(n+1:2*n,3) = -bc1(1:n,1)
      T(2*n+1:3*n,3) = -bc1(1:n,2)

      ! Boundary 2
      T(3*n+1:6*n,1:2) = RESHAPE(SOURCE = (/ (/n*nx+1:n*(nx+1)/),
     +               (/n*nx+1:n*(nx+1)/), (/n*nx+1:n*(nx+1)/),
     +               (/n*(nx-2)+1:n*(nx+1)/) /),SHAPE = (/3*n,2/))
      T(5*n+1:6*n,3) = 1
      T(4*n+1:5*n,3) = -bc2(1:n,1)
      T(3*n+1:4*n,3) = -bc2(1:n,2)

      BB(1:n*(nx+1)) = 0
      BB(1:n) = bc1(1:n,3)
      BB(nx*n+1:n*(nx+1)) = bc2(1:n,3)

      END SUBROUTINE
```

```
!-------------------------------------------------------------------------
!     Continuity matrix
!-------------------------------------------------------------------------
      SUBROUTINE continuity(nx,dx,x,a,T)

      INTEGER i, nx
      DOUBLE PRECISION dx, x(nx+1), a
      DOUBLE PRECISION T(2*(nx-1)+4,3)
```

```
    T(1:2*(nx-1)+4,1:3) = 0
    T(1,1:3) = (/ 1,1,1 /)
    IF (a .GT. 0) THEN
      DO i = 2,nx
        T(1+2*(i-2)+1,1:2) = (/ i,i-1 /)
        T(1+2*(i-2)+1,3)   = -x(i-1)/x(i)/dx
        T(1+2*(i-1),1:2)   = (/ i,i /)
        T(1+2*(i-1),3)     = 1/dx
      END DO
      T(2*(nx-1)+2,1:2) = (/ nx+1,nx-1 /)
      T(2*(nx-1)+2,3)   = (x(nx+1)-x(nx))/(x(nx)-x(nx-1))
      T(2*(nx-1)+3,1:2) = (/ nx+1,nx   /)
      T(2*(nx-1)+3,3)   = -(x(nx+1)-x(nx-1))/(x(nx)-x(nx-1))
      T(2*(nx-1)+4,1:3) = (/ nx+1,nx+1,1 /)
    ELSE
      DO i = 2,nx
        T(1+2*(i-2)+1,1:2) = (/ i,i+1 /)
        T(1+2*(i-2)+1,3)   = x(i+1)/x(i)/dx
        T(1+2*(i-1),1:2)   = (/ i,i /)
        T(1+2*(i-1),3)     = -1/dx
      END DO
      T(2*(nx-1)+2,1:2) = (/ nx+1,1 /)
      T(2*(nx-1)+2,3)   = (x(2)-x(1))/(x(3)-x(1))-1
      T(2*(nx-1)+3,1:3) = (/ nx+1,2,1 /)
      T(2*(nx-1)+4,1:2) = (/ nx+1,3 /)
      T(2*(nx-1)+4,3)   = -(x(2)-x(1))/(x(3)-x(1))
    END IF

    END SUBROUTINE


!-------------------------------------------------------------------------------
!    Convection matrix
!-------------------------------------------------------------------------------
    SUBROUTINE convection(n,nx,dx,x,U,a,T)

    INTEGER i, n, nx
    DOUBLE PRECISION dx, x(nx+1), a
    DOUBLE PRECISION U(nx+1)
    DOUBLE PRECISION T(2*n*(nx-1),3)

    T(1:2*n*(nx-1),1:3) = 0
    IF (a .GT. 0) THEN
      DO i = 2,nx
        T((i-2)*2*n+1:(i-2)*2*n+n,1) = (i-1)*n+(/1:n/)
        T((i-2)*2*n+1:(i-2)*2*n+n,2) = (i-2)*n+(/1:n/)
        T((i-2)*2*n+1:(i-2)*2*n+n,3) = -(U(i-1)*x(i-1)/x(i)/dx)

        T((i-2)*2*n+n+1:(i-1)*2*n,1) = (i-1)*n+(/1:n/)
        T((i-2)*2*n+n+1:(i-1)*2*n,2) = (i-1)*n+(/1:n/)
```

```
      T((i-2)*2*n+n+1:(i-1)*2*n,3) = (U(i)/dx)
    END DO
  ELSE
    DO i = 2,nx
      T((i-2)*2*n+1:(i-2)*2*n+n,1) = (i-1)*n+(/1:n/)
      T((i-2)*2*n+1:(i-2)*2*n+n,2) = (i)*n+(/1:n/)
      T((i-2)*2*n+1:(i-2)*2*n+n,3) = (U(i+1)*x(i+1)/x(i)/dx)

      T((i-2)*2*n+n+1:(i-1)*2*n,1) = (i-1)*n+(/1:n/)
      T((i-2)*2*n+n+1:(i-1)*2*n,2) = (i-1)*n+(/1:n/)
      T((i-2)*2*n+n+1:(i-1)*2*n,3) = -(U(i)/dx)
    END DO
  END IF

  END SUBROUTINE


!-------------------------------------------------------------------------------
!   Diffusion matrix
!-------------------------------------------------------------------------------
  SUBROUTINE diffusion(model,n,nx,dx,x,xh,D,Dk,U,c,etau,T)

  INTEGER i, j, k, n, nx
  INTEGER ii(3*n**2), jj(3*n**2)
  CHARACTER (LEN=*) :: model
  DOUBLE PRECISION dx, x(nx+1), xh(nx), c, etau(nx+1)
  DOUBLE PRECISION D(n+1,n+1), Dk(n+1), U((nx+1)*n)
  DOUBLE PRECISION DD(n,n,nx+1)
  DOUBLE PRECISION xi(n+1), Di(n,n), Dc(n,3*n)
  DOUBLE PRECISION T(3*n**2*(nx-1),3)

  k = 0
  DO i = 1,3*n
    DO j = 1,n
      k = k+1
      ii(k) = j
      jj(k) = i
    END DO
  END DO

  DD(1:n,1:n,1:nx+1) = 0
  DO i = 1,nx+1
    xi(1:n) = U((i-1)*n+1:i*n)
    xi(n+1) = 1-sum(U((i-1)*n+1:i*n))
    CALL diffusionmat(model,D*etau(i),Dk,xi,n+1,Di)
    DD(1:n,1:n,i) = Di
  END DO

  ! Inner nodes
  DO i = 2,nx
    Dc(1:n,1:n) = (DD(1:n,1:n,i-1)+DD(1:n,1:n,i))*xh(i-1)
```

```
      Dc(1:n,n+1:2*n) = -(DD(1:n,1:n,i-1)*xh(i-1)+
     +            DD(1:n,1:n,i+1)*xh(i)+(xh(i)+xh(i-1))*DD(1:n,1:n,i))
      Dc(1:n,2*n+1:3*n) = (DD(1:n,1:n,i+1)+DD(1:n,1:n,i))*xh(i)
      Dc = Dc*c/(x(i)*2*dx**2)

      T((i-2)*3*n**2+1:(i-1)*3*n**2,1) = ii+(i-1)*n
      T((i-2)*3*n**2+1:(i-1)*3*n**2,2) = jj+(i-2)*n
      T((i-2)*3*n**2+1:(i-1)*3*n**2,3) = RESHAPE(Dc,(/3*n**2/))
    END DO

    END SUBROUTINE
!-------------------------------------------------------------------------------
!    Computation of diffusion matrix
!-------------------------------------------------------------------------------
    SUBROUTINE diffusionmat(model,D,Dk,x,n,Dij)

    INTEGER i, j, n
    CHARACTER (LEN=*) :: model
    DOUBLE PRECISION D(n,n), Dk(n), x(n), Dij(n-1,n-1)
    DOUBLE PRECISION B(n-1,n-1), xx(n,n), Dn(n,n), xD(n,n)

    SELECT CASE (model)
    CASE ("F")
      B(1:n-1,1:n-1) = 0
      DO i = 1,n
        B(i,i) = 1/D(i,n)+1/Dk(i)
      END DO

    CASE ("M")
      B(1:n-1,1:n-1) = 0
      DO i = 1,n
        xx(i,1:n) = x(i)
      END DO
      xD = xx/D
      DO i = 1,n-1
        B(i,i) = (sum(xD(1:n,i))-x(i)/D(i,i))/(1-x(i))+1/Dk(i)
      END DO

    CASE ("S")
      DO i = 1,n
        xx(i,1:n) = x(i)
        Dn(i,1:n) = D(i,n)
      END DO
      xD = xx/D
      DO j = 1,n-1
        B(1:n-1,j) = xx(1:n-1,j)/Dn(1:n-1,j)-xD(1:n-1,j)
        B(j,j) = B(j,j)+sum(xD(1:n,j))+1/Dk(j)
      END DO

    END SELECT
```

```
    CALL inversesub(B,n-1,Dij)

    END SUBROUTINE

!-------------------------------------------------------------------------------
!    Computation of inverse matrix
!-------------------------------------------------------------------------------
    SUBROUTINE inversesub(A,n,B)

    INTEGER i, j, n
    DOUBLE PRECISION A(n,n), B(n,n), Aa(n,2*n)

    DO i = 1,n
      DO j = 1,n
        B(i,j) = 0
      END DO
      B(i,i) = 1
      Aa(i,1:n) = A(i,1:n)
      Aa(i,n+1:2*n) = B(i,1:n)
    END DO
    DO j = 1,n-1
      DO i = j+1,n
        IF (Aa(j,j) .NE. 0) THEN
          Aa(i,1:2*n) = Aa(i,1:n*2)-Aa(i,j)/Aa(j,j)*Aa(j,1:2*n)
        END IF
      END DO
    END DO
    DO j = n,2,-1
      DO i = 1,j-1
        IF (Aa(j,j) .NE. 0) THEN
          Aa(i,1:2*n) = Aa(i,1:n*2)-Aa(i,j)/Aa(j,j)*Aa(j,1:2*n)
        END IF
      END DO
    END DO
    DO i = 1,n
      B(i,1:n) = Aa(i,n+1:2*n)/Aa(i,i)
    END DO

    END SUBROUTINE


!-------------------------------------------------------------------------------
!    Reaction rates
!-------------------------------------------------------------------------------
    SUBROUTINE rates(n,ns,nr,k,nu,c,x,cs,cs0,alpha,rp)

    INTEGER n, ns, nr
    DOUBLE PRECISION k(nr), nu(n+ns,nr), c, x(n)
    DOUBLE PRECISION cs(ns), cs0(ns), alpha
    DOUBLE PRECISION rr(nr), rp(n+ns)
```

```
    rr(1:nr) = 0
    IF (cs(1) .GT. 0) THEN
      rr(1) = k(1)*c*x(1)*(cs(1)/cs0(1))**alpha
    END IF
    IF (cs(2) .GT. 0) THEN
      rr(2) = k(2)*c*x(1)*(cs(2)/cs0(2))**alpha
    END IF

    CALL mtimes(nu,rr,(/n+ns,nr/),(/nr,1/),rp)

    END SUBROUTINE

!-------------------------------------------------------------------------------
!    Jacobian
!-------------------------------------------------------------------------------
    SUBROUTINE grates(n,ns,nr,k,nu,c,x,cs,cs0,alpha,jrp)

    INTEGER n, ns, nr
    DOUBLE PRECISION k(nr), nu(n+ns,nr), c, x(n)
    DOUBLE PRECISION cs(ns), cs0(ns), alpha
    DOUBLE PRECISION jrr(nr,n+ns), jrp(n+ns,n+ns)

    jrr(1:nr,1:n+ns) = 0

    IF (cs(1) .GT. 0) THEN
      jrr(1,1) = k(1)*c*(cs(1)/cs0(1))**alpha
      jrr(1,n+1) = k(1)*c*x(1)/cs0(1)**alpha*alpha*cs(1)**(alpha-1)
    END IF
    IF (cs(2) .GT. 0) THEN
      jrr(2,1) = k(2)*c*(cs(2)/cs0(2))**alpha
      jrr(2,n+2) = k(2)*c*x(1)/cs0(2)**alpha*alpha*cs(2)**(alpha-1)
    END IF

    CALL mtimes(nu,jrr,(/n+ns,nr/),(/nr,n+ns/),jrp)

    END SUBROUTINE

!-------------------------------------------------------------------------------
!            Matrix product
!-------------------------------------------------------------------------------
    SUBROUTINE mtimes(a,b,sa,sb,c)

    INTEGER sa(2), sb(2), i, j, k
    DOUBLE PRECISION a(sa(1),sa(2)), b(sb(1),sb(2)), c(sa(1),sb(2))

    DO i = 1, sa(1)
      DO j = 1, sb(2)
        c(i,j) = 0
        DO k = 1, sa(2)
          c(i,j) = c(i,j) + a(i,k)*b(k,j)
        END DO
```

```
      END DO
    END DO

    END SUBROUTINE mtimes


!-------------------------------------------------------------------------
!    Porosity field
!-------------------------------------------------------------------------
    SUBROUTINE porosity(n,ns,nx,cs,rs,cst,c,por,E,ES,ESc)

    INTEGER i, n, ns, nx
    DOUBLE PRECISION c, cst(ns)
    DOUBLE PRECISION cs(ns*(nx+1)), rs(ns*(nx+1))
    DOUBLE PRECISION por(nx+1), ESc(nx+1), dpordt(nx+1)
    DOUBLE PRECISION E((n+ns)*(nx+1)), ES((n+ns)*(nx+1))
    DOUBLE PRECISION csi(nx+1,ns), rsi(nx+1,ns)

    DO i = 1,nx+1
      csi(i,1:ns) = cs((i-1)*ns+1:i*ns)
      rsi(i,1:ns) = rs((i-1)*ns+1:i*ns)
    END DO

    CALL mtimes(csi,1/cst,(/nx+1,ns/),(/ns,1/),por)
    CALL mtimes(rsi,1/cst,(/nx+1,ns/),(/ns,1/),dpordt)
    por = 1-por
    dpordt = -dpordt

    E(1:(n+ns)*(nx+1))  = 1
    ES(1:(n+ns)*(nx+1)) = 0
    ESc(1:nx+1)         = 0
    DO i = 2,nx
      E((i-1)*n+1:i*n) = 1/(c*por(i))
      ES((i-1)*n+1:i*n) = -c*dpordt(i)
    END DO
    ESc(2:nx) = -c*dpordt(2:nx)

    END SUBROUTINE


!-------------------------------------------------------------------------
!    Source vector
!-------------------------------------------------------------------------
    SUBROUTINE source(n,ns,nx,nr,k,nu,c,x,cs,cs0,alpha,S)

    INTEGER i, n, ns, nx, nr
    DOUBLE PRECISION k(nr), nu(n+ns,nr), c, x(n*(nx+1))
    DOUBLE PRECISION cs(ns*(nx+1)), cs0(ns*(nx+1)), alpha
    DOUBLE PRECISION rp(n+ns), S((n+ns)*(nx+1))

    S(1:(n+ns)*(nx+1)) = 0
```

```
      DO i = 1,nx+1
        CALL rates(n,ns,nr,k,nu,c,x((i-1)*n+1:i*n),
     +           cs((i-1)*ns+1:i*ns),cs0((i-1)*ns+1:i*ns),alpha,rp)
        IF ((i .NE. 1) .AND. (i .NE. nx+1)) THEN
          S((i-1)*n+1:i*n) = rp(1:n)
        END IF
          S(n*(nx+1)+(i-1)*ns+1:n*(nx+1)+i*ns) = rp(n+1:n+ns)
      END DO

      END SUBROUTINE

!-----------------------------------------------------------------------------
!     Jacobian matrix
!-----------------------------------------------------------------------------
      SUBROUTINE jacobian(n,ns,nx,nr,k,nu,c,x,cs,cs0,alpha,T)

      INTEGER i, j, l, m, n, ns, nx, nr
      DOUBLE PRECISION k(nr), nu(n,nr), c, x(n*(nx+1))
      DOUBLE PRECISION cs(ns*(nx+1)), cs0(ns*(nx+1)), alpha
      DOUBLE PRECISION ij(n+ns), jrp(n+ns,n+ns)
      DOUBLE PRECISION T((n+ns)**2*(nx+1)-2*n*(n+ns),3)

      m = 0
      T(1:(n+ns)**2*(nx+1)-2*n*(n+ns),1:3) = 0
      DO l = 1,nx+1
        ij = (/ (l-1)*n+1:l*n, n*(nx+1)+(l-1)*ns+1:n*(nx+1)+l*ns /)
        CALL grates(n,ns,nr,k,nu,c,x((l-1)*n+1:l*n),
     +           cs((l-1)*ns+1:l*ns),cs0((l-1)*ns+1:l*ns),alpha,jrp)
        DO i = 1,n+ns
          IF (((l .NE. 1) .AND. (l .NE. nx+1)) .OR. (i .GT. n)) THEN
            DO j = 1,n+ns
              m = m+1
              T(m,1:3) = (/ ij(i), ij(j), jrp(i,j) /)
            END DO
          END IF
        END DO
      END DO

      END SUBROUTINE
```

References

[1] J. Szekely, J. W. Evans, and H. Y. Sohn, *Gas solid reactions*: Academic Press, 1976.

[2] P. A. Ramachandran and L. K. Doiraiswamy, "Modeling of Noncatalytic Gas-Solid Reactions," *AIChE J.,* vol. 28, pp. 881-900, 2004.

[3] Y. C. Wen, "Noncatalytic heterogeneous solid fluid reaction models," *Ind. Eng. Chem.,* vol. 60, pp. 34-54, 1968.

[4] S. P. Trushenski, K. Li, and W. O. Philbrook, "Non-Topochemical reduction of iron oxides," *Metall. Trans.,* vol. 5, pp. 1149-1158, 1974.

[5] S. K. Bhatia and D. D. Perlmutter, "A random pore model for fluid-fluid reactions, I: isothermal, kinetic control," *AIChE J.,* vol. 26, pp. 379-386, 1980.

[6] A. K. Sadhukhan, P. Gupta, and R. K. Saha, "Characterization of porous structure of coal char from a single devolatilized coal particle: Coal combustion in a fluidized bed," *Fuel Proc. Tech.,* vol. 90, pp. 692-700, 2009.

[7] A. Gomez-Barea and P. Ollero, "An approximae method for solving gas-solid non-catalytic reactions," *Chem. Eng. Sci.,* vol. 61, pp. 3725-3735, 2006.

[8] F. Patisson, M. G. Francois, and D. Ablitzer, "A non-isothermal, non-equimolar transient kinetic model for gas-solid reactions," *Chem. Eng. Sci.,* vol. 53, pp. 697-708, 1998.

[9] M. S. Valipour and Y. Saboohi, "Modeling of multiple noncatalytic gas-solid reactions in a moving bed of porous pellets based on finite volume method," *Heat Mass Transfer,* vol. 43, pp. 881-894, 2007.

[10] J. Szekely and J. W. Evans, "Studies in gas–solid reactions: part I. A structural model for the reaction of porous oxides with a reducing gas," *Metall. Trans. 2,* pp. 1691–1711, 1971.

[11] L. D. Schmidt, *The Eingineering of Chemical Reactions*. New York: Oxford University Press, 1998.

[12] S. Yagi and D. Kunii, "Studies on combustion of carbon particles in flames and fluidized beds," *The 5th symposium on combustion,* vol. New York, USA, pp. 231-236, 1955.

[13] A. Abad, J. Adanez, A. Cuadrat, F. Garcia-Labiano, P. Gayan, and L. F. de Diego, "Kinetics of redox reactions of ilmenite for chemical-looping combustion," *Chem. Eng. Sci.,* vol. 66, pp. 689-702, 2011.

[14] A. Amiri, G. D. Ingram, A. V. Bekker, I. Livk, and N. E. Maynard, "A multi-stage, multi-reaction shrinking core model for self-inhibiting gas-solid reactions," *Adv. Powder Technol.,* vol. 24, pp. 728-736, 2013.

[15] P. K. Gbor and C. Q. Jia, "Critical evaluation of coupling particle size distribution with the shrinking core model," *Chem. Eng. Sci.,* vol. 59, pp. 1979-1987, 2004.

[16] H. Kruggel-Emden, S. Rickelt, F. Stepanek, and M. A., "Development and testing of an interconnected multiphase CFD-model for chemical looping combustion," *Chem. Eng. Sci.,* vol. 65, pp. 4732-4745, 2010.

[17] H. Kruggel-Emden, F. Stepanek, and M. A., "A study on the role of reaction modeling in Multi-phase CFD-based simulations of Chemical Looping Combustion," *Oil Gas Sci. Tech.,* vol. 66, pp. 313-331, 2011.

[18] D. R. Parisi and M. A. Laborde, "Modeling of counter current moving bed gas-solid reactor used in direct reduction of iron ore," *Chem. Eng. J.,* vol. 104, pp. 35-43, 2004.

[19] E. D. Negri, O. M. Alfano, and M. G. Chiovetta, "Direct Reduction of Hematite in a Moving-Bed Reactor. Analysis of the Water Gas Shift Reaction Effects on the Reactor Behavior," *Ind. Eng. Chem. Res.,* vol. 30, pp. 474-482, 1991.

[20] M. Ohmi and T. Usui, "Improved theory on the rate of reduction of single particles and fixed beds of iron oxide pellets with hydrogen," *Trans. ISIJ,* vol. 22, pp. 66-74, 1982.

[21] Y. Hara, M. Tsuchiya, and S. Kondo, "Intraparticle temperature of iron-oxide pellet during the reduction," *Tetsu-to-Hagane,* vol. 60, pp. 1261-1270, 1974.
[22] Comsol Multiphysics v4.2, COMSOL Inc. www.comsol.com [Online]. Available: www.comsol.com
[23] MathWorks MATLAB R2011a www.mathworks.com [Online].
[24] D. Dalle Nogare, A. Zugliano, A. Primavera, T. Melchiori, and P. Canu, "Multiphysics simulation of a DRP shaft furnace," *Proc. Steelsim2013,* 2013.
[25] R. Artoni, A. Zugliano, A. Primavera, P. Canu, and A. Santomaso, "Simulation of dense granular flows: comparison with experiments," *Chem. Eng. Sci.,* vol. 66, pp. 548-557, 2011.
[26] H. Yamaoka and Y. Kamei, "A three dimensional mathematical simulation model of shaft type reduction furnace and cupola type melting furnace," *Tetsu-to-Hagané,* vol. 74, pp. 2254–2261, 1988.
[27] J. Xu, S. Wu, M. Kou, and K. Du, "Numerical analysis of the characteristics inside pre-reduction shaft furnace and its operation parameters optimization by using a three-dimensional full scale mathematical model," *ISIJ Intern.,* vol. 53, pp. 576–582, 2013.
[28] N. Towhidi and J. Szekely, "The influence of carbon deposition of the reduction kinetics of commercial grade hematite pellets with CO, H2 and N2," *Metall. Trans. B,* vol. 148, pp. 359–366, 1983.
[29] Q. T. Tsay, W. H. Ray, and J. Szekely, "The modeling of hematite reduction with hydrogen plus carbon monoxide mixtures. Part I: the behavior of single pellets," *AIChE J.,* vol. 22, pp. 1064-1072, 1976.
[30] Q. T. Tsay, R. W.H., and S. J., "The modeling of hematite reduction with hydrogen plus carbon monoxide mixtures: Part II. The direct reduction process in shaft furnace arrangement," *AIChE J.,* vol. 22, pp. 1072–1079, 1976.
[31] Y. Shigeno, T. Sakakibara, and Y. Omori, "In situ measurement of effective gas diffusivity through hematite pellets during stepwise reductions," *Metall. trans. B,* pp. 677–687, 1990.
[32] GRImech3.0, Gas Research Institute, Berkeley Mechanical Engineering Dept. www.me.berkeley.edu/grimech/ [Online].
[33] R. B. Bird, W. E. Stewart, and E. N. Lightfoot, *Transport phenomena*, 2nd edition ed.: Wiley, 2002.
[34] R. Taylor and R. Krishna, *Multicomponent mass transfer*: Wiley, 1993.
[35] G. Salejova, Z. Grofa, O. Solcovab, P. Schneiderb, and J. Koseka, "Strategy for predicting effective transport properties of complex porous structures," *Comp. Chem. Eng.,* vol. 35, pp. 200-211, 2011.
[36] F. J. Valdes-Parada and J. Alvarez-Ramirez, "On the effective diffusivity under chemical reaction in porous media," *Chem. Eng. Sci.,* vol. 65, pp. 4100-4104, 2010.
[37] A. Abad, F. Garcıia-Labiano, L. de Diego, P. Gayan, and J. Adanez, "Reduction kinetics of Cu-, Ni-, and Fe-based oxygen carriers using syngas (CO + H2) for Chemical-Looping Combustion," *Energy Fuels,* vol. 21, pp. 1843-1853, 2007.
[38] A. Rubel, K. Liu, J. Neathery, and D. Taulbee, "Oxygen carriers for chemical looping combustion of solid fuels," *Fuel,* vol. 88, pp. 876-884, 2009.
[39] H. Jin and M. Ishida, "Reactivity study on a novel hydrogen fueled chemical looping combustion," *Int. J. Hydr. Energy* vol. 26, pp. 889-894, 2001.
[40] P. Erri and A. Varma, "Diffusional effects in nickel oxide reduction kinetics," *Ind. Eng. Chem. Res.,* vol. 48, pp. 4-6, 2009.
[41] S. Roux, A. Bensakhria, and G. Antonini, "Study and improvement of the regeneration of metallic oxides used as oxygen carriers for a new combustion process," *Int. J. Chem. React. Eng.,* vol. 4, p. A38, 2006.
[42] H. Tian, K. Chaudhari, T. Simonyi, J. Poston, T. Liu, T. Sanders, G. Veser, and R. Siriwardane, "Chemical-looping combustion of coal-derived synthesis gas over copper oxide oxygen carriers," *Energy Fuels,* vol. 22, pp. 3744-3755, 2008.
[43] L. F. de Diego, F. García-Labiano, J. Adánez, P. Gayán, A. Abad, and B. M. e. a. Corbella, "Development of Cu-based oxygen carriers for chemical-looping combustion," *Fuel,* vol. 83, pp. 1749-1757, 2004.

[44] Q. Zafar, T. Mattisson, and B. Gevert, "Redox investigation of some oxides of transition-state metals Ni, Cu, Fe, and Mn supported on SiO2 and MgAl2O4," *Energy Fuels,* vol. 20, pp. 34-44, 2006.

[45] H. Leion, T. Mattisson, and A. Lyngfelt, "Use of ores and industrial products as oxygen carriers in chemical-looping combustion," *Energy Fuels,* vol. 23, pp. 2307-2315, 2009.

[46] H. Leion, A. Lyngfelt, M. Johansson, E. Jerndal, and T. Mattisson, "The use of ilmenite as an oxygen carrier in chemical-looping combustion," *Chem. Eng. Res. Des.,* vol. 86, pp. 1017-1026, 2008.

[47] J. Adanez, A. Cuadrat, A. Abad, P. Gayan, L. F. de Diego, and F. Garcia-Labiano, "Ilmenite activation during consecutive redox cycles in Chemical-Looping Combustion," *Energy Fuels,* vol. 24, pp. 1402-1413, 2010.

[48] D. Bhogeswara Rao and M. Rigaud, "Kinetics of the oxidation of Ilmenite," *Oxid. Metals,* vol. 9, pp. 99-116, 1975.

[49] M. M. Azis, E. Jerndal, H. Leion, T. Mattisson, and A. Lyngfelt, "On the evaluation of synthetic and natural ilmenite using syngas as fuel in chemical-looping combustion (CLC)," *Chem. Eng. Res. Des.,* vol. 88, pp. 1505-1514, 2010.

[50] S. Noorman, F. Gallucci, M. Van SintAnnaland, and J. A. M. Kuipers, "A theoretical investigation of CLC in packed beds. Part 1: Particle model," *Chem. Eng. J.,* vol. 167, pp. 297-307, 2011.

[51] Z. Zhou, L. Han, and G. M. Bollas, "Model-based analysis of bench-scale fixed-bed units for chemical-looping combustion," *Chem. Eng. J.,* vol. 233, pp. 331-348, 2013.

[52] L. Han, Z. Zhou, and G. M. Bollas, "Heterogeneous modeling of chemical-looping combustion. Part1: Reactor model," *Chem. Eng. Sci.,* vol. 104, pp. 233-249, 2013.

[53] S. Sotirchos and H. Yu, "Mathematical modelling of gas-solid reactions with solid product," *Chem. Eng. Sci.,* vol. 40, pp. 2039-2052, 1985.

[54] K. Dam-Johansen, P. Hansen, and K. Ostergaard, "High temperature reaction between sulphur dioxide and limestone- III. A grain-micrograin model and its verification," *Chem. Eng. Sci.,* vol. 46, pp. 847-853, 1991.

[55] P. den Hoed and A. Luckos, "Oxidation and reduction of Iron-Titanium oxides in Chemical Looping Combustion: A phase-chemical description," *Oil Gas Sci. Technol.,* vol. 66, pp. 249-263, 2011.

[56] G. Boole, *A treatise on the calculus of finite differences, 2nd ed.*: Macmillan and Company, 1872.

[57] J. Cranck and P. Nicolson, "A practical method for numerical evaluation of solutions of partial differential equations of the heat conduction type," *Proc. Camb. Phil. Soc.,* vol. 43, pp. 50-67, 1947.

[58] A. Niksiar and A. Rahimi, "A study on deviation of noncatalytic gas–solid reaction models due to heat effects and changing of solid structure," *Powder Technol.,* vol. 193, pp. 101-109, 2009.

[59] F. Patisson and D. Ablitzer, "Physicochemical and thermal modelling of the reaction between a porous pellet and a gas," *Powder Technol.,* vol. 128, pp. 300-305, 2002.

[60] A. K. Sadhukhan, P. Gupta, and R. K. Saha, "Modelling of combustion characteristics of high ash coal char particles at high pressure: Shrinking reactive core model," *Fuel,* vol. 89, pp. 162-169, 2010.

[61] O. Levenspiel, *Chemical Reaction Engineering, 3rd edition*: John Wiley and Sons, 1999.

[62] M. Ishida and C. Y. Wen, "Comparison of zone-reaction model and unreacted-core shrinking model in solid-gas reactions - I Isothermal analysis," *Chem. Eng. Sci.,* vol. 26, pp. 1031-1041, 1971.

[63] D. D. Do, "On the validity of the shrinking core model in non catalytic gas solid reaction," *Chem. Eng. Sci.,* vol. 37, pp. 1477-1481, 1982.

[64] T. Melchiori and P. Canu, "Improving the quantitative description of reacting porous solids: critical analysys of the shrinking core model by comparison to the generalized grain model," *Ind. Eng. Chem. Res., accepted, in press*.

[65] J. Villadsen and M. L. Michelsen, *Solution of differential equation models by polynomial approximation*: Prentice-Hall, 1978.

[66] A. Afshar Ebrahimi, H. Ale Ebrahim, and E. Jamshidi, "Solving partial differential equations of gas–solid reactions by orthogonal collocation," *Comp. Chem. Eng.,* vol. 32, pp. 1746-1759, 2008.

Acknowledgements

I would like to thank prof. Martin van Sint Annaland and prof. Fausto Gallucci, who hosted me in the Multiphase Reactors research group at TU/e for eight months, and gave me the opportunity to improve my research activity. Many thanks to all the people from SMR group, particularly to Maria for her support on the experimental part. I would also like to mention Luca, Arash, Lucia, Valentina, José, and all the other friends that I met in Eindhoven.

Ringraziamenti

Vorrei fare un grosso ringraziamento al mio relatore, prof. Paolo Canu, per tutto quanto fatto per me in questi anni, e con cui posso dire di aver trovato un bellissimo rapporto. Grazie a lui ho scelto la strada del dottorato, e con il senno di poi gli sono molto riconoscente per avermi spinto in questa direzione. Da lui ho imparato moltissimo, non solo a livello della ricerca in sé ma anche per quanto riguarda tutto il mondo che le sta attorno. Insomma è stato per me molto più che una guida. Un ringraziamento particolare a Nicola, che ha trasformato l'atmosfera del nostro gruppo di ricerca rendendola fantastica, dentro e fuori le mura dell'Università. Vorrei anche ringraziare Alberto e Micol, e tutti i ragazzi tesisti che ho conosciuto purtroppo solo nell'ultimo anno, con cui abbiamo condiviso quest'ultimo periodo assieme. Non da ultimo, vorrei ringraziare la mia famiglia per tutto il supporto datomi in questi anni, e per avermi sostenuto in ogni mia scelta che ho fatto fino ad ora. Infine un grandissimo grazie al mio gruppo di amici storici, in particolare Pip, Leo e Nick, e tutti gli altri per cui la vita ha voluto che le nostre strade si separassero nel tempo. A tutte le persone che mi sono care, e che ora sto per lasciare, va un forte abbraccio di affetto e riconoscenza.